CRANFIELD UNIVERSITY

WILLIAM CAMILLERI

AN ASSESSMENT OF HIGH OVERALL PRESSURE RATIO INTERCOOLED ENGINES FOR CIVIL AVIATION

SCHOOL OF ENGINEERING

PhD Thesis
Academic Year: 2011 - 2014

Supervisor: Dr.Vishal Sethi
January 2014

CRANFIELD UNIVERSITY

SCHOOL OF ENGINEERING

PhD Thesis

Academic Year 2011 - 2014

WILLIAM CAMILLERI

AN ASSESSMENT OF HIGH OVERALL PRESSURE RATIO INTERCOOLED ENGINES FOR CIVIL AVIATION

Supervisor: Dr. Vishal Sethi

January 2014

This thesis is submitted in partial fulfilment of the requirements for the degree of PhD

ABSTRACT

As gas turbine technology matures, further significant improvements in engine efficiency will be difficult to achieve without the implementation of new aero-engine configurations. This thesis delivers an original contribution to knowledge by comparing the design, performance, fuel burn and emission characteristics of a novel geared intercooled reversed flow core concept with those of a conventional geared intercooled straight flow core concept. This thesis also outlines a novel methodology for the characterisation of uncertainty at the conceptual design phase which is useful for the comparison of competing concepts. Conventional intercooled aero-engine concepts suffer from high over-tip leakage losses in the high pressure compressor, high pressure losses in the intercooler installation and increased weight and drag whereas the geared intercooled reversed flow core concept overcomes some of these limitations.

The HP-spool configuration of the reversed core concept allows for an increase in blade height, a reduction in over-tip leakage losses and an increase in overall pressure ratio. It was concluded that a 1-pass intercooler would be the lightest and most compact design while a 2-pass intercooler would be easier to manufacture. In the reversed flow core concept the increased length of the 2-pass intercooler could be accommodated. In this concept the mixer also allows for a reduction in fan pressure ratio and a useful reduction in component losses. Both intercooled concepts were shown to benefit from the use of a variable area bypass nozzle for the reduction of take-off combustor outlet temperature and cruise specific fuel consumption.

The intercooled cycles were optimised for minimum fuel burn and it was found that the reversed flow core concept benefits from higher overall pressure ratio and lower fan pressure ratio for an equivalent specific thrust. This leads to an improvement in thermal efficiency and more than a 1.6% improvement in block fuel burn. The NO_x during landing and take-off as well as during cruise was found to be slightly more severe for the reversed flow core concept due to its higher overall pressure ratio. The contrails emissions of this concept were occasionally higher than for a year 2000 turbofan but only slightly higher than for the straight core concept. This dissertation shows that in spite of input uncertainty the reversed flow core intercooled engine is a promising concept. Further research should focus on higher fidelity structural and aerodynamic modelling.

ACKNOWLEDGMENTS

I would especially like to thank Dr. Vishal Sethi, my thesis supervisor, for his guidance, encouragement and patience during the course of this research work. Without his support this thesis would not have been possible.

I am grateful to Andrew Rolt (Rolls-Royce plc) for providing his technical guidance. His willingness to share his time and expertise is very much appreciated.

I would like to thank John Borradaile, Dr. Panagiotis Laskaridis and Dr. Konstantinos Kyprianidis (Cranfield University) for the valuable assistance which they offered throughout this research. I am also thankful to Professor Tomas Grönstedt and Xin Zhao (Chalmers University of Technology) for the assistance they provided with respect to the modelling of the intercooler.

I am particularly grateful to Dr. David Zammit-Mangion who made it possible for me to pursue this research. I will always be thankful for his encouragement and conviction.

During my time at Cranfield University I have been fortunate to work with Eduardo Anselmi Palma who has been a good friend and colleague. I would like to offer him my heartfelt thanks. I have also worked closely with Rukshan Navaratne. I appreciate greatly his advice and friendship.

My deepest gratitude is reserved for my parents Vivien and Emanuel and for my wife Cathryn to whom I am eternally indebted for all their love and support.

This work is financially supported by the E.U. under the "LEMCOTEC – Low Emissions Core-Engine Technologies", a Collaborative Project co-funded by the European Commission within the Seventh Framework Programme (2007-2013) under the Grant Agreement n° 283216

Dedicated to my beautiful wife Cathryn

TABLE OF CONTENTS

LIST OF FIGURES

LIST OF TABLES

1 Research Context and Objectives

1.1 Nomenclature

ACARE	Advisory Council for Aeronautics Research in Europe
CAEP	Committee on Aviation Environmental Protection
CO	Carbon Monoxide
EASA	European Aviation Safety Agency
GISFC	Geared Intercooled Straight Flow Core Engine Concept
GIRFC	Geared Intercooled Reversed Flow Core Engine Concept
HP	High Pressure
HPC	High Pressure Compressor
ICAO	International Civil Aviation Organization
IPC	Intermediate Pressure Compressor
IPCC	Intergovernmental Panel on Climate Change
LEMCOTEC	Low Emission Core Engine Technologies
LP	Low Pressure
LTO	Landing and Take-Off Cycle
NO_x	Nitrogen Oxides
OPR	Overall Pressure Ratio
SFC	Specific Fuel Consumption
SFN	Specific Thrust
TRL	Technology Readiness Level
UEET	Ultra-Efficient Engine Technologies
UHC	Unburned Hydrocarbons

1.2 Introduction

The objective of this thesis is to report the main findings of a detailed analysis carried out on a novel intercooled aero-engine concept. The concept is a geared intercooled reversed-flow core (GIRFC) turbofan engine and was conceived in order to overcome several limitations encountered with previous generations of intercooled turbofan concepts. These limitations included the decline in component efficiencies at high OPRs, high losses in the intercooler matrix and ducting as well as increased weight and drag due to the intercooler installation. This dissertation explores specific design features of the GIRFC concept and through an interdisciplinary performance analysis shows how some of these difficulties can be mitigated.

The primary aim of this chapter is to outline the context within which this dissertation has been carried out and to identify the necessity for this research. The objectives of this thesis, which lead to a valid contribution to knowledge, are to:

a. Assess the novel design features of the GIRFC concept.
b. Compare the performance characteristics of the GISFC and GIRFC concept.
c. Evaluate and compare the fuel burn and emission characteristics of the GISFC and GIRFC.
d. Assess the uncertainty in the predicted performance of the GISFC and GIRFC.

This dissertation contributes towards a European Union 7th Framework Programme called LEMCOTEC. The objective of LEMCOTEC is to further enhance "*Low Emission Core Engine Technologies*" from where the name derives. LEMCOTEC is mainly intended to evaluate technologies intended for entry into service around the year 2020 in line with the European Union's vision for aviation discussed hereafter. In LEMCOTEC, conceptual design work is also being carried out on new concepts which could be viable beyond 2020 in order to prepare for the next generation of turbofan technology. This dissertation is looking at one such concept, which could further enhance the environmental credentials of turbofan technology beyond what is expected to be reached by 2020.

1.3 Context and Motivation

The civil aviation market has grown steadily at a rate of approximately 5% per annum since the early 1960's [(1)]. According to market surveys carried out by Airbus [(2)] and Boeing [(3)], this growth is expected to continue at a similar rate within the 2010 to 2030 period and is being driven by the increasing size of the global middle class especially in emerging markets. Airbus [(2)] suggests that within this period, fleet replacements and market growth will represent 38% and 62% of the market share respectively. The total number of in-service single aisle aircraft is expected to more than double by 2032 with the sale of new single aisle aircraft expected to represent the largest revenue. This trend is brought about by the increase in regional flights in Asia, the growth of regional travel in emerging economies as well as the expansion of low cost carriers [(3)]. By 2032, twin aisle jets are expected to represent 31% of the world fleet in terms of units but 44% in terms of value. The growth of the twin-aisle market is being driven by fleet replacement with more efficient aircraft such as the B787 and the A350 as well as by significant new demand [(3)]. The significance of this growth to aero-engine manufacturers is also considerable. Trends in the commercial aircraft market, for the 2010 to 2029 period are reported by Rolls-Royce [(4)]. Engines with thrust in excess of 45,000lb, intended mainly for twin aisle commercial-aircraft, represent the major share of the market in terms of value. Single aisle aircraft engines represent the second most valuable sector and these are typically within the 22,000lb to 45,000lb class. Given the extent to which both engines types are used and the market value which they represent, it is understandable that the majority of investment in aero-engine research and development is targeted at these two broad engine classes.

The growth in air traffic which has occurred over the last 50 years has meant that the environmental impact of civil aviation has increased dramatically. These concerns are not new and it can be seen that, in the past, much effort has gone towards improving local air quality and reducing noise levels at and around airports. Growing concern about climate change has placed new pressure on legislators and aircraft and engine manufacturers to address CO_2 and pollutant emissions at all phases of flight and not only during LTO phases. The IPCC is a scientific body established by the United Nations and the World Meteorological Organisation to study the

effects of climate change. At the request of the ICAO, the IPCC carried out a first assessment of the impact of aviation on climate change [5]. In the updated Fourth Assessment Report of the IPCC [6], it was reaffirmed that aviation is responsible for 2% of global greenhouse gas emissions through engine related CO_2 emissions. In addition, the report states that for the global mean temperature increase to be limited to within 2°C, CO_2 emissions must be reduced by 50% - 85% by 2050. At present there is no legally binding international agreement for the reduction of CO_2 emissions from aviation sources. The Copenhagen Accord recognises that a significant reduction in global anthropogenic emissions is required to limit the continued increase in global mean temperatures as suggested by the IPCC Fourth Assessment Report. Although the Kyoto Protocol expired in 2012, the Copenhagen Accord does not enact a new legally binding framework.

The ICAO [7] recognises the importance of not only CO_2 but also of other pollutant species such as water vapour, NO_x, sulphur oxides, hydrocarbons and black carbon (or soot) particles. The contribution of CO_2 emissions towards radiative forcing are relatively well understood. However, the contribution of NO_x, taking into account its role in ozone formation and methane destruction, is less understood. Similarly, water vapour from aero-engines can trigger the formation of contrails if the atmospheric conditions are favourable. Particulate emissions and aerosol formation can also serve as cloud condensation nuclei which encourage the formation of condensation trails. As for NO_x, the exact contribution of water vapour towards global warming is not fully understood. A suitable metric relating the different types of emissions is difficult to define making it difficult for legislators to properly implement a binding legal framework.

The only international agreement currently limiting the emission from civil aviation is contained within Annex 16 of the Convention on International Civil Aviation which deals with Environmental Protection. Volume 1 of Annex 16 is related to aircraft noise while Volume 2 of Annex 16 is related to aircraft emissions. In 1981 the ICAO set limits on LTO NO_x, CO, UHC as well as soot. Noise as well as air quality are mainly of concern to residents living in the vicinity of airports for reasons of personal health and comfort. The Committee on Aviation Environmental Protection (CAEP) has continued to develop the standards set in Annex 16 of the original

convention. Since the establishment of the CAEP, several major updates to Annex 16 have occurred establishing more stringent noise and NO_x limits for newly produced engines. As shown in Figure 1.1, CAEP/8 is the most recent tier and sets stringent NO_x limits. For noise the CAEP Chapter 4 requirements came into force in 2006. Noise levels are limited at three certification points: flyover, side-line and approach level. The CAEP Chapter 4 requirements reduce the allowed noise levels by a further 2EPNdb at each certification point and by 10EPNdb cumulatively when compared with the CAEP Chapter 3 requirements. Figure 1.2 summarises the changes in cumulative noise requirements that have occurred over time.

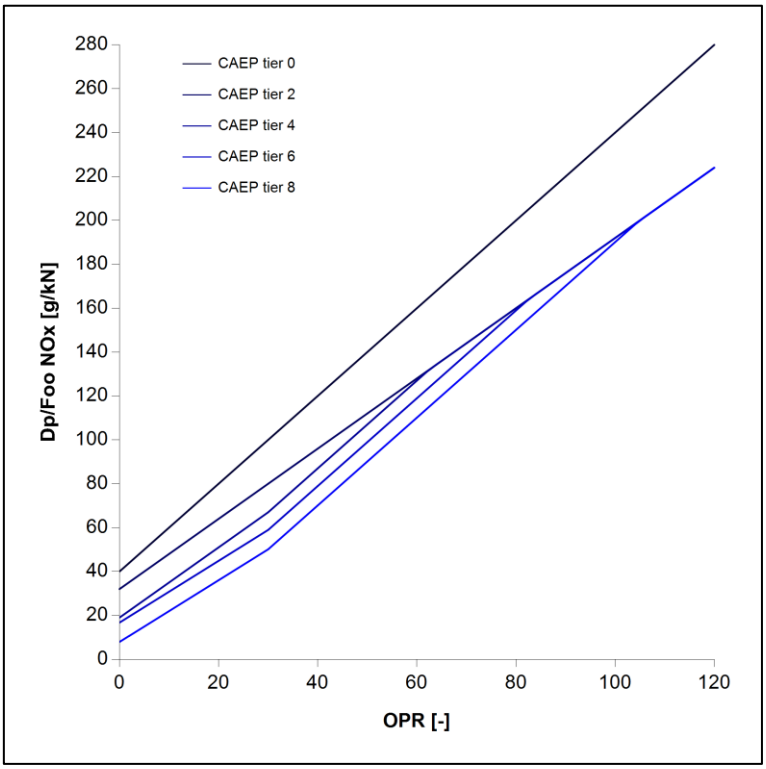

Figure 1.1 – CAEP NO_x Restrictions (tiers from Environmental Protection Agency [8])

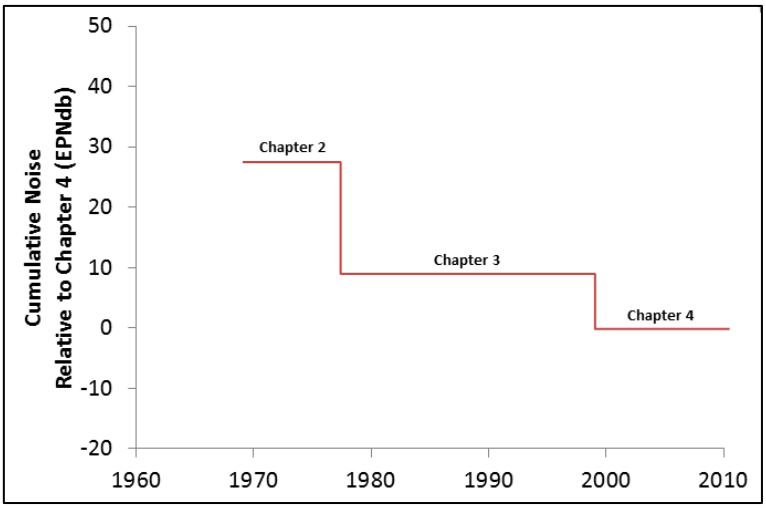

Figure 1.2 – CAEP Noise Restrictions (adapted from ICAO [7])

European legislation refers to the Convention on International Civil Aviation in two legislative acts, specifically Regulations No. 216/2008 and No. 1702/2003. These regulations establish the EASA as well as lay out the basis for obligatory type certification criteria outlined in EASA Certification Specifications. These regulations adopt the requirements outlined in the Convention on International Civil Aviation. This means that in the European Union, the requirements outlined in Annex 16 of the Convention on International Civil Aviation are legally binding. Nevertheless, in the European Union efforts are underway to reduce the environmental impact of aviation beyond the internationally recognised limits. The highly contentious Emissions Trading Scheme was intended to include aviation within its fold starting in 2012. In the Emissions Trading Scheme airline operators are given a number of CO_2 allowances which can be traded or banked. Each year a number of allowances has to be surrendered corresponding to the actual amount of CO_2 produced. This carbon trading scheme puts pressure on the operator to reduce CO_2 emissions by treating CO_2 allowances as a commodity that can be bought or sold. Within the European Union, the Emissions Trading Scheme has come into force but outside the bloc there has been significant resistance to the plan. In response, the scheme has been postponed by one year in the hope that a broader agreement can be reached through the ICAO. The reduction of fuel consumption, emissions and the management of climate change are a central part of the EU's vision for aeronautics. The Advisory Council for Aeronautics Research in Europe (ACARE) is a group of European public

and private stakeholders that has set ambitious goals for the European aviation industry. Part of the Strategic Research Agenda is aimed at the environment [9]. The ACARE 2020 environmental objectives aim to:

a. Reduce fuel consumption and CO_2 emissions by 50%.
b. Reduce perceived external noise by 50%.
c. Reduce NO_x by 80%.
d. Make substantial progress in reducing the environmental impact of the manufacture, maintenance and disposal of aircraft and related products.

These objectives are for the complete aircraft system and therefore include improvements in airframe and engine technologies as well as operational and air traffic management changes. The engine contribution towards these goals must account for:

a. A 6 EPNdB reduction in noise at each certification point.
b. An 80% reduction in NO_x emissions.
c. A 20% reduction in CO_2 emissions.

In Europe, significant public investment has been allocated towards achieving these goals. Several European Framework Programmes dealing with aviation and the environment have been jointly funded through public private investments. Among the most well-known of these projects in the field of aero-engine development are VITAL [10] [11], NEWAC [12], and LEMCOTEC. Several research papers have come out of these projects and, where relevant, are referred to in this thesis. While involvement in these projects is voluntary, both academic and industrial partners from all sectors of aeronautics participate due to the high degree of public investment geared towards developing the next generation of technologies that will be required to meet future legislation. The European Union's long term goals for aviation have now also been established [13]. The objective for 2050 is to develop technologies (both aircraft and engine) to allow for a 75% reduction in CO_2 emissions per passenger kilometre, a 90% reduction in NO_x emissions and a reduction in perceived noise emission of 65% relative to the year 2000.

In the USA, work is also underway to reduce the environmental impact of aviation. Projects such as Ultra-Efficient Engine Technologies (UEET) [14] and Continuous Low Energy, Emission and Noise (CLEEN) [15] are being carried out with the involvement of major engine manufacturers such as Pratt and Whitney and General Electric as well as NASA and several academic institutions. The NASA N+3 objectives also set out ambitious goals for 2025 including the development of technology (to a technology readiness level of 4-6) aimed at reducing NO_x by 75% compared with CAEP/6, fuel burn by 70% and noise by 70dB below chapter 4 requirements.

1.4 Overview of Concept

The pursuit of higher thermo-propulsive efficiency is motivated by the need to reduce fuel consumption and CO_2 emissions. These goals are moving engine designs towards higher OPRs and lower SFNs. As OPR continues to increase, problems related to compressor weight, HPC exit blade height, compressor delivery temperature and NO_x emissions are likely to be aggravated. An intercooler transfers heat from the core compression system to a secondary cooling flow thereby reducing compressor delivery temperature and compressor specific work. Although intercooling can be seen as a loss of available energy from the core, it allows higher OPRs to be reached and it increases the available combustor temperature rise for a given combustor temperature limit. Intercooled cycles optimised for higher OPRs can therefore deliver improvements in thermal efficiency when compared with conventional cycles of similar component size but with lower OPRs.

In this dissertation, a novel GIRFC engine, depicted in Figure 1.3, is considered. The GIRFC concept was conceived in response to some of the limitations which were encountered with previous intercooled engine concepts described in Rolt et al. [16] which were studied in the NEWAC project [12]. These limitations included high losses in the intercooler matrix and headers, high structural loads and small HPC blade heights leading to high over-tip leakage losses which limit OPR. In the GIRFC concept the HP-spool is located in tandem with the LP-spool. The core flow is directed from the exit of the booster to the rear of the engine from where it is re-directed forwards through the reversed HPC, combustor and turbine stages. The

repositioned HP spool offers several advantages including isolation from high structural loads in the forward part of the engine. Without the LP-shaft restriction, the HPC diameter can also be reduced, thereby allowing for longer blades and faster rotation. These changes lead to lower tip losses and reduced penalties for smaller blades at higher OPR, significantly improving efficiency. In the GIRFC design the IPC and HPC are widely separated, allowing for increased design freedom when positioning the intercooler. Efficient diffusion of the IPC exit and bypass off-take flows in the intercooler entry ducts is necessary in order to minimise intercooler inlet and matrix losses. The length available in the GIRFC design allows for gradual diffusion of the flows, hence minimising losses. A requirement of this layout is the need to redirect the core exhaust emerging from the reversed flow turbines in the middle of the engine. This favours a mixed exhaust configuration with chutes which turn the core exhaust flow around to mix it with the bypass flow. Clearly, several challenges are associated with this design including the implementation of cross-over ducting, the effect of mixing and the implications of the architecture on the overall weight of the concept. The evolution of the GIRFC as well as a more detailed description of the concept is provided in chapter 2.

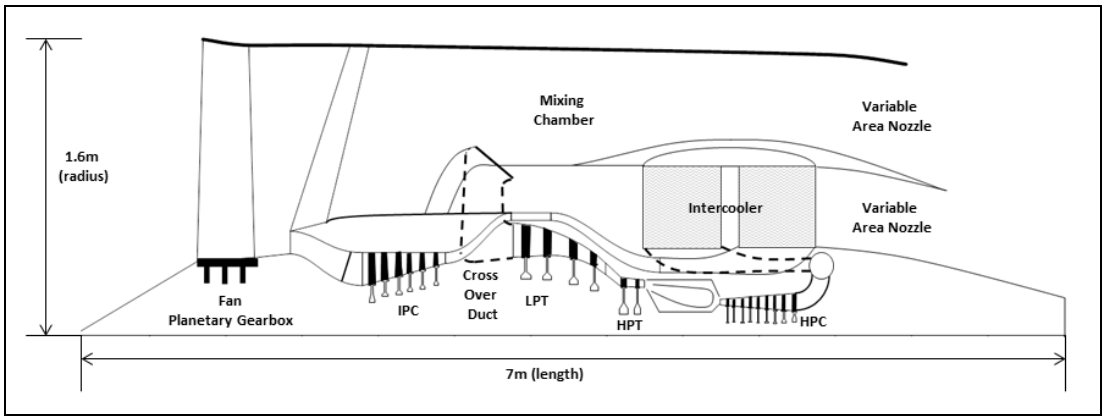

Figure 1.3 – GIRFC Concept (Optimised Configuration)[1]

[1] The author recognises the contribution of Eduardo Anselmi Palma, a PhD student at Cranfield University, who prepared the engine general arrangement shown in this figure. In his research Eduardo Anselmi Palma is investigating the mechanical arrangement and losses within the GIRFC concept.

1.5 Contribution to Knowledge and Scope

The research carried out within this thesis is restricted to a feasibility assessment of a novel intercooled engine concept aimed at 2025. The focus of this research is the comparison of the novel GIRFC concept's performance with that of the more conventional GISFC concept. The GISFC and GIRFC concepts are also benchmarked against an existing conventional turbofan; specifically the Trent 772, although in this case the performance benefits are not examined in detail. A detailed examination of the differences between a turbofan with a conventional core and an advanced turbofan with an intercooled core is not given in this dissertation as this was already addressed in previous research activities carried out in NEWAC [(12)]. In this thesis, the TF2000 engine model, which represents a Trent 772 type engine, is only used as a year 2000 reference point. The studies presented in this thesis are carried out at a relatively low level of fidelity as is typical at the conceptual design phase. The main objectives of this thesis are to:

a. Assess the novel design features of the GIRFC concept.
b. Compare the performance characteristics of the GISFC and GIRFC concept.
c. Evaluate and compare the fuel burn and emission characteristics of the GISFC and GIRFC.
d. Assess the uncertainty in the predicted performance of the GISFC and GIRFC.

The intercooled engine configuration, outlined in this research, incorporates a number of features including an intercooler, an isolated HP-spool, a mixed exhaust, a variable area intercooler nozzle and a variable area common nozzle. Each of these features is studied in detail in this thesis. This thesis contributes to knowledge through:

a. A coupled performance and installation analysis for the intercooler modules.
b. The simultaneous optimisation of the bypass nozzle and intercooler nozzle area for minimum fuel burn and so as to limit take-off combustor outlet temperatures.
c. The evaluation of the GIRFC HP-spool, including discs, blades and annulus in order to show to how these are affected by the absence of the LP-shaft constraint.
d. The study of the effects of a mixed exhaust in a high bypass ratio engine.

A multi-disciplinary approach has been used to optimise and assess the concepts outlined in this thesis. Cycle optimisation for minimum fuel burn has been carried out for each concept. Cruise operation has also been optimised for minimum fuel burn, NO_x and contrail emissions. The studies contribute to knowledge through:

a. The comparison of the fuel burn character tics of two intercooled concepts as well as the comparison to a year 2000 concept.
b. The integration of an LDI NO_x model within the optimisation framework as well as the evaluation and comparison of cruise NO_x for each engine.
c. The optimisation of intercooler variable area nozzle operation, bypass variable area nozzle operation and cruise altitude for minimum cruise NO_x for each concept.
d. The integration of a contrail prediction model within the optimisation framework as well as the evaluation and comparison of persistent contrail emissions for each engine for a given set of test cases.
e. The optimisation of intercooler variable area nozzle operation, bypass variable area nozzle operation and cruise altitude for minimum persistent contrail emissions.

Conceptual engine design is often carried out at a relatively low level of fidelity. The feasibility of a concept is therefore subject to a high degree of uncertainty. The uncertainty in the predicted engine performance is usually not considered at this stage which means that it can be difficult to firmly state that an engine concept is promising when compared to an objective or when compared to another concept. Therefore this thesis contributes to knowledge by introducing a subjective uncertainty analysis methodology for use at the conceptual design stage. This method allows for the early evaluation of input parameter uncertainty. In this thesis, this method has been used to assess the effect of uncertainty on the predicted fuel burn and weighted NO_x predictions. The implementation of this method has been restricted to the input parameters which differentiate the GIRFC and GISFC. The method established in this work could also be used to compare other competing designs and could easily be extended to assess the effect of uncertainty on other critical parameters such as cost, risk and noise.

1.6 Thesis Structure

This chapter provides a general introduction to the project goals and scope. In chapter 2 a detailed background to the research is presented. This chapter outlines the main trends in aero-engine development, previous work on intercooled engines and describes engine configurations similar to the GIRFC. This is necessary as it shows how the GIRFC concept was conceived. A detailed description of the GIRFC is also provided. In chapter 3, the general methodology applied in this thesis is discussed. It identifies that the research activities carried out within this thesis fall within the scope of conceptual design. The methodology is presented at a high level and outlines the main steps required for interdisciplinary conceptual engine design. More detailed methodology regarding the design or evaluation of specific features is presented as required in the following chapters and appendices.

Chapters 4 to 6 investigate three of the main features which differentiate the GIRFC from the GISFC; specifically the design of the HP-spool, the design of the intercooler and the performance of the mixer. Each of these chapters incorporates relevant background and methodology as well as detailed parametric analysis required for the understanding and sizing of each component. In chapter 7, the results of an interdisciplinary optimisation are presented where all the features of the GISFC and GIRFC are examined in unison. The fuel-burn characteristics of each concept are the focus of chapter 7 although some attention is also given to the NO_x and contrail characteristics. In chapter 8, the general conclusions of this research are highlighted and recommendations for further research are made. In the appendices additional details regarding the engine, aircraft, weight and emissions models are given.

1.7 Publications

The work carried out during the course of this dissertation led to the following publications:

a. **Chircop, K., Camilleri, W., Sethi, V. & Zammit-Mangion, D.** "Multi-Objective Optimisation of a constrained 2000 km Trajectory using Genetic Algorithms", 3rd CEAS Air & Space Conference, 24-28 October 2011, Nice, France
b. **Camilleri, W., Chircop, K., Zammit-Mangion, D., Sabatini, R. & Sethi, V.** "Design and Validation of a detailed Aircraft Performance Model for Trajectory Optimization", AIAA Modelling & Simulation Technologies Conference, 13-16 August 2012, Minneapolis, Minnesota
c. **Camilleri W., Anselmi E., Vishal S., Laskaridis P., Rolt A., Cobas P.** "Performance Assessment of a Geared Turbofan with Intercooling and a Reverse Flow Core", ISABE Conference, September 2013, Busan, South Korea
d. **Sethi V., Camilleri W., Singh R., Pilidis P., Ogaji S., Celis C., di Lorenzo G., Zammit-Mangion D.** "Energy Plant Selection and Asset Management The TERA (Techno-Economic Environmental Risk Analysis)" ISABE Conference, September 2013, Busan, South Korea
e. **Navaratne R., Camilleri W., Najafi E., Sethi V., Pilidis P.** "Preliminary engine life assessment in techno-economic environmental risk analysis framework", ASME Turbo Expo 2013: Turbine Technical Conference and Exposition, June 3–7, 2013, San Antonio, Texas, USA

The following publications will appear in the Proceedings of the IMechE, Part G: Journal of Aerospace Engineering in 2014:

a. **Camilleri, W., Anselmi, E., Sethi, V., Laskaridis, P., Grönstedt, T., Zhao, X., Rolt, A., Cobas, P.,** "Concept Description and Assessment of the Main Features of a Geared Intercooled Reversed Flow Core Engine".
b. **Camilleri, W., Anselmi, E., Sethi, V., Laskaridis, P., Rolt, A., Cobas, P.,** "Performance Characteristics and Optimization of a Geared Intercooled Reversed Flow Core Engine".

1.8 Conclusion

Environmental concerns as well as continually rising fuel prices are driving research into clean efficient aero engines. The civil aviation sector is responsible for about 2% of global greenhouse gas emissions through engine related CO_2 emissions. The civil aviation sector has experienced a sustained growth of about 5% per annum for the past 50 years and a similar rate of growth is forecast for the next 20 years. Therefore, the environmental impact of aviation is likely to be further aggravated without significant improvements in airframe and engine technology as well as radical changes in air traffic management. Within the EU, there are several projects which are looking at novel engine concepts for 2020 and beyond. This research forms part of one such project which is called LEMCOTEC.

In this thesis a novel intercooled engine cycle which promises to deliver marked improvements in thermo-propulsive efficiency and fuel burn with respect to current configurations is evaluated. The research outlined in this report is confined to the feasibility assessment at the conceptual level but aims to deliver a useful statement as to the potential of this new design. The first part of this thesis outlines the rationale for this design, while the second part investigates specific design features. Finally, the whole concept is evaluated on the mission level. The thesis concludes by summing up the findings of this research and includes recommendations for future work.

2 Concept Evolution

2.1 Nomenclature

BPR	Bypass Ratio
CO	Carbon Monoxide
Dp/Foo	Units of Mass of Pollutant per Unit Thrust (g/kN)
FAA	Federal Aviation Authority
FPR	Fan Tip Pressure Ratio
GIRFC	Geared Intercooled Reversed Flow Core Engine Concept
GISFC	Geared Intercooled Straight Flow Core Engine Concept
HC	Hydrocarbon
HP	High Pressure
HPC	High Pressure Compressor
HPT	High Pressure Turbine
ICAO	International Civil Aviation Organization
IGV	Inlet Guide Vane
IP	Intermediate Pressure
IPC	Intermediate Pressure Compressor
IPT	Intermediate Pressure Turbine
LDI	Lean Direct Injection
LP	Low Pressure
LPC	Low Pressure Compressor
LPP	Lean Pre-Mixed Pre-Vaporised
LPT	Low Pressure Turbine
LTO	Landing and Take-Off Cycle
MC	Mid-Cruise
NO_x	Nitrogen Oxides
OPR	Overall Pressure Ratio
P_2	Fan Entry Pressure
P_3	Combustor Entry Pressure
RQL	Rich Burn, Quick-Quench, Lean Burn
SFC	Specific Fuel Consumption
SFN	Specific Net Thrust
T_2	Inlet Temperature
T_3	Combustor Entry Temperature
T_4	High Pressure Turbine Entry Temperature
TO	Take-Off
TOC	Top-of-Climb
UHC	Unburned Hydrocarbons

2.2 Introduction

This chapter describes the background to the research presented in this dissertation and includes general information regarding aero-engine design as well as specific descriptions of concepts which can be considered pre-cursors to the new concept reported in this dissertation. This chapter identifies historical trends in aero-engine development. These are important as they set the tone for current research projects and in many ways reflect current research and development trends. Some of these recent trends are also highlighted in this chapter as they allow for a better understanding of why some features were included in the engine concept under consideration in this dissertation.

The concept under consideration in this thesis is a geared intercooled reversed flow core (GIRFC) engine and draws inspiration from the Garrett ATF-3 which similarly incorporates an HP-spool which is located in tandem with the LP-spool. In a reversed flow core engine, the core flow is directed from the exit of the booster to the rear of the engine from where it is re-directed forwards through the reversed HPC, combustor and turbine stages. The adoption of this configuration is intended to address some of the limitations imposed by previous intercooled engine designs which are discussed as well in this chapter.

This chapter begins with a discussion of the historical and current trends in aero engine development. Then a description of the Garrett ATF-3 and current intercooled engine concepts is given. Finally, a general description of the GIRFC concept is provided. Further design and performance details regarding the GIRFC are provided throughout the thesis as is relevant.

2.3 Historical Trends in Aero Engine Development

The gas turbine has evolved considerably from its early roots in the 1950s and today the turbofan is the powerplant of choice on many commercial passenger aircraft. Past trends in aero-engine manufacturing have led to improved reliability and safety, reduced costs, improved maintainability and component life, as well as reduced fuel consumption, noise and pollutant emissions [17]. The focus of this thesis is the reduction in fuel burn which can be achieved through the implementation of a novel concept. Therefore, it is worthwhile to outline the

measures which have already led to more than a 50% reduction in jet engine SFC over the past 60 years [17].

Fossil fuels are a limited, non-renewable and hence valuable resource. Jet A/A1 is the main hydrocarbon derivative used in modern civil turbofan engines and due to past volumes of air traffic, aviation related CO_2 emissions are considered to be a major source of global warming [18]. The reduction of fuel consumption is, therefore, of both economic and environmental benefit. SFC is a measure of fuel consumption for a given level of thrust and it is an important indicator of an engine's performance with respect to key economic and environmental objectives in the aviation industry. The reduction of SFC can lead to increased aircraft range or conversely greater payload capacity, reduced CO_2 emissions and reduced running costs. SFC is essentially a measure of engine overall efficiency which is currently around 40% for the best large turbofan engines in high altitude cruise [19]. Engine overall efficiency is a function of core thermal efficiency, propulsive efficiency and transfer efficiency. Installation losses also play a major role in the overall propulsion system efficiency.

The core thermal efficiency of conventional turbofans is in the range of 50% [19]. In the ideal Brayton cycle, efficiency is a direct function of pressure ratio (P_3/P_2) as can be seen in Equation (2.1) from Kurzke [20]. However, system inefficiencies lead to a further dependence on the temperature ratio (T_4/T_2) as shown in Equation (2.2) from Kurzke [20] which leads to an optimal T_4/T_2 for each P_3/P_2 [20]. T_4/T_2 must increase along with P_3/P_2 if higher P_3/P_2 is to deliver better thermal efficiency. As stoichiometric conditions are approached, T_4 will no longer increase proportionally to fuel-to-air ratio, and therefore a practical limit exists beyond which further increases will no longer deliver improvements in thermal efficiency. T_4/T_2 and P_3/P_2 cannot be increased indeterminately and the optimum condition is quite difficult to reach. T_4 is limited by hot section materials integrity, especially for the HPT nozzle guide vanes, blades and disc assembly, as well as cooling methods [21]. The maximum permissible temperatures will determine the thrust available at take-off and top of climb [22]. Over the past 40 years, there has been a gradual increase in T_4 limits [23] that has made higher P_3/P_2 feasible. This has been made possible by advances in turbine blade material leading to adequate blade integrity at

higher temperatures. Cooling bleed air, extracted from a tapping in a compressor, can be used to cool hot parts of the engine such as the HPT. This is usually required in order to maintain structural integrity and to prolong the life of critical components such as turbine blades, discs and nozzle guide vanes [19]. However, cooling flows also have a negative impact on thermal efficiency and so any strategy which involves a significant increase in cooling flows will, in its extreme, be self-defeating. An increase in T_4, for a fixed P_3/P_2 allows for a smaller core to be adopted which leads to shorter compressor and turbine blades. Higher P_3/P_2, for a given T_4 will also result in shorter HPC exit blades. Overall an increase in T_4/T_2 and P_3/P_2 will result in a smaller core which is susceptible to blade over-tip leakage which can reduce efficiency. It is suggested by Birch [1], that the benefit from higher T_4/T_2 and P_3/P_2 could be lost unless they are accompanied by improvements in cooling methods and component efficiencies.

$$\eta_{th} = 1 - \left(\frac{P_3}{P_2}\right)^{\frac{1-\gamma}{\gamma}} \qquad \textbf{(2.1)}$$

$$\eta_{th} = \frac{\left(\frac{\gamma_t}{\gamma_t - 1} R_t \frac{T_4}{T_2}\left[1 - \left(\frac{P_2}{P_3}\right)^{\frac{\gamma_T - 1}{\gamma_T}}\right]\eta_T\right) - \left(\frac{\gamma_c}{\gamma_c - 1} R_c \left[1 - \left(\frac{P_3}{P_2}\right)^{\frac{\gamma_c - 1}{\gamma_c}}\right] \Big/ \eta_c\right)}{\left(\frac{T_4}{T_2} - \frac{T_3}{T_2}\right)\left(\frac{\gamma_c}{\gamma_c - 1} R_c + \frac{\gamma_t}{\gamma_t - 1} R_t\right)/2} \qquad \textbf{(2.2)}$$

where:

- *2* *engine inlet*
- *3* *compressor exit*
- *4* *burner exit*
- γ *ratio of specific heat capacities*
- η *component efficiency*
- η_{th} *thermal efficiency*
- *c* *compressor*
- *t* *turbine*
- *P* *total pressure*
- *R* *gas constant*
- *T* *total temperature*

Propulsive efficiency for current turbofan engines is in the region of 80% [19]. It improves as SFN decreases and is achieved through an increase in fan mass flow rate and a reduction in bypass jet velocity [24]. There is an optimum BPR and FPR at each level of SFN for a given

thrust. The optimum occurs when the ratio of bypass to core jet velocities is approximately equal to the transfer efficiency. For a given core size, a reduction in SFN can be achieved through an increase in BPR coupled with a reduction in FPR which in turn results in an increase in fan diameter. Fan spool speed must be reduced as fan diameters increase in order to reduce transonic losses [21] as well as noise. However, low speed fans aggravate the speed mismatch between the fan and the driving turbine [22] and can potentially lead to lower LP component efficiencies and fan turbine increased stage count. Historical and future trends in aero-engine thermo-propulsive efficiency are illustrated in Figure 2.1.

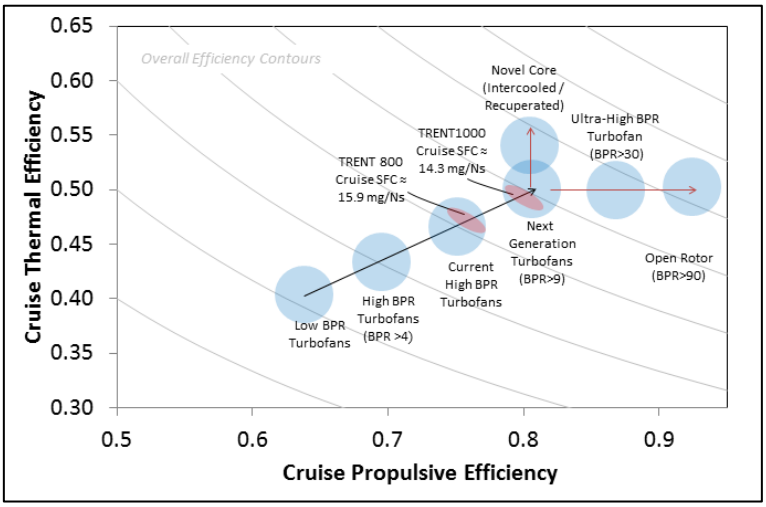

Figure 2.1 – Thermal and Propulsive Efficiency Trends (adapted from [25])

Birch [1] and Koff [23] suggest that during the 1950-2000 period a 50% improvement in SFC_{MC} was achieved although the baseline for these comparisons is prior to the implementation of turbofan technology. Much of this improvement was delivered through higher component, cycle and propulsive efficiency [26] [27]. In Table 2.1, a selection of specification data sourced from FAA type approvals and the ICAO emissions databank [28] is presented for a number of large turbofan engines. It shows the trend towards higher BPR and higher OPR which have driven, in part, the historical improvements in thermo-propulsive efficiency. Higher OPR has also been accompanied by higher T_4 which has been made possible by improvements in high temperature materials and cooling technology.

Manufacturer	Type	FAA Certification	FN_{TO} [kN]	BPR	OPR
General Electric	CF6-50A	1969	215	4.3	26.9
Rolls Royce	RB211-524B	1977	219	4.5	28.0
Pratt and Whitney	JT9D-7R4E4	1984	222	5.0	24.2
General Electric	CF6-80C2A1	1984	257	5.1	31.0
Pratt and Whitney	PW4060	1989	267	4.5	32.4
Rolls Royce	RB211-524G	1989	253	4.3	32.1
General Electric	CF6-80E1A1	1989	282	5.1	32.4
Rolls Royce	Trent 772	1994	316	5.0	35.8
General Electric	GE90-77B	1995	363	8.5	35.1
Pratt and Whitney	PW4074D	1998	345	6.7	31.8
Rolls Royce	Trent 877	1999	361	5.7	41.5
Rolls Royce	Trent 970-84	2002	334	7.5	39.0
Engine Alliance	GP7270	2006	332	8.7	36.6
Rolls Royce	Trent 1000-C	2007	334	9.3	43.8
General Electric	GEnx-1B70	2008	321	8.8	43.5

Table 2.1 – Historical Trends in Aero Engine Development [28] [29]

According to Koff [23], turbine material temperature limits have increased by over 500°F over the 1950-2000 period. Figure 2.2 shows how T_4 has increased steadily over time as new turbine materials and coatings have been introduced. The introduction of more effective cooling techniques and technology has also contributed to this trend.

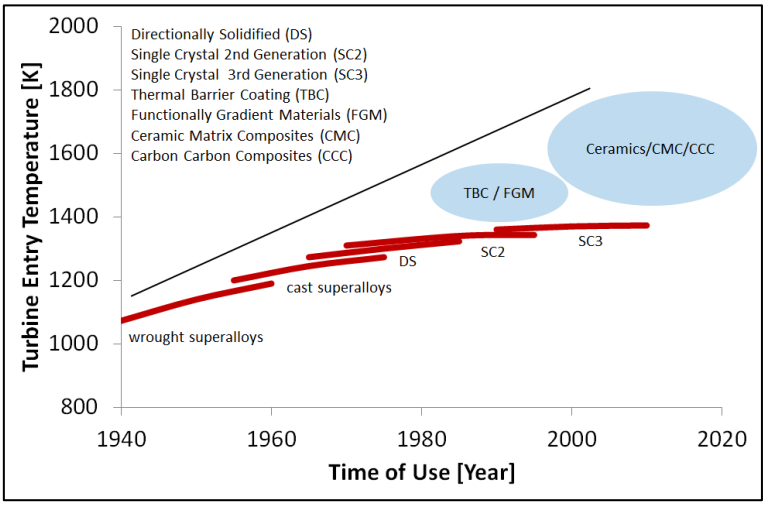

Figure 2.2 – Turbine Entry Temperature Limit Trend [1] [23] [26]

Perhaps the greatest challenge in terms of pollutant emission control is currently the reduction in LTO NO_x. Visible smoke and particulate emissions were a problem in the early days of gas turbines but efforts in the late 1950's and 1960's practically eliminated smoke from the visible spectrum due to better air-fuel preparation [26]. At high power settings, combustion efficiency is typically high. At low power settings UHC and CO emissions can be a problem. Since the 1970's there have been, however, significant reductions in both these emission types. UHC and CO emissions will be difficult to reduce further as combustion efficiencies are now quite high even at low power settings [23]. Since the late 1980s, the main focus has been on the reduction of NO_x emissions.

Currently, NO_x emissions are regulated only during the landing and take-off phases due to their contribution towards ground level ozone and smog. However, as aircraft are unique in that NO_x emissions are produced during the high altitude cruise phase, there is a definite concern that they may contribute towards acid rain and atmospheric ozone depletion [23] [26]. As stated previously, in order to improve core thermal efficiency, OPR and T_4 levels have been increasing steadily with time. As NO_x emissions are aggravated at elevated combustion temperatures, it is not surprising that the relative reduction in NO_x has not been as significant as for other emission types. Figure 2.3, which has been assembled from data available within the ICAO emissions databank [28], shows that LTO NO_x is highly dependent on OPR for a given combustor type. New combustor technologies have alleviated the impact of elevated OPRs; otherwise even the current reductions in NO_x emissions would not have been feasible.

Combustor types range from the early single annular combustors, to double annular combustors, to modern Rich Burn, Quick-Quench, Lean Burn (RQL) type combustors which are favoured on current large turbofan engines. Early single annular combustors are the most proven technology and contain one rich burning zone and can be found on engines such as the CF6. Double annular combustors contain a rich pilot stage optimised for ignition. Radial fuel staging allows for better optimisation of the combustor for different regimes where the main stage is then optimised for low NO_x emissions at take-off by favouring lean combustion. A

double annular combustor can, however, lead to high CO and UHC emission levels at the low regime.

In RQL combustors the combustion takes place in three stages. First, a fuel rich mixture is reacted at low temperatures causing only low levels of NO_x to be formed. This is because the combustion occurs at both a low temperature and a low oxygen concentration. Secondly, in order to follow a low NO_x formation route, air is mixed rapidly into the combustion zone which effectively quenches the reaction. In the third stage, the now lean-burn must occur at temperatures sufficiently high to consume residual CO, UHC and soot but low enough to avoid the formation of thermal NO_x [(30)]. Typical examples of RQL technology can be found in the GE90 Performance Enhanced Combustor (PEC), TRENT Phase 5 combustor and PW Technology for Advanced Low NO_x (TALON) II combustor. The Twin Annular Premixing Swirler (TAPS) found on the GEnx appears to offers the lowest LTO NO_x of any modern combustor. In this type of combustor, the two fuel domes are combined into one with fuel staging. Premixing caused by the swirler makes the mixture more homogeneous allowing for a leaner burn and reduces NO_x while advanced control of the fuel spray also reduces HC.

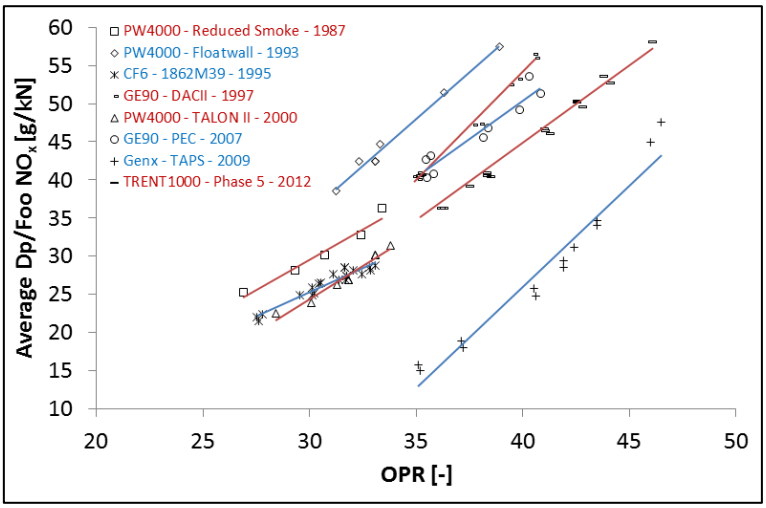

Figure 2.3 – Dp/Foo NO_x for Several Engine/Combustor Types (data from ICAO [(28)])

Aircraft are now 75% quieter than they were in the 1960s and yet noise is still the single factor that generates the most complaints from the public [(7)]. Perceivable large turbofan engine noise occurs during the take-off and landing phases where fan and core exhaust jets as well as

turbomachinery are the main sources of disturbance. The primary audible noise from turbomachinery occurs at the fan tips, front compressor stages and the rear turbine stages. Birch [1] suggests that noise problems for large turbofan engines can be alleviated by the reduction of fan tip speeds and the reduction of jet velocity as well as careful design of aerofoils and stators including the shape, number and spacing. A reduction in SFN, corresponding to an increase in BPR, is the single most significant factor in the reduction of noise which has occurred over the past 40 years [1]. As BPR has increased, aircraft cumulative noise has decreased although clearly the reduction in noise cannot be contributed entirely to engine related effects. Fan jet and bypass jet noise is already quite low for large turbofans and Riegler [31] claims that further significant reductions in noise for conventional direct drive turbofans are unlikely. Nevertheless, the advent of geared turbofan technology and even lower SFN engines could present new opportunities for further noise reduction.

2.4 Current Trends in Aero Engine Development

The current generation of aero engines such as the GEnx, PW1000 and Trent1000 is a product of several decades of development. These new engines have BPRs in excess of 9 and OPRs in excess of 40. The OPR and BPR of new conventional turbofan engines are likely to increase significantly beyond these specifications through the use of advanced materials, improved turbomachinery and better cooling designs. There is a limit beyond which, however, novel configurations must be considered. It is clear that all the major engine manufacturers are targeting lower SFN engines. However, as fan diameter increases to accommodate higher airflow, the mismatch of the fan with the LPT increases. Modern direct drive turbofans already have very large LPT diameters in order to reduce stage number at an acceptable loading and efficiency.

Geared turbofans could allow for further reductions in SFC and fuel burn beyond what is possible for a direct drive turbofan. At BPRs in excess of 10-13, geared turbofan technology becomes an increasingly preferable option as direct-drive engine inefficiencies in the LP-system begin to dominate. A good example is the PW1000G which, with a BPR of 12, is a new state-of-the-art geared turbofan engine from Pratt and Whitney. A geared turbofan allows the IPC and

LPT to rotate at markedly higher velocities than the fan. This allows for a reduction in stage count as well as LPT diameter while maintaining high efficiency. In the studies by Riegler [21], it was found that a 3-stage geared LPT intended for the V2500, while significantly heavier per stage, was far more compact than a conventional 5-stage LPT thus resulting in lower weight. The loading of a geared LPT is a trade-off between efficiency, weight and stage number. A reduced stage count does not necessarily lead to lower component weight as high speed stages can result in sizeable discs. Beyond the geared turbofan other options exist including counter rotating fans and un-ducted or open rotor configurations which could allow for vast increases in BPR. With the possible exception of the open-rotor, where challenges still exist, the continued decrease in SFN should allow for a further significant reduction in noise.

Further improvements in core thermal efficiency are also hindered by material, component efficiency and core size limits. In order to move beyond the state-of-the-art, radically different engine concepts are being explored. Forecasts of when these new concepts might reach the market vary widely from one manufacturer to another. Intercooled and intercooled recuperated cores are examples of radical cycle changes which could vastly improve the core efficiency of turbofan engines. However, several challenges remain not least of which is the development of low loss, high effectiveness but lightweight heat exchangers.

Several new combustor technologies are also under consideration. The GE TAPS is already a highly advanced design. Rolls Royce, based on the work carried out in the Affordable Near-Term Low Emissions (ANTLE) project, and Pratt and Whitney with the upcoming TALON X combustor for the PW1000G are likely to move in a similar direction. Going forward, the emphasis is likely to remain on lean combustion technologies. Three combustion technologies, each of which is being investigated in NEWAC [12] and LEMCOTEC, are finding favour in modern combustor design. These include Lean Pre-Mixed Pre-Vaporised (LPP) combustors for OPRs less than 25, Partial Evaporation & Rapid Mixing (PERM) combustors for OPRs between than 20 and 35, and, Lean Direct Injection (LDI) combustors for OPRs greater than 30. LPP combustors are not suitable for high OPR concepts due to the risk of flashback and auto-ignition. LDI combustors on the other hand are stable even at very high OPRs [12].

In this section only a brief flavour of the current trends on aero engine development has been given. More detail regarding combustor and other technologies is beyond the scope of this thesis where the focus is conceptual design and performance analysis. There are several other areas where modern turbofan technology is being improved including composite structures, ceramic coatings, advanced alloys, active and passive tip clearance control, active cooling control, advanced axial and axi-centrifugal compressors and advanced turbine designs. However, the scope of this research does not extend to all of these technologies. Rather this work focusses on one avenue of research concerning intercooled cores. The next section is, therefore, restricted to intercooling and the intercooled turbofan engine concept.

2.5 The Intercooled Core Turbofan Concept

Intercooling is an enabler of higher OPR which in turn leads to fuel burn improvements [12]. Compared with conventional engines, for a given T_4 and OPR the compressor work of an intercooled engine would be reduced, driving an increase in core thermal efficiency [16]. As the T_3 is reduced through the use of intercooling, it is possible to either increase the OPR or to increase the combustor temperature rise, leading to a smaller core. Both an increase in OPR and a reduction in compressor work will increase the core thermal efficiency [12] [16]. For intercooling to be feasible, pressure losses in ducts as well as the intercooler size in terms of both weight and volume need to be reduced. As can be seen in Figure 2.4, at low OPR pressure losses in the intercooler and headers can negate any benefits from intercooling. In a typical intercooled cycle, heat rejection can be viewed as a loss. However, in some intercooled configurations such as that proposed by Rolt [16], heat is rejected into the bypass flow which reduces slightly the load on the fan and fan turbine. Intercooling can lead to a reduction in core size which coupled with an increase in OPR can lead to increased over-tip leakage losses in the HPC thereby lowering component efficiency. For this reason, an intercooled engine can only be considered for large turbofan engines with a typically large core flow. The component efficiency penalties and pressure losses that would be incurred due to the introduction of intercooling in small turbofans with compact cores would be excessive [32].

The work-split between the IPC and HPC must take into consideration the intercooler which is typically placed between these two components. For maximum efficiency, it is essential that the intercooler is placed early in the compression stage [16] [22] [33] [34]. At low IPC pressure ratio, high effectiveness is difficult to achieve due to the low core side intercooler inlet temperature. Rolt [16] reports that for a large turbofan with an OPR of 80 at top of climb an HPC pressure ratio of 12 is best with an intercooler effectiveness of not more than 60-70% for the intercooler size and weight to be acceptable.

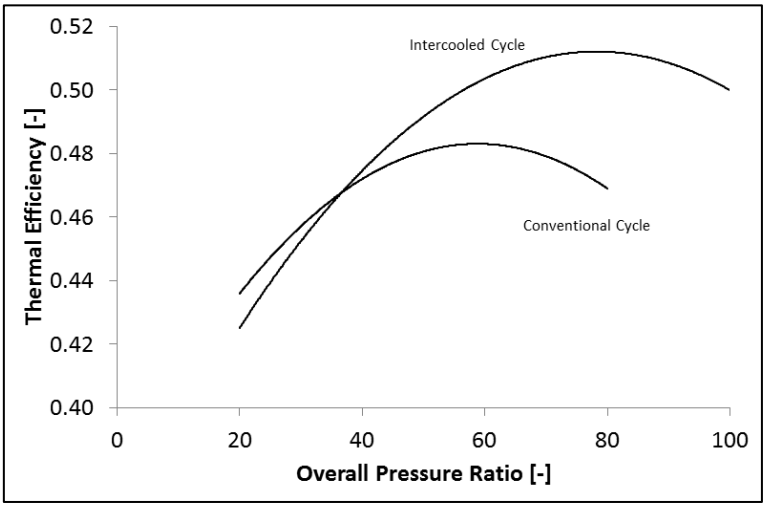

Figure 2.4 – Typical Thermal Efficiency for an Intercooled and Conventional Core

Off-design performance is also of importance when implementing intercooling. While an intercooler might be properly configured for a cruise design point or a take-off condition, it may not be ideally configured for other typical mission conditions. Kyprianidis et al. [22] suggest that through the use of a variable intercooler exhaust nozzle or bypass mixer, it is possible to regulate the mass flow through the intercooler, hence regulating pressure losses and intercooler effectiveness. This can be used to optimise the intercooler operation for specific mission conditions rather than simply for a single performance point, which can result in meaningful performance benefits [22]. Intercooling also has an effect upon turbine stage cooling. Cooling bleed air taken from any stage after the intercooler is at a lower temperature when compared with a conventional engine which therefore reduces the amount of cooling air required [12]. Intercooled engines offer other challenges in terms of core structural design. Intercooling leads to smaller core diameter sizes which are more susceptible to thrust and manoeuvre loads

leading to more casing distortion, increased tip clearance requirements and tip leakage [16]. Higher pressures and consequently temperatures in the core also increase difficulties related to corrosion and mechanical integrity [35].

Intercooling can offer a direct reduction in CO_2 as this is approximately proportional to fuel burn. Wilfert et al. [12] suggest that intercooling can reduce engine NO_x emissions significantly. Lundbladh and Sjunnesson [33], on the other hand, state that intercooling can lead to higher NO_x emissions due to high OPRs. In Lundbladh and Sjunnesson [33] the engine is optimised for minimum fuel burn, minimum system weight and minimum direct operating costs but not for minimum NO_x. It is clear from the findings of Lundbladh and Sjunnesson [33] that the T_4 has been significantly increased for the intercooled cycle. While this may offer the best solution for the optimisation objectives it would also lead to an increase in NO_x emissions. This is reflected as well in Kyprianidis et al. [22] where comparisons are made between very high OPR engines and conventional engines. It is clear that to reach high levels of OPR, higher levels of T_4 must be implemented as well. Therefore, one can say that NO_x is reduced for an intercooled engine with equivalent T_4 but for higher T_4 this benefit can be lost.

Recent research [16] [22] [33] [34] [36] into intercooled core concepts has been carried out mainly within the European Union's 7th Framework Program called NEWAC [12] while other research activities [32] [37] [38] have considered quite similar intercooled engine types and configurations. Figure 2.5 shows the standard configuration from NEWAC [12]. In this direct drive configuration the intercooler is positioned above the HPC. An S-duct connects the IPC exit and the intercooler entrance while a C-duct reverses the flow from the intercooler exit to the HPC entrance. The severity of the geometry can lead to severe losses especially for the C-duct where flow separation can occur along the inside radius of curvature. The definition of these ducts has been the subject of detailed research carried out by Walker et al. [39] [40]. The cooling passage can also lead to losses due to rapid diffusion and has also been studied in detail by Walker et al. [41]. The position of the intercooler in this design also increases the nacelle diameter which increases drag.

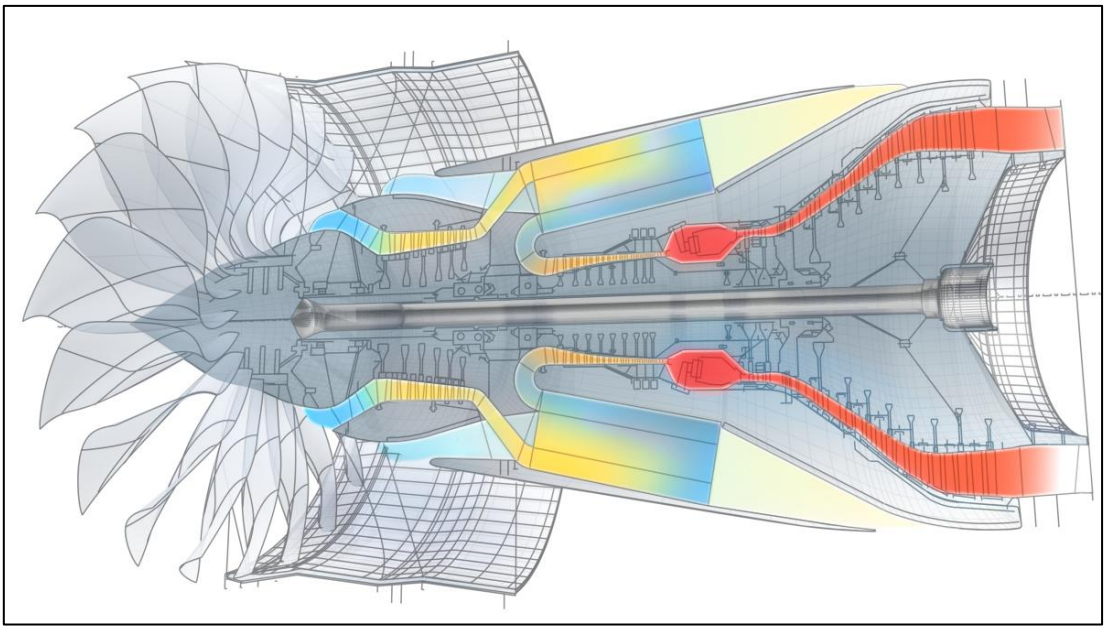

Figure 2.5 – NEWAC Intercooled Core Turbofan Concept [12]

Perhaps the main objective related to the implementation of an intercooled cycle is the reduction of block fuel consumed for a typical mission; although the reduction of flow temperatures can be beneficial for NO_x and compressor rear stage material integrity. All of the aforementioned studies [16] [22] [32] [33] [34] [36] [37] [38] report significant fuel savings, in the range of 2-7% for an intercooled core when compared with a conventional core for a large turbofan configuration. In each case the fuel savings is accompanied by a significant increase in OPR as well as T_4. Rolt and Kyprianidis [36] report that the NEWAC [12] intercooled engine, which is perhaps the most advanced and widely researched concept in the public domain, did not meet all of its design targets. The NEWAC [12] objectives for the intercooled engine were for a 4% reduction in block fuel burn when compared with the state-of-the-art. Only a 3.2% reduction was achieved in spite of the fact that the duct pressure loss targets were successfully achieved [22]. The main difficulties were due to high losses in the intercooler matrix which were surmised from a limited test regime, as well as increased drag and engine system weight. The main challenges associated with the NEWAC [12] intercooled engine are summarised in Figure 2.6.

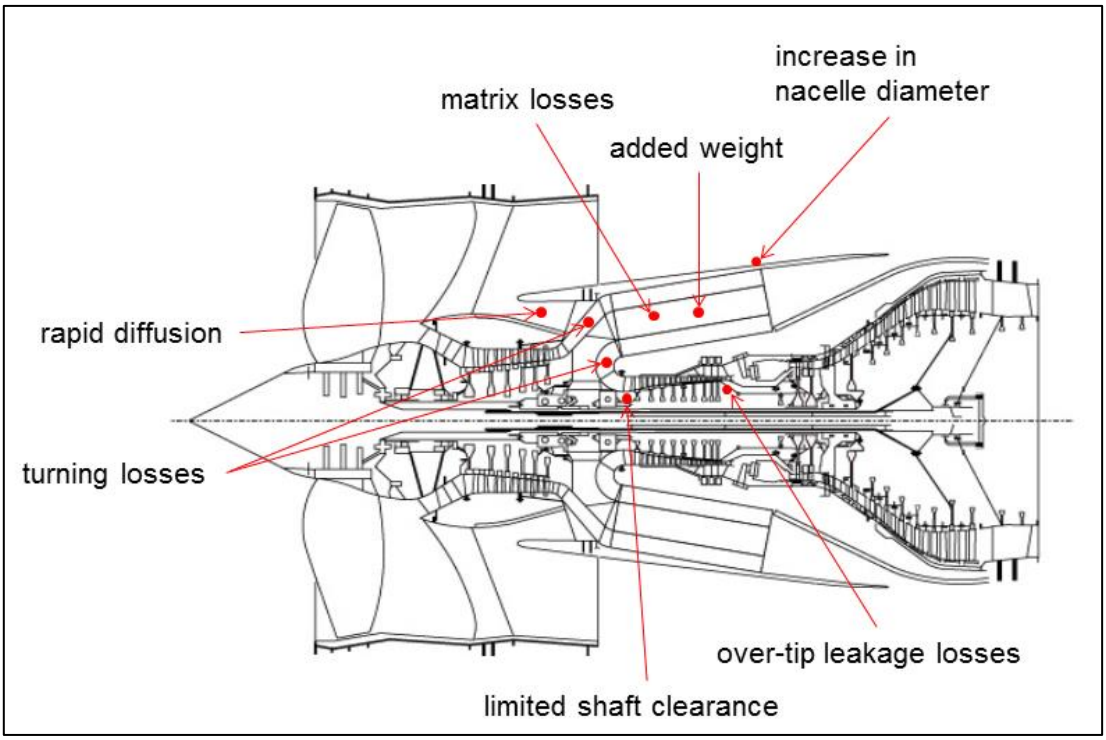

Figure 2.6 – Challenges Associated with NEWAC Intercooled Core Turbofan Concept [12]

There is much discrepancy in some of the prominent studies [22] [32] [33] [34] [37] with regards to the implication of intercooling on engine system weight. Intercooling reduces core size and reduces the load across the HPC which in turn leads to a lighter HPC and HPT. The IPT and LPT are also lighter due to the higher pressure levels across the turbines [22] [34] [37]. Of course, the intercooler has a huge impact on the overall engine system weight and changes to the nacelle required to accommodate the intercooler can also negatively affect the weight. The intercooler weight will also vary significantly with effectiveness. There is a mixed picture when comparing conventional and intercooled engines. Shinmyo et al. [32] and Kyprianidis et al. [22] reported a 6.8% and 16.5% increase in weight respectively for an intercooled turbofan. Xu and Grönstedt [34] and Lundbladh and Sjunnesson [33] reported a small increase in weight below 3%, while Grönstedt and Kyprianidis [37] reported a small decrease in weight for an intercooled cycle when compared to a conventional cycle. Clearly, the assumptions that back these studies are not identical and cannot be easily replicated. Without a detailed understanding of the weight estimation methods used as well as a detailed description of the heat exchanger a more rigorous comparison is difficult.

2.6 Existing Reversed Flow Core Engines and Concepts

In a reversed flow core gas turbine engine part, or all, of the core air flow is reversed. In a conventional aero gas turbine engine the passage of air through the core takes place from the front to the rear, while in a reversed flow core gas turbine engine, part or all of the internal flow is from the rear to the front. It is pertinent to mention that engines with reversed flow combustors also reverse the core flow. However, these do not fall within the scope of this discussion and are not included within the term reversed flow core engine as used within this document. Unlike intercooled aero engines, several examples of operational reversed flow core engines exist such as the Garrett ATF3 and the PW PT6 family of engines. The PT6 is a successful family of turboprop/turboshaft engines; however, the ATF3 is currently the only operational turbofan engine with a reversed flow core. The ATF3 was developed in the 1970s by Garrett Aero Engines and cannot compare with current modern large turbofan engines in terms of BPR, OPR, T_4 or indeed SFN. However, the ATF3 configuration, shown in Figure 2.7 and Figure 2.8, bears a remarkable similarity to the concept proposed in this dissertation and for this reason it is explored in more detail. The ATF3 engine specifications are given in Appendix A.

The design of the ATF3 was intended to increase propulsive efficiency when compared with similar engines of its time and hence to deliver a comparatively lower SFC. To achieve this, a low pressure fan stage was incorporated at the front of the engine. Garrett adopted a three spool turbofan layout similar to the Turbo-Union RB199. This was a radical decision as, at the time, the much larger RB199 was the smallest engine to incorporate three spools [(42)]. The mechanical and structural integration of three spools within such a compact layout necessitated an innovative approach to the spool layout. Garrett determined that mounting three shafts co-axially within such a small engine was not practical. Instead, the high-pressure shaft was mounted axially but to the rear of the other shafts which allowed the engine to benefit from all the thermodynamic advantages of a three spool design without incurring the mechanical disadvantages normally associated with a coaxial layout [(43)].

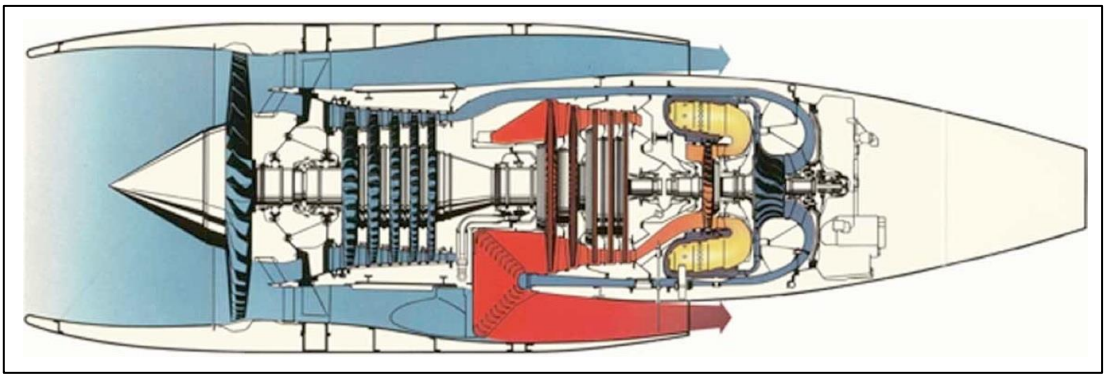

Figure 2.7 – Garrett ATF3 Schematic [44]

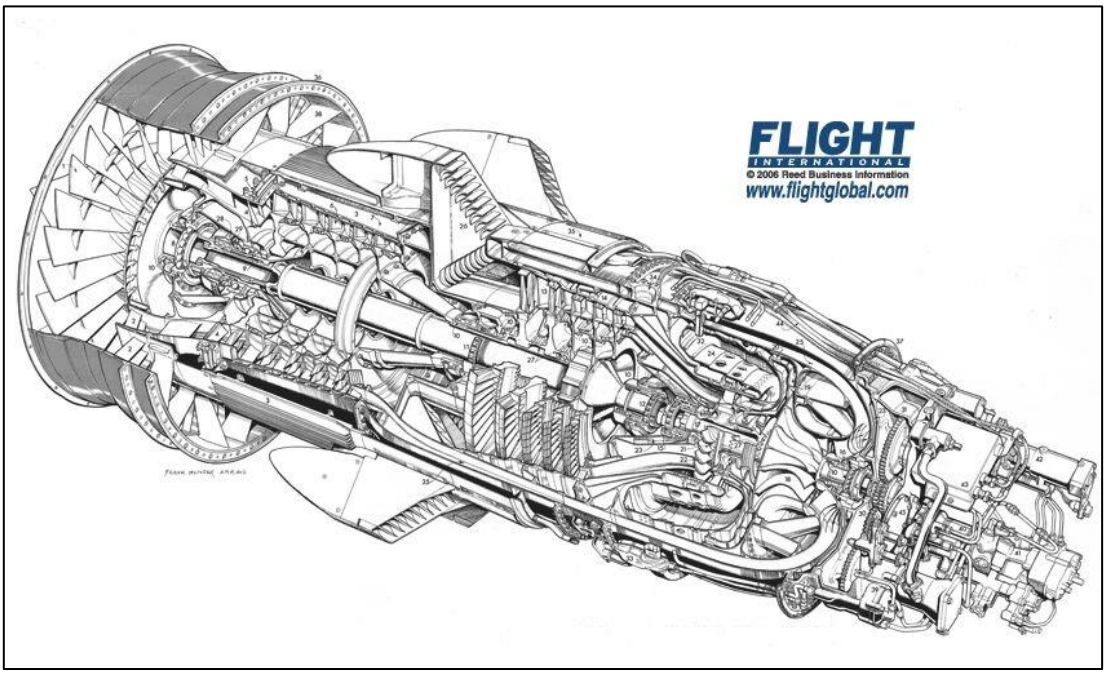

Figure 2.8 – Garrett ATF3 Cutaway [45]

Mounting the HP-spool to the rear of the engine had a number of unavoidable consequences. Chief among these was the route which the airflow would have to follow through each of the turbomachinery sections. As can be seen in Figure 2.8, the core airflow is compressed in a conventional manner by a five stage IPC. However, in order to reach the HPC the airflow has to be diverted to the rear of the engine. This is carried out by means of eight concentric ducts which circumvent the turbine stages. At the rear of the engine the airflow is rotated through 180° towards the front of the engine. Here the flow is recombined in order to feed a common centrifugal HPC. The HPC feeds a reversed flow combustor. It is likely that this type of combustor was incorporated as it built upon knowledge which Garrett had built up for the

TFE731 and similar programs. A reversed flow combustor also allows the air and subsequent exhaust flow to be turned back inwards towards the engine centreline allowing for a simplified and compact entry configuration to the HPT. As can be seen in Figure 2.8, following the combustor, the exhaust is expanded through a single stage HPT, a three stage IPT and finally a two stage LPT.

It now becomes apparent why the IPC to HPC ducting is divided into eight parts. The LPT is located towards the front of the engine. In order for the expanding exhaust to be ejected, it must pass through the plane containing the compressor ducting. For this intersection of paths to be possible both the compressor ducting as well as the exhaust ducting must be divided in order to allow for the crossover. In the ATF3 the exhaust is turned again rearwards and mixed through eight diffuser chutes into the bypass stream. Each chute is contained within an aerodynamic fairing to reduce the drag in the bypass stream. In addition the turning of the flow prior to the exhaust chutes is assisted by a number of guide vanes to prevent separation in the duct vertices. The mixed core and bypass stream is finally ejected out of a mixed common rear facing nozzle. In summary, the core gas path is approximately twice the length of the engine. The engine configuration is also unique as the compressor to turbine coupling is unconventional. It is inevitable in this configuration that the hot exhaust stream will pass through the turbine coupled to the fan before passing through the turbine coupled to the IPC. Therefore, the fan is coupled to the IPT turbine as opposed to the LPT and vice-versa for the IPC.

The United Technologies Corporation (UTC) has also filed a patent [46] for a novel configuration incorporating many of the aspects of the ATF3 design which can perhaps be considered as an indicator of renewed interest in the concept. The patent, filed in 2009, also describes a reversed flow core gas turbine engine design for a turbofan engine and also highlights its possible applicability as an intercooled or intercooled-recuperated configuration. No performance data is available for this concept and no actual studies have as yet been made public. Nevertheless it is useful to assess some of the design features outlined in this patent. The gas path, the placement of the turbomachinery, as well as the approximate positioning of the IPC to HPC ducts and exhaust ducts is very similar to that of the ATF3 engine.

The major differences visible in this patent are:

c. The combustor type, which in this case appears to be a typical annular design as opposed to a reversed flow combustor.
d. The HPC which is a multi-stage axial machine as opposed to a centrifugal type.
e. The increased number of both compressor as well as turbine stages which suggests a high OPR engine.
f. The fan, which is not driven by a separate spool as in the case of the ATF3, but rather makes use of a gear drive system which again indicates a low SFN design.
g. The design accommodates the possibility of using intercooling as well as recuperation.

The particular turbomachinery configuration and gas path of the ATF3 have a number of consequences on the overall performance of the engine. The length and complexity of the gas path adversely impacts the flow losses in the core [42]. The ATF3 makes use of a centrifugal HPC. In order to maintain high efficiency across the whole compressor operating range, a high tip to eye ratio on a small impeller was used. The HPT operates choked at all normal throttle settings and the more energetic IPT, which is at a higher than typical fan-turbine entry temperature, allows for a more compact turbine design. The ATF3 is reported to have a good transient performance in terms of surge prevention during acceleration due to a favourable surge margin. However, this is not retained during deceleration making necessary the use of a single stage of variable IGVs at the LPC inlet.

The location of the HP-shaft gives rise to unique possibilities in terms of the placement of the accessory gearbox. In the ATF3 this is located to the rear of the engine where it is coupled to the HP-shaft. According to Van Nimwegen [43], this is advantageous for various reasons:

a. It facilitates maintenance as the gearbox is located outside of the main engine sections and can be easily accessed. Access is simplified to the extent that it is possible to maintain the gearbox while installed on the wing of an aircraft.
b. A simple axial quill shaft couples the accessory drive and the HP-shaft.
c. The HP-spool usually requires the most attention in terms of maintenance as it is more highly stressed during operation due to the high temperatures, pressures and rotational

speed. As the HP-spool is physically separate from the other spools, its maintenance is simplified. In this engine, it is possible to separate the front and rear section for easy access or replacement. The entire engine is built around modularity allowing for easy interchange of and access to components.

The double wall of the crossover duct and the shell structure of the turbine provide good structural rigidity. However, a major consequence of having a reversed flow core is the resulting loads both on the bearings as well as in the duct bends. In a gas turbine engine, if one considers a conventional LP-spool, the axial load on the fan is counteracted by the axial load on the fan-turbine. This is not so in a reversed flow core engine. In this case the load on the fan thrust bearings is made up of two components: the compressor reaction and the turbine reaction both acting in the same direction. This is also the case for the IP-spool where the IPC is driven by a reversed LPT. Van Nimwegen [(43)] claims that the bearing system of the ATF3 is relatively simple when compared with a conventional turbofan of that time. The main bearings in the ATF3, as described by Hirst [(42)] and Evans [(44)], consist of:

a) Fan thrust bearing and LP-shaft roller bearings,
b) LP thrust bearing and IP-shaft roller bearings, and
c) HP thrust bearing and HP-shaft roller bearings.

Of these bearings the fan and LP thrust bearings are under particularly high loads. In Evans [(44)] it is reported that a string of major in-service upgrades were required on the main shaft bearing seals due to problems such as leakage, sticking and overheating. Although no detailed assessment is available of the actual causes of these problems, a likely conjecture is that the in-service demands of this spool arrangement were not sufficiently catered for. More details regarding the Garrett ATF3 can be found in Appendix A.

2.7 The Geared Intercooled Reversed Flow Core Concept

The GIRFC engine concept brings together some of the features of the ATF3 and the intercooled engine concepts from NEWAC [12] and was originally conceived by Rolt[1]. A conceptual drawing of the engine is given in Figure 2.9. In many ways the concept is similar to the Garrett ATF3 in that it includes a reversed flow core and a mixed exhaust. However, the concept merges characteristics from the NEWAC [12] intercooled engine including a large geared fan to enable low SFN and an intercooled core to enable high OPR. This advanced turbofan engine concept was conceived assuming a potential entry into service in 2025. A conventional GISFC concept is also shown in Figure 2.9. In this research, the parallel evaluation of the GISFC concept allows for a reasonable assessment of how the reversed flow core design compares with current intercooled engine concepts.

Both concepts share some common features, specifically:

a. A large diameter fan to allow for a high BPR and low SFN.
b. A geared fan which allows for a faster running IPC and LPT. This leads to better component efficiencies and a reduction in LPT diameter.
c. An intercooled core to improve thermal efficiency through higher OPR. In the reversed flow core concept there is significantly more freedom in the placement of the intercooler than in the straight flow core due to the separation between the IPC exit and the HPC entrance which could allow for less severe header designs. Intercooler cold side headers can also be made longer leading to lower diffusion losses.
d. An LDI combustor necessary for reducing the increased severity of LTO NO_x due to the high OPR targeted in both concepts.

[1] The GIRFC was conceived by Andrew M. Rolt who is a Senior Systems Specialist at Rolls-Royce plc. Andrew M. Rolt greatly assisted in the work carried out by Cranfield University within LEMCOTEC and his contribution is kindly acknowledged.

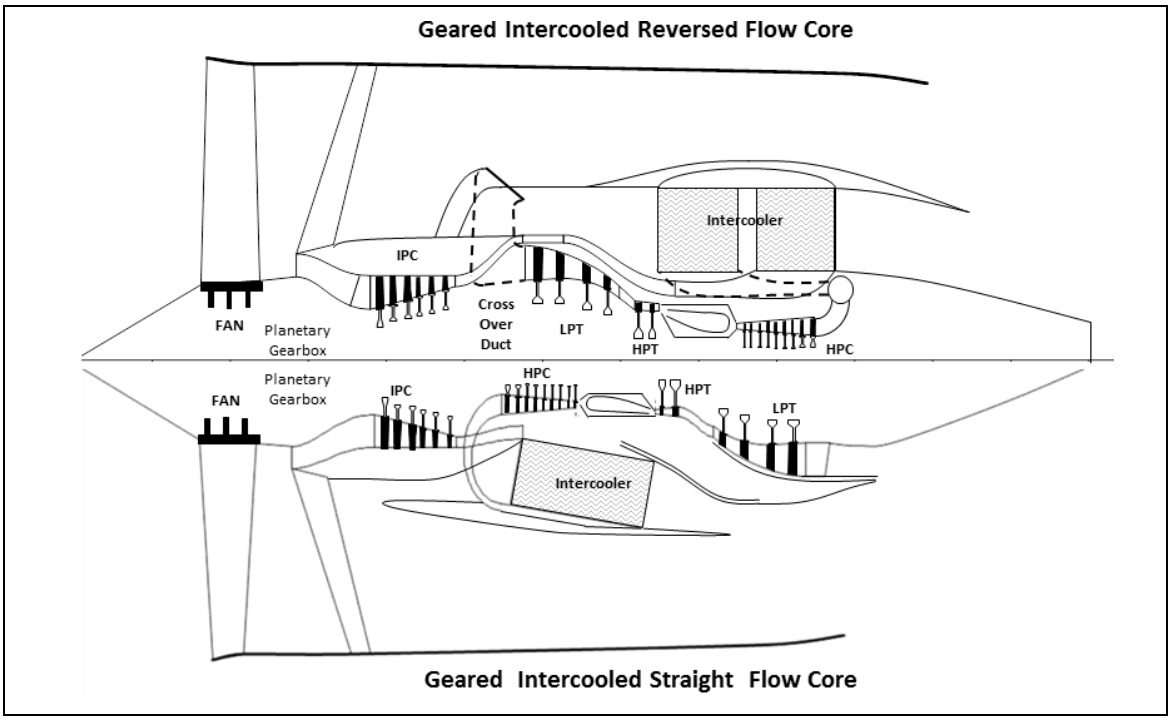

Figure 2.9 – GIRFC and GISFC Concepts[1]

The main features of the geared intercooled reversed flow core concept include:

a. A compact fast running HP-spool isolated at the rear of the engine away from major bending loads in the forward part of the engine allowing for more aggressive tip clearances. In addition, the absence of the concentric LP-spool could allow for a reduction in blade root diameter, an increase in blade height and consequently even lower over-tip leakage losses.

b. A mixed exhaust and common flow nozzle brought about by the reversed flow core arrangement. Mixing occurs far upstream in the bypass duct allowing for increased mixing length. Mixing gain from a mixed exhaust could allow for a small improvement in fuel consumption but the mixer chutes could lead to additional pressure losses in the core exhaust and bypass duct.

c. Challenging cross-over and intercooler ducting which could, however, be used to provide additional structural rigidity as well as to support the isolated HP-spool suspended at the

[1] The author recognises the contribution of Eduardo Anselmi Palma, a PhD student at Cranfield University, who prepared the engine general arrangement shown in this figure. In his research Eduardo Anselmi Palma is investigating the mechanical arrangement and losses within the GIRFC concept.

rear of the engine. Increased ducting length and turns especially due to the cross-over ducting could lead to higher pressure losses.

d. An accessory gearbox with a simplified drive train positioned in the tail cone of the engine.

In this dissertation the GIRFC is compared with a conventional geared intercooled straight flow core (GISFC) engine concept such as that described by Rolt et al. [16]. The conventional geared intercooled engine was researched in the NEWAC project [12]. In NEWAC [12] the intercooled engine was compared against a year 2000 baseline as well as an advanced high bypass ratio turbofan concept for the year 2020. As extensive research comparing a conventional turbofan with an intercooled turbofan has already been carried out in NEWAC [12], further comparison in this dissertation is not warranted. In this dissertation the year 2000 baseline, which was also adopted in NEWAC [12], is assumed to be the Trent 772. The TF2000 engine model created for this research is representative of the Trent 772 and is used only as a year 2000 reference point. In reality turbofan engines currently coming into service are already far superior to the Trent 772 in terms of fuel consumption as well as emissions. The main characteristics of the TF2000 are compared with those of the initial GISFC and the initial GIRFC configurations in Table 2.2. A more detailed specification is given in section 7.5.

Parameter	**Operating Point**	**Units**	**TF2000**	**GISFC**	**GIRFC**
OPR	TOC	-	38.17	80	80
SFN	TOC	m/s	190	146	150
BPR	TOC	-	4.85	11.25	11.25
FPR	TOC	-	1.8	1.67	1.63
IPC PR	TOC	-	5.2	4.5	4.5
HPC PR	TOC	-	4.4	13.70	13.70
Intercooler W_c/W_h	TOC	-	-	1.50	1.50
T_4	TOC	K	1654	1920	1920
Intercooler Effectiveness	TOC	-	-	0.6	0.6
Year	-	-	2000	2025	2025

Table 2.2 – Baseline TF2000, initial GISFC and initial GIRFC Concept Comparison

The initial GISFC and GIRFC specifications are based upon manufacturer specifications established in NEWAC [12] for a similar engine type. There are several key differences between the TF2000 and the intercooled concepts. First of all, the OPR of the initial GISFC and GIRFC far exceed that of the TF2000 which is enabled by a significant increase in T_4, intercooling, higher component efficiencies and improved material temperature limits. Secondly, the SFN and consequently FPR of the initial GISFC and GIRFC are far lower than that of the TF2000. A number of factors enable the higher BPR and lower SFN. These include adoption of a geared large diameter fan which alleviates the fan to LPT speed mismatch, the reduction in core size enabled by an increase in T_4 and improvements in LP-system materials which allow for large lightweight components to be considered. The GISFC and GIRFC also incorporate bypass variable area nozzles which allow for control of the fan running line so that higher fan cruise efficiency can be achieved. This also allows for the offset of take-off T_4 and increase in surge margin.

2.8 Conclusion

The development of a new aero engine is driven by the need for higher thermo-propulsive efficiency which leads to lower fuel burn as well as lower noise and pollutant emissions. In order to achieve these goals, there has been a steady increase in OPR and decrease in SFN which have been accompanied by improvements in component efficiency, cooling methods and material thermal limits. Further significant advances in thermo-propulsive efficiency require the consideration of novel engine cycles such as a turbofan with an intercooled core. In order to overcome the limitations identified in previous generations of intercooled core concepts, a new intercooled concept has been identified which integrates some of the features of the Garrett ATF3. In this thesis some of the major characteristics of the GIRFC engine concept are evaluated. These evaluations are intended to assess whether the GIRFC concept can offer any benefits when compared with the more conventional intercooled engine concept and whether further more detailed studies of the GIRFC are warranted. A rigorous evaluation procedure, described in the next chapter, was adopted in order to assess the feasibility of the GIRFC design.

3 Research Method and Foundation

3.1 Nomenclature

BPR	Bypass Ratio
CAEP	Committee on Aviation Environmental Protection
CDA	Conceptual Design and Assessment
DDICLR	Direct Drive Intercooled Long Range Engine Concept from NEWAC
Dp/Foo	Units of Mass of Pollutant per Unit Thrust (g/kN)
GIRFC	Geared Intercooled Reversed Flow Core Engine Concept
GISFC	Geared Intercooled Straight Flow Core Engine Concept
GTICLR	Geared Intercooled Long Range Engine Concept from NEWAC
HP	High Pressure
LEMCOTEC	Low Emission Core Engine Technologies
LTO	Landing and Take-Off Cycle
NSGA	Neighbourhood Search Genetic Algorithm
OPR	Overall Pressure Ratio
PROOSIS	Propulsion Object Oriented Simulation Software
SFC	Specific Fuel Consumption
SFN	Specific Net Thrust
T_4	High Pressure Turbine Entry Temperature
TERA	Techno-Economic and Environmental Risk Analysis
TO	Take-off
TOC	Top-of-Climb

3.2 Introduction

This chapter describes the rationale behind the research methods applied within the scope of this dissertation. In this chapter, the specific implementation of numerical tools and models is not provided. Rather the discussion is limited to the high level implementation of all the tools and methods. Specific techniques and model descriptions are given in subsequent chapters and in the appendices.

The first goal of this chapter is to identify and to justify the scope of this research. The focus of this research is inherently broad, and therefore careful selection of boundaries is necessary in order to reach the overall project goals. Although the detailed evaluation of the GIRFC concept is impossible within the confines of this research, the identification of key areas of interest allows for a useful contribution and a better understanding of this novel design. The second goal of this thesis is to outline and justify the approach which was selected for carrying out the characterisations and feasibility assessments reported within this thesis. Two general concepts are investigated in this dissertation specifically: a more conventional GISFC concept and a novel GIRFC concept. This is necessary in order to highlight the specific advantages and challenges of the new concept when compared with a more conventional design of similar sophistication. The methods for describing and comparing these concepts are highlighted in this chapter. The techniques described in this section were chosen in order to deliver a contribution to knowledge through the assessment of a novel engine concept. The fundamental goals of the thesis are to:

a. Assess the novel design features of the GIRFC concept.
b. Compare the performance characteristics of the GISFC and GIRFC concept.
c. Evaluate and compare the fuel burn and emission characteristics of the GISFC and GIRFC.
d. Assess the uncertainty in the predicted performance of the GISFC and GIRFC.

This chapter begins with a discussion of the research scope and is followed by a description of the main assessment methods. Finally, a description of the main modelling techniques is given. These techniques are consistent throughout the work presented in the thesis.

3.3 Scope of Research and General Approach

The research carried out within the scope of this project lies solidly within the conceptual design phase of a typical engineering design process. Fielding [47] gives a brief discussion of what constitutes a typical high level engineering design process within the field of aircraft design. In Figure 3.1 a typical concurrent engineering design process, as suggested by Fielding [47], is shown. This process is applicable across a wide range of product designs and is suitable for understanding the role of this research within the aero-engine design process. Within a concurrent engineering design process there is significant overlap between the different phases of design which is necessary in order to accelerate the product development. This thesis is concerned with the assessment of a novel engine concept, specifically the GIRFC, at the conceptual design stage.

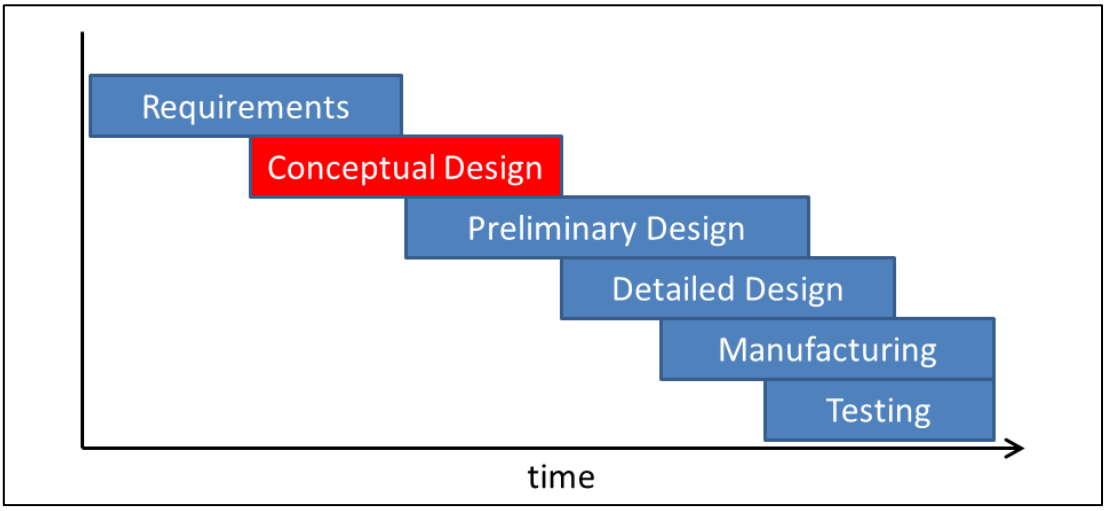

Figure 3.1 – Typical Concurrent Engineering Design Process (adapted from [47])

Understanding the role of this research within the conceptual design process requires an appreciation of the objectives and interactions which take place within a typical conceptual design activity. Raymer [48] suggests that "it is in conceptual design that the basic questions of configuration arrangement, size and weight, and performance are answered". Raymer [48] also points out that conceptual design is a fluid process, although fluidity should not be mistaken for lack of structure. The conceptual design stage is intended to uncover design attributes which could promote a given design or conversely to identify challenges which could eliminate a given design from consideration. Design challenges, given the nature of concurrent design, often lead

to a revision of the design requirements as scientific, technological or financial limitations become more apparent.

There is often overlap between the conceptual and preliminary design phases and occasionally the terms are used interchangeably. If the overall concept is already properly defined and deemed feasible, as may be the case for a standard engine development, a low fidelity conceptual design phase may not be required and hence the preliminary design stage is in reality the starting point. It is clear that, given the aforementioned definition, this project falls within the conceptual design envelope as this project attempts to answer the basic questions related to feasibility, performance and configuration of the concept at hand.

The conceptual design process for aero-type engines has been widely discussed in literature [24] [49] [50]. Today, given the advancement of processing power, multi-disciplinary design and numerical optimisation have also come to the fore. This is compatible with the concurrent design philosophy where multiple disciplines are applied simultaneously for the improvement and evaluation of the design. The following sections discuss typical conceptual design and assessment (CDA) methods as well as multi-disciplinary CDA methods and how these have been applied within this research.

3.4 Standard Aero-Engine CDA

Several authors have proposed methodologies for conceptual or preliminary engine design. The methodology from Mattingley [49] is given in Figure 3.2 and that from Stricker [50] in Figure 3.3. Prior to undertaking a complex engine conceptual design, it is useful to adopt some of the common threads which are found in these and other engine design methodologies. Clearly the starting point for any design is the specification of requirements. In this project the requirements are clear and can be summarised as follows:

a. Aircraft requirements: The baseline aircraft is the A330E. The field and flight requirements are set by the baseline aircraft. The aircraft model description and validation can be found in Appendix B.

b. Engine requirements: Fixed thrust requirements have been assumed at TOC and at TO and are equivalent to those of the baseline TF2000 engine presented in Appendix A.

The second step in the conceptual design process is the assessment of the engine cycle. This is reported in this dissertation through a number of parametric assessments which describe the performance of the engine with special focus on the implication of novel components such as the intercooler. Basic component design must also be carried out at the conceptual design stage. The sizing and performance of components such as the turbomachinery is essential for the correct behaviour of the engine, and therefore cannot be ignored. In this dissertation, special attention has been given to the HP-spool design, intercooler design and the exhaust system design which are reported in chapters 4 to 6. These specific areas have been selected as they are the main areas where the concepts under evaluation in this thesis differ from previous concepts such as the DDICLR and GTICLR from NEWAC [12].

Based on the results of the engine performance studies and the component analysis, it is possible to carry out more detailed engine sizing and performance studies. Clearly, several design iterations must be carried out until a conceptual design can be finalised. In addition, the aircraft requirements and performance may need to be updated in order to cater for installation effects and changes in engine weight. Stricker [50] also suggests that other considerations related to noise and cost need to be addressed at the conceptual design stage. Noise prediction and cost estimation have not been considered in this thesis. Noise estimation requires specialised models for assessing both internal and external engine noise sources. As these were not available within the scope of this work, no specific noise prediction could be undertaken. Similarly cost estimation was not attempted due to the presence of novel components for which an adequate cost model was not available and could not be produced within the scope of this research. Basic emission prediction is however undertaken as is discussed in chapter 7. Component design was carried out following an initial performance analysis as suggested by the aforementioned methodologies. However, the performance assessments and optimisation were carried out using multidisciplinary strategies as will be discussed next.

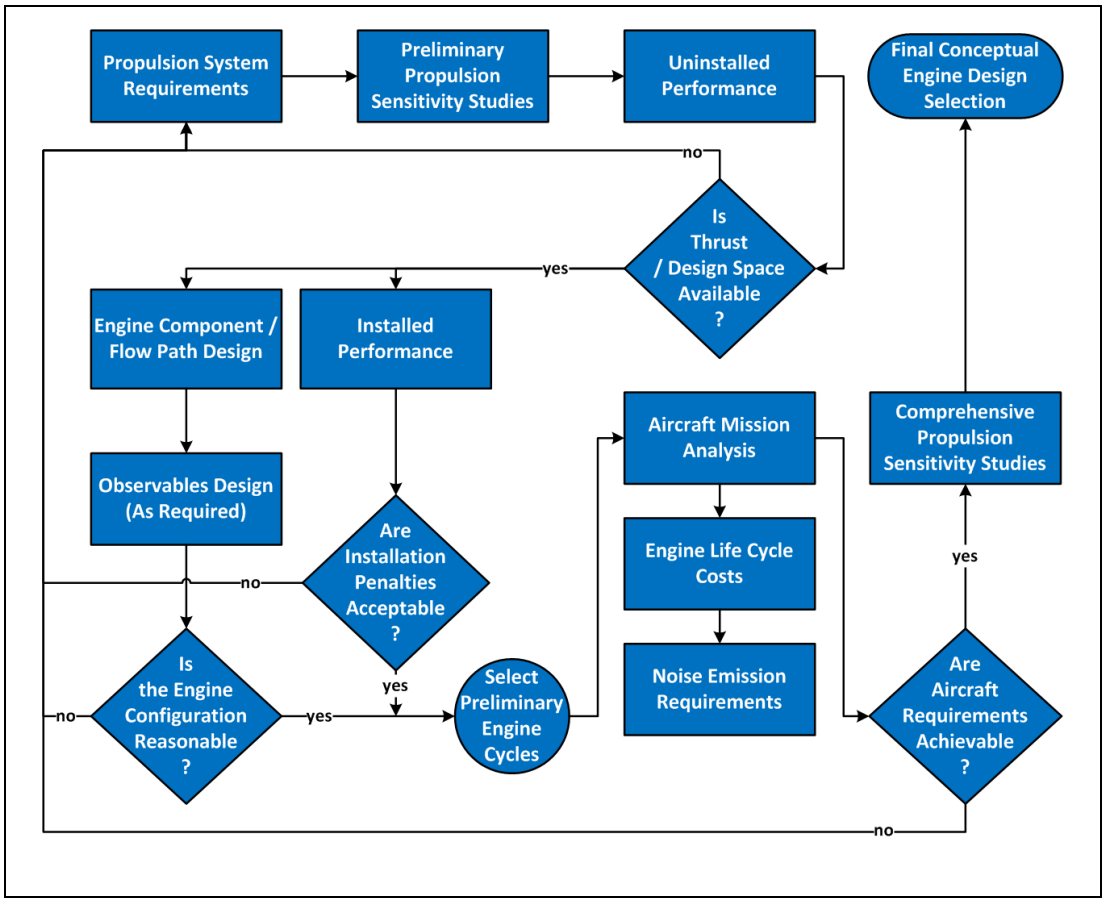

Figure 3.2 – Engine Conceptual Design Process (adapted from Stricker [50])

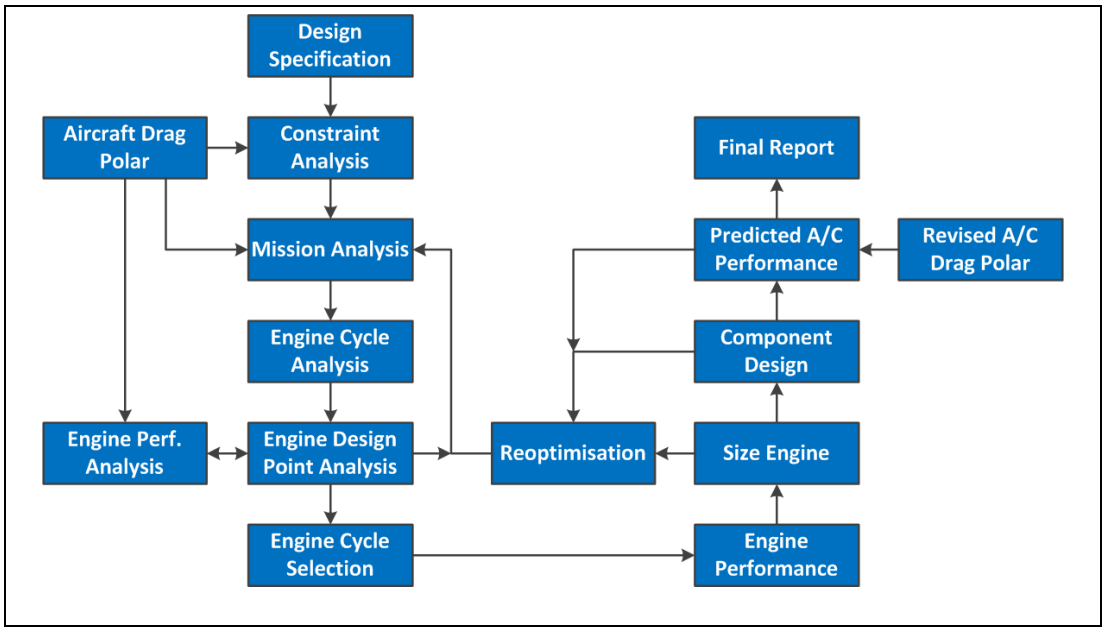

Figure 3.3 – Engine Design Process (adapted from Mattingley [49])

3.5 Multidisciplinary Aero-Engine CDA

3.5.1 The Cranfield University TERA

This research is intended to evaluate the feasibility of a novel engine concept. The Department of Power and Propulsion within Cranfield University has developed a simulation methodology for the evaluation and development of different concepts within the early stages of design. Several implementations of this method have been employed to investigate both thermal power and propulsion concepts ranging from the industrial and marine applications to the aeronautic sector. The TERA method has been widely recognised within academic publications and further information can be obtained in Ogaji et al. [51].

The main interest within this research effort is the application of the TERA in the field of aeronautics. The TERA has contributed to the work and results of several recent European projects including VITAL [10] [11] and NEWAC [12] in which it has played a central role. The application of this method within these projects is important as the LEMCOTEC project, to which this research effort contributes, builds upon the work and results presented in both VITAL [10] [11] and NEWAC [12]. The TERA strategy is useful for determining the feasibility of a given concept based upon a pre-defined set of objectives. In general the TERA method involves the linking of multi-disciplinary tools or models into a common framework. This allows for integrated systems to be evaluated from different perspectives taking into account interdependencies. Even at the conceptual engine design level relatively detailed information regarding component performance and design is required which means that the level of fidelity of the tools and models within the TERA must be carefully selected.

The most recent implementation of the TERA, illustrated in Figure 3.4, was in NEWAC [12]. The scope of the NEWAC [12] research extended to several disciplines including environmental, operational and economic. Several partners contributed tools and expertise to the TERA based work in NEWAC [12]. It is important to remember that while the TERA strategy employed in this dissertation is on the one hand a continuation of previously established methods, it is also a new work, as the engine concepts under investigation are novel. The tools used in NEWAC [12] but provided by institutions outside Cranfield University were not made available for this

dissertation and hence necessitated a re-evaluation of the modelling strategy in order to properly approach the research.

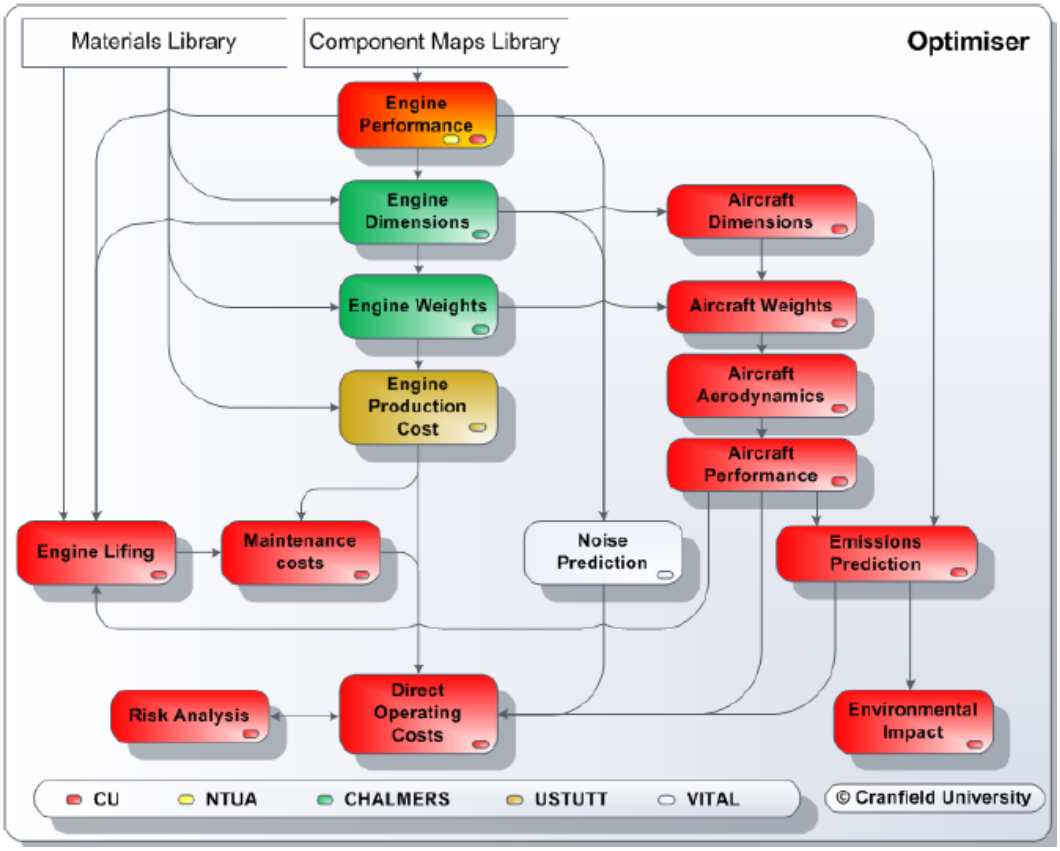

Figure 3.4 – TERA2020 [52]

3.5.2 Current Implementation

In this research, a customised version of the Cranfield University TERA was implemented. The simulation environment, which was required to carry out the research objectives of this study, is a collection of multi-disciplinary tools. The main disciplines considered in this dissertation were engine performance, engine weight prediction, aircraft performance and basic NO_x and contrail prediction. Unlike in previous research efforts carried out with the Cranfield University TERA, only tools obtainable in-house were available for this work. The current simulation environment is made up of three distinct levels. Specifically:

a. Lowest Level: The tools and models for each discipline.

b. Intermediate Level: The integration framework able to link the individual models.

c. Highest Level: A set of numerical tools to investigate the design space.

The lowest level is where the calculations are carried out for each discipline. The intermediate level is responsible for exchanging data between the highest level and the lowest level as well as exchanging data between the individual models on the lowest level. The intermediate level essentially creates an all-encompassing model from the individual components within its domain. The integration framework can be seen as linking all the stages of the classic conceptual design process together into a cohesive unit and so rather than completing each design phase consecutively, the whole concept can be optimised taking into consideration each phase simultaneously. Aside from accelerating the design process, this allows for the effect of more interactions to be considered. At the highest layer, numerical tools for the completion of parametric studies, sensitivity studies, uncertainty analyses and optimisation studies are used.

The required models together with their major interactions are shown in Figure 3.5. The TERA integration framework which was developed specifically for this project ties the suite of models together. The trajectory builder is used to construct a complete trajectory definition. From a limited set of inputs, the trajectory builder creates a more dense set of flight coordinates and engine control sequences using polynomial interpolation. The computational resources available for this project do not allow for the optimisation of hundreds of input variables related to the mission profile. Therefore, the trajectory builder is useful as it reduces the complexity of the problem. The engine performance model is required in order to predict the characteristics and behaviour of the given engine concepts. This information can be used to estimate the weight and general arrangement of the engine concept. The mission characteristics can then be determined through the use of an aircraft performance model. Both the design range and business case ranges are evaluated. The design range is used to check climb times and take-off distances while the business case, which represents a typical mission for the given aircraft type, is used for the fuel burn optimisations. The final models are related with the prediction of NO_x emissions during the flight, landing and take-off phases, and also with the prediction of contrails. Further details regarding these models are given in Appendix A to Appendix E.

In the current TERA implementation, the highest level activities are carried out through the use of a commercial package from SIMULIA. Isight from SIMULIA [53] is a powerful tool which makes

possible the integration of software models with design of experiment, optimisation and Monte Carlo tools [54]. In this work full parametric studies and sensitivity studies have been carried out using the in-built functionality of Isight. A number of optimisation routines are available within Isight, although only a selection of these was suitable for this research. The main routines used are given in Table 3.1 together with their main features.

The features given in Table 3.1 are important for the successful optimisation of the concepts under investigation. Only optimisers capable of handling a non-linear and discontinuous problem and design space could be chosen. The design space in this case is highly non-linear due to higher order effects in the engine, aircraft and weight models. Discrete weight changes due to variations in stage number mean the design space is also somewhat discontinuous. None of these methods is gradient based which is not surprising as typically gradient based methods cannot handle problem discontinuities.

	Downhill Simplex	**Advanced Simulated Annealing**	**NSGA-II**
Type	Local/Global	Global	Global
Gradient Based	No	No	No
Problem Space	Linear, Non-Linear, Discontinuous	Linear, Non-Linear, Discontinuous	Linear, Non-Linear, Discontinuous
Convergence	Fast	Slow	Slow
Inequality Constraints	Yes	Yes	Yes
Number of Objectives	Single	Single	Multi

Table 3.1 – Optimiser Types and Features

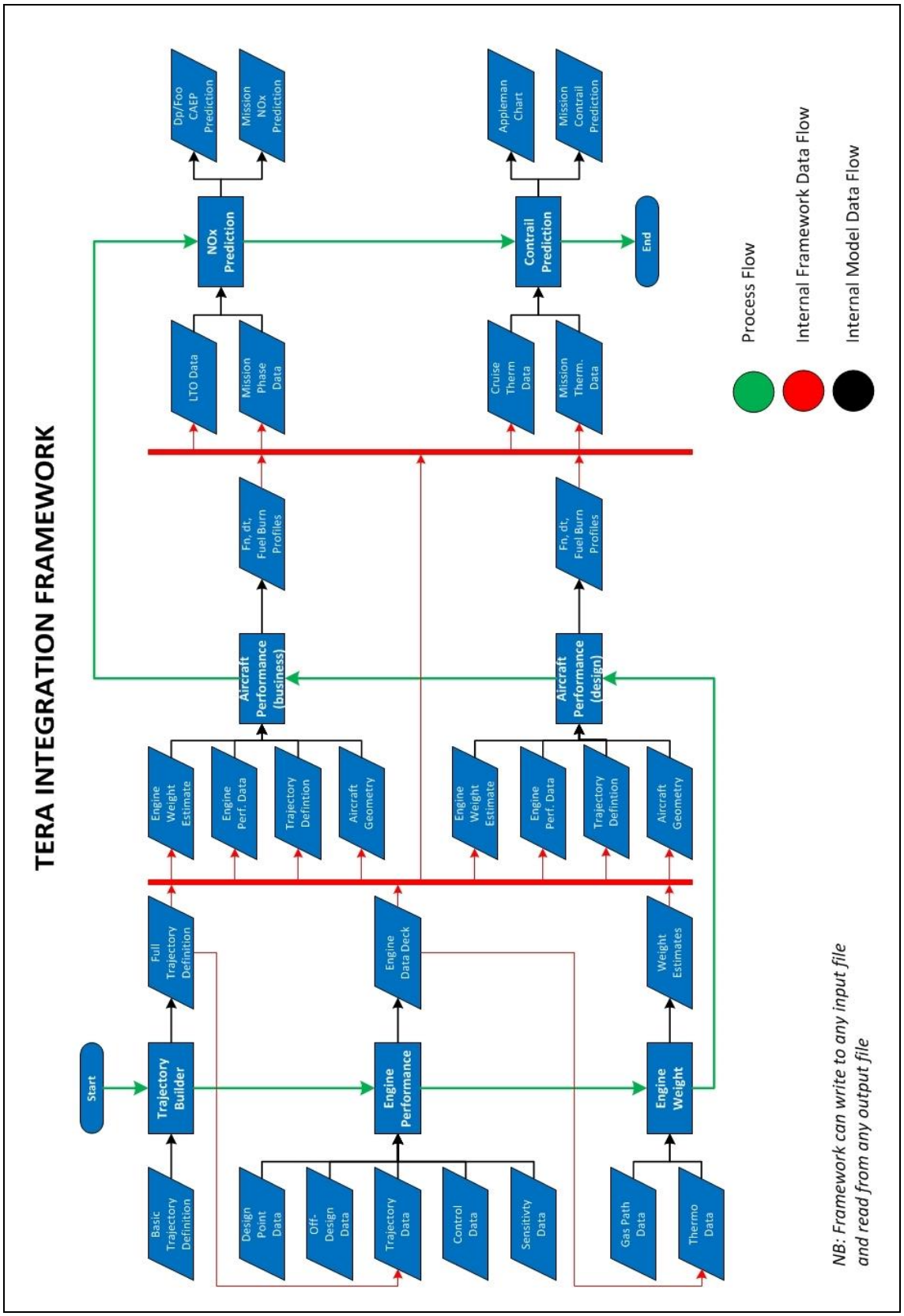

Figure 3.5 – Model and Data Interdependencies within TERA

As will be described in later sections, only optimisers capable of handling inequality constraints were selected as this feature was required in order to limit fan dimensions, $T_{4,TO}$ as well as specific mission parameters. Single objective optimisation has been used to configure the concepts for minimum fuel burn while multi-objective optimisation has been used to assess the impact of engine controls on contrails and NO_x emissions. In these cases the Advanced Simulated Annealing optimiser was used to identify an initial configuration. Then the downhill simplex method was used in its capacity as a local optimiser to refine the estimate. The NSGA-II optimiser was only used for multi-objective optimisation.

3.6 Management of Uncertainties and Validation

In this project, much of the research and consequently the resulting conclusions are built upon the simulation of the primary systems and the operating environment. Therefore, the validity of the results is highly dependent on the validity of each model and the validity of the whole simulation environment. Verification and validation do not share the same goals. Verification encompasses checks and tests which must be carried out to ensure that the specified model accurately implements the underlying mathematical or procedural formulation. Therefore, if a model can be shown to behave as expected it is considered to be verified, even if the underlying theory or expected behaviour is incorrect. On the other hand, for a model to be valid it must faithfully represent the underlying physics to a useful degree of accuracy. Verification is relatively well understood [(55)] and so does not require specific consideration here. However, model validation is a significantly more challenging prospect and is discussed in more length in this section.

It has already been established that the research carried out within this project lies firmly within the domain of conceptual design. Therefore, when considering validation strategies it is important to select a procedure which is suitable for the required fidelity level. There are, however, two main problems when attempting to validate a conceptual model. First of all, general validity does not exist and secondly there is typically no real world information with which to make a comparison [(56)]. The first point highlights the fact that a model can only be used for its intended purpose because a model is only valid as long as the criteria which underpin its

validity remain unchanged. It is for this reason that even at the conceptual level great care must be taken in the implementation of correlations or model elements which are already available as they may not be suitable for the required application. It is this point which has led to the creation of new models and the update and re-development of many of the models for this dissertation. The new models developed for this research are explained in detail in subsequent chapters as well as in the appendices.

The second point is of more concern when considering the validity of the simulation models both individually and as a collection. The engine concepts under evaluation are considered to be candidate solutions for entry into service beyond the year 2025. Consequently, much of the technology being simulated does not yet exist in any physical form and thus the attributed performance is subject to a degree of uncertainty. Robinson [56] suggests that it is often preferable to speak of confidence in model predictions rather than validity as there are no formal methods for validating a conceptual model. Robinson [56] suggests that a model should, at least in theory, be able to provide all the necessary information. Clearly this calls for proper specification of the model in question but also for a rigorous literature survey and where necessary the development of theory and methods.

Two techniques can be useful when attempting to increase confidence in a model's behaviour specifically; data and white-box validation. As the name suggests, data validation entails the careful selection of appropriately accurate data for use within a conceptual model. Although the model itself might be novel, all the constituent parts may not be and so it is important to ascertain whether the known input data is of value. This leads to white-box validation, which is essentially the validation of all the constituent parts of the model. Again, while a model or a system of models might represent an entirely new application, it is unlikely that each component of that application is novel. Useful validation can, therefore, be carried out for the model components which are well understood. Sargent et al. [57] and Law [58] propose several white-box validation techniques. The techniques from Sargent et al. [57] and Law [58] which are applicable to this study are listed in Table 3.2 in order of preference.

Empirical Data Test	Preference: High
To determine whether results compare well with published results.	
Equivalent Model Test	Preference: Medium
To compare the results obtained against results from a similar trusted model.	
Degenerate Test	Preference: Medium
To determine whether the behaviour in terms of reported trends is as expected.	
Face Validity Test	Preference: Low
To have an expert determine whether the behaviour of trends is as expected.	

Table 3.2 – Model Validation Strategies

In white-box testing it is assumed that if each constituent within a simulation environment is valid then the overall system behaviour should also be valid. While this argument does hold some weight it is perhaps not appropriate when the system is quite complex. In a complex system, the presence and propagation of uncertainties can be a real factor in determining the feasibility of a design and the inherent development risk. Aero gas turbines are quite complex and require significant investment in research and development before a new design can be finalised. Thus, even at the earliest stages of design careful consideration of uncertainty is required.

Sensitivity analyses and Monte Carlo analyses appear to be favoured for uncertainty analyses in aerospace systems. A sensitivity analysis can be used to evaluate both model input uncertainty as well as model structural uncertainty. In a sensitivity analysis, model responses to small perturbations in a selection of the input values are assessed. The inputs can include parameters such as component efficiency and pressure losses but also can include component weight assessments which are inputs predicted by another model. By analysing each of these factors independently a response surface can be built up. This type of sensitivity analysis is useful for suggesting which parameters are driving uncertainties in the system. The responses obtained from this type of study can also be useful to designers for correcting model predictions as more data becomes available as long as the input variations are not large. This type of method is useful for gauging the independent effect of uncertainties on the model responses but does not provide an absolute value for overall system uncertainty. Below is the general mathematical form of sensitivity type study from Hills and Trucano [55].

$$z = f(a, b, x) \quad \textbf{(3.1)}$$

$$\Delta z_i = c^T \Delta d_i \quad \textbf{(3.2)}$$

$$c^T = \left[\frac{\partial f}{\partial a} \frac{\partial f}{\partial b}\right] \quad \textbf{(3.3)}$$

$$\Delta d_i{}^T = [\Delta a_i \, \Delta b_i] \quad \textbf{(3.4)}$$

where:

- *a, b* *independent parameters*
- *i* *indicates that the z is for the i^{th} sample of a and b.*
- *x, y* *independent variables*
- *z* *sensitivity matrix*

Conceptual engine design is often carried out at a relatively low level of fidelity and therefore the predicted performance is subject to a high degree of uncertainty. Input parameter uncertainty is usually not considered at this stage beyond a basic sensitivity analysis. Therefore, it is difficult to firmly state that a concept is promising when compared to an objective or when compared to another concept. In this section, a subjective uncertainty analysis methodology for use at the conceptual design stage is outlined and allows for the early evaluation of input parameter uncertainty. This method has been used to assess the effect of uncertainty on the predicted fuel burn and weighted NO_x predictions but has been restricted to the input parameters which differentiate the GIRFC and GISFC.

A Monte Carlo analysis builds model response surfaces based upon input uncertainties characterised by probability distributions. This method is commonly used for analysing the system uncertainty of highly non-linear problems and takes into account interrelating effects of uncertainty. Monte Carlo assessments are computationally expensive as they require the evaluation of a large number of input sample points based upon the predefined probability distributions. The computational requirements can be reduced by limiting the number of uncertainty parameters. This can be achieved by down selecting only the most influential parameter set based upon the results of a sensitivity analysis. For a conceptual design problem the main difficulty is in selecting the input probability distribution for each parameter. Typically establishing a suitable probability distribution requires that a data sample of suitable size is obtained through some form of experiment. This is not possible for a conceptual design and

even more so at the academic level where the absence of historical data precludes the adoption of historical trends which might be available to an aero engine manufacturer. Law [58] proposes a general structure for selecting probability distributions in the absence of data. It is suggested that since an objective assessment of uncertainty cannot be achieved, a subjective assessment should instead be adopted. This is perhaps in line with the claim from Robison [56] which states that a conceptual model cannot be fully validated, but rather the degree of confidence in the predictions should be increased. Consequently, the best option for the quantification of input uncertainty is by eliciting expert opinions. In Law [58] it is suggested that a subject matter expert can recommend adequate parameters for defining a probability distribution which can be used for a basic estimate of uncertainty. Kirby and Mavris [59] propose a similar method of uncertainty analysis specifically for preliminary aircraft design. In this method expert opinions are used to suggest the impact of changes in technology on key design outputs. These suggestions are then used as distribution means for a subsequent Monte Carlo assessment. In this dissertation, the problem formulation is somewhat similar. Several of the parameters which define the concept, such as efficiencies and pressure losses, have been put together with the assistance of subject matter experts from the aero-engine industry. These parameter estimates have been used as distribution means.

Clearly, the next challenge is to define a suitable probability distribution. Law [58] recommends triangular, beta or Weibull distribution but these distributions require specific descriptions from subject matter experts. Kirby and Mavris [59] also selected the Weibull distribution. As the Weibull distribution can assume the properties of other distributions, it is possible to carry out a large number of Monte Carlo assessments for several different distributions and hence build up a response surface for many different combinations. The advantage of this method is that no specific knowledge of the distribution is required as it characterises many of the potential outputs. As knowledge of the system is improved, the applicability of the data can then be re-assessed. The major disadvantage of this method is that it is extremely computationally intensive as many Monte Carlo studies need to be carried out. This feature disqualified this method from consideration. Hill [55], on the other hand, recommends the use of a normal distribution if the true shape of the input distribution is unknown. This can be misleading and,

therefore Hill [55] suggests that worst case distributions should be considered as part of any such study. For this reason, in this dissertation, two Monte Carlo simulations at two different confidence levels were carried out.

None of these methods can give an absolute figure for uncertainty and, therefore as already suggested, there can never be an absolute validation. These methods do however increase confidence in the results. The sensitivity analysis helps to indicate where further research must be focussed in order to reduce uncertainty. The Monte Carlo assessments help to guide the designer by establishing likely deviances in the expected values. In addition, Monte Carlo assessments allow for the comparison of risk between different concepts as long as similar assumptions are made in the definition of the input criteria.

3.7 Engine Modelling

Throughout this dissertation, reference is made to several different engine models. The engine models have all been developed using the PROOSIS [60] environment. The standard turbo library has been used for the most part in the assembly of the respective engine decks, although several modifications and additions have been made as necessary for the completion of this work. The main engine models and validation activities are described in Appendix A. This section serves only as a guide to the different engine models which were developed in the course of this research and which are referred to throughout this thesis.

The first stage of engine modelling was intended to demonstrate the capability of the tools to investigate the different concepts and features to be evaluated in this project. For this reason, an RFC70, a TF2000 and a GTICLR model were developed based on the Garrett ATF3, Rolls-Royce Trent 772 and the NEWAC [12] GTICLR respectively. The NEWAC [12] DDICLR engine was also evaluated but a full engine model was not required for this research. These engine models encompassed between them the main features of the GIRFC engine which include intercooling, a reversed flow core and a mixed exhaust as well as a high BPR, high OPR and low SFN. In the second stage, the GIRFC and GISFC models were created based upon the successful implementation of these models and represent the reversed flow core and

conventional intercooled option respectively. These engines are the basic architectures studied, although several variants were considered through a number of parametric and optimisation studies.

3.8 Conclusion

In this chapter a general overview of the research and simulation methods used throughout the course of this research was given. It is established that the work carried out within the scope of this thesis falls within the domain of conceptual design. The models and work outlined henceforth should therefore be interpreted in this light. The typical conceptual design procedure is an iterative technique where model requirements inform initial performance evaluations which then provide the boundary conditions for the component design phase. Based on information garnered from the component design, the requirements, engine performance and the expected aircraft performance can be updated. Modern design techniques based upon multi-disciplinary tools and methods integrate and automate much of this process and allow better optimisation of the final design. Validation and the analysis of uncertainty are difficult at this level of fidelity and given the predictive nature of the work. However, suitable techniques such as sensitivity analyses and Monte Carlo assessments can be used to provide indicative trends which can help decision makers evaluate risk and to properly assign resources.

4 Implication of the HP-Spool Configuration

4.1 Nomenclature

BPR	Bypass Ratio
CFD	Computational Fluid Dynamics
DDISFC	Direct Drive Intercooled Straight Flow Core Concept
D_i/D_o	Inner to Outer Diameter Ratio of Hollow Shaft
FN	Net Thrust
GIRFC	Geared Intercooled Reversed Flow Core Engine Concept
GISFC	Geared Intercooled Straight Flow Core Engine Concept
HP	High Pressure
HPC	High Pressure Compressor
HPT	High Pressure Turbine
IP	Intermediate Pressure
LPT	Low Pressure Turbine
OPR	Overall Pressure Ratio
Q	Torque
T_4	High Pressure Turbine Entry Temperature
TO	Take-Off
W_c	Corrected Mass Flow Rate

4.2 Introduction

Over-tip leakage losses, especially in the final stages of the HPC, tend to become more significant at higher OPR where relatively short compressor blades must be used. Although the blades of the HPT tend to be longer, highly loaded designs can also suffer appreciably from over-tip leakage. HPT discs tend to be quite large so as to sustain high stresses at elevated temperatures whilst retaining a suitable lifetime. In the GIRFC design the HP-spool is located behind the LPT. In the absence of concentric shafts, the mean diameter of the HPC and HPT can be reduced leading to longer blades and relatively smaller over-tip leakage losses. This chapter considers the differences in the HP-spool designs of the GISFC and GIRFC concepts. The objective is to understand the main limitations on the principal dimensions of the GIRFC HP-spool design and to highlight the effect on the efficiency of the HPC and HPT.

The novelty of the research presented in this chapter lies in the analysis of the HP-spool for a new concept: the GIRFC. The impact on the design of the HP-spool for several different configurations, including a two spool geared turbofan, a three spool direct drive turbofan and a three spool geared turbofan is compared with that for a reversed flow core concept.

This chapter provides a background to this work together with a description of the main supporting theory and correlations used. The validation of the main techniques is also provided. The evaluation of the HP-spool design is limited to basic high level component assessments. A comparison of the resulting designs and a qualitative discussion of some detailed design points are also given.

4.3 Background

4.3.1 Limitation of Blade Height

It is beyond the scope of this thesis to detail the fundamental turbomachinery loss mechanisms but a detailed account can be found in Denton [61] and Koch [62]. Losses due to changes in tip clearance or Reynolds number do not vary linearly and rely on a number of parameters including tip-clearance, blade loading and aspect ratios. In addition, the variation from root to tip must also be considered. The sensitivity of compressor efficiency towards tip-clearance is

widely recognised. In a 1974 lecture [63], describing the development of the RB211 turbofan, the importance of careful design for the reduction of tip-clearance is highlighted. This work outlines how relatively large tip clearances are a product of high hub-to-tip ratios at the end of the HPC (typically around 0.92) brought about by large drum and casing diameters which in turn lead to small blade heights. For the RB211, significant effort went into rig-testing in order to establish the minimum possible tip-clearances while recognising that this specific area held much scope for future research. Given the complexity and sensitivity of the designs towards mechanical criteria it is, however, sometimes difficult to approach this problem at the conceptual design stage.

This problem has been highlighted in recent works [64]. The approach taken by several researchers [32] [34] [50] [65] is to impose a lower limit on blade height at the end of the HPC. In Shinmyo et al. [32] a lower limit of 15mm is suggested while in Xu and Grönstedt [34] and Guynn et al. [65] 12mm and 12.7mm respectively are recommended. When using this type of constraint it is assumed that the efficiency of the compressor can be maintained down to the boundary limit. Of course this is not the case as the size-effects come into play gradually as core size is reduced and they accelerate rapidly at blade heights below approximately 15mm. There are two main causes for the reduction in efficiency as core size is reduced. The increase in over-tip leakage as blade heights decrease is an important loss mechanism but there is also a low Reynolds number effect which comes into play. Compressor polytropic efficiency is often related to core-size through the use of a size effect curve. Such curves have been presented by Glassman [66] and Philpot [67] (cited in Kurzke [68]). There are significant differences between these size effect curves and so they are difficult to apply correctly without specific information related to the core in question.

Schreiber at al. [69] suggest that Reynolds number losses are exhibited when HPC stages operate at Reynolds numbers below 5×10^5 and that these losses increase rapidly below 2×10^5. Schreiber at al. [69] and Schaffler [70] suggest that the Reynolds number in an HPC decreases rapidly with altitude but that typically the critical Reynolds number is only reached for very high altitude cruise. However, Schaffler [70] suggests that during a typical cruise the HPC of a civil

engine could operate at 35% of the sea-level Reynolds number and possibly fall below 5×10^5. The HPC of an intercooled engine for a given OPR tends towards higher Reynolds numbers as intercooling, due to a decrease in core flow temperature, increases flow density and reduces viscosity. At a standard cruise altitude it was found that the HPC rotor Reynolds numbers varied between 5×10^5 and 7×10^5 when estimated at the rotor entry and based on the mid-chord length as recommended by Schaffler [70]. These estimates were carried out for the initial GISFC configuration. The GIRFC, given the same specification, would exhibit higher Reynolds numbers due to increased blade height and consequently chord length. This suggests that the Reynolds number losses are perhaps not critical for these concepts. In DiOrio [71], a very good outline of both tip clearance and Reynolds number effects on HPC efficiency is given for three different HPC sizes. For a core size of 3 lbm/s DiOrio [71] shows that a 0.2% efficiency penalty due to Reynolds number effects alone can be expected at high altitude cruise. The core size of the GISFC and GIRFC at a normal cruise altitude is approximately 4-5lbm/s which suggests that the Reynolds number losses should be even lower. Given this information no specific correction for changes in Reynolds number were applied to the HPC in either the GISFC or GIRFC designs. In Claus et al [72], it is suggested that Reynolds number effects due to small compressors is a second order effect which can be neglected in the early stages of design but must be considered for accurate compressor modelling.

As with the HPC, the HPT is also susceptible to over-tip losses. Kurzke [73] presents a graphical correlation which can be used to correct the efficiency of a single stage shroudless HPT for the effects of tip-clearance as a function of blade span. The HPT is typically quite highly loaded which can aggravate the losses which occur especially due to tip-leakage. In order to mitigate the over-tip leakage in the HPT, shrouded blades are often used. However, shrouded blades increase drag [61] and, therefore are not without a penalty. A blade shroud also adds weight at the end of the blade disc assembly. This can lead to difficulties related to mechanical integrity if a high speed HPT is assumed, as is the case in this dissertation. Also additional weight will lead to an increase in the size of the HPT discs. For these reasons the original GIRFC concept was conceived as a shroudless design especially as it is expected that the HP-spool configuration can offset some of the over-tip leakage difficulties.

4.3.2 HP-Spool Comparisons

In the NEWAC [12] intercooled engine concepts, it was found that the high pressure ratios across the HPC necessitated a 2-stage HPT. The situation is much the same for the GISFC and GIRFC engine concept. As this chapter focusses on the design of the HP-spool at the conceptual stage, it is relevant to qualitatively look at a selection of in-service turbofan engines which have a similar HP-spool setup. Figure 4.1 and Figure 4.2 show cross-sectional drawings of the GE90 and PW4000 engines respectively. These are not the only engines with 2-stage HPT. Others include the CF6, V2500, GEnx, GP7000 and PW1000G. Typically diagrams such as these are not dimensionally accurate but are useful for making a number of observations. In each case the HPC discs, especially for the rear stages, are very thin. This is due to the low mean radius, small blades and low temperature gradients when compared with the HPT. The first HPC stage is quite large, especially for the GE90, which has sizeable first stage compressor blades. There are no restrictions in terms of inter-disc spacing in the HPC as the separation is sufficient. Perhaps only the first HPC disc may present difficulties in terms of disc height as the blade roots approach the outer diameter of the shaft. The first stage of the HPC must also allow for a linkage to the bearing arrangement which can be seen in each diagram to the left of the first HPC stage. Typically the drive arm of each HPC stage is bolted together and finally a drive arm links the last stage of the HPC to the HPT discs.

In each case the spacing between the HPT discs is quite small. The HPT discs themselves are quite long and thick which is brought about by high temperature gradients, large blades and high radial stresses due to the larger mean radius of the designs when compared with the last HPC stage. The way in which the HPT stages are linked to the HPC stages varies. In Figure 4.1 for the GE90, the drive arm coming from the last stage of the HPC is linked to the centre of the disc pertaining to the first stage of the HPT. The first stage HPT disc is then linked from its base to the bearing arrangement which is to the right of the second HPT stage. The second HPT stage is also linked to the bearing arrangement. In this case, the second HPT disc is shorter to allow for the passage of the arm linking the first disc to the bearing arrangement. In Figure 4.2

for the PW4000 there is a roller bearing arrangement positioned below the combustor. The arm arrangement is reversed from that of Figure 4.1.

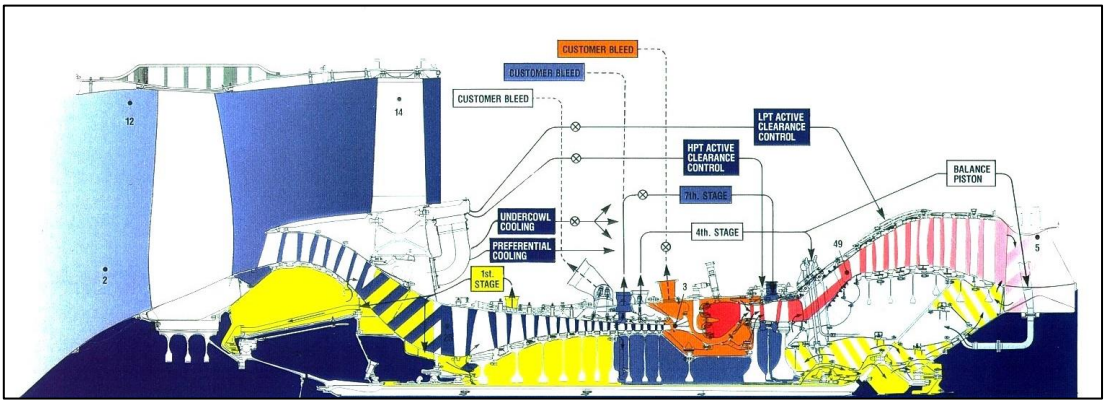

Figure 4.1 – GE90 Cross-Section (adapted from diOrio [71])

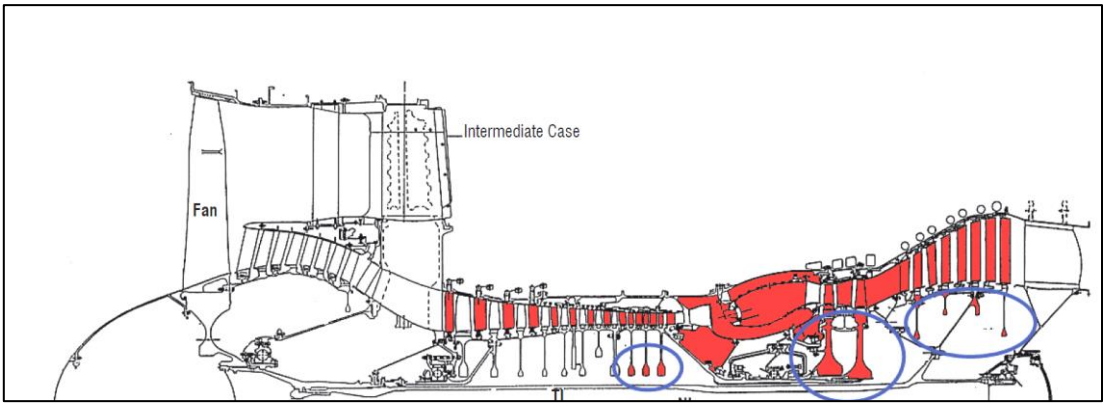

Figure 4.2 – PW4000 Cross-Section (adapted from Locq and Caron [74])

In the GE CF6 engine, shown in Figure 4.3, the HPT arrangement is similar to that of the PW4000 where the HPC drive arm is linked to the second stage disc of the HPT. In the CF6, as in the PW4000, the first stage HPT disc is shorter. In Barak and Domas [75], it is suggested that in the CF6 engine, cooling air passes through the gap below the first HPT disc to help cool the second disc. The CF6 also includes a roller bearing arrangement below the HPC exit diffuser.

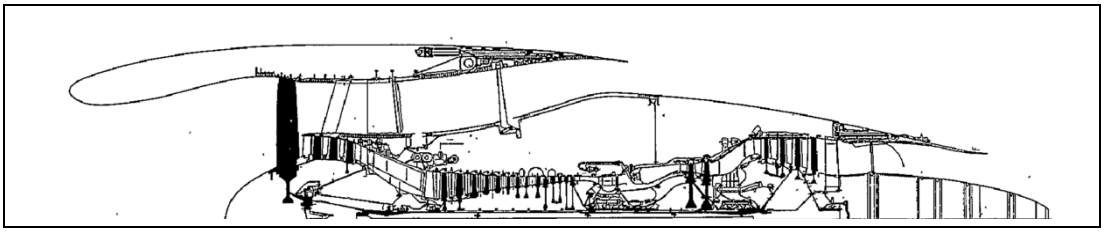

Figure 4.3 – CF6 Cross-Section (adapted from Barak and Domas [75])

The placement of a roller bearing arrangement below the combustor or HPC diffuser could be considered in the GISFC and GIRFC as it could allow for a more longitudinally compact design. However, positioning the bearing arrangement in such a way could limit the reduction in annulus diameter of the HP-spool of the GIRFC by placing an additional inner restriction on the combustor. This would result in smaller blades and higher losses across the rear HPC stages and is therefore undesirable. The HPT configuration of the PW4000 and CF6, where the first HPT disc is shorter than the second, has been adopted for the GISFC and GIRFC although an HPT configuration similar to that of the GE90 could also be practical.

4.4 Methodology

In order to study the characteristics of the HP-spool design and component efficiency the methodology, described in this section was applied. This methodology consists of two distinct parts. The first is concerned with the geometric representation of the HP-spool. This is carried out for both straight flow core and reversed flow core designs. The geometric representation is based upon generic design rules as well as a basic disc stress analysis. The second is concerned with the effect of blade height and tip clearance on compressor and turbine efficiency. This is explored in order to capture the implications of HP-spool design on the overall performance of the engine concepts.

4.4.1 Outline of General Procedure

The sizing of discs and blades is an iterative process that must take into account aerodynamic and structural considerations. The designs evaluated in this chapter are based on the initial configurations listed in chapter 2 and Appendix A. Therefore, a 9-stage HPC and a 2-stage HPT have been retained in each case based upon an equivalent level of stage loading. Aerodynamic considerations set the spacing between turbine guide vanes, rotor and stator [(76) (77)]. The discs must, therefore, be optimised for minimum height while respecting the restrictions imposed by the shaft as well as the inter-disc positioning.

The procedure for estimating the general dimensions of the HP-spool annulus and discs is given in Figure 4.4. The first step in the procedure is the estimation of the HP-shaft diameter. In

reality, the HP-shaft is a series of drive arms and not a shaft as such. However, it has been assumed that some additional clearance for the bearing links is required and, therefore has been modelled as a thin walled HP-shaft. For the straight flow core options, concentric shafts are considered while for the reversed flow core options, the calculation is carried out for an isolated HP-shaft. Next a basic estimation of the annulus dimensions is carried out. Initially, key design parameters such as shaft rotational speed are assumed. Next, the HPC and HPT disc dimensions are estimated based upon the material limitations. The inner diameter of the discs is limited by the outer diameter of the shaft. The outer diameter of the disc is determined by the radial stress produced by the dead weight of the blade and root assembly. Having established the disc height, the annulus dimensions are revised.

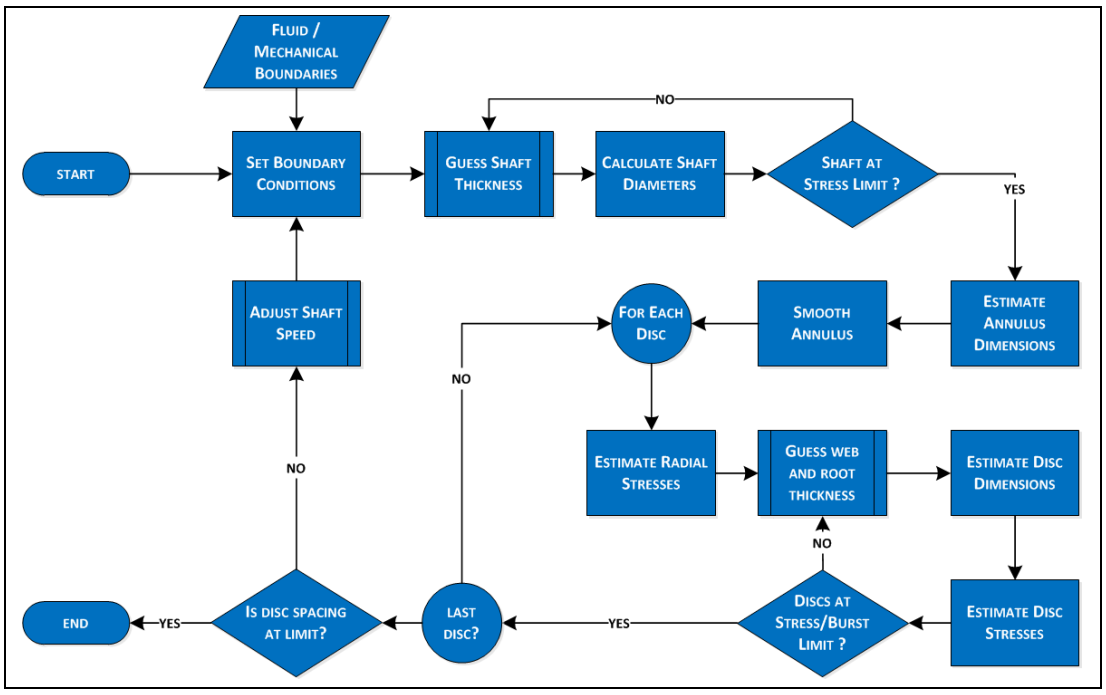

Figure 4.4 – General Methodology for HP-Spool Design

The procedure is repeated until the shaft, annulus and disc dimensions are consistent and no overlap occurs. Given the overall dimensions of the HP-spool it is possible to define the boundary conditions for the efficiency calculation. The efficiency calculation then gives the efficiency penalty which must be attributed due to falling blade height. This methodology was automated into a computer code capable of carrying out the required calculations, design iterations and plotting of relevant geometry.

4.4.2 Estimation of Shaft Diameter

The outer diameter of the HP-shaft limits the root diameter of both HPC and HPT discs. The reversed flow core allows for the HP-shaft diameter to be greatly reduced due to the absence of internal concentric shafts. Therefore, an estimate for the shaft diameter is required in order to assess to what degree the HP-spool design is affected in the reversed flow core concept. An initial estimate for the diameter of a gas turbine shaft can be made based upon a limited centrifugal stress analysis alone as suggested by Sanghi et al. [(78)]. Although this simplification can be made, the dimensions of a shaft can be dominated by other factors such whirling speeds, vibrations and transverse loading. The detailed design of any rotating shaft would need to take these factors into account. However, in order to achieve this level of detail a good understanding of the structural layout of the engine is required because the position and design of the shaft bearings as well as the flexure of the engine architecture will impact the aforementioned criteria. At the conceptual design stage, this information is not available, and therefore a more simplified approach must be adopted. The relationship relating limit stress to shaft dimensions for a hollow rotating shaft loaded only in torsion is given in Equation (4.1) which is based on the ASME code for shaft design and is defined by Purohit and Sharma [(79)].

$$\tau_{\max} = \frac{16}{\pi d_o^3 (1 - K^4)} (C_t Q)^2 \qquad \textbf{(4.1)}$$

where:

- τ_{max} *limit shear stress*
- d_o *shaft outer diameter*
- C_t *fatigue factor*
- K *ratio of inner to outer shaft diameters for a hollow shaft*
- Q *torque*

A fatigue factor of 1.3 has been assumed in Equation (4.1) and lies within the range recommended by Purohit and Sharma [(79)] for minor shock loads. Hollow shaft designs have been assumed in all cases. Solid shafts are more compact in terms of the outer diameter but the core material of a solid shaft does not contribute to the centrifugal strength of the system to the same degree as at the rim. As a hollow shaft can be lighter, it is often preferred. A D_i/D_o ratio of 0.85, as suggested by Sanghi et al. [(78)], has been assumed for non-concentric shafts and

the innermost concentric shaft in multi-shaft designs such as for the straight flow core concepts. In order to determine the geometry of outer shafts in multi-shaft designs an iterative process is required. For these shafts, the D_i/D_o ratio is repeatedly adjusted until a clearance of 0.5mm can be obtained between concentric shafts as suggested by Sanghi et al. [78].

4.4.3 Annulus Dimensions

Given an initial estimate for the shaft diameter, the annulus dimensions are subsequently estimated as outlined in the overall methodology discussed previously. The weight estimation tool, described in Appendix C, was used to define the mean blade speed at the entry and exit of the HPC and HPT of the initial configurations. The thermo-fluid conditions at the entry and exit of the HPC and HPT were obtained from the engine models. Given this information, it was possible to determine the position of the annulus with respect to the shaft. Blade aspect ratios, inlet and outlet Mach number and stage loading of the HP-spool annulus have been estimated according to the guidelines outlined in Grönstedt [80]. These correlations do not take into account detailed blading criteria but are based upon historical trends in the development of gas turbine compressors and turbines. Some input parameters such as aspect ratios were also adjusted according to features in existing engine designs such as the GE90 and PW4000. A constant temperature ratio was assumed to occur at every stage for both the HPC and the HPT. Stage Mach numbers and blade aspect ratios were linearly interpolated in order to estimate the annulus dimensions. Finally a cubic interpolation was used to smooth the interfaces between stages while correcting for area and Mach number throughout. In this dissertation, further detailed blading design was not carried out. Rather, as has just been described, a simpler but more readily automated approach was adopted. The feasibility of the designs was confirmed by Anselmi[1] through higher fidelity annulus designs for the final GISFC and GIRFC configurations.

[1] Eduardo Anselmi Palma, a PhD student at Cranfield University, is investigating in his PhD the mechanical arrangement and losses within the GIRFC concept.

4.4.4 Sizing of the HPC and HPT Discs

This module allows for the initial estimation of disc dimensions based upon thermo-mechanical stress calculations described hereafter. The blade-disc assembly is composed of several parts including the blade and the blade root including platform, neck post and fir tree. These constitute the dead weight which when rotating set up the radial stress at the outer rim of the disc. The disc itself constitutes the live weight of the assembly. The disc linkages vary in nature depending on the specific design and are often ignored in the early stages of design. Different techniques exist for modelling the stresses in the blade-disc assembly. This dissertation is restricted to the conceptual design stage, and therefore certain detailed elements such as cooling passages and complex linkages have been ignored.

Several low-fidelity disc design methodologies are reported in literature. In Mattingley et al. [49], the disc design and stress analysis method simplifies considerably the blade disc assembly and relates the blade radial stress to the upper rim stress of the disc using a simple ratio. The NASA gas turbine weight estimation tool WATE [81] also makes use of a basic disc stress estimation module. In this code the blade weight and dimensions are specified by the user while the remainder of the dead-mass is estimated based upon pre-defined factors. The live weight stress estimation is carried out for radial and tangential components including thermal effects. The geometry of the disc is also pre-defined but is iteratively optimised in order to observe the material limitations. In GasTurb [73], a more detailed approach is taken for estimating the dead weight. Here the blade and fixture masses are estimated individually. The disc stress and optimisation procedures are similar to those in WATE [81]. TAXI [82] [83] delivers similar fidelity to the previous codes but is specifically targeted at disc design alone. Consequently, this tool incorporates a number of disc optimisation routines as well as several different disc geometries. In this dissertation a combination of these methods has been used to establish the geometry of the disc. A custom disc optimisation technique has also been implemented which is applied to every disc present in the HP-spool.

The radial load due to the rotating blades attached at the outer rim of the discs was estimated according to Equation (4.2). A turbine blade density of 7730kg/m^3 and a compressor blade

density of 4638kg/m^3 were assumed together with a taper ratio (A_t/A_h) in both cases of 0.8. The compressor blade density assumes a titanium based material. For a very high OPR engine with a conventional core, the blades of the final HPC stages would have to be made of a nickel based material so as to sustain the high temperatures which would be encountered. Nickel blading would slightly increase the weight of the core. In this work, it has been assumed that a titanium based material is sufficient as the intercooler reduces the core flow temperatures significantly. The radial load from the blades is spread out over the rim. For this reason, the radial load at the rim is corrected using Equation (4.2) and Equation (4.4) from Mattingley et al [49]. The first equation relates the two load points based upon the relationship between rim and blade root areas. The second relates the number of blades to the rim area. Given typical values of solidity, the correction for radial load at the outer rim can be made. A hollow disc was assumed which by definition leads to the absence of radial load at the disc bore. The radial loads due to the blade root and post are evaluated based on the dimensions and mass estimates suggested by Kurzke [73] and Tong et al. [81] and are estimated using Equation (4.5).

$$\sigma_c = \frac{\rho\omega^2 {r_h}^2}{4}\left(1 - \left(\frac{\mathrm{r}_h}{\mathrm{r}_t}\right)^2 - \left(\frac{2\frac{A_t}{A_h}}{3\left(1 - \left(\frac{\mathrm{r}_h}{\mathrm{r}_t}\right)^3\right)}\right)\right) \qquad \textbf{(4.2)}$$

$$\sigma_{c,b} = \frac{\sigma_c N_b A_h}{2\pi r_h W_r} \qquad \textbf{(4.3)}$$

$$N_b = \frac{\pi D_t (\mathrm{C}/S)}{(\mathrm{AR}/H_b)} \qquad \textbf{(4.4)}$$

$$\sigma_{c,p+r} = \frac{N_b \omega^2}{2\pi r_h}\left(m_{p+r} r_{cg,p+r}\right) \qquad \textbf{(4.5)}$$

where:

- ρ *density*
- σ_c *rotor aerofoil centrifugal stress*
- $\sigma_{c,b}$ *average blade stress*
- $\sigma_{c,p}$ *average platform stress*
- ω *rotation rate*
- h *hub*
- m_{p+r} *mass of blade post and root*

- r *radius*
- $r_{cg,p+r}$ *centre of gravity of blade post and root*
- t *tip*
- A *area*
- $\frac{A_t}{A_h}$ *taper ratio (0.8)*
- AR *blade aspect ratio*
- C/S *solidity*
- D *tip diameter*
- H_b *blade height*
- N_b *number of blades*
- W_r *aerofoil axial chord*

Web and hyperbolic disc profiles, as shown in Figure 4.5, are widely used. Hyperbolic profiles allow for more optimisation of the disc thickness and typically result in lighter designs. As discussed later in this chapter, the HPT typically requires quite large discs, and therefore self-supporting designs are typically not considered. Although the self-supporting designs could perhaps be considered for an advanced HPC disc design, it is beyond the scope of this thesis. There are several geometric parameters which define the design of the disc. The full optimisation of the disc would require the evaluation of all these parameters. In this work, the variables were assumed to be the web and the inner rim thickness of each disc and were optimised until adequate stress and burst margins were achieved for each disc. Typical values were assumed for the remainder of the basic shape factors for each disc.

In literature there are several suggestions as to how the geometry of a hyperbolic disc, as shown in Figure 4.5, should be defined. The following equations represent some common hyperbolic profiles. There is no clear evidence to suggest that any of these equations represent a “better” disc profile. Equation (4.7) results in far less curvature of the disc profile, meaning that the disc thickness tends to be larger throughout and is not consistent with typical 2-stage hyperbolic disc designs. The remaining two relationships can result in similar profiles. However, Equation (4.6) allows for more flexibility in the variation of the profile gradient through modification of the disc scaling factor. This gives the designer more choices, and therefore this relationship has been adopted.

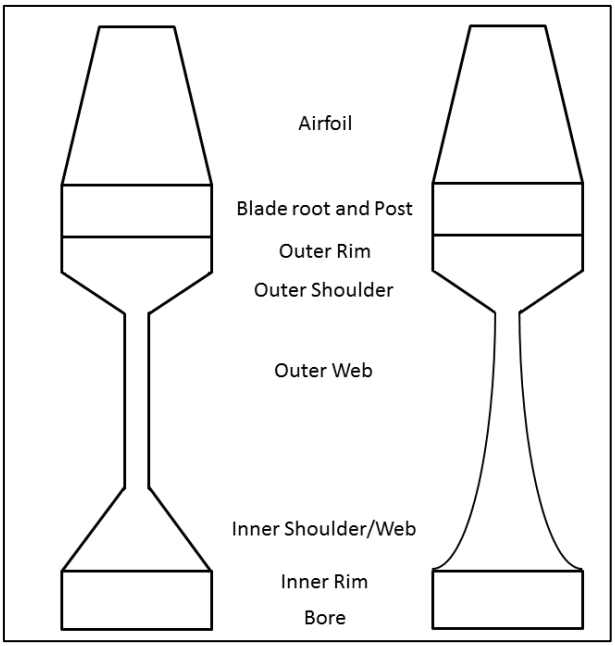

Figure 4.5 – Web Disc and Hyperbolic Disc Geometry (adapted from Tong et al. [81])

$$\mathrm{t} = t_{\mathrm{o}} + (t_{\mathrm{i}} - t_{\mathrm{o}})\left(\frac{\mathrm{r} - r_{\mathrm{i}}}{r_{\mathrm{o}} - r_{\mathrm{i}}}\right)^{dsf}$$

Equation (4.6) – Hyperbolic disc function [81]

$$t = \alpha e^{-\beta r^{4/3}}$$

$$\beta = \frac{2.303}{r_o^{4/3} - r_i^{4/3}} log_{10}\left(\frac{t_i}{t_o}\right)$$

Equation (4.7) – Hyperbolic disc functions [84]

$$t = \alpha r^{-s}$$

$$s = -\frac{log_{10}\left(\frac{t_i}{t_o}\right)}{log_{10}\left(\frac{r_{\mathrm{i}}}{r_{\mathrm{o}}}\right)}$$

Equation (4.8) – Hyperbolic disc functions [85]

where:

- α *proportionality constant*
- dsf *disc scaling factor*
- *i* *inner*
- *o* *outer*
- r *disc element radius*
- t *disc element width*

In order to determine whether a given disc design is feasible, it is necessary to carry out a thermo-mechanical stress analysis. Disc stresses are usually determined through the use of finite element analysis or else through elemental planar analysis. The former technique is typically used in the later stages of design as it involves the modelling of all the complex features of a disc. Due to its simplicity, the latter technique is more suitable for the early stages of design within which this work is classified. A number of key assumptions were made in the development of the stress analysis module. The discs were modelled as a biaxial stress system where only radial and tangential stresses were considered. Longitudinal loads in the discs, while present, do not represent a major failure criterion and although in a rigorous analysis these loads would need to be evaluated, at the conceptual design stage, these are often ignored.

The next major factor in the design of the discs is the selection of a representative material. In this work, it was assumed that the material properties are isotropic. Information on material properties is available for several super-alloys but these do not necessarily represent the current state-of-the-art much less the state-of-the-art for engines intended for a concept with an entry into service in 2025. Materials such an INCO718 are in use but do not represent the ideal candidates for advanced concepts. For the HPT disc material, Barak and Dumas [75] considered the use of René 95 as a substitute for INCO718. The material properties of René 95 are superior to those of INCO718 in terms of ultimate tensile strength, yield strength and creep resistance at elevated temperatures. The material properties of René 95 can be found in Barak and Dumas [75] and Gean [86]. Shamblen et al. [87] suggest that René 95 is suitable for both high strength turbine and compressor discs. The compressor discs, especially the front stages, which operate at lower temperatures, can make use of lighter titanium based alloys which are easier to manufacture. The first stage compressor disc height could be a limiting factor, and therefore its minimisation is desirable and warrants the use of an advanced material. The fundamental radial and tangential stress equations used for the calculation of disc stresses are given in Equation (4.9) and Equation (4.10).

$$\sigma_h = \frac{(3+\nu)}{8}\rho\omega^2\left[r_o^2 + r_i^2 + \frac{r_o^2 r_i^2}{r^2} - \left(\frac{1+3\upsilon}{3+\upsilon}\right)r^2\right] \quad \textbf{(4.9)}$$

$$\sigma_r = \frac{(3+\nu)}{8}\rho\omega^2\left[r_o^2 + r_i^2 - \frac{r_o^2 r_i^2}{r^2} - r^2\right] \quad \textbf{(4.10)}$$

where:

- α *proportionality constant*
- ρ *material density*
- σ_h *hoop stress*
- σ_r *radial stress*
- υ *poisson's ratio*
- ω *rate of rotation*
- *i* *inner*
- *o* *outer*
- r *disc element radius*

In order to complete the disc stressing exercise, a ring discretisation technique was adopted. This method involves dividing each disc into finite planar segments and integrating the result from root to tip. In order to solve the equations for each plane the "sum and difference" form of the principal stress equations together with the thermal stress equations were used. This method is outlined in Smith [88]. For each planar segment Equations (4.11) to (4.18) were solved iteratively.

$$S = \sigma_h + \sigma_r \quad \textbf{(4.11)}$$

$$D = \sigma_h - \sigma_r \quad \textbf{(4.12)}$$

$$\sigma_{hoA} = \frac{S_{oA} + D_{oA}}{2} \quad \textbf{(4.13)}$$

$$\sigma_{roA} = \frac{S_{oA} - D_{oA}}{2} \quad \textbf{(4.14)}$$

$$S_{oA} = S_{iA} - \frac{1+\upsilon}{2}\rho\omega^2(r_{oA}^2 - r_{iA}^2) \quad \textbf{(4.15)}$$

$$D_{oA} = D_{iA}\left(\frac{r_{iA}^2}{r_{oA}^2}\right) - \frac{(1-\upsilon)\rho\omega^2}{4}\left[\frac{r_{iA}^4}{r_{oA}^2} - r_{oA}^2\right] \quad \textbf{(4.16)}$$

$$\delta\sigma_r = \sigma_{roA}\left(\frac{h_A}{h_B} - 1\right) \quad \textbf{(4.17)}$$

$$\delta\sigma_h = (\sigma_{hoA} - \nu\sigma_{roA})\left[\frac{E_B}{E_A} - 1\right] + E_B(\alpha_A T_A - \alpha_B T_B) + \delta\sigma_r \qquad \textbf{(4.18)}$$

where:

- α *coefficient of thermal expansion*
- ρ *material density*
- σ_h *hoop stress*
- σ_r *radial stress*
- υ *poisson's ratio*
- ω *rate of rotation*
- i *element inner plane*
- o *element outer plane*
- r *disc element radius*
- A finite element A
- B finite element B
- D difference
- E Young's Modulus
- S sum

Disc stresses should be evaluated under conditions representing the maximum operational rotational speed and maximum temperature [73]. If these points do not coincide, then both points would need to be evaluated. In this thesis, the take-off condition represents the highest operating temperature and HP-spool rotational speed, and therefore is adequate for the analysis of disc stresses. The disc design module was designed to automatically adjust the geometry of each disc in order to meet a given set of boundary conditions and criteria. The radial load at the disc outer rim is a function of the dead weight position and speed. The radial load at the bore is assumed to be negligible while the tangential stress at the bore is found iteratively. Given an initial estimate for the tangential stress at the bore, the stress profile can be discretely evaluated in the radial direction until the radial stress boundary condition is met. This gives an initial estimate for the disc height. The tangential stress at the bore is then adjusted through a Newton-Raphson algorithm until the required disc height is achieved. Given this information a complete stress profile can be obtained for a given disc height. Nevertheless, the disc design must also satisfy a number of criteria in order to ensure its integrity over the typical operation of the disc.

The disc design module checks automatically a number of criteria in order to establish whether the disc geometry is feasible. If the geometry is found to be infeasible two variables are adjusted, namely the lower rim width which has a major influence on the peak tangential stress and the minimum web thickness which has a major influence on the peak radial stress. The criteria which must be observed include a minimum desk margin of 1.0 as defined by Equation (4.19). This relates the von Mises criterion as defined by Equation (4.20) to the material yield stress at the local temperature.

$$Desk\ Margin = \frac{\sigma_y}{sf.\sigma_{vm}} > 1 \qquad \textbf{(4.19)}$$

$$\sigma_{vm}^2 = \sigma_h^2 - \sigma_r\sigma_h + \sigma_r^2 \qquad \textbf{(4.20)}$$

where:

- σ_{vm} *von Mises stress*
- σ_y *yield strength*
- σ_h *hoop stress*
- σ_r *radial stress*
- sf safety factor (1.1)

In addition, Sawyer [89] suggests that radial disc burst can occur in the circumferential plane if high radial stresses are present and recommends that the radial stress should not exceed the average tangential stress. The burst criteria can be observed by limiting the design stress as per Equation (4.21) where the design stress can be assumed to be the mean stress [89]. This constraint was found to result in fairly conservative designs and was relaxed. However, the general condition that radial stress should not exceed the average tangential stress was in general observed.

$$\sigma_D < minimum[\frac{2}{3}\ \sigma_y, \frac{1}{3}\ \sigma_u] \qquad \textbf{(4.21)}$$

where:

- σ_u *ultimate tensile strength*
- σ_y *yield stress*
- σ_D *design stress*
- R *element radial thickness*
- T *temperature*

The burst margin is also checked during the disc sizing routine. Sawyer [89] defines burst margin as given by Equation (4.22). This formula also suggests that burst speed should exceed design speed by a factor of at least 1.3. The *k* term is a safety factor where 0.75 yields the most conservative design. Similarly, Kurzke [73] recommends that burst speed should exceed design speed by a factor of 1.3-1.5.

$$Burst\ Margin = \frac{N_B}{N_D} = \sqrt{\frac{k * \sigma_u}{\sigma_{h_a}}} > 1.3 \qquad \textbf{(4.22)}$$

$$0.75 < k < 1.0$$

where:

- σ_u *ultimate tensile strength*
- σ_{h_a} *average hoop stress*
- N_B *burst speed*
- N_D *design speed*

4.4.5 Model Validation

The HP-spool design model is based upon a number of individual modules where the most fundamental component is related to disc design. The shaft and annulus sizing, while important, are far less complex than the disc design as they rely upon a simple set of design rules and historical trends. The disc design module makes use of a system of equations to characterise the bi-axial stress system at thousands of elemental sections for each compressor and turbine disc. Gutzwiller at al. [83] claim that unconstrained hyperbolic disc design can lead to very high out-of-plane stresses. In such a case, a bi-axial stress system cannot be assumed and the theoretical model suggested in the previous section would need to be replaced with more complex finite element analysis for reasonable results to be obtained. Gutzwiller at al. [83] suggests that if the disc scaling factor is constrained to a lower limit of 0.2 then the out-of-plane stresses should not exceed 5% of the corresponding in-plane stresses. In this dissertation, the eccentricities of the hyperbolic web designs have been assumed to be far lower than would be the case for a disc scaling factor of 0.2 as suggested by Gutzwiller at al. [83]. Therefore a bi-axial stress system has been assumed to be representative. The disc stress theory described in the previous section has been widely documented and used in several engineering disciplines and therefore no attempt has been made to further validate this theory within the scope of a bi-axial stress system. For validating the functionality of their models, Gutzwiller at al. [83] and Faragher [90] both used the closed form analytical solutions describing the fundamental bi-axial stress distribution of simplified disc geometries for comparison. Similarly, in order to validate the stress prediction module used in this dissertation the same benchmarking procedure as described by Faragher [90] has been used.

The first validation case is for a rotating annular disc of uniform thickness. The radial and tangential disc distributions based on the closed form solutions, the material properties and the disc dimensions for the validation case have been replicated from Faragher [90]. Figure 4.6 and Figure 4.7 compare the radial and tangential stress distribution as predicted by the closed form solutions defined in Faragher [90] and as predicted by the previously described model. Clearly,

the model accurately describes the bi-axial stress distribution throughout the disc when compared with a theoretical prediction.

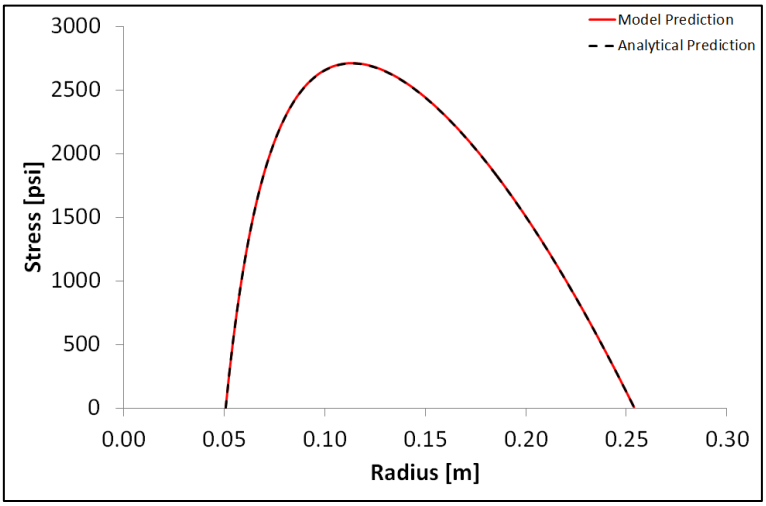

Figure 4.6 – Comparison of Model and Analytical Radial Disc Stress Predictions

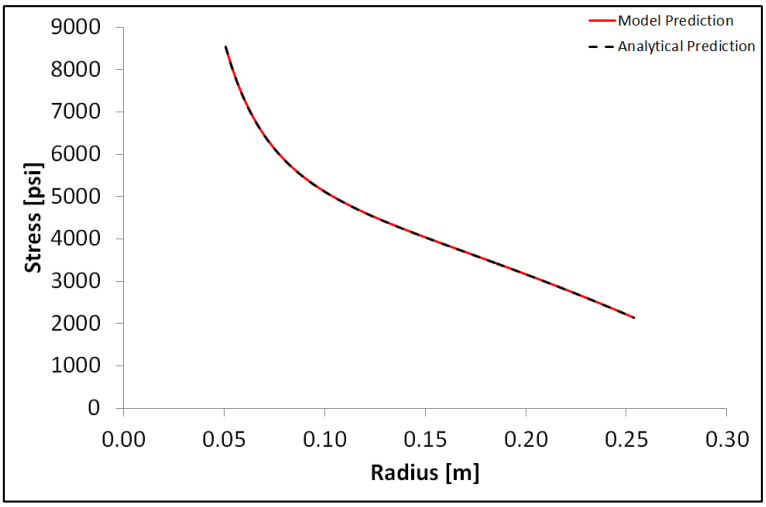

Figure 4.7 – Comparison of Model and Analytical Tangential Disc Stress Predictions

The second validation case is for a rotating annular disc of hyperbolic thickness. As in the previous case, the radial and tangential disc distributions based on the closed form solutions, the material properties and the disc dimensions for the validation case have been replicated from Faragher [(90)]. Figure 4.8 and Figure 4.9 also show that the model developed in this thesis accurately describes the bi-axial stress distribution throughout the disc when compared with a theoretical prediction. Clearly, the discs considered in this dissertation are more complex in geometry as they include an inner and outer rim as well as a temperature gradient. However, as

the model divides the complex geometry into finite planes the solution procedure is no different from what was carried out in this validation case. This lends confidence to the results predicted by the model and suggests that the stress estimates are reliable at least at the level of fidelity required for conceptual design.

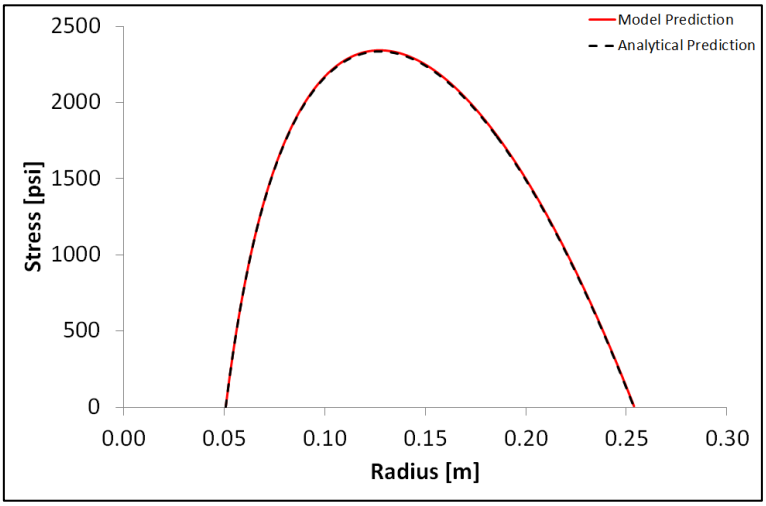

Figure 4.8 – Comparison of Model and Analytical Radial Disc Stress Predictions

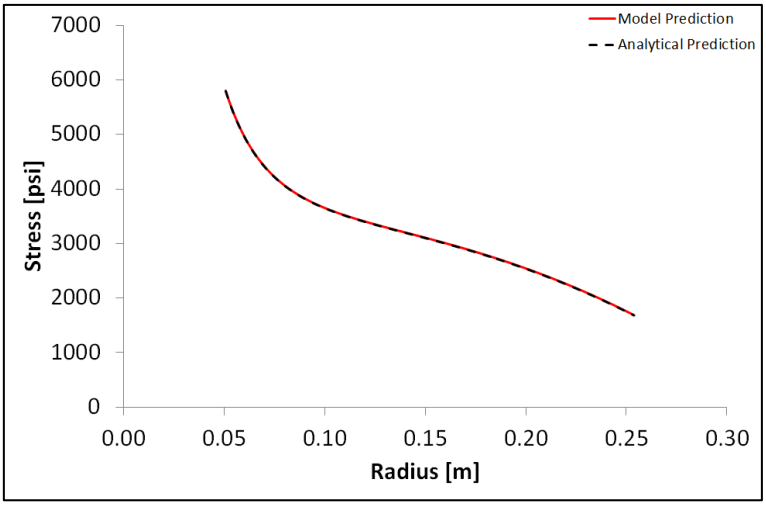

Figure 4.9 – Comparison of Model and Analytical Tangential Disc Stress Predictions

As described in the previous section, the HP-spool design tool is capable of carrying out a basic disc characterisation based on simplified design rules and stress analyses. Aside from generating disc stress profiles the tool also provides a basic geometrical description of the HP-spool. In Figure 4.10 an example is given of a full, although basic, HP-spool design. The schematic of the Trent 700 was obtained from Gunston [91]. Superimposed on the cross-section

of the Trent 700 is the HP-spool design generated by the current model. The similarity between the model and Trent 700 HP-spool design is considerable in terms of annulus dimensions, disc spacing, disc thickness and shaft clearance. Of course, the schematic presented in Figure 4.10 may not be precise and in any case cannot be used for exact measurements. Also, the Trent 700 model described in the Appendix A, which is required in order to provide the thermodynamic inputs to the current HP-spool design module, is also subject to a degree of uncertainty. Nevertheless, the similarity in designs increases confidence in the HP-spool model predictions.

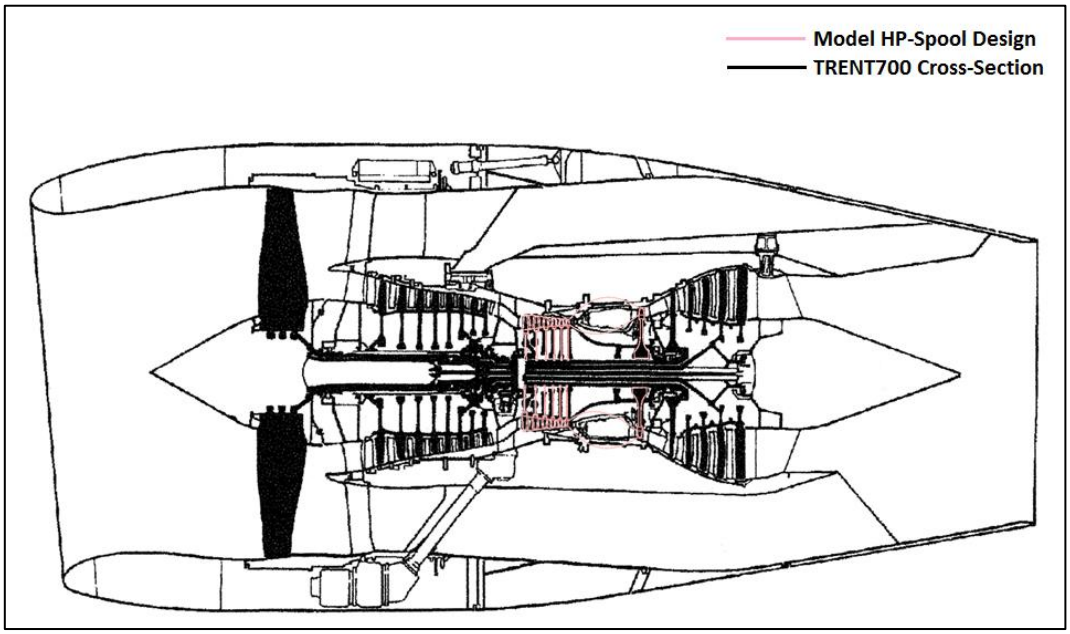

Figure 4.10 – Trent 700 HP-Spool Design (adapted from Gunston [91])

4.4.6 Prediction of Over-Tip Losses

The selection of stage count and the implication of over-tip losses and stage loading on efficiency is an important aspect in the evaluation of the GIRFC concept. Several efficiency prediction methods for turbo-machines exist, many of which require the complete definition and characterisation of the annulus. At the conceptual design stage it is typical to make use of simplified correlations for the estimation of compressor or turbine efficiency such as those from Glassman [66], Matias [92] and Grönstedt [93]. In order to capture the decrease in efficiency due to tip clearance effects, the correction proposed by Lakshminarayana [94] and shown in Equation (4.23) has been implemented.

$$\Delta\eta = \frac{0.7\lambda\psi}{\cos\beta_m}\left[1 + 10\sqrt{\frac{\phi\lambda A}{\psi\cos\beta_m}}\right] \qquad \textbf{(4.23)}$$

where:

- β_m *mean air angle*
- λ *non dimensionalised clearance (clearance / blade height)*
- $\Delta\eta$ *decrease in stage efficiency due to clearance*
- ϕ *flow coefficient*
- ψ *blade loading coefficient*
- A *blade aspect ratio*

In this work this equation was applied to each HPC and HPT stage. The overall component efficiency was then estimated based on the overall loss across each machine. While other methods are available for estimating over-tip losses, Sitram [95] describes this method as one of the most widely used and accurate correlations. Although the work of Sitram [95] is not in itself recent, the correlation in Equation (4.23) was still used in recent works such as in the investigations of Montella and Buijtenen [96] where a simplified method for evaluating the impact of component design on engine performance is proposed and Equation (4.23) is recommended for the evaluation of over-tip losses for unshrouded blades.

4.5 Evaluation

The goal of the evaluation presented in this section is to determine the implication of the GIRFC HP-spool configuration on annulus dimensions and to define the consequent effects on over-tip leakage losses. The aim of this thesis is to compare the GIRFC with existing intercooled engine concepts. Therefore, the GIRFC HP-spool configuration is compared in more detail with the HP-spool of a three spool direct-drive intercooled straight flow core engine (DDISFC) and of a two spool geared intercooled straight flow core engine (GISFC). The HP-spool design of the GIRFC is also compared with that of the TF2000 engine model which is based on the Trent 772. The Trent 772 is assumed to be a reasonable reference point for a year 2000 turbofan configuration of similar thrust levels. The dimensions of the combustor have not been optimised in this work, and therefore the combustor diagrams presented in this section are not accurate representations.

4.5.1 Comparison of Competing Conceptual Designs

Rotational Speed Limitation

The GISFC and GIRFC concepts call for a 2-stage HPT. As the design rotational speed of the HP-spool is increased, the lower rim width of the disc must be increased in order to prevent an increase in tangential stresses beyond the given material limitations. Nevertheless, for a feasible disc design to be achieved the spacing between the two discs must be maintained. For a given loading and blade speed, an increase in rotational speed will lead to a reduction in mean annulus diameter for both HPC and HPT. The first stage disc design of the HPC may present difficulties if the blade root is too close to the shaft. Figure 4.11 compares the HP-spool design of the GISFC for two different design speeds; specifically 16600rpm and 18000rpm. In this example, the blade aspect ratios for both compressor and turbine stages have been kept constant. The disc stresses have been limited according to the guidelines outlined in the previous section. In addition, mean blade speed and consequently stage loading has been kept the same in order to maintain the same stage count. At a design rotational speed of 16600rpm, the disc designs of both the HPC and HPT are feasible. At 18000rpm the HPT discs overlap leading to an infeasible disc design. In this work detailed CFD and experimental work were not

attempted, and therefore the optimum turbine axial spacing has been assumed to be consistent with the typical values suggested by Grönstedt [80] which are also consistent with the optimum suggested by Ummiti [76]. If these criteria are assumed then increasing the axial spacing to allow for thicker discs would reduce the stage efficiency. Increasing the axial spacing would definitely increase the engine length and weight. The first stage HPC disc, under this condition appears to be practical. This example assumed a fixed shaft diameter. The concepts under consideration are not, however, restricted by the same shaft design and must be assessed individually.

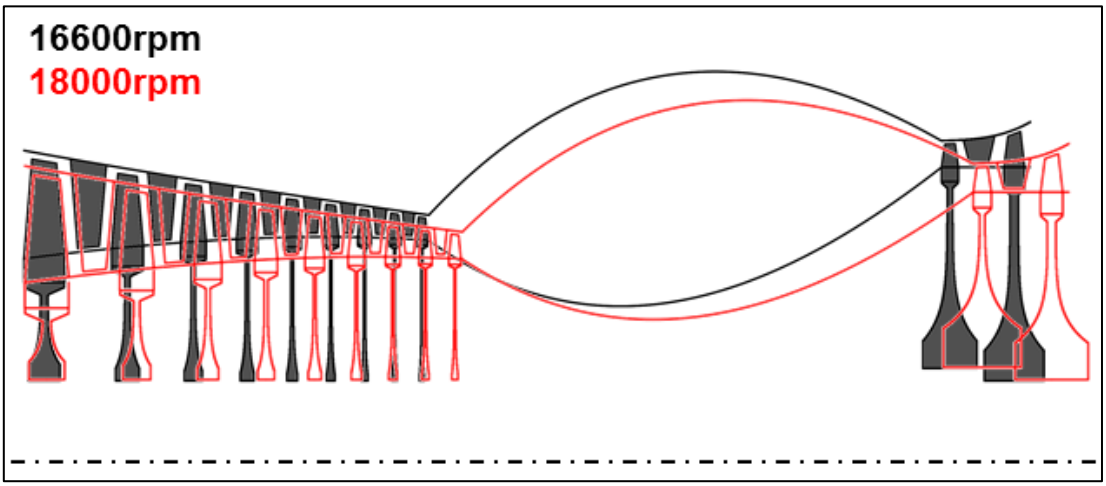

Figure 4.11 – Implication of Increase in Design Rotational Speed

HP-Shaft Characteristics

In a conventional direct drive or geared turbofan the LP-shaft, IP-shaft and HP-shaft are fitted concentrically. The HP-shaft diameter is thus restricted and cannot be selected independently of the other shafts. A geared configuration does allow for the reduction of the HP-shaft diameter when compared with a direct drive configuration as the LP-shaft is run at a higher rotational speed and hence delivers the same power at a reduced torque. These trends can be seen in Table 4.1 for the initial engine configurations. Due to the absence of concentric LP-shaft and IP-shaft, the reversed flow core engine concept frees the HP-shaft from inner constraints. This allows for a significant reduction in the HP-shaft diameter. In this thesis, a minimum D_i/D_o ratio of 0.85 has been maintained for all the HP-shafts under consideration. Due to the absence of a core nozzle, in a reversed flow core configuration it is reasonable to consider a rear mounted accessory gearbox. This was also the case in the ATF3-6A engine from Garrett. The rear

mounted gearbox could make use of the HP-shaft for drive power. By allowing for a hollow HP-shaft it is also possible to consider the use of the LP-shaft for accessory drive power. This has the advantage of running at a lower speed which means that a lower gear ratio could be adopted for reducing the rotational speed into the gearbox.

		DDISFC	GISFC	GIRFC
LP-shaft speed	**rpm**	2,700	8,000	n/a
IP-shaft speed	**rpm**	8,500	n/a	n/a
HP-shaft speed	**rpm**	14,500	16,600	21,000
LP-shaft torque	**kNm**	182	83	n/a
IP-shaft torque	**kNm**	21	n/a	n/a
HP-shaft torque	**kNm**	47	24	19
HP-shaft diameter	**mm**	180	132	72

Table 4.1 – Shaft Characteristics

Annulus Comparison

In section 4.5.1, it was shown how an increase in rotational speed can lead to an infeasible design due to a growth in disc thickness for a given shaft diameter. However, the current concepts enable a reduction in shaft diameter which allows for higher rotational speeds to be obtained and furthermore sufficient space for feasible disc designs. Figure 4.12 to Figure 4.13 show how the annulus and disc design of the DDISFC and GISFC compare with that of the GIRFC. The rotational speed of each concept has been increased until a minimum clearance was obtained between HPT discs or until the first stage of the HPC was no longer practical in the assumed form. It is clear that as shaft diameter decreases, a higher rotational speed and hence smaller blade mean diameter can be adopted. The final rotational speeds are listed in Table 4.1. As the outer shaft diameter is reduced, there is a growth in HPT disc thickness as rotational speed and hence radial stress at the outer rim is increased. This increase in thickness is also partly due to the increase in blade chord as the blade aspect ratios have been kept constant. Table 4.2 summarises the main annulus dimensions. These tables show how blade height is affected by the given designs. It is clear that the GIRFC benefits from a significant increase in blade height which for a given tip-clearance should allow for a reduction in over-tip leakage.

Component	Parameter	DDISFC [m]	GISFC [m]	GIRFC [m]
HPC	Inlet Mean Diameter	0.374	0.326	0.258
	Outlet Mean Diameter	0.372	0.325	0.257
	Inlet Blade Height	0.07	0.080	0.101
	Outlet Blade Height	0.015	0.017	0.022
HPT	Inlet Mean Diameter	0.489	0.427	0.337
	Outlet Mean Diameter	0.504	0.440	0.348
	Inlet Blade Height	0.017	0.019	0.025
	Outlet Blade Height	0.023	0.026	0.033

Table 4.2 – Comparison of DDISFC, GISFC and GIRFC Annuli

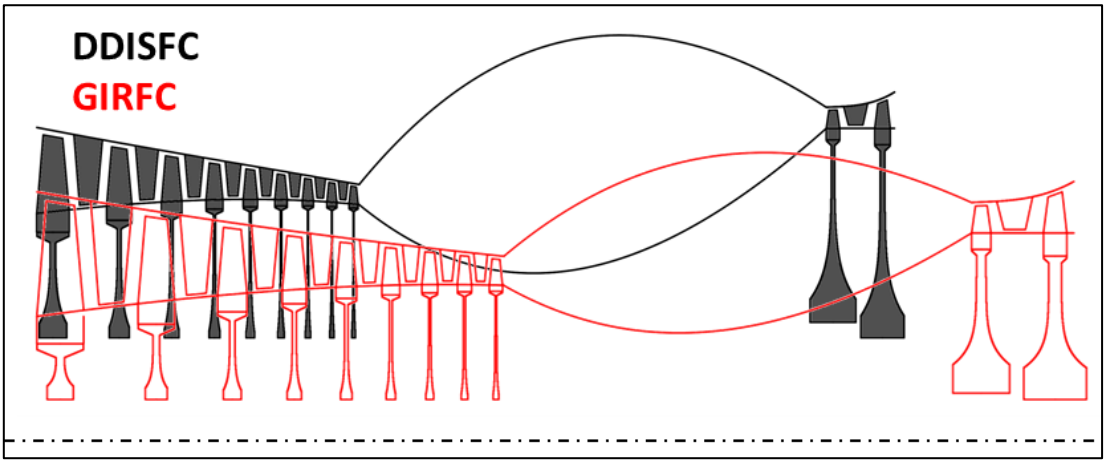

Figure 4.12 – Comparison of DDISFC and GIRFC HP-Spools

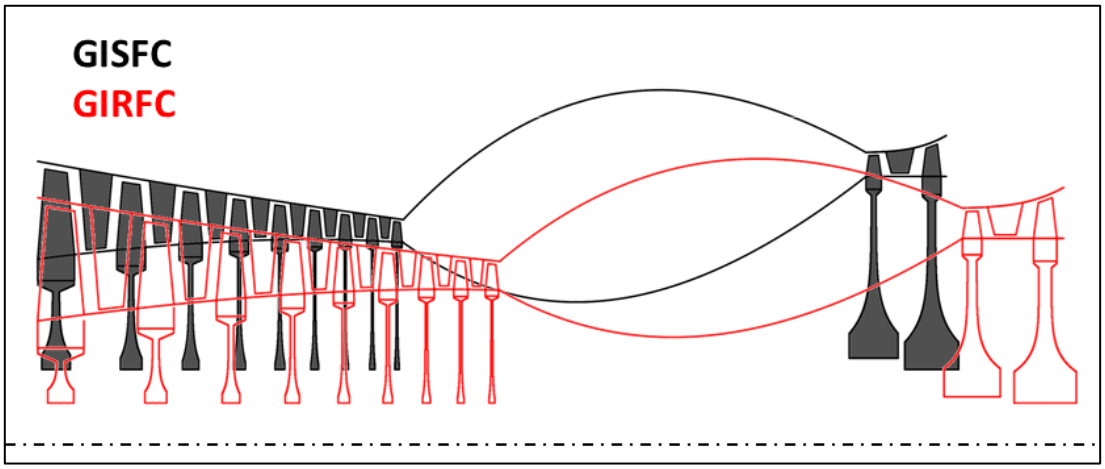

Figure 4.13 – Comparison of GISFC and GIRFC HP-Spools

Comparison of Discs

The HPC and HPT discs have been optimised for minimum lower rim and web thickness while respecting the material limitations as established through the criteria described previously. The shaft and annulus calculations establish the boundary conditions which determine the respective disc height. The discs of the DDISFC and GISFC are compared with those of the GIRFC in Figure 4.14 to Figure 4.21. Only the first and last stage discs of the HPC have been shown, as the intermediate stages can be interpolated from this information.

As rotational speed is increased, when moving to concepts with shaft designs of smaller diameter, it is apparent that a reduction in absolute disc height is also obtainable. That is to say that the reduction in mean annulus diameter is greater than the reduction in shaft diameter as there is a contribution as well from a reduction in disc height. The upper rim radial stress is consistently larger for the GIRFC concept. Although the solidity has been assumed constant, which leads to a lower blade count, the higher rotational speed and longer blades tend to offset any benefit.

The hyperbolic compressor disc design yields a relatively flat radial and tangential stress distribution throughout much of the disc web. Therefore, the von Mises stress, which is not shown here, also does not vary greatly through the hyperbolic web of the compressor discs. Although only the web minimum thickness and lower rim width have been adjusted, this distribution suggests that the chosen geometry results in a relatively well optimised disc where high but tenable stresses exist throughout. This makes the most use of the material and helps to reduce weight. The HPT discs exhibit more variation in the stress profiles due to the larger thermal gradients. This suggests that further optimisation of the geometry, including more complex web designs, could perhaps benefit the disc in terms of further weight reduction.

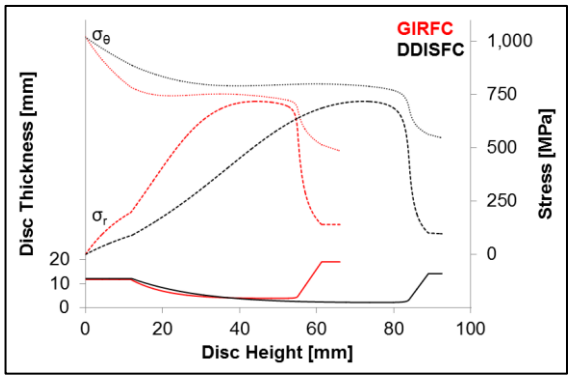

Figure 4.14 – HPC First Stage Disc Stress

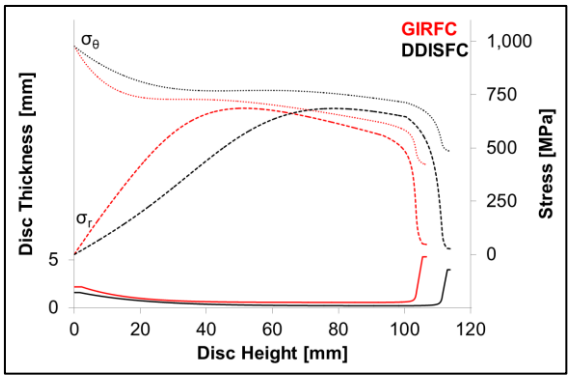

Figure 4.15 – HPC Last Stage Disc Stress

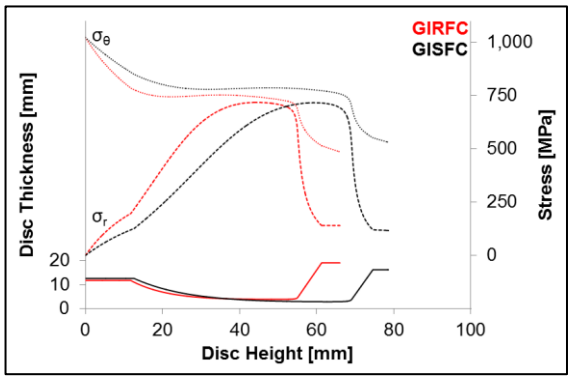

Figure 4.16 – HPC First Stage Disc Stress

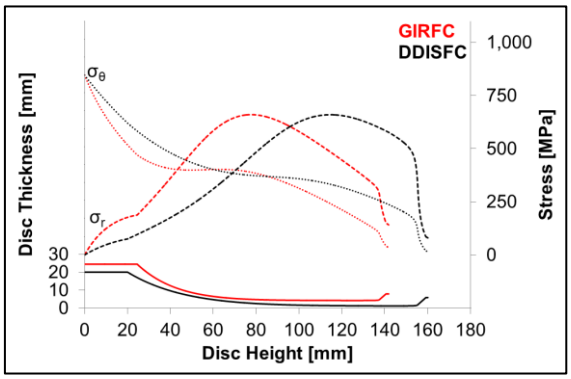

Figure 4.17 – HPC Last Stage Disc Stress

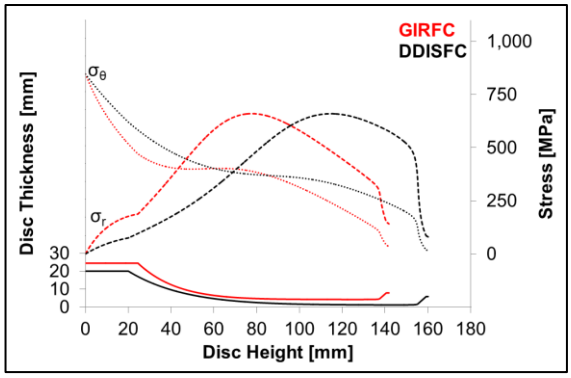

Figure 4.18 – HPT Last Stage Disc Stress

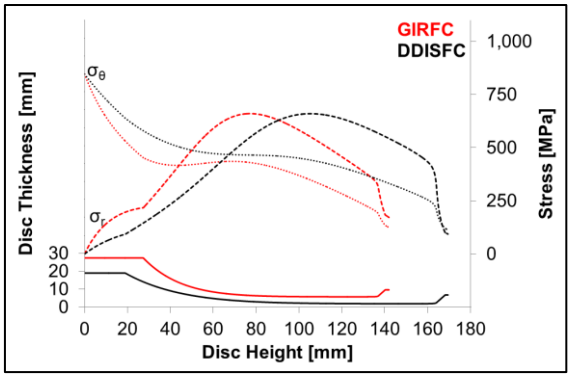

Figure 4.19 – HPT last Stage Disc Stress

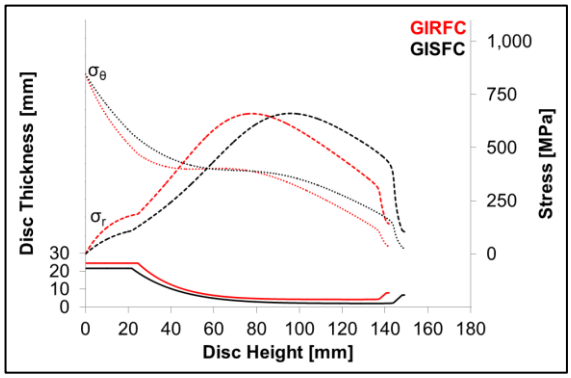

Figure 4.20 – HPT Last Stage Disc Stress

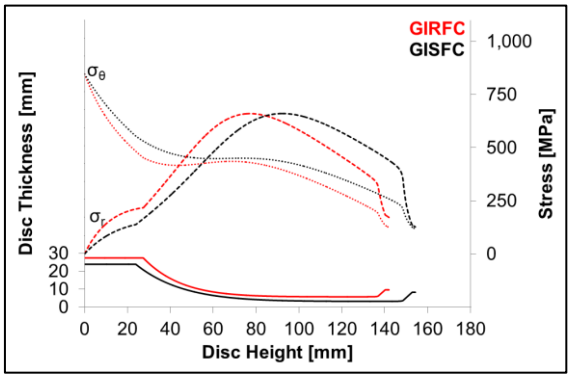

Figure 4.21 – HPT Last Stage Disc Stress

4.5.2 Implication of HP-Spool Dimensions on HPC and HPT Efficiency

In the HPC relatively short blades are used especially in the rear stages of the machine which can lead to high over-tip leakage losses. The relationship between blade height and efficiency for a range of HPC dimensions is given in Figure 4.22. The main assumptions are that the HPC pressure ratio and mean blade speeds are constant at each point. For a given stage count, the stage loading is therefore constant. In order to maintain a constant blade loading the rotational speed of the machine has to be increased as the mean radius is reduced. The efficiency clearly suffers as the blade height is reduced. Below 15mm the over-tip leakage losses become quite significant leading to a relatively high efficiency penalty. The efficiency of the machine improves as stage count increases and stage loading decreases. The sensitivity towards tip clearance is also shown in Figure 4.22. As expected, increasing tip-clearance aggravates the over-tip leakage losses leading to a higher efficiency penalty. The sensitivity towards tip clearance is even higher for shorter blades. The DDISFC is at a critical limit, and therefore any further decrease in blade height due to, for example, an increase in OPR would carry a significant efficiency penalty. A decrease in core size in the GISFC and to a greater extent in the GIRFC could be achieved without significant efficiency penalties. Therefore, higher OPRs might yield some benefit for these concepts. Further optimisation of the GISFC and GIRFC is presented in chapter 7.

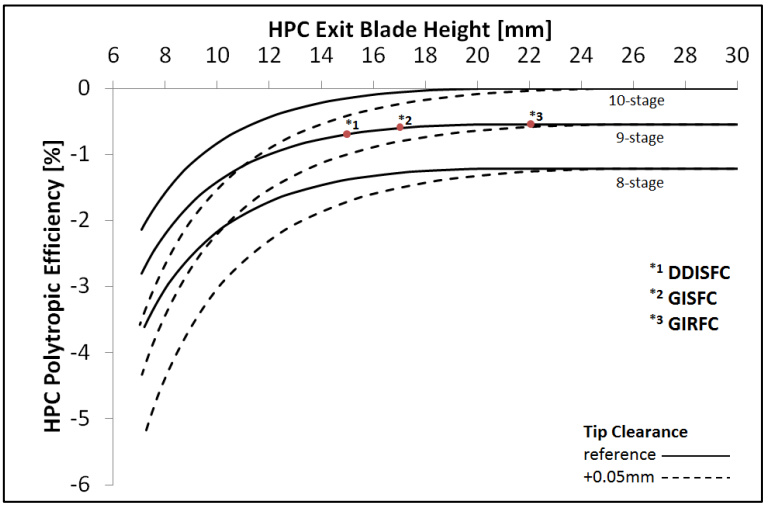

Figure 4.22 – HPC Polytropic Efficiency Variation with Blade Height

Figure 4.23 shows the implication of variations in blade height on HPT efficiency. The decrease in HPT blade height is brought about by the variation in the HPT mean radius. The main assumptions are that the HPT pressure ratio and stage loading are constant for a given stage count. The mean blade speed is however increased as stage number is reduced in order to limit the efficiency penalty. From Figure 4.23 it is clear that as the HPT mean blade height decreases, so does the HPT efficiency. The tip clearance penalty as function of blade height is non-linear and increases in severity as the blade height is reduced. Figure 4.23 also depicts the implication of adjusting the stage count. For a 2-stage HPT the stage loading is far higher and leads to a significant efficiency penalty when compared with the 3-stage solution. Nevertheless in this design a 2-stage HPT has been selected as it appears to give the best trade-off between efficiency, complexity and weight. The sensitivity towards tip clearance is also shown in Figure 4.23. As for the HPC, when the tip clearance is increased, a marked efficiency penalty is incurred. The DDISFC is again at a critical limit in terms of blade height. The HPT of the GISFC and to a greater extent the HPT of the GIRFC could maintain high efficiency at even smaller blade heights and therefore support a smaller core size. Given that the DDISFC HP-spool configuration is at the design limit in both the HPC and HPT, further optimisation of the concept has not been attempted.

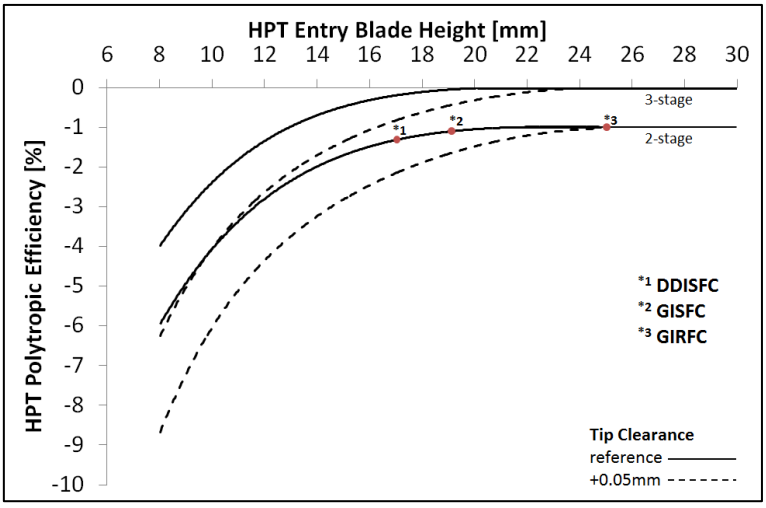

Figure 4.23 – HPT Polytropic Efficiency Variation with Blade Height

4.5.3 Comparison of TF2000 and GIRFC HP-Spool

The GIRFC HP-spool is quite different from the baseline TF2000 concept. The GIRFC incorporates a nine-stage HPC and two-stage HPT while the TF2000 only has a six-stage HPC and a one-stage HPT. The main specifications the TF2000 engine and the GIRFC concept are given in Table 4.3. It is clear that the OPR, T_4 and BPR of the GIRFC are all significantly higher than for the TF2000. The GIRFC HP-spool rotational speed is also more than twice that of the TF2000 and the material properties of the GIRFC discs are superior to those of the TF2000 where the mean stress levels are approximately 10% higher for the former. These characteristics have a number of implications. In the GIRFC intercooling, high OPR and high T_4 all reduce core size when compared with the TF2000. Table 4.3 shows the main boundary conditions for the HP-spools of both the GIRFC and TF2000. It is clear that the W_c for the TF2000 is significantly larger than for the GIRFC which results in much larger flow areas throughout. However, similar to the DDISFC, the TF2000 is a three spool engine which together with the inferior disc material tends to increase the mean annulus diameter to almost twice that of the GIRFC.

Component	Parameter	Unit	TF2000	GIRFC
General	OPR	[-]	38	80
	BPR	[-]	4.9	11.3
	T4	[K]	1654	1920
HPC	Entry W_c	[kg/s]	25.9	19.6
	Exit W_c	[kg/s]	5.76	1.7
	Pressure Ratio	[-]	4.4	12.7
HPT	Entry W_c	[kg/s]	9.9	5.8
	Exit W_c	[kg/s]	22.4	9.4
	Pressure Ratio	[-]	2.5	3.3

Table 4.3 – Comparison of TF2000 and GIRFC HP-Spools

The reduction in mean diameter allows the GIRFC to maintain relatively long blades yet the reduction in core size still results in a significant reduction in blade height at the end of the HPC and in the HPT when compared with the TF2000. This is apparent in Figure 4.24. The weight of

the GIRFC HPC discs is only 33% of the weight of the TF2000 HPC discs based on the estimated material volume. The reduction in size is due to a reduction in shaft diameter and superior materials. The TF2000 incorporates a single-stage HPT design while the GIRFC incorporates a two-stage HPT design. As can be seen in Figure 4.24, the two stage design is far more compact in terms of height and does not lead to a significant increase in overall width when compared with the single stage HPT in the Trent 700. The GIRFC HPT blades are also significantly smaller than those of the Trent 700. The weight of both the GIRFC HPT discs combined is only 30% that of the TF2000 HPT disc based on the estimated material volume.

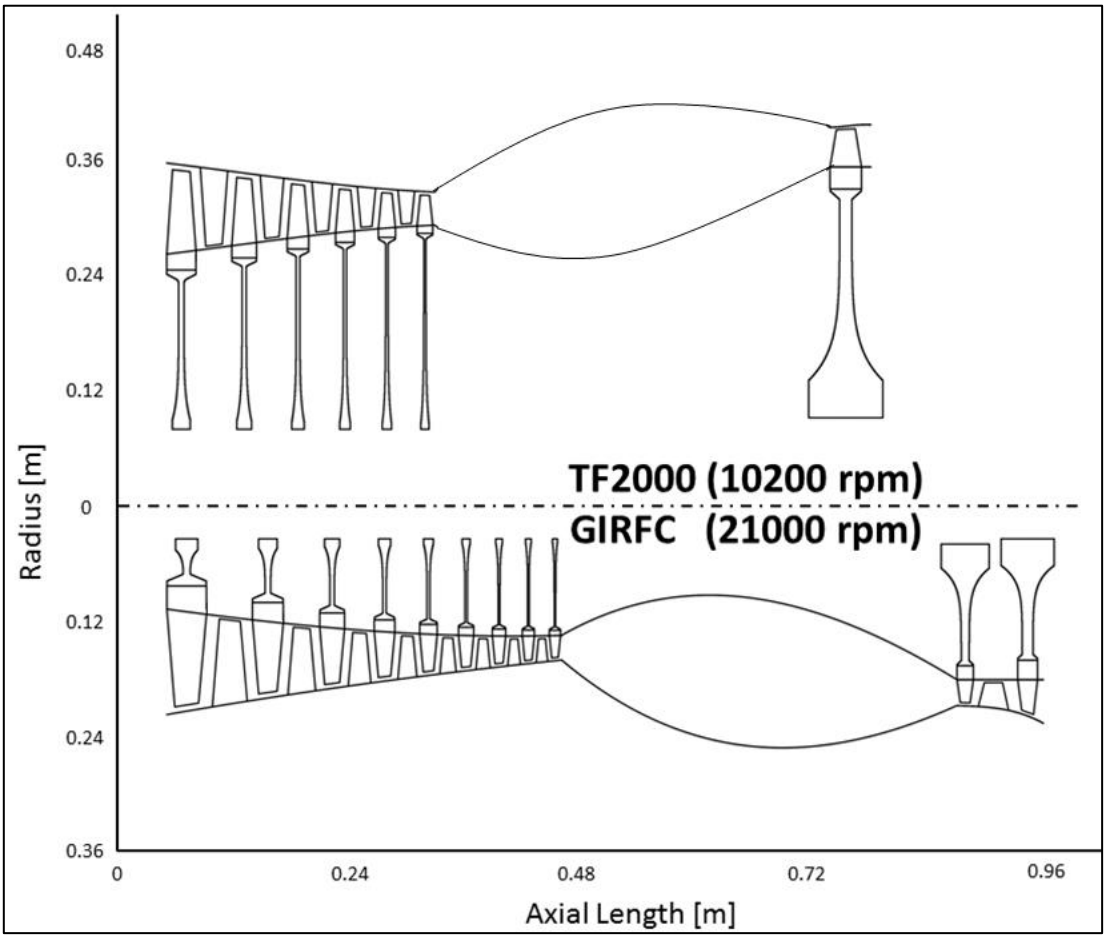

Figure 4.24 – Comparison of TF2000 and GIRFC HP-Spool

4.6 Discussion and Conclusion

In this chapter, the HP-spool design and performance of several different intercooled concepts was considered. High OPR as well as intercooling reduce core size and limit thermal efficiency due to severe over-tip leakage losses which come about as a result of small blades at the end of the HPC and also to some extent at the entrance to the HPT. Although the HPT can make use of shrouds, these also carry an efficiency penalty. In addition, shrouded blades lead to comparatively higher centrifugal stresses and consequently thicker discs. The advantage of the GIRFC configuration is that the LP-shaft no longer limits the reduction in the inner bore diameters of the HP-spool discs. This allows for a reduction in disc height and a further reduction in HPC and HPT mean diameters while maintaining aerodynamic loading by increasing the spool rotational speed.

The design of HP-spool assemblies is highly complex and has only been attempted at the conceptual level. Although a typical HP-spool makes use of drive arms to link bearing assemblies to each HPC and HPT stage, these have not been considered in this work. Other factors such a whirling speeds have also not been considered. In the current estimation, longitudinal disc loads have been ignored. For a web design these are typically quite low. However, for a hyperbolic design greater care must be taken. If the lower part of the web of a hyperbolic disc is assumed to be very thin, the longitudinal stresses can be quite high [(71)]. For this reason a conservative hyperbolic disc scaling factor has been assumed.

A trade-off exists between stage efficiency and stage count, aerodynamic loading and blade and disc weight. In this thesis, standard guidelines related to stage loading, flow coefficients and flow Mach numbers were adopted for the sizing of the HPC and HPT. Although a preliminary blading exercise was carried out by Anselmi[1] for the GIRFC, a further more detailed blading design could allow for greater optimisation of stage loading, flow coefficient and Mach numbers. A steeper gradient falling line HPC could be adopted in order to increase the blade height at the

[1] Eduardo Anselmi Palma, a PhD student at Cranfield University, is investigating in his PhD the mechanical arrangement and losses within the GIRFC concept.

end of the HPC. As a consequence, the mean blade speed for a given rotational speed would be reduced resulting in higher blade loading. This would need to be offset by additional blade rows or higher rotational speed which in turn carry an additional weight and stress penalty respectively. Reducing the HPC exit diameter would reduce the shaft clearance at the entry to the combustor and could complicate the installation of bearings. Also a larger combustor tilt would be required which could create design and installation difficulties. Clearly, a higher stage count for either the HPC or HPT could be adopted to improve the component efficiency. However, additional stages undesirably increase engine weight, length, complexity and cost.

The GIRFC was compared with competing intercooled designs including a direct-drive and geared arrangement with a more conventional core arrangement. The direct-drive version of the intercooled engine has not been pursued further as both in NEWAC [12] and in this thesis it was found that blade height limitations excessively restrict the increase in OPR and therefore limit further potential growth in thermal efficiency. The GIRFC discs are mostly thicker than for the other concepts but the disc frontal areas are significantly reduced meaning that the GIRFC discs are for the most part lighter than for the other concepts. It was shown that the GIRFC can deliver a 26% to 45% increase in blade height depending on which component and arrangement are being evaluated. This increase in blade height results in a lower over-tip leakage loss penalty and should allow for a greater increase in OPR. In chapter 7, the GISFC and GIRFC are re-optimised in order to identify the designs which result in the lowest block fuel burn. The HP-spool designs were adjusted iteratively throughout the course of this research in order to reflect changes brought about by the optimisation process. The final HP-Spool configurations for the GISFC and GIRFC are subsequently presented in chapter 7.

5 Implication of the Intercooler Configuration

5.1 Nomenclature

$\Delta P/P$	Loss in Total Pressure
ε	Intercooler Effectiveness
η_t	Thermal Efficiency
A_{ff}	Free Flow Area
A_{fr}	Frontal Area
BPR	Bypass Ratio
CFD	Computational Fluid Dynamics
E_{std}	Friction Power Expended per Unit Surface Heat Transfer Area
FN	Net Thrust
FPR	Fan Tip Pressure Ratio
GIRFC	Geared Intercooled Reversed Flow Core Engine Concept
GISFC	Geared Intercooled Straight Flow Core Engine Concept
HP	High Pressure
HPC	High Pressure Compressor
HPT	High Pressure Turbine
h_{std}	Unit Conductance for Thermal-Convection Heat Transfer
IC	Intercooler
IPC	Intermediate Pressure Compressor
ISA	International Standard Atmosphere
j	Colburn Factor
LEMCOTEC	Low Emission Core Engine Technologies
MC	Mid-Cruise
NTU	Number of Transfer Units
OPR	Overall Pressure Ratio
P_c/P_h	Ratio of Total Pressure in the Mixing Plane
PR	Pressure Ratio
Re	Reynolds Number
SFC	Specific Fuel Consumption
SFN	Specific Net Thrust
T_3	Combustor Entry Temperature
T_4	High Pressure Turbine Entry Temperature
TO	Take-Off
TOC	Top-of-Climb
V_c/V_h	Jet Velocity Ratio
W_c	Intercooler Cold Mass Flow Rate
W_c/W_h	Intercooler Cold Mass Flow to Hot Core Mass Flow Ratio
W_h	Intercooler Hot Mass Flow Rate

5.2 Introduction

Heat transfer from the core stream to the bypass stream by means of an intercooler reduces the work done by the HPC and allows for higher OPR. This in turn drives an increase in η_t when compared with non-intercooled designs. The improvement in η_t is conditional, as the losses which are introduced in the system due to frictional and form drag in the intercooler matrix can reduce or negate the benefit which could ideally be achieved. This chapter evaluates specific elements related to the configuration and performance of an advanced intercooler concept within the GISFC and within the GIRFC. The objective of this study is to suggest a preliminary intercooler configuration suitable for integration within the GISFC or the GIRFC. This chapter also aims to give a thorough analysis of the performance of the given intercooler concept and how this relates to the overall performance of the engine concepts under evaluation. The focus of this chapter is restricted to a single component. This is necessary for understanding the behaviour of the engine as a whole and leads to the complete evaluation and optimisation of the GISFC and GIRFC concepts.

The performance studies presented in this chapter assess the behaviour of both the GISFC and GIRFC across their performance envelope. Special attention has been given to the implication of sizing on the integration of the intercooler modules. The assessments carried out within the scope of this research are limited to a tubular intercooler type. A qualitative comparison is made for other intercooler types and technologies where appropriate. This chapter describes previous work carried out in intercooled core technology. In addition, a description of the intercooler model used in this work is given including the main theory, correlations, components and validation. Finally, a performance evaluation is carried out for the different intercooler configurations.

5.3 Background

An intercooled aero-engine has yet to be introduced into service, as significant technical challenges still need to be overcome. These points were addressed in chapter 2. In NEWAC [12], as well as in the current LEMCOTEC project, much effort has been directed towards research and initial testing of intercooler technology. Several types of heat exchanger technologies exist, of which the main candidates for an intercooled turbofan application appear to be a cross-corrugated design [16] and a tubular design [34]. The main requirements for a heat exchanger intended for use in an aero-engine are related to the minimisation of the size, weight and pressure losses in the intercooler matrix. Clearly, these requirements must be satisfied while still retaining a sufficient level of effectiveness. Size and weight are important as they affect the installation of the intercooler. A large intercooler could necessitate an increase in nacelle dimensions leading to higher drag. A heavy intercooler would increase fuel burn as well as make the unit difficult to handle during installation and maintenance. Other considerations related to intercooler design include maintainability, icing prevention and protection against foreign object damage. Although it is premature to consider the latter issues at the very early stages of design, these aspects will play a role in the eventual adoption of intercooler technology.

Cross-corrugated heat exchanger designs have been widely investigated outside the aero-engine application [97] [98] [99]. Of greatest interest is, however, the work carried out related to the integration of this type of heat exchanger as an intercooler within a turbofan configuration. The cross-corrugated designs in NEWAC [12], while promising, did not meet the required weight targets for a given effectiveness and pressure loss [36]. The installation of the intercooler also led to an increase in nacelle diameter which increased drag. Figure 5.1 shows the cross-corrugated concept which appears in Kwan et al. [100] where a detailed CFD study was carried out in order to evaluate the effect on the downstream flow field due to the cross-corrugated concept.

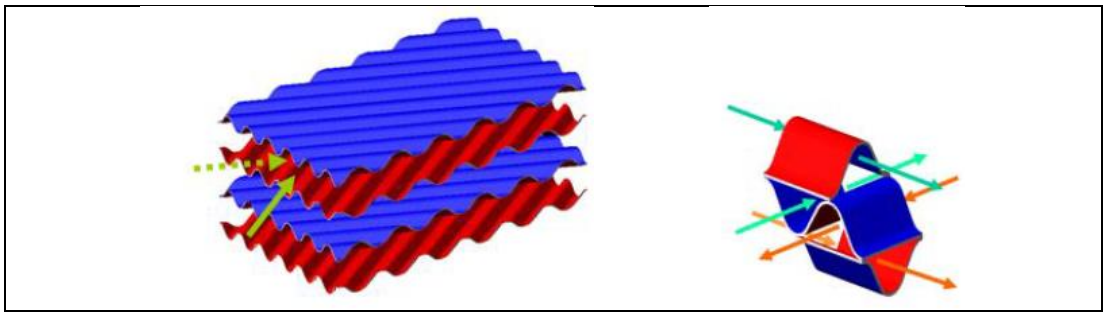

Figure 5.1 – Cross-Corrugated Intercooler Concept (adapted from Kwan et al. [100])

The heat exchanger matrix was modelled as a porous media and the friction factor which was established based on experimental studies [101] is defined according to Equation (5.1). This friction factor was established over a Re range between 500-5000. Doo et al. [102] [103] [104] also present the friction factors for several cross-corrugated designs for Re up to 16000 based on theoretical and CFD predictions. Other cross-corrugated intercooler matrix geometries are also assessed in Fukui et al. [105] who present a study for a similar plate type intercooler although only a limited number of operating points are evaluated. For the prediction of heat transfer Kwan et al. [100] made use of a correlation from Utriainen and Sundén [106] which is given in Equation (5.2). The validity of this correlation is limited to a Re range between 200 and 1000 beyond which the results were extrapolated. Doo et al. [102] illustrate the Colburn factor for a set of configurations over a wider range of Re but do not propose a characteristic equation. Given the different assumptions and limited range of data, it can be difficult to interpret these results across a wide spectrum of conditions. However, as there has been great interest in this design a recent study was carried out by Guerra [107] which looked at the cross-corrugated intercooler as a candidate for the GISFC and GIRFC.

$$f = 1.126Re^{-0.1826} \quad \textbf{(5.1)}$$

$$Nu = 0.01648Re + 6.288 \quad \textbf{(5.2)}$$

where:

- f *Darcy friction factor*
- Nu *Nusselt number*
- Re *Reynolds number*

The second design of interest is the tubular intercooler configuration from Lei and Grönstedt [34] shown Figure 5.2. The intercooler matrix consists of a bank of staggered elliptical tubes. Elliptical tubes reduce losses in the cooling stream by adopting a more aerodynamic profile compared with circular tubes which are more typical. An elliptical profile also has a larger surface area when compared with a circular profile with the same internal flow area which benefits heat transfer. Lei and Grönstedt [34] admit that, from the studies of Kays and London [108], staggered arrangements tend to have higher frictional losses than other types of arrangements. Combined with the high flow speeds which are typical in the cooling channel such arrangements can, therefore, lead to quite high losses. The staggered tubular arrangement has been considered in this thesis thanks to the co-operation of Zhao and Grönstedt [109] who supplied additional data regarding this configuration which made it possible for this concept to be modelled. In section 5.4.2 a comparison has been made with other heat transfer and friction loss models for circular tubular profiles.

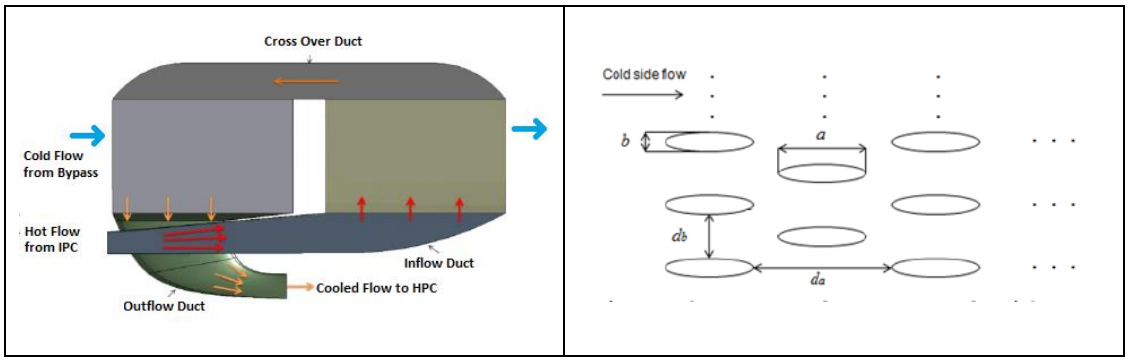

Figure 5.2 – Tubular Intercooler Concept from Zhao et al. [109]

The intercooler technologies which were studied in NEWAC [12] are generally similar in implementation in that they rely upon multiple intercooler modules each extracting heat from between the IPC and HPC while using bypass air as a cooling medium. A major challenge in the implementation of both concepts is the design of the hot and cold side headers. The main requirements for these headers are similar to those of the intercooler matrix, specifically reduction in weight and pressure losses. The header configuration is a challenging aspect of the design. Several studies have been carried out into header design and pressure loss characterisation [39] [40] [41] [40] [109]. In Rolt and Kyprianidis [36], it is stated that the design targets in

NEWAC [12] for the inlet and outlet headers on the intercooler installation were met and demonstrated in rig testing. Walker et al. [39] [41] [40] list the system losses for the bypass and core side headers of the intercooler and show that these met the design targets. In these cases the optimum geometry was defined through a number of shape factors. These have been considered in the GISFC and GIRFC concept drawings prepared by Anselmi[1] and shown in chapter 2. Unfortunately, the NEWAC [12] studies are intrinsically specific to the assumed geometry, and therefore are not easily applied to the designs considered in this dissertation. To evaluate header losses complex CFD and experimental work is required. However, available correlations tend to be valid either for quite specific geometry or for relatively simple designs, and therefore in this work detailed header design could not be undertaken and typical fixed pressure losses were assumed. Due to this uncertainty intercooler header losses are evaluated as part of a sensitivity analysis presented in chapter 7.

[1] Eduardo Anselmi Palma, a PhD student at Cranfield University, is investigating in his PhD the mechanical arrangement and losses within the GIRFC concept.

5.4 Methodology

5.4.1 Overview

In this dissertation, the turbofan intercooler concept proposed by Zhao et al. [109] has been investigated within the GISFC and GIRFC concepts. In its original form, it consists of a cross-flow two-pass configuration comprised of staggered elliptical tube banks. In this dissertation, a number of correlations describing the heat transfer and head loss characteristics have been implemented within a heat exchanger model. The implementation and scaling of these correlations was governed by a fixed set of geometrical rules which led to a fixed tube eccentricity, transverse spacing ratio and longitudinal spacing ratio in all the studies carried out. The intercooler model was developed in C++ to estimate the performance of the intercooler in relation to a given set of dimensions. The model was used to evaluate the intercooler both as a standalone component and as an integrated component within the engine performance codes.

In this chapter, a basic comparison is made between the performance of banks of circular tubes, based on experimentally derived correlations published in literature, and banks of elliptical tubes, based on the correlations published in Zhao et al. [109]. The performance of an intercooler with circular tube banks differs from that of an intercooler with elliptical tube banks. However, the performance trends and magnitudes of the two matrix geometries are found to be similar which increases confidence in the validity of the elliptical tube bank correlations. These correlations are then evaluated within the context of the GISFC and GIRFC designs with focus on the sizing and performance of the modules. A brief discussion is finally given comparing this concept with a cross-corrugated design from the results of the work of Guerra [107].

5.4.2 Theoretical Foundation

There are numerous references from which the basic theory surrounding heat exchanger performance can be derived. Kays and London [108] is perhaps the most comprehensive work for the analysis of the performance and design of compact heat exchangers. The basic theory which is applicable to any heat exchanger as well as the results of several physical tests on different heat exchanger geometries are outlined in Kays and London [108]. This basic theory

served as the main theoretical foundation for intercooler design in this dissertation but was augmented with material from Hausen [110] and Holman [111]. The heat transfer and pressure drop correlations that were developed through the research of Zhao et al [109] were implemented in the intercooler model used in this dissertation. The theory is presented here in the order in which it was applied within the heat exchanger module developed for this work.

Definition of Heat Exchanger Geometry

The basic dimensions of a rectangular heat exchanger module are clearly length, width and height. However, the relationship of these overall dimensions to the internal matrix is of importance when formulating the general theory of a heat exchanger based on matrix design. Therefore, it is necessary to define a number of standard parameters. The frontal area (A_{fr}) refers to the total cross sectional area of the hot or cold side of the heat exchanger. It is easily defined by the outer dimensions of the module as can be seen in Equation (5.3) and (5.4).

$$A_{fr,c} = H \times W \quad \textbf{(5.3)}$$

$$A_{fr,h} = L \times W \quad \textbf{(5.4)}$$

where:

- $A_{fr,c}$ *intercooler cold side frontal area*
- $A_{fr,h}$ *intercooler hot side frontal area*
- H *intercooler height*
- L *intercooler length*
- W *intercooler width*

The ratio of the total transfer area on one side of the heat exchanger to the total volume of the heat exchanger (α) is defined according to Equation (5.5) and Equation (5.6) and is dependent upon the number and perimeter of the tubing. The perimeter of an ellipse can be defined by Equation (5.7).

$$\alpha_c = \frac{P\ N\ H}{A_{fr,c}.L} \tag{5.5}$$

$$\alpha_h = \frac{P\ N}{A_{fr,h}} \tag{5.6}$$

$$P = \pi\left[\frac{3(a+b)}{2} - \sqrt{\left(\frac{3a+b}{2}\right)\left(\frac{3b+a}{2}\right)}\right] \tag{5.7}$$

where:

- α *total transfer area to total heat exchanger volume for each side*
- a *major tube diameter*
- b *minor tube diameter*
- c *cold side*
- h *hot side*
- A_{fr} *intercooler frontal area*
- P *tube perimeter*
- H *intercooler height (tube length)*
- L *intercooler length*
- N number of tubes

Given the previous identities, the total area available for heat transfer on either side of the heat exchanger can be found through the use of Equation (5.8). The ratio of A_{ff} to A_{fr} (σ) is defined according to Equation (5.11). In order to establish this ratio, knowledge of the hydraulic radius (r_h) of each side of the heat exchanger is required. For the internal side of the tube bank this is simply the hydraulic radius corresponding to an elliptical profile which can be found using Equation (5.9). The definition of hydraulic radius for the cold side of the tubular bank is slightly more complex as it corresponds to the flow across a bank of tubes. Hydraulic radius is generally defined as cross sectional area over wetted perimeter. In this case the wetted perimeter is the sum of the outside perimeter of the tubes in the bank. The cross sectional area is the A_{ff}, and therefore refers to the area between the adjacent tube columns. Based on this definition, Equation (5.10) defines the hydraulic radius for the cold side. Equation (5.12) can then be used to define the A_{ff}.

$$A = \alpha\, L\, W\, H \tag{5.8}$$

$$r_{h,h} = \frac{\pi\, a\, b}{4P} \tag{5.9}$$

$$r_{h,c} = \frac{W - N_c\, b}{N\, P} \tag{5.10}$$

$$\sigma = \alpha\, r_h \tag{5.11}$$

$$A_{ff} = \sigma\, A_{fr} \tag{5.12}$$

where:

- α *total transfer area to total heat exchanger volume for each side*
- σ *free flow to frontal area for each side*
- a *major tube diameter*
- b *minor tube diameter*
- c *cold side*
- h *hot side*
- r_h *hydraulic radius*
- A *transfer area*
- A_{ff} *free flow area*
- A_{fr} *frontal area*
- P *tube perimeter*
- H *intercooler height*
- L *intercooler length*
- W *intercooler width*
- N *number of tubes*

Definition of Heat Transfer Equations

The heat transfer coefficient (h) can be established for both sides of a heat exchanger. It is useful in these types of calculations to define a number of standard relations. Equation (5.13) and Equation (5.14) define the flow-stream mass velocity and Re respectively. Equation (5.15) defines the Prandtl number which relates the viscous and thermal diffusion rates which in turn determine the thickness of the hydrodynamic and thermal boundary layers. For air as well as combustion products the Prandtl number is typically well below 1.0 which indicates that heat is diffused more quickly than momentum. Equation (5.16) defines the Stanton number which relates the fluid heat transfer to thermal capacity. The Nusselt number, defined in Equation

(5.17), is a ratio which relates heat transfer which occurs by convection to that by conduction alone. For a tube it can also be considered as the ratio of tube diameter to boundary layer thickness [110]. The Colburn factor and heat transfer coefficient are also defined in Equation (5.18) and Equation (5.19) as these are used in many of the following calculations.

$$G = \frac{\dot{m}}{A_{ff}} \tag{5.13}$$

$$Re = \frac{4\, r_h\, G}{\mu} \tag{5.14}$$

$$Pr = \frac{\upsilon}{\alpha} = \frac{c_p \mu}{k} \tag{5.15}$$

$$St = \frac{h}{c_p G} = \frac{Nu}{Re\ Pr} \tag{5.16}$$

$$Nu = \frac{\alpha L}{\lambda} \tag{5.17}$$

$$j = St\ Pr^{2/3} \tag{5.18}$$

$$h = St\ G\ c_p = \frac{j\ G\ c_p}{Pr^{2/3}} \tag{5.19}$$

where:

- α *thermal diffusivity*
- λ *longitudinal conduction parameter*
- μ *viscosity coefficient*
- υ *kinematic viscosity*
- c_p *specific heat capacity at constant pressure*
- h *convective heat transfer coefficient*
- j *Colburn factor*
- k *thermal conductivity*
- $\dot{m}$ *mass flow rate*
- r_h *hydraulic radius*
- A_{ff} *free flow area*
- G *flow-stream mass velocity*
- L *length*
- Nu *Nusselt number*

- Pr *Prandtl number*
- Re *Reynolds number*
- St *Stanton number*

The cold side of the heat exchanger consists of a bank of staggered elliptical tubes which are arranged as can be seen in Figure 5.2. Kays and London [108] present performance data for flattened tubes which are close in shape to elliptical tubes. However, the Re range for which the data is given is below the levels required for the current work which makes comparisons difficult. There are many works which have investigated cross-flow in circular staggered tube banks [110] [112] [113]. Zukauskas [114] (cited in [111]) proposes a set of correlations which are given in Equations (5.21) to (5.22) which were established based on tube banks with more than 16 rows. Figure 5.3 compares the Colburn factor for each of these correlations across a range of Reynolds numbers. Equation (5.22) seems to compare quite well to that of Equation (5.20) even though the profiles they represent are somewhat different. At higher Re the elliptical tubes tend to a higher Colburn factor than do the circular tube profiles. This suggests that the heat transfer characteristics of the elliptical tubes could be better at higher Re. A more rigorous comparison is not possible as the elliptical tube correlations were not established based on experimental results. The similarity in performance, however, increases confidence in the validity of the elliptical tube bank correlations.

Correlations from Zhao et al. [109]

$$j = 0.002967e^{-6.734e^{-5}Re} + 0.00329e^{-3.385e^{-6}Re} \qquad \textbf{(5.20)}$$

Correlations from Zukauskas [114] *(cited in* [111]*)*

$$Nu = 0.71\,Re^{0.5}\,Pr^{0.36}\left(\frac{Pr}{Pr_w}\right)^{0.2} \quad for\ 5\times10^2 < Re < 10^3 \qquad \textbf{(5.21)}$$

$$Nu = 0.35\left(\frac{X_t}{X_l}\right)Re^{0.6}\,Pr^{0.36}\left(\frac{Pr}{Pr_w}\right)^{0.2} \quad for\ 10^3 < Re < 10^4 \qquad \textbf{(5.22)}$$

where:

- a *major tube diameter*
- b *minor tube diameter*
- j *Colburn factor*
- Nu *Nusselt number*

- Pr *Prandtl number (evaluated at average fluid temperature)*
- Pr_w *Prandtl number (evaluated at average wall temperature)*
- Re *Reynolds number*
- X_l longitudinal tube spacing ratio
- X_t tangential tube spacing ratio

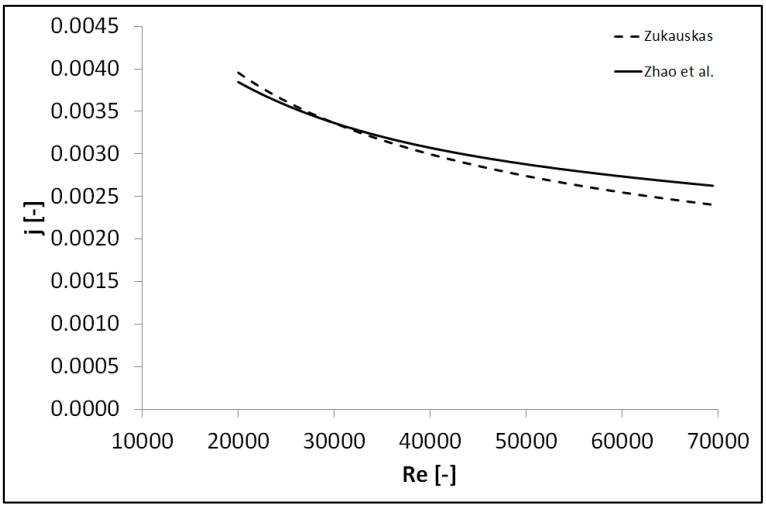

Figure 5.3 – Colburn Factor vs. Reynolds Number (Cold Side) [(109) (114)]

The hot side of the heat exchanger refers to the inside of the elliptical tube banks. Zhao et al. [(109)] assume a circular profile and recommend the use of Equation (5.23), originally proposed by Gnielski [(115)], for the estimation of the Colburn factor. As for the cold side, this correlation can be easily compared with other correlations for circular tube profiles available in literature. Equation (5.24) from Hausen [(110)] is valid for Re in excess of 10000. Figure 5.4 shows how the Colburn factors resulting from these three correlations vary with Reynolds number. The correlation from Hausen [(110)] and Gnielski [(115)] compare well. This is expected as in essence they represent the same type of tube profile.

Correlations from Gnielski [(115)]

$$Nu = \frac{\frac{f}{8}(Re - 1000)\,Pr}{1 + 12.7\sqrt{\frac{f}{8}\left(Pr^{2/3} - 1\right)}} \qquad \textbf{(5.23)}$$

Correlations from Hausen [110]

$$Nu = 0.024\left[1 + \left(\frac{d}{L}\right)^{2/3}\right] Re^{0.786}\, Pr^{0.45} \quad for\ 10^4 < Re \qquad \textbf{(5.24)}$$

where:

- d *tube diameter*
- f *Darcy friction factor*
- L *tube length*
- Nu *Nusselt number*
- Pr *Prandtl number (evaluated at average fluid temperature)*
- Re *Reynolds number*

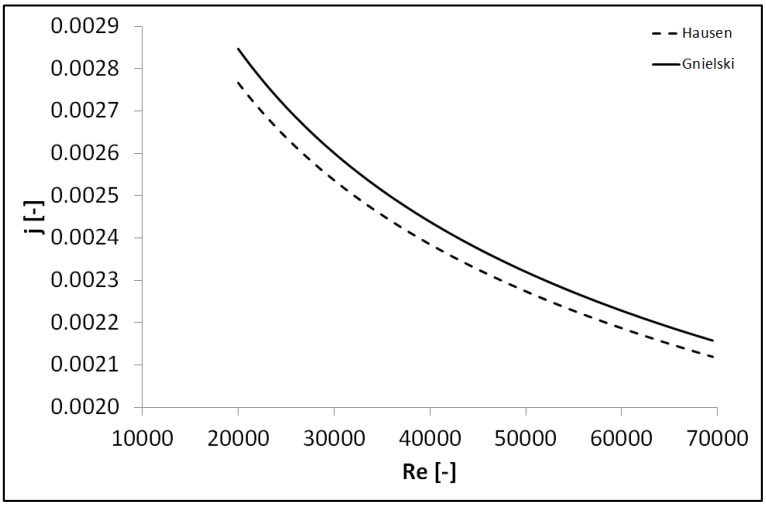

Figure 5.4 – Colburn Factor vs. Reynolds Number (Hot Side) [110] [115]

Definition of Friction Factors

Several methods exist for defining the pressure drop across a bank of tubes. Equation (5.25) from Jakob [116] (cited in [113] and [111]) defines the pressure drop across a bed of tubes. Equation (5.26***)*** from Kays and London [108] is a more rigorous model which takes into account both friction and flow acceleration. Both equations contain a friction factor term which is specific to the geometry under consideration. The external friction-factor correlation for an elliptical tube bank is based upon the Kays and London [108] definition. However, as in the previous cases, the data on friction factors from Kays and London [108] was established across a low Re range. It is therefore necessary to make a number of assumptions in order to match as closely as possible the elliptical tube bank correlation with other correlations available in published literature. In this

case, the correlation from Jakob [116] (cited in [111] and [113]) was adopted for comparison only. It was assumed that no flow acceleration occurred so that Equation (5.26) reduces to Equation (5.27). Common geometry was assumed in both cases and the friction factor from Jakob [116] (cited in [111] and [113]) was corrected by multiplying a factor of ($N_L A_{ff}/A$).

$$\Delta p = \frac{G_{max}^2 N_L}{\rho}\left(\frac{\mu_w}{\mu_b}\right)^{0.14} f_f \qquad \textbf{(5.25)}$$

$$\Delta p = \frac{G^2 v_1}{2}\left[(1+\sigma^2)\left(\frac{v_2}{v_1}-1\right) + f_d \frac{A}{A_{ff}}\frac{v_m}{v_1}\right] \qquad \textbf{(5.26)}$$

$$\frac{\Delta p}{2G^2 v} = \frac{A}{A_{ff}} f_f = N_L f_f \qquad \textbf{(5.27)}$$

where:

- 1 *inlet*
- 2 *outlet*
- Δp *pressure loss*
- σ *free-flow area to frontal area*
- μ *viscosity coefficient*
- ρ *density*
- v *kinematic viscosity*
- f_d *Darcy friction factor*
- f_f *Fanning friction factor*
- m *mean*
- w *wall*
- $\frac{A}{A_{ff}}$ *total transfer area to minimum free flow area*
- G *flow-stream mass velocity*
- N_L *number of tubes*

The friction factor for an elliptical tube bank is defined according to Equation (5.28) while that from Jakob [116] (cited in [111] and [113]) is defined according to Equation (5.29) and is valid only for staggered tube banks with 10 or more rows. In this case, Figure 5.5 compares the two correlations over a range of Re. The two relationships display very similar trends. However, the circular tube bank exhibits far higher friction factors than does the elliptical tube bank. Clearly, without experimental verification it is difficult to judge the accuracy of the friction factor proposed

by Zhao et al [109] but as explained in section 5.3, the elliptical tube profiles are more aerodynamic and therefore should lead to markedly lower losses as suggested in Figure 5.5.

Correlations from Zhao et al [109]

$$f_d = 0.009581e^{-6.043\times10^{-5}Re} + 0.009015e^{-1.617\times10^{-6}Re} \quad \textbf{(5.28)}$$

Correlations from Jakob [116]

$$f_d = Re^{-0.16}\left[1 + \frac{0.47}{(a-1)^{1.08}}\right] \quad \textbf{(5.29)}$$

where:

- f_d *Darcy friction factor (in this case represents the equivalent shear stress per unit area due to both viscous shear and pressure forces)*
- a *tangential tube spacing ratio*
- Re *Reynolds number*

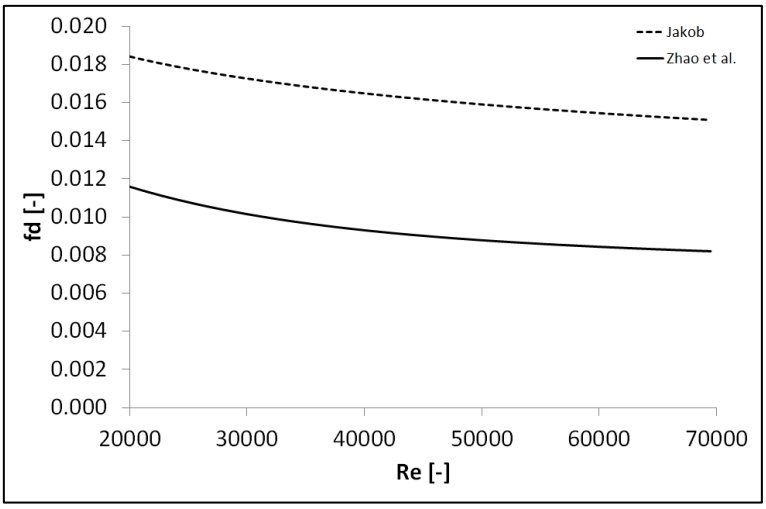

Figure 5.5 – Darcy Friction Factor vs. Reynolds Number (Cold Side) [109] [116]

A similar set of expressions can be defined for the internal side of the heat exchanger tubes. The pressure drop equation used in the intercooler model is equivalent to Equation (5.30). The friction factor used for the elliptical tube banks [109] is that from Haaland [117] which is actually for circular tube banks and is defined in Equation (5.31). Another friction factor for circular tube banks from Hermann and Burbach [118] (cited in [110]) is also compared with that from Haaland [117] in Figure 5.6 and is defined in Equation (5.32). As expected the correlations match quite closely. Both correlations are for circular tubes as no specific work was carried out on the friction inside

tubes with elliptical profiles. Equation (5.31) does contain an expression to account for roughness but in this comparison it has been assumed to be negligible.

$$\Delta p = \frac{G^2 \upsilon}{2g} \frac{L}{d} f_d \qquad \textbf{(5.30)}$$

Correlations from Haaland [117]

$$f_d = \left[\frac{1}{-1.8 \log_{10} \left(\frac{6.9}{Re} \right) + \left(\frac{\varepsilon}{3.7} \right)^{1.11}} \right]^2 \qquad \textbf{(5.31)}$$

Correlations from Hermann and Burbach [118]

$$f_d = 0.00540 + 0.3964 Re^{-0.3} \qquad \textbf{(5.32)}$$

where:

- Δp *pressure loss*
- ε *roughness factor*
- υ *kinematic viscosity*
- d *tube diameter*
- g *acceleration due to gravity*
- f_d *Darcy friction factor*
- G *flow-stream mass velocity*
- Re *Reynolds number*

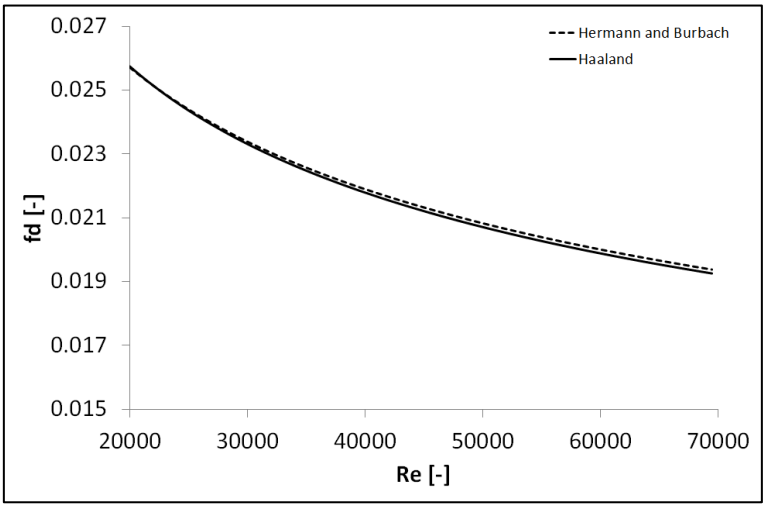

Figure 5.6 – Darcy Friction Factor vs. Reynolds Number (Hot Side) [117] [118]

Definition of NTU and Effectiveness

In this dissertation, the NTU method has been used to describe the heat transfer performance of the given intercooler designs. The Log Mean Temperature Difference (LMTD) method has not been considered in this case as the supporting material to this thesis was formulated around the NTU method. The fundamental equation of the NTU method is defined in Equation (5.33). The overall heat transfer coefficient of the unit, which is defined in Equation (5.34), unites the heat transfer coefficients from both sides of the heat exchanger. The transfer area in Equations (5.34) and (5.35) can refer to either side of the intercooler depending on how the problem is formulated. The NTU value can be used to define a range of effectiveness values for a range of capacity rate ratios. Kays and London [108] recommend the use of a look-up table to deduce the effectiveness; however, Holman [111] suggests the use of the expression given in Equation (5.35). Both methods are valid and compare well as can be seen in Figure 5.7.

$$NTU = \frac{AU}{C_{min}} \tag{5.33}$$

$$\frac{1}{UA} = \frac{1}{h_1 A_1} + \frac{1}{h_2 A_2} \tag{5.34}$$

$$\epsilon = 1 - e^{\left[\frac{e^{\left(-{C_{min}}/{C_{max}} NTU^{(1-0.22)}\right)}-1}{{C_{min}}/{C_{max}} NTU^{-0.22}}\right]} \tag{5.35}$$

where:

- ϵ *effectiveness*
- A *total transfer area*
- C_{min} $\left(\dot{m}c_p\right)_c$ *mass flow x heat capacity of cold side*
- C_{max} $\left(\dot{m}c_p\right)_h$ *mass flow x heat capacity of hot side*
- NTU *number of transferunits*
- U *overall heat transfer coefficient*

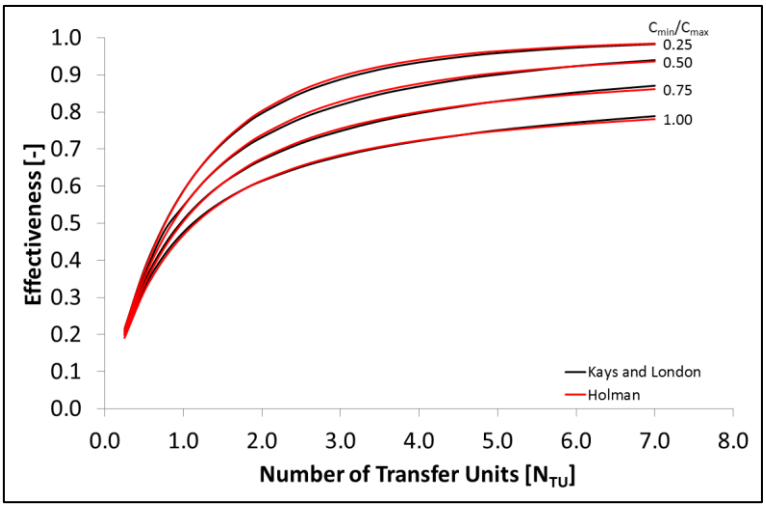

Figure 5.7 – Cross-Flow N_{tu} vs. Effectiveness

5.4.3 Numerical Intercooler Model

The aim of the intercooler model was to predict the effectiveness and pressure losses of different heat exchanger configurations both outside and within the engine performance codes developed for this work. In order to meet this requirement, the model was created as a C++ dynamic link library which could be called from a standalone program or from the engine performance code. The main inputs required by the model are the conditions at the entry to the hot and cold sides of the heat exchanger. These include the total temperature and pressure as well as the mass flow rate. In addition, the major diameter of the tubing, the number of rows and the number of columns for each module are required for the calculation. The model carries out the calculations related to the heat exchanger geometry. Based upon the inlet areas, the static temperatures and pressures are then established using compressible flow relations.

As can be seen in Figure 5.8, the fluid properties are established from empirical correlations but in order to establish the mean fluid properties the effectiveness and pressure losses need to be initially assumed. Given the initial estimates, the heat transfer and pressure loss calculations can be carried out. From these calculations, which are based on the assumed geometry, new estimates for effectiveness and pressure losses are found. A three variable Newton-Raphson algorithm is then used to improve upon the initial estimate until the differences between the assumed and the resulting values are eliminated.

In a multi-pass configuration the calculations are slightly more complex as illustrated in Figure 5.8. The current intercooler concept is a counter cross flow heat exchanger. This means that each individual module is a cross flow heat exchanger but the modules themselves are arranged counter to the cooling flow. Consequently, the core gases enter the module that is furthest downstream and leave the intercooler from the module that is furthest upstream. This arrangement maintains a high temperature difference across each module but does present some difficulty in terms of modelling the behaviour. The calculations for each module are carried out individually. Unlike for a 1-pass configuration, the boundary conditions are dependent on other intercooler modules. As the modules are arranged counter to the flow the calculations cannot be carried out consecutively. Therefore, a further Newton-Raphson algorithm must be used. In this case, the estimates relate to fluid entry temperatures and pressures for the hot and cold sides of each intercooler module except the first. The individual module calculations can then be used to update these estimates based on the resulting effectiveness and pressure drops.

The verification and validation of the intercooler performance model was carried out with data from Kays and London [108] as well as data provided directly by the authors of Zhao et al [109]. The Colburn and friction factor correlations are the product of a previous research effort [109]. By comparing these relations over a range of Reynolds numbers with similar published correlations, a measure of confidence was obtained in the validity of the current equation set.

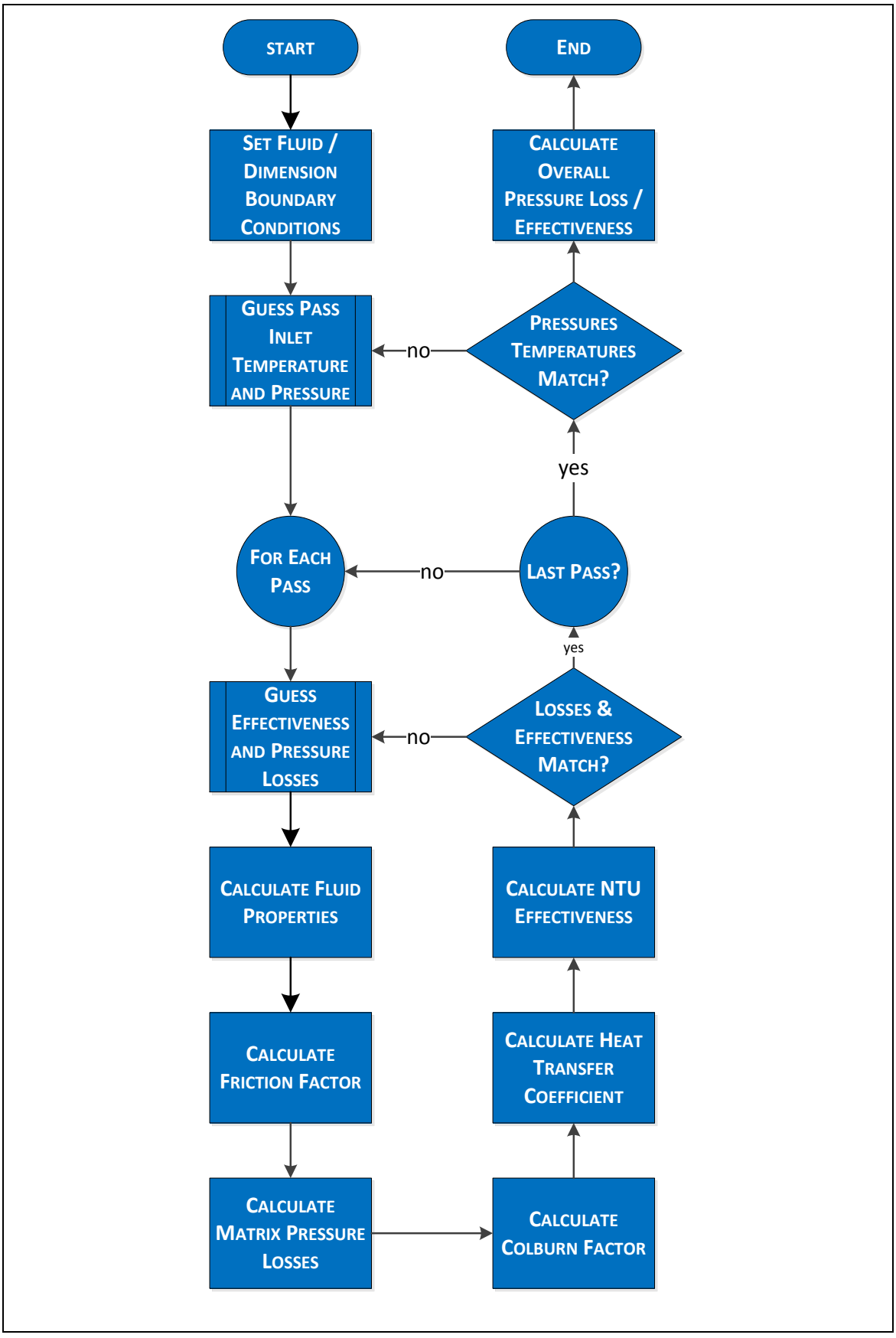

Figure 5.8 – Intercooler Model Schematic

The verification of the model operation and implementation was carried out against test cases provided in Appendix B of Kays and London [108]. The test cases which make use of experimentally derived data to establish the effectiveness and pressure losses in typical heat exchanger configurations were replicated exactly. However, the Colburn factors and friction factors in the test cases were obtained from data tables describing different heat exchanger geometries and types. In order to verify that the model could predict correctly the performance of the intercooler in question, performance data was obtained directly from Zhao et al [109]. A comparison was carried out based on this data and the results are shown in Figure 5.9. As can be seen from this chart, the maximum difference between the model data and the data from Zhao et al [109] is less than 2% which increases confidence in the implementation of the model.

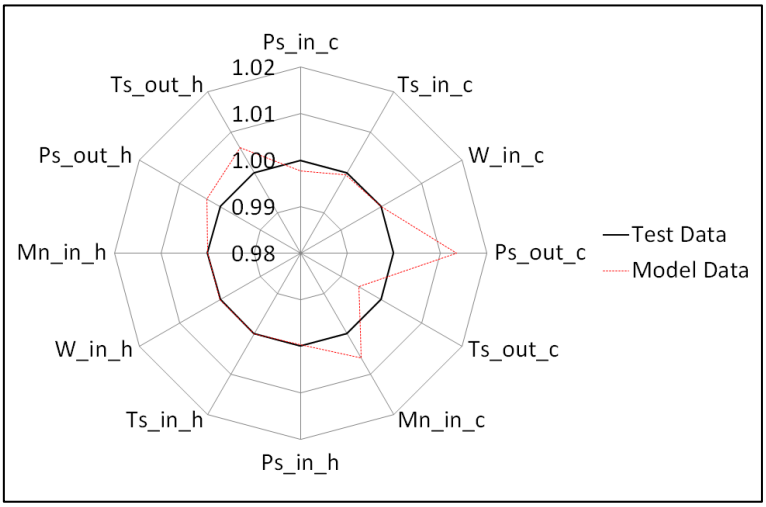

Figure 5.9 – Verification of Intercooler Model[1]

[1] The author would like to thank Dr. Tomas Grönstedt and Xin Zhao of Chalmers University of Technology for providing the data required for the verification of the intercooler model. Further information regarding the research carried out on tubular intercoolers by the aforementioned researchers can be found in (105).

5.5 Evaluation

The evaluation of intercooler performance is intrinsically tied to the dimensions and shape of the intercooler which in turn is also constrained by the surrounding structure and components which make up the engine as a whole. Typically an intercooler is placed between the IPC and HPC. In the GISFC the separation between the IPC-exit and HPC-entry is fairly small. Therefore, relatively severe ducting is required in order to split and then re-direct the flow through a bank of intercooler modules. In the GIRFC, as the HPC entry is at the rear of the engine, there is considerably more freedom for placement of the intercooler as well as for positioning the headers. Conceptually therefore, a design which fully makes use of this space could lead to lower losses and possibly less severe ducting.

5.5.1 Basic Sizing and Constraints

In the GISFC design, the intercooler modules must be placed radially outwards of the IPC. This could affect the nacelle diameter which would have to be increased in order to accommodate the intercooler units. The GIRFC engine offers several possibilities regarding the installation of intercooler modules. The intercoolers can be positioned above the comparatively compact HP-spool. While this could allow for the intercooler modules to be brought radially inwards, this configuration would also reduce the circumferential space available for the intercoolers. For a given intercooler A_{fr} there is a compromise between intercooler height and circumferential space which results in an optimum configuration where radial height is minimised as is demonstrated in Figure 5.10. As A_{fr} increases for a rectangular profile the minimum outer radius is obtained for wider designs. In order to accommodate a wider design the intercooler inner radius must be pushed outwards so as to increase the circumferential space.

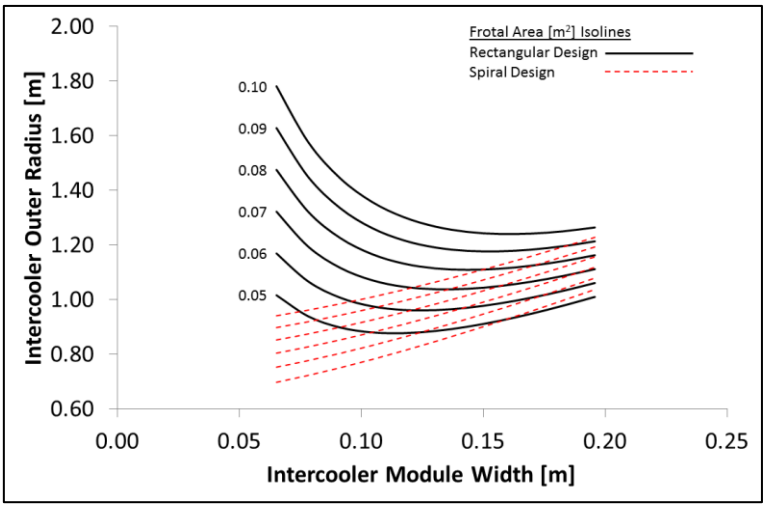

Figure 5.10 – Effect of Module Width on Outer Radius for Rectangular and Spiral Designs

In the GIRFC, the intercooler is positioned above the relatively compact HP-spool and so there is more possibility for reducing the inner radius of the intercooler module. However, for a given A_{fr} it is impractical to reduce the inner radius beyond the stated limits as overall taller modules would result. In order to maximise the use of space available in the GIRFC it is sensible to consider other geometries. In an involute spiral configuration, adjacent modules are wrapped tangentially and hence eliminate the inter-module space. This also allows for a reduction in the outer radius encompassing the intercooler modules. Figure 5.11 shows how the rectangular and involute spiral designs compare for an A_{fr} of $0.08m^2$ and inner radius of 0.45m. In Figure 5.10 a comparison is made between intercooler frontal dimensions for a rectangular and involute spiral design. Unlike for the rectangular design, the involute spiral configuration continues to reduce in outer radius as the module width and consequently the inner radius of the modules are reduced. The reduction in outer radius as the modules are made narrower is also more pronounced than for the rectangular designs within the range given in Figure 5.11. Clearly, it has been assumed up to this point that the aerodynamic and heat transfer characteristics of the intercooler are constant for a given A_{fr} irrespective of the dimensions, which is not the case. This necessitates a more careful analysis of the matrix design and the implication on pressure losses and effectiveness.

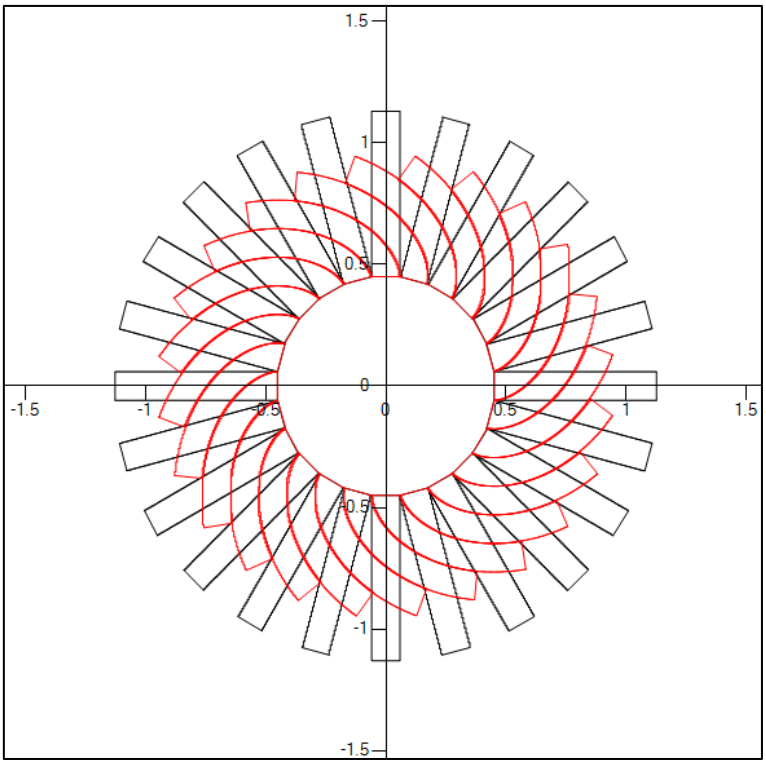

Figure 5.11 – Comparison of Rectangular and Involute Spiral Designs

5.5.2 Intercooler Matrix Design

Given the design rules outlined in the previous sections, several degrees of freedom exist for the definition of the intercooler dimensions. These include the tube length, major diameter of the elliptical tube profile, the intercooler module width as well as the number of intercooler passes. In this concept, the intercooler unit is subdivided into several modules as was the case in Lei and Grönstedt [(34)]. This facilitates assembly and disassembly of the units as well as handling. In reality, the number of modules chosen is not important at this level of fidelity. Had a different number of modules been selected, the number of tube columns as well as the hot and cold side mass flow rates would simply be scaled leading to identical effectiveness and pressure drops. In this section, each of the degrees of freedom are evaluated as proper understanding of the intercooler physical characteristics on the intercooler performance is required in order to select a suitable geometry. The geometry is further limited by the space available in the engine and must therefore respect the boundaries suggested by the general arrangement. In order to define an initial matrix configuration, intercooler entry conditions based upon an initial configuration at take-off have been assumed and are listed in Table 5.1.

Number of Modules	24	-
Entry Total Pressure (Cold)	150	kPa
Entry Total Temperature (Cold)	342	K
Entry Total Pressure (Hot)	681	kPa
Entry Total Temperature (Hot)	550	K
Mass Flow Rate per Module (Hot)	3.5	kg/s

Table 5.1 – Intercooler Entry Conditions

In the following sections four test cases are evaluated. Unless otherwise stated, a W_c/W_h of 1.7 has been assumed across the intercooler. This is a practical figure which allows for high ε_{TO} where it can be difficult to reach the required thrust within a given T_4 limit. In the first two test cases, the hot side inlet area has been fixed at $0.022m^2$ which fixes the Mach number at the hot side entrance. In case 3 and 4 the Mach numbers for both hot and cold side are a function of the selected pressure losses and effectiveness. The sensitivity towards mass flow ratio is explored in case 4.

Case 1: Selection of Tube Diameter and Length

Figure 5.12 and Figure 5.13 show the relationship between h_{std} and E_{std} for a 1-pass intercooler configuration of different tube diameters and lengths. Three tube diameters have been evaluated; specifically major ellipse diameters of 10mm, 12mm and 14mm. For each tube diameter, tube lengths between 0.4m and 1.0m were considered. As tube length increases for a given tube diameter the cold side A_{fr} increases and the following trends can be established:

a. $E_{std,cold}$ and $h_{std,cold}$ decrease due to a reduction in flow stream mass velocity and in spite of an increase in the friction factor and Colburn factor respectively. The factors decrease as Re increases with flow stream mass velocity.
b. $E_{std,hot}$ and $h_{std,hot}$ do not vary greatly as the flow stream mass velocity is constant. As tube length increases, the hot side flow density and Re increase. The $E_{std,hot}$ and $h_{std,hot}$ fall slightly due to a decrease in friction factor and Colburn factor brought about by an increase in Re. However, increasing flow density eventually reverses the decline in $E_{std,hot}$.

On the other hand, for a fixed tube length, as tube diameter is increased, both the hot and cold side A_{ff} are maintained constant as outlined in the assumptions. The following trends can be established:

a. $E_{std,hot}$ and $h_{std,hot}$ decrease even though the flow stream mass velocity is constant. Re increases for the hot side as the hydraulic radius increases and, therefore, the friction factor decreases. The Colburn factor also decreases due to an increase in Re and a decrease in friction factor.

b. $E_{std,cold}$ and $h_{std,\ cold}$, as for the hot side, decrease due to an increase in Re brought about by an increase in the cold side hydraulic radius which lowers the friction and Colburn factors.

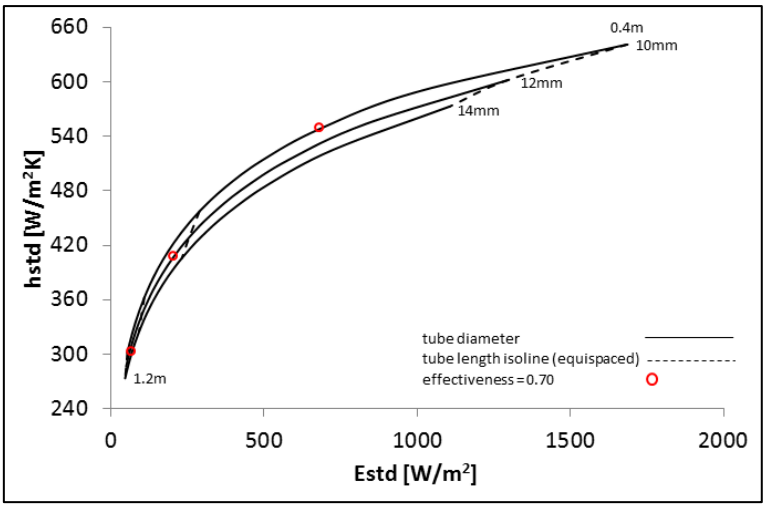

Figure 5.12 – Cold Side Characteristics

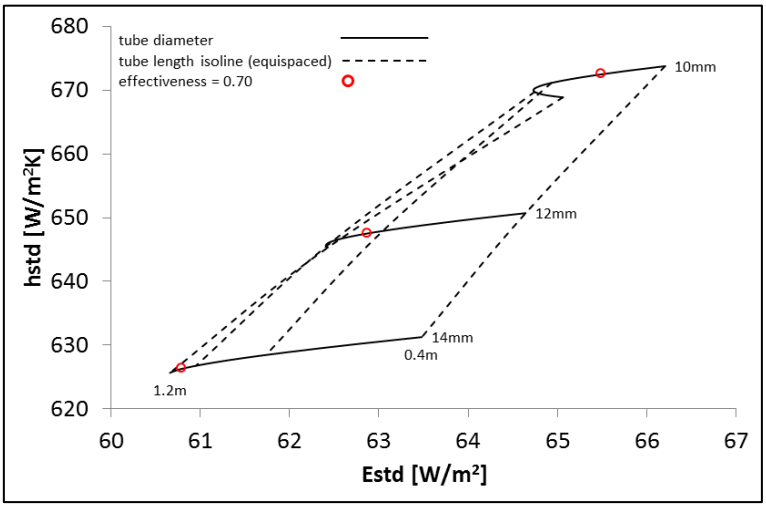

Figure 5.13 – Hot Side Characteristics

Comparing E_{std} and h_{std} at various tube diameters for a given length can be deceptive because the levels of effectiveness vary significantly between the configurations. Three points of similar effectiveness are shown in Table 5.2. These points are also marked in Figure 5.12 and Figure 5.13. It is clear that as tube diameter is increased longer tubes must be adopted in order to maintain high effectiveness levels. The cold side pressure losses are, therefore, reduced dramatically but the hot side pressure losses will inevitably increase as much longer tubes must be used. If one compares the three points in terms of size, it can also be observed that decreasing the tube diameter results in a much more compact design reflected by the tube and module dimensions. The smallest tube diameter also results in the lighter matrix design as reflected by the matrix surface area and the higher h_{std} values.

Major Tube Diameter	**[m]**	0.010	0.012	0.014
Configuration	**[-]**	1-pass	1-pass	1-pass
Rows (per pass)*	**[-]**	56	47	40
Columns (per pass)*	**[-]**	40	33	28
Depth (per pass)	**[m]**	0.53	0.53	0.53
Width (per pass)	**[m]**	0.15	0.15	0.15
Tube Length (per pass)	**[m]**	0.51	0.72	1.04
Transfer Area (per pass)	**[m^2]**	23.2	27.5	34.0
Effectiveness	**[-]**	0.70	0.70	0.70
$\Delta P/P_{cold}$	**[-]**	-0.265	-0.091	-0.037
$\Delta P/P_{hot}$	**[-]**	-0.037	-0.041	-0.049
$E_{std,cold}$	**[W/m^2]**	684	205	68
$E_{std,hot}$	**[W/m^2]**	65	63	61
$h_{std,cold}$	**[W/m^2K]**	549	408	302
$h_{std,hot}$	**[W/m^2K]**	672	648	626
W_{cold}/W_{hot}	**[-]**	1.7	1.7	1.7

** nearest integer value*

Table 5.2 – Intercooler Characteristics (for Effectiveness of 0.7)

Case 2: Selection of Module Width and Tube Length

The criteria for the selection of module width are not only related to performance but also to installation as the module width is constrained by the circumference at the module inner radius. For a given hot flow area there is a trade-off between module width and depth. Three module widths have been evaluated specifically; 0.15m, 0.20m and 0.25m. A number of tube lengths have also been considered ranging again from 0.4 to 1.2m. For a fixed module width, the variation of tube length affects the performance of the intercooler as explained in the previous section. In Figure 5.14 and Figure 5.15 the implication of varying module width can be observed. From these figures and from Table 5.3 the following observations can be made regarding the cold side characteristics:

a. An increase in module width has the same effect on $E_{std,cold}$ and $h_{std,cold}$ as an increase in tube length. This is logical as both an increase in tube length and an increase in module width result in an increase in A_{ff} which reduces the flow stream mass velocity. The decrease in $h_{std,cold}$ with module width occurs in spite of an increase in the Colburn factor and a decrease in Re.
b. At a given effectiveness the variations in $E_{std,cold}$ and $h_{std,cold}$ are quite large. Clearly, larger module widths result in much lower E_{std} which is beneficial but also much lower h_{std} which is detrimental.

The $h_{std.hot}$ and the $E_{std.hot}$ are almost unchanged with module width. This is not surprising as the geometry of the tubes is unchanged with module width. Therefore, the only differences in the hot side are due to differences in the temperature profile up the length of the tubes which in this case will vary due to differences in the cold side. For a given tube length:

a. The $E_{std.hot}$ will increase with module width. Wider modules lead to lower heat transfer as can be seen from the cold side characteristics which lead to lower hot side mean density. This leads to a decrease in Re inside the tubes which leads to a higher friction factor and consequently higher E_{std}.
b. The h_{std} for the hot side will increase with module width. This is because a slightly lower Re leads to a slightly higher Colburn factor.

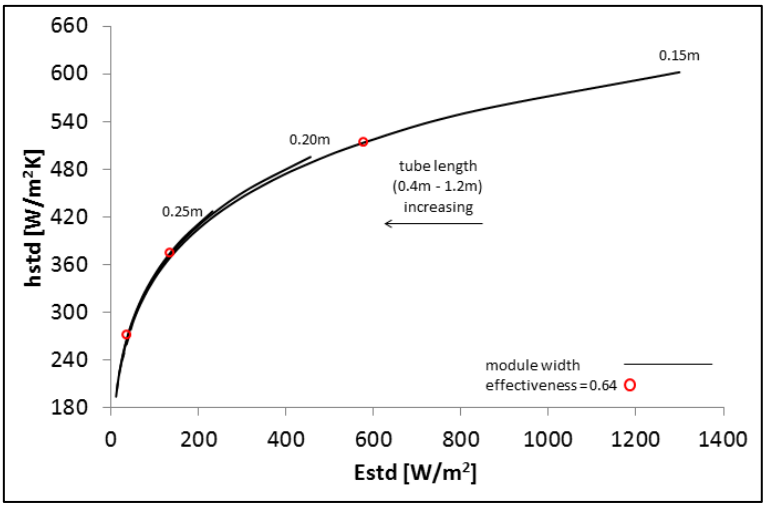

Figure 5.14 – Cold Side Characteristics

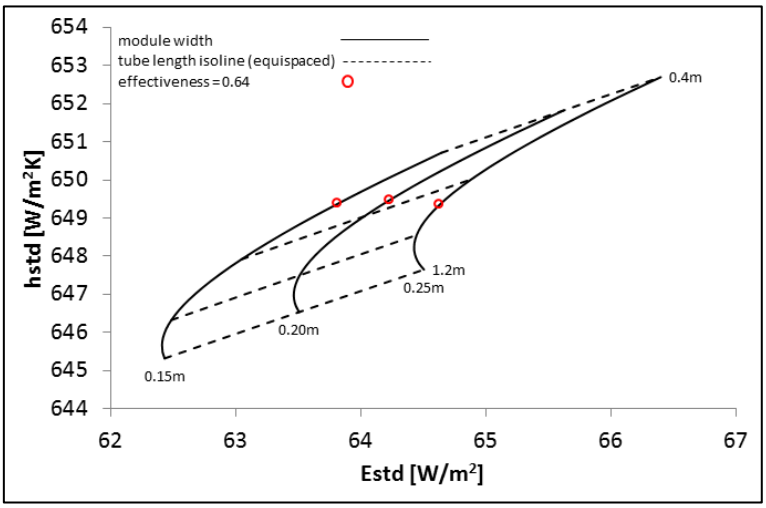

Figure 5.15 – Hot Side Characteristics

Table 5.3 shows more detail regarding the three points of similar effectiveness also shown in Figure 5.14 and Figure 5.15. The trade-off between width and depth is quite apparent. Wider designs also tend to have longer tubes which lead to lower cold side pressure losses but higher hot side pressure losses. Clearly, the narrower the heat exchanger, the lighter it becomes as weight is proportional to the transfer area which is proportional to tube length given that the number of tubes in this case is constant.

Width (per pass)	**[m]**	0.15	0.20	0.25
Configuration	**[-]**	1-pass	1-pass	1-pass
Rows (per pass)*	**[-]**	47	35	28
Columns (per pass)*	**[-]**	33	44	55
Depth (per pass)	**[m]**	0.53	0.40	0.32
Tube Length (per pass)	**[m]**	0.51	0.61	0.77
Transfer Area (per pass)	**[m^2]**	19.4	23.4	29.5
Major Tube Diameter	**[m]**	0.012	0.012	0.012
Effectiveness	**[-]**	0.64	0.64	0.64
$\Delta P/P_{cold}$	**[-]**	-0.189	-0.052	-0.018
$\Delta P/P_{hot}$	**[-]**	-0.029	-0.035	-0.045
$E_{std,cold}$	**[W/m^2]**	579.2	136.8	38.4
$E_{std,hot}$	**[W/m^2]**	63.8	64.2	64.6
$h_{std,cold}$	**[W/m^2K]**	514.1	373.5	271.5
$h_{std,hot}$	**[W/m^2K]**	649.4	649.5	649.3
W_{cold}/W_{hot}	**[-]**	1.7	1.7	1.7
** nearest integer value*				

Table 5.3 – Intercooler Characteristics (For Effectiveness of 0.64)

Case 3: Selection of Module Number and Effectiveness

In the previous cases, only a 1-pass cross-flow intercooler configuration is considered. However, multi-pass cross-counter flow configurations are also possible using the same components as for the current intercooler. Three intercooler configurations have been considered in this chapter including a 1-pass, 2-pass and 3-pass option. The configurations are given in Figure 5.16.

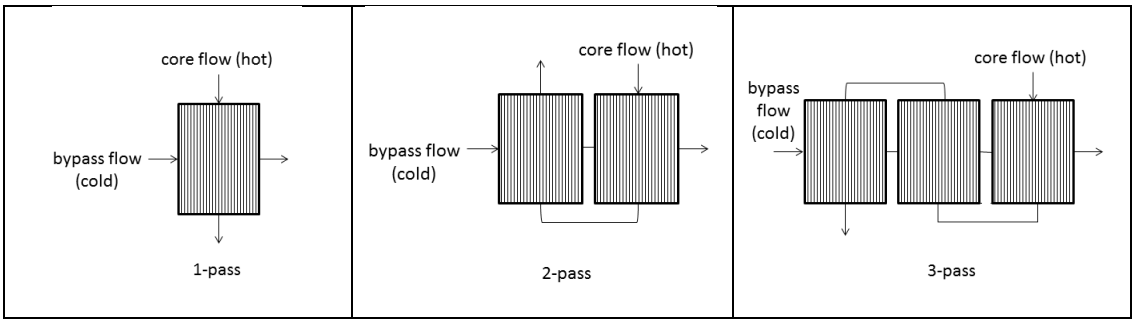

Figure 5.16 – Single and Multi-Pass Intercooler Configurations

Although it is possible to retain the same basic dimensions for each module in the 1-pass, 2-pass and 3-pass configurations, this could result is vastly different values of effectiveness and pressure losses. Therefore, in this case a fixed intercooler performance has been assumed and

the characteristics of the three options at different levels of effectiveness have been observed. For each design point a given effectiveness in the range of 0.5-0.9, a fixed cold side pressure loss ($\Delta P/P$) of 0.12 and a fixed hot side pressure loss ($\Delta P/P$) of 0.05 have been maintained. In order to achieve these values an iteration involving tube length, tube diameter and number of tubes was carried out. Unlike in the previous cases, this type of matching results in different hot side free flow areas and Mach numbers.

Figure 5.17 and Figure 5.18 show the E_{std} and h_{std} for the cold and hot side respectively. It is immediately apparent that designs for higher effectiveness result in lower h_{std} and E_{std} for both sides of the intercooler. An increase in intercooler surface transfer area does not lead to a proportional increase in effectiveness as the mean temperature difference between the two flows is reduced. As in this case the hot and cold side pressure losses have been maintained constant it is also natural that an increase in intercooler size would lead to lower E_{std} for both hot and cold sides. For much of the effectiveness range considered, the h_{std} of both hot and cold sides is lower as additional passes are considered. In order to understand this behaviour a more detailed analysis of the geometric implications is required.

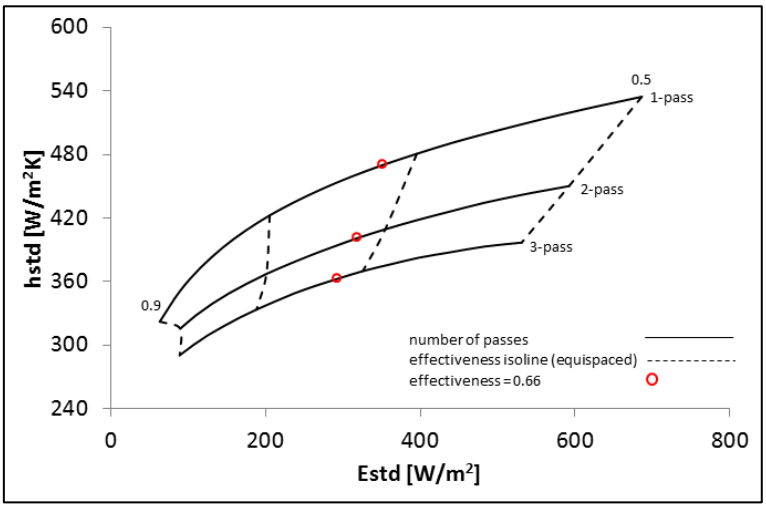

Figure 5.17 – Cold Side Characteristics

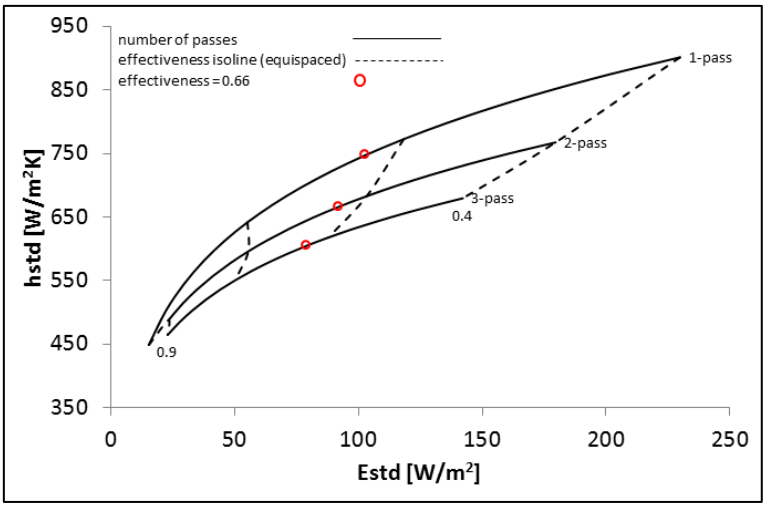

Figure 5.18 – Hot Side Characteristics

Table 5.4 summarises the main characteristics of three specific configurations each with an ε of 0.66. At this effectiveness level, the 1-pass design is the more compact in terms of both size and weight. However, the 1-pass design does have the longest tubes and would, therefore, result in the most interference with the bypass duct and possibly increase the nacelle diameter beyond what would be the case for the 2-pass or 3-pass designs. Nevertheless, the height difference corresponding to the tube length is not that significant.

Configuration	**[-]**	1-pass	2-pass	3-pass
Rows (per pass)*	**[-]**	43	24	18
Columns (per pass)*	**[-]**	35	20	14
Depth (per pass)	**[m]**	0.45	0.45	0.46
Width (per pass)	**[m]**	0.15	0.15	0.15
Tube Length (per pass)	**[m]**	0.598	0.573	0.571
Transfer Area (per pass)	**[m^2]**	20.6	11.1	8.0
Major Tube Diameter	**[m]**	0.011	0.020	0.028
Effectiveness	**[-]**	0.66	0.66	0.66
$\Delta P/P_{cold}$	**[-]**	-0.12	-0.12	-0.12
$\Delta P/P_{hot}$	**[-]**	-0.05	-0.05	-0.05
$E_{std,cold}$	**[W/m^2]**	351	319	294
$E_{std,hot}$	**[W/m^2]**	103	92	79
$h_{std,cold}$	**[W/m^2K]**	470	401	363
$h_{std,hot}$	**[W/m^2K]**	747	666	605
W_{cold}/W_{hot}	**[-]**	1.7	1.7	1.7

** nearest integer value*

Table 5.4 – Intercooler Characteristics (for Effectiveness of 0.66)

Figure 5.19 to Figure 5.24 show detailed information about the matrix designs for the 1-pass, 2-pass and 3-pass configurations. To achieve higher effectiveness, the intercooler transfer area must be increased. Transfer area increases more rapidly than does the effectiveness requirement as the mean temperature difference between the flows is reduced. Up to an effectiveness of about 0.75 the surface area of the 1-pass configuration is lower than that of the 2-pass or 3-pass configuration. Interestingly, the difference in surface area between the three configurations within this range is not that large. In order to maintain a pressure drop similar to that of the 1-pass configuration, the 2-pass and 3-pass configurations have to adopt fewer tubes of larger diameters but shorter length. Essentially the pressure drop per module of the 2-pass configuration must be half that of the 1-pass and for the 3-pass only a third. As the effectiveness requirement increases, the tube diameters must be reduced while the tube number and length must be increased. As tube diameter decreases, the surface transfer area per unit flow and the hot side pressure losses increase rapidly. To mitigate the increase in losses, an increase in tube number is required. This occurs more rapidly for the 1-pass designs as the cold flow mass velocity is lower. Of course to mitigate the increase in cold side losses with tube number, the tube lengths must then also be increased. Clearly, these factors are interrelated as both an increase in tube number and length lead to higher effectiveness and increased tube length will also increase hot side pressure losses. After several design iterations, the net result is that due to a rapid increase in size with effectiveness, the 1-pass design surface transfer area surpasses that of the 2-pass configuration beyond an effectiveness level of 0.75. The same trait is visible when comparing the 2-pass with the 3-pass configuration beyond an effectiveness level of approximately 0.9.

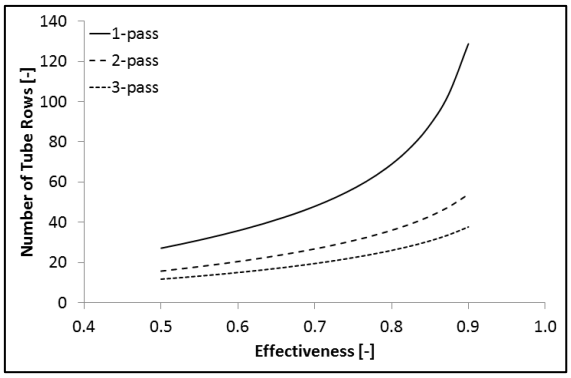

Figure 5.19 – N_{rows} vs. Effectiveness

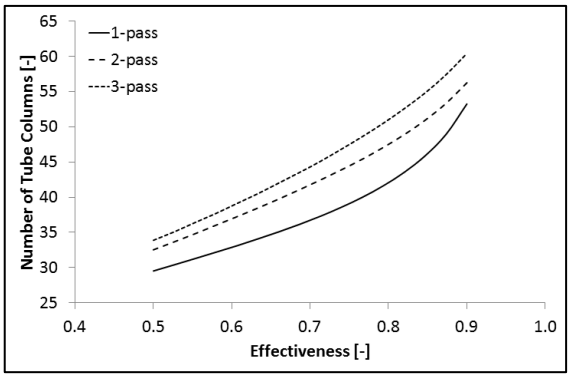

Figure 5.20 – $N_{columns}$ vs. Effectiveness

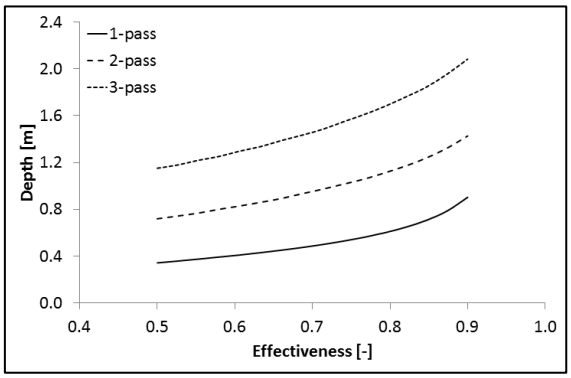

Figure 5.21 – IC Depth vs. Effectiveness

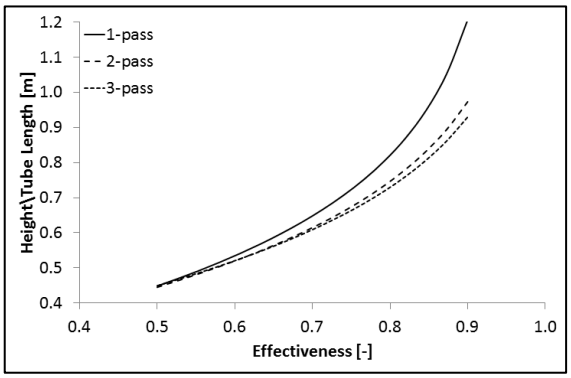

Figure 5.22 – Tube Length vs. Effectiveness

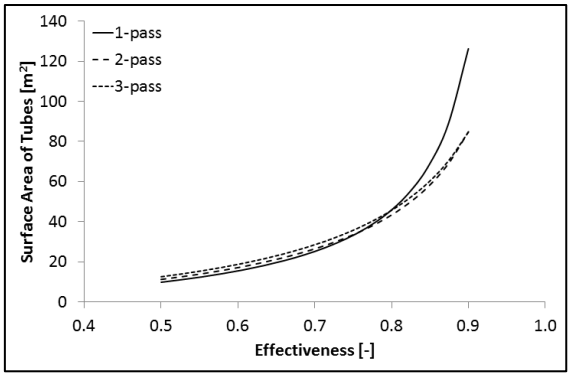

Figure 5.23 – Surface Area vs. Effectiveness

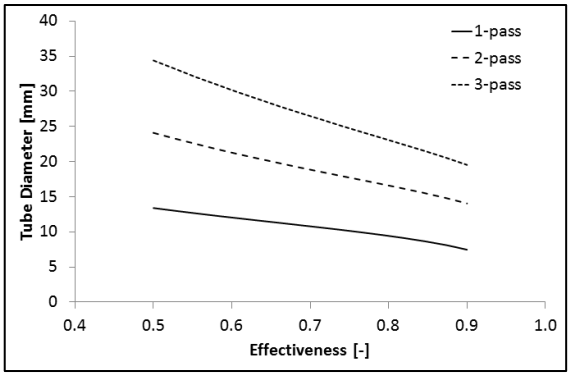

Figure 5.24 – Diameter vs. Effectiveness

<u>Case 4: Selection of Mass Flow Ratio and Effectiveness</u>

In the previous set of evaluations the W_c/W_h is constant throughout. However, the design W_c/W_h has a very big effect upon the size and specific dimensions of the intercooler. In this evaluation, the effect of changing the W_c/W_h given a fixed set of performance characteristics is considered. As in the previous case a cold side ΔP/P of 0.12, a hot side ΔP/P of 0.05 and a given effectiveness between 0.4 and 0.9 are considered. Table 5.5 shows three 1-pass intercooler configurations at an effectiveness level of 0.66. The W_c/W_h levels considered are 1.3, 1.5 and

1.7. An increase in W_c/W_h, for a given pressure loss and effectiveness will lead to a significant increase in both h_{std} and E_{std} in the cold stream as well as a lesser increase in the hot stream. As W_c/W_h is increased, in order to reduce the pressure losses the tube diameters and lengths have to be increased so as to reduce the mass flow velocity by increasing the cold side A_{ff}. Although an increase in tube diameter typically reduces h_{std}, the increase in W_c/W_h as well as the slight increase in tube length more than offsets this trend.

W_{cold}/W_{hot}	**[-]**	1.30	1.50	1.70
Configuration	**[-]**	1-pass	1-pass	1-pass
Rows (per pass)*	**[-]**	57	48	43
Columns (per pass)*	**[-]**	42	38	35
Depth (per pass)	**[m]**	0.50	0.47	0.45
Width (per pass)	**[m]**	0.15	0.15	0.15
Tube Length (per pass)	**[m]**	0.57	0.58	0.60
Transfer Area (per pass)	**[m^2]**	26.61	22.85	20.61
Major Tube Diameter	**[m]**	0.009	0.010	0.011
Effectiveness	**[-]**	0.66	0.66	0.66
$\Delta P/P_{cold}$	**[-]**	-0.12	-0.12	-0.12
$\Delta P/P_{hot}$	**[-]**	-0.05	-0.05	-0.05
$E_{std,cold}$	**[W/m^2]**	219.21	286.24	351.45
$E_{std,hot}$	**[W/m^2]**	79.98	92.94	102.81
$h_{std,cold}$	**[W/m^2K]**	433.71	454.86	470.13
$h_{std,hot}$	**[W/m^2K]**	713.66	734.98	747.46
* nearest integer value				

Table 5.5 – Intercooler Characteristics (for Effectiveness of 0.66)

Figure 5.25 to Figure 5.30 show how the individual geometric parameters for the three W_c/W_h levels are changing with different levels of effectiveness. It is clear that the size of the intercooler grows rapidly with ε. Also it is clear that, in terms of tube number, surface area and overall dimensions, higher W_c/W_h leads to a smaller unit. The exception to this statement is tube length where it is clear from Figure 5.28 that below an effectiveness of 0.6, a W_c/W_h of 1.3 leads to the shortest design while beyond a W_c/W_h of 1.7 it leads to the tallest design. Intercooler effectiveness at take-off should lie between 0.6 and 0.7. Within this range there is little difference in module height with W_c/W_h.

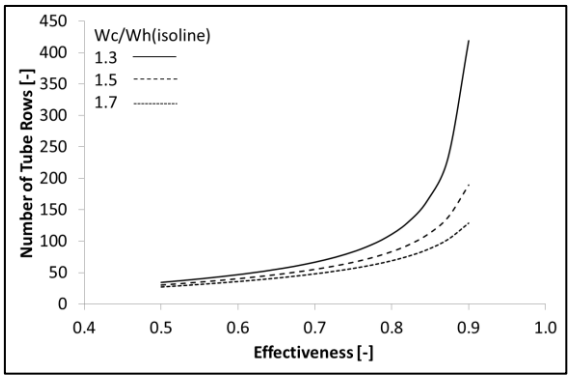

Figure 5.25 – N_{rows} vs. Effectiveness

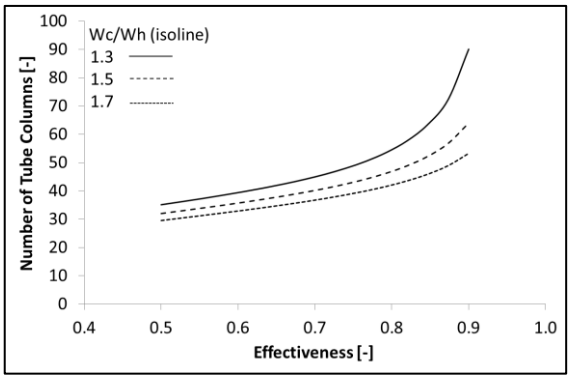

Figure 5.26 – $N_{columns}$ vs. Effectiveness

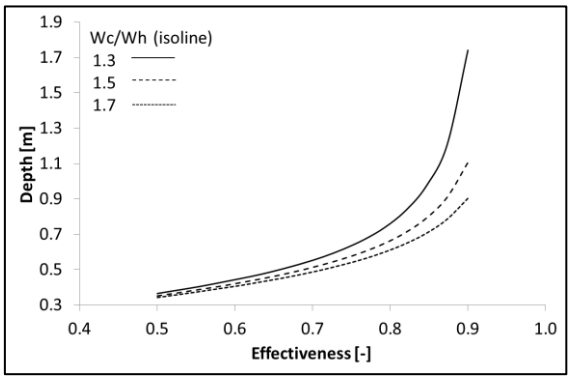

Figure 5.27 – IC Depth vs. Effectiveness

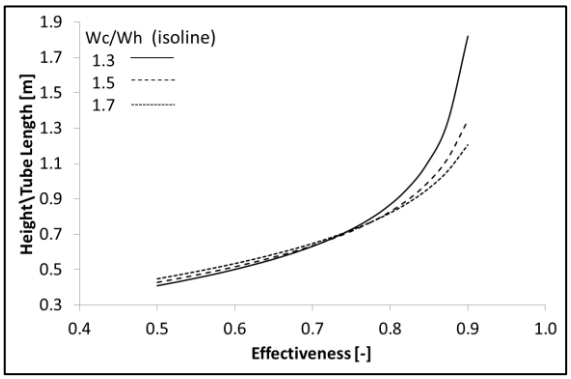

Figure 5.28 – Tube Length vs. Effectiveness

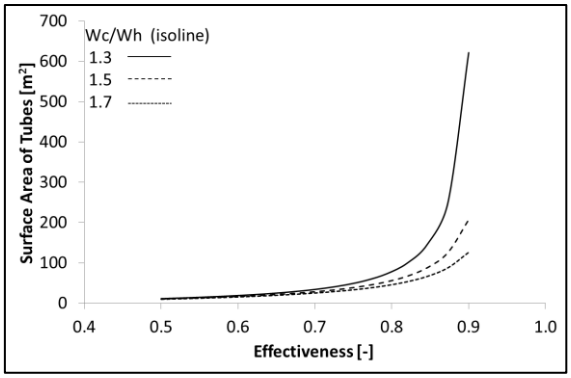

Figure 5.29 – Surface Area vs. Effectiveness

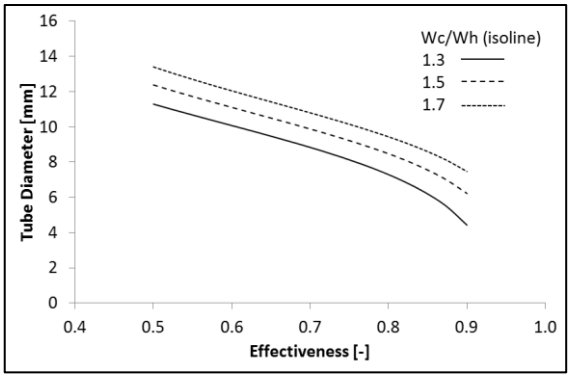

Figure 5.30 – Diameter vs. Effectiveness

<u>The Cross-Corrugated Configuration</u>

This chapter has mainly dealt with the design and performance of a tubular intercooler concept derived from the research of Zhao et al [(109)]. As previously mentioned, a cross-corrugated concept was also evaluated in NEWAC [(12)]. The integration of the cross-corrugated intercooler concept in the GISFC and GIRFC was investigated by Guerra [(107)]. Before discussing these results, it is useful to consider some of the high level differences between these intercooler concepts. In the background section of this chapter the Colburn and friction factors of the

tubular concept were compared with similar correlations for circular tubes. In Zhao et al [109] the hot side characteristics of the elliptical tube bank concept are modelled using correlations for circular tube profiles [109], and therefore as expected are similar to correlations for circular tubes discussed in literature. The cold side characteristics of the elliptical tube bank concept were also quite similar to the circular tube bank correlations but did show greater variance due to the differences in shape and arrangement.

In order to model a cross-corrugated design, Kwan et al. [101] and Guerra [107] assume that the friction factors and Colburn factors can be modelled by Equation (5.1) and Equation (5.2) respectively. However, the Re range for which the Colburn factor is valid is limited to near laminar conditions. In the research carried out for this dissertation, higher Re needed to be considered. In Doo et al. [103] detailed CFD studies were carried out up to Re of 12000 and in addition compared against experimental values. The friction-factors are similar in magnitude to those predicted for internal circular tube flow as well as for predictions using Equation (5.1) and therefore are not discussed further.

At Re below 1000, Equation (5.2) for cross-corrugated surfaces is somewhat similar to the data presented in Doo et al. [103]. At Re beyond 2000 the Colburn factors predicted by Equation (5.2) and those given by Doo et al. [103] begin to diverge. For the "*CC90_2.5*" and "*TCC90*" profiles, given by Doo et al. [103], the Colburn factor obtained through experiment is closer to what would be expected for the internal side of a circular profiled tube rather than to the Colburn factor predicted by Equation (5.2). It is not being suggested that Colburn factors for circular tubes can be used for modelling a cross-corrugated surface. However, this comparison does suggest that the Colburn factor and consequently the heat transfer in Kwan et al. [101] and Guerra [107] might be well overstated in the turbulent regime. In Guerra [107] it is suggested that in a cross-corrugated design Re approaching 4000 can be expected in the hot side and Re beyond 2300 can be expected in the cold side. These are well beyond the limits of Equation (5.2). In Fukui [105], friction factors and Colburn factors are also presented for a cross-corrugated design. The Colburn factors in this case are far lower than those predicted by Equation (5.2) even at Re below 1000. Clearly, this is only indicative as the intercooler design is quite different. However,

there is some doubt as to the validity of modelling the Colburn factor using Equation (5.2) as done by Kwan et al. [101] and Guerra [107]. Not surprisingly, Guerra [107] showed intercooler designs which are far more compact than those characterised in this chapter. This is due to the significantly higher Colburn factors of these designs. No definitive answer can be given as to whether these Colburn factors are excessive for such low friction factors, and therefore further research is warranted. The tubular designs, although larger than the cross-corrugated, have been retained in this study as they show better agreement with literature and the assumptions are better understood.

5.5.3 Integrated Intercooler Performance

In this section the intercooler is evaluated as a component within the GISFC and GIRFC. The intercooler performance strongly affects the selection of OPR, BPR, IPC and HPC pressure ratios as well as having an important effect on core size. At off-design conditions the use of a variation area intercooler nozzle allows for the regulation of mass flow through the cold side of the intercooler. This permits better matching of the intercooler to the take-off and cruise conditions.

Implication on Blade Height and Combustor Outlet Temperature

Increasing OPR can present challenges for the integrity of the HPC final stages and drive cone. The resulting flow temperatures may necessitate the use of increasingly heat resistant materials. Increasing T_3 can also increase NO_x emissions as thermal NO_x formation pathways are favoured at high temperatures. Higher OPR also results in increased end-wall losses especially in the later stages of the HPC due to the reduction in exit blade height. Intercooling reduces T_3, which for a given T_4 reduces core size. This will compound the reduction in blade height. Figure 5.31 shows the effect of increasing OPR_{TOC} on $T_{3,TOC}$ as well as on blade height for the GIRFC and GISFC concepts. Increasing OPR_{TOC} for a given ε_{TOC} results in a significant increase in $T_{3,TOC}$ as well as a reduction in HPC exit blade height. Increasing ε_{TOC} can offset the increase in $T_{3,TOC}$ at a given OPR_{TOC} by reducing the HPC inlet temperature; but the HPC exit blade height continues to shrink as ε_{TOC} and OPR_{TOC} are increased. For the GISFC the limited radial space available for HPT discs between concentric shafts and HPT blade roots limits any

potential reduction in mean radius. On the other hand, in the GIRFC concept there is a significant reduction in the diameter of the HP-shaft and rotor disc bore when compared with the GISFC. Consequently, a lower hub-to-tip ratio at the exit of the HPC and entry of the HPT can be achieved and is accompanied by longer blades at the HPC exit and HPT entry for a given flow area. Figure 5.31 shows the change in HPC blade height that can be achieved by adopting a reversed flow core design.

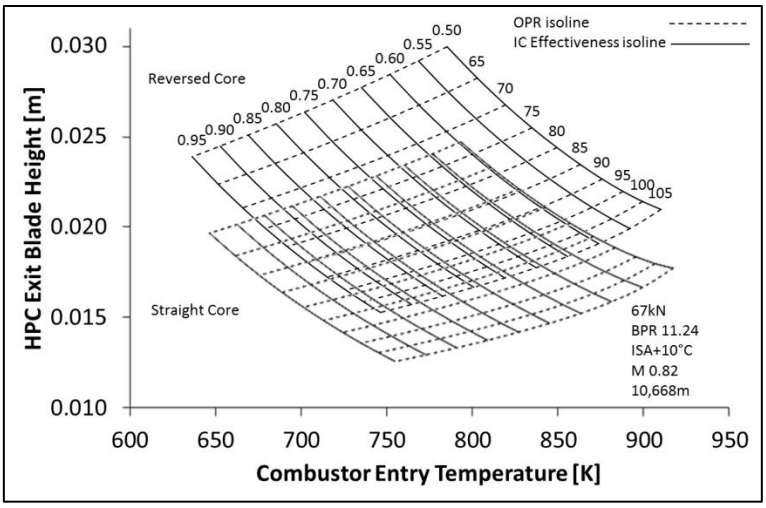

Figure 5.31 – Comparison of HPC Blade Heights for GISFC and GIRFC Engines

Selection of OPR and SFN will have an important effect upon the thermo-propulsive efficiency of the concepts. Thermal efficiency is strongly affected by OPR while propulsive efficiency is highly dependent on the reduction of SFN. Figure 5.32 shows the implication of the selection of BPR_{TOC} and OPR_{TOC} on SFC_{MC} for the GISFC and GIRFC respectively. An initial benefit from increasing OPR_{TOC} can be observed at every BPR_{TOC}. However, as over-tip losses increase and the HPT and HPC polytropic and isentropic efficiencies decline, the SFC_{MC} improvement is reversed. When comparing the GIRFC and the GISFC, it is clear that the GIRFC, which suffers less from over-tip leakage, is able to achieve higher levels of OPR_{TOC} at each level of BPR_{TOC}. The optimum OPR_{TOC} at a BPR_{TOC} of 15 is 80-85 for the GISFC while it is 90-95 for the GIRFC. A lower design SFN and FPR will improve propulsive efficiency, but the associated increase in nacelle drag and propulsion system weight must also be considered when searching for an optimal design.

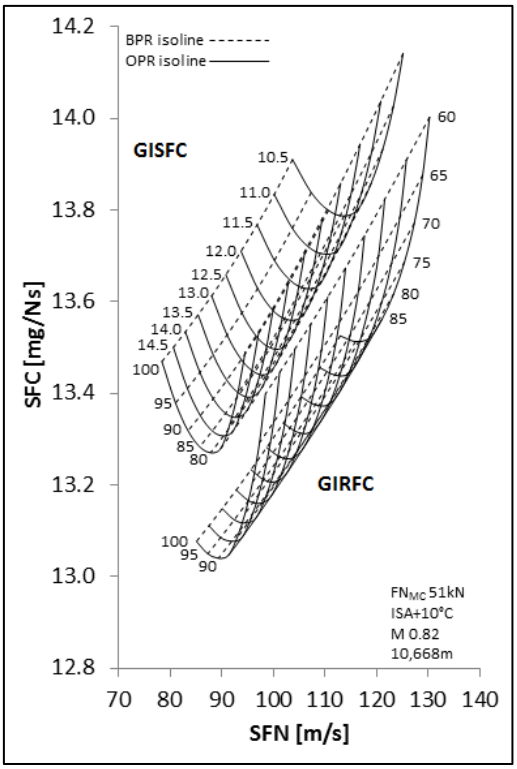

Figure 5.32 – Implication of BPR_{TOC} and OPR_{TOC} on SFC_{MC} and SFN_{MC}

<u>Selection of IPC-HPC Work Split</u>

An intercooled cycle usually benefits from a work split which favours high pressure ratios across the HPC and in this case is also favoured due to higher higher polytopic efficiency when compared to the IPC. The intercooler reduces the work that must be carried out by the HPC to achieve the required increase in pressure. However, if the IPC pressure ratio is too small then the intercooler will be operating across a relatively small temperature difference and will not be able to transfer much heat from the core to the bypass stream. In such a case the benefits of intercooling may also be reduced. In this study, a fan mass flow rate of 550kg/s, a $P_c/P_{h,TOC}$ of 1.0, a $T_{4,TOC}$ of 1920K and an FN_{TOC} of 67kN have been maintained throughout. The pressure ratio exponent (n) and the OPR_{TOC} have been varied to see how the optimum work split varies. Over-tip leakage losses have also been ignored in this case. In order to meet these conditions the BPR_{TOC}, FPR_{TOC} and fuel flow have been varied.

Figure 5.33 shows the relationship between SFC_{TOC} and IPC pressure ratio at various OPR_{TOC} and pressure ratio exponents. As OPR_{TOC} is increased for a fixed n, the $T_{3,TOC}$ is also increased. In order to limit the temperature rise in the combustor and to maintain the same

$T_{4,TOC}$ the core mass flow rate has to be increased which leads to a reduction in BPR_{TOC}. Increasing core mass flow rate increases the pressure losses in the intercooler which reduces the SFC_{TOC} benefit. Increasing pressure ratios also increases component losses. For a fixed OPR_{TOC}, there is an optimum pressure ratio exponent which will yield the lowest SFC_{TOC}. As the IPC pressure ratio increases so does the ε_{TOC}. An increase in ε_{TOC} lowers $T_{3,TOC}$, and therefore leads to a decrease in core mass flow rate and a decrease in intercooler pressure losses. At low IPC pressure ratios, therefore, there is a combination of high pressure losses and high HPC work which reduce SFC_{TOC}. As OPR_{TOC} increases, the optimum pressure ratio exponent and also the optimum IPC pressure ratio increase.

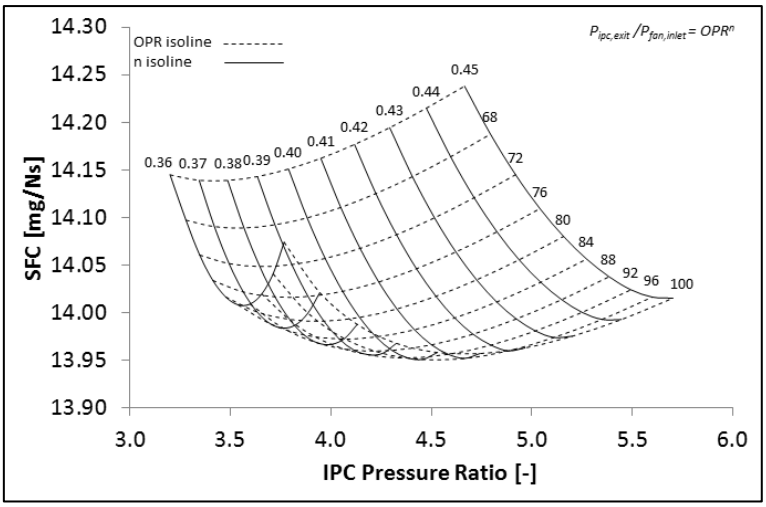

Figure 5.33 – Optimum IPC PR at TOC for Different Intercooler Configurations (GIRFC)

<u>Selection of Intercooler W_c/W_h at Top-of-Climb and at Mid-Cruise</u>

Figure 5.34 shows the effect of varying the intercooler mass flow ratio ($W_c/W_{h,TOC}$) and fan inlet mass flow rates at TOC, on SFC_{MC}. In this case, a fixed ε_{MC} of 0.55 is maintained through regulation of the $W_c/W_{h,MC}$. As fan diameter and inlet mass flow rate increase, SFC_{MC} reduce due to an improvement in propulsive efficiency. This does not take into account penalties which would be incurred due to increased nacelle drag and weight as the fan diameter increases. For a given fan mass flow rate, an increase in $W_c/W_{h,TOC}$ and consequently ε_{TOC}, is accompanied by an increase in intercooler matrix pressure losses. However, the increase in ε_{TOC} leads to a decrease in $T_{3,TOC}$ which allows for a reduction in core mass flow rate (and corrected mass flow rate). Therefore, $W_{c,TOC}$ does not increase linearly with $W_c/W_{h,TOC}$ as $W_{h,TOC}$ is falling due to an

increase in ε_{TOC}. As $W_c/W_{h,TOC}$ increases, the $W_{c,MC}$ required to reach an ε_{MC} of 0.55 is also reduced which leads to relatively lower losses in the cold side of the intercooler. As the increase in ε_{TOC} with increasing $W_c/W_{h,TOC}$ slows the increase in pressure losses become dominant.

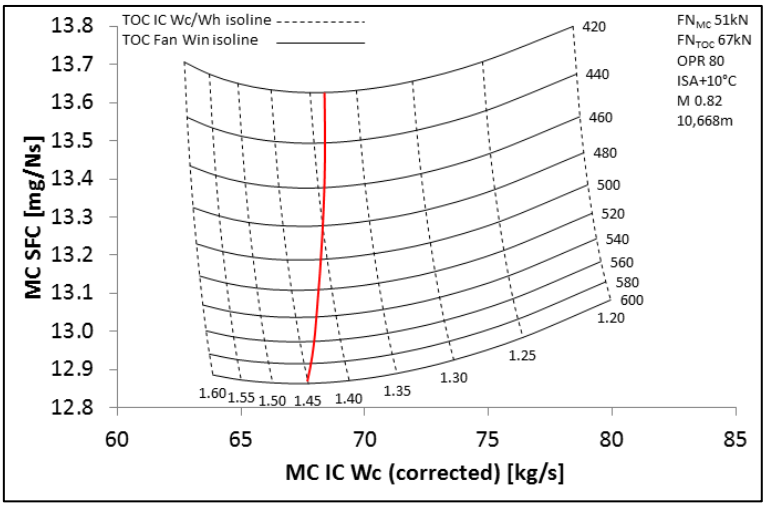

Figure 5.34 – Variation of SFC_{MC} for Different TOC Designs (GIRFC)

Thermal efficiency is limited by losses in the intercooler matrix and ducting. In order to limit these losses, the intercooler cooling air exhaust nozzle allows the mass flow rate through the cold side to be reduced at cruise, reducing pressure losses associated with high cooling air flow speeds. Figure 5.35 shows how SFC_{MC} varies according to ε_{MC} due to off-design variations in cooling air mass flow rate. Initially, thermal efficiency benefits from higher ε_{MC}. Yet, as flow speeds increase, pressure losses in the intercooler matrix become dominant. The ε_{MC} is lowered through a reduction in cold mass flow brought about by a reduction in intercooler nozzle area. This also makes the fan running line shallower, resulting in higher FPR_{MC} and lower fan mass flow at cruise resulting in lower fan efficiency and an increase in SFC_{MC}.

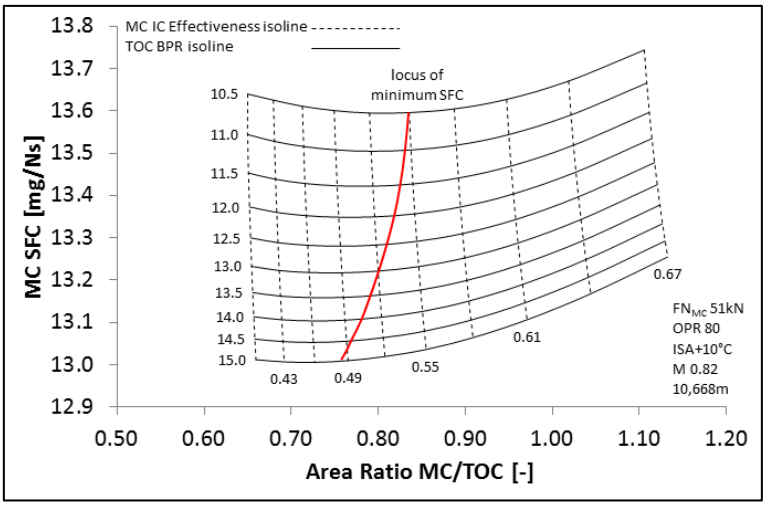

Figure 5.35 – Effect of ε_{MC} on SFC_{MC} (GIRFC)

<u>Selection of Intercooler Effectiveness at Take-Off</u>

Turbofan engines are typically sized for the TOC condition where the rate of climb is most difficult to achieve. However, the maximum T_4 is often required to meet the FN_{TO}. Typically, FN_{TO} is time limited as a high $T_{4,TO}$ has a detrimental effect on engine life due to turbine blade creep. These issues are aggravated in high OPR designs where T_3 and turbine cooling air temperatures are higher. $T_{4,TO}$ can be reduced through the use of intercooling. Higher ε_{TO} can lower $T_{4,TO}$ by rejecting more heat from the core to the cooling stream as demonstrated by Kyprianidis et al. [22]. Intercooler effectiveness is a function of intercooler type, size and cooling flow rates. The intercooler should be sized for the take-off condition if high ε_{TO} is to be achieved. Although ε_{TO} can be increased through increased cooling air flow rates, increasing matrix pressure losses which lead to higher fuel flow rates eventually reverse the reduction in $T_{4,TO}$. On the other hand, significant weight penalties would be incurred by increasing the intercooler size. In order to vary ε_{TO} at a given operating point, a variable intercooler cooling air exhaust nozzle is incorporated in both GIRFC and GISFC designs. Figure 5.36 shows the effect of varying cooling flow rates through the intercooler on $T_{4,TO}$.

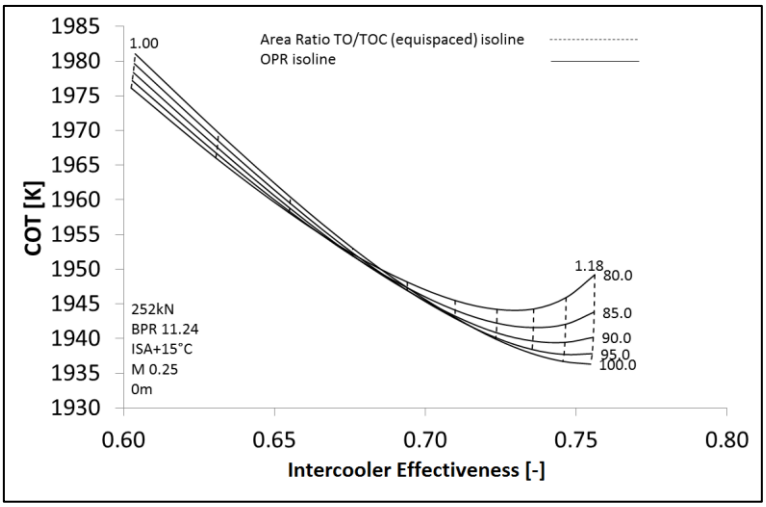

Figure 5.36 – $T_{4,TO}$ vs. ε_{TO} for a Range of OPRs (GIRFC)

5.6 Discussion and Conclusion

Based on the evaluations presented in this chapter, two intercooler configurations were established. The final configurations are the result of several design iterations although only the main design sensitivities were presented in this report. The design pressure loss and effectiveness levels were established based on work carried out in NEWAC [(12)] as well as in this dissertation. These levels represent the minimum acceptable performance for an intercooler if it is to be introduced within a practical engine. Clearly, higher effectiveness and lower pressure losses could be achieved but realistically the size and weight of the intercooler would be difficult to justify. From the evaluations carried out in this section several conclusions can be drawn:

a. By adopting an involute spiral configuration the outer radius of each intercooler can be reduced. The reduction in intercooler height is significant for intercooler widths below 0.15m for a frontal area of 0.09m^2 as is the case for the final configurations.

b. Narrower intercooler modules favour a reduction in outer diameter when adopting a spiral configuration. A module width of 0.15m appears to offer the best trade-off between losses and size and therefore has been retained for both the GIRFC and GISFC concept. Narrower modules would necessitate more tube rows to maintain the required effectiveness level. The tubes would, however, need to be far wider in diameter and longer in order to mitigate cold side losses. Such a design would negatively affect the installation and weight of the intercooler. Therefore, although feasible, there is little advantage to be gained from

reducing the GIRFC intercooler module width. By retaining an inner module radius similar to that of the GISFC, more space is also available for the positioning of the headers.

c. The performance studies outlined in this chapter suggest that the intercooler should be sized for high effectivenss at TOC to reduce T_4 and core size respectively. The engine performance at cruise benefits greatly from reduced mass flow through the intercooler due to a reduction in pressure losses. The variable area intercooler nozzle is therefore required to make large adjustments to the flow area so as to optimise the intercooler performance at different flight conditions.

d. For an ε_{TO} of 0.66 and a fixed level of pressure losses at take-off, the intercooler module height is similar at each W_c/W_h level explored. A $W_c/W_{h,TO}$ of 1.7 results in the most compact design. The off-design performance also plays a critical role in determining the optimum design $W_c/W_{h.}$ From the parametric studies presented in this chapter it is clear that a high $W_c/W_{h,TOC}$ is beneficial. W_c/W_h, for a given nozzle area, reduces between TO and TOC. Therefore, to maintain a high $W_c/W_{h,TOC}$ without increasing pressure losses, a relatively high $W_c/W_{h,TO}$ should be selected. It has been shown that a reduction of $W_c/W_{h,MC}$ can lead to a marked improvement in SFC_{MC}. The efficacy of this strategy is dependent on high $W_c/W_{h,TOC}$. A low $W_c/W_{h,TOC}$ would result in a very low $W_c/W_{h,MC}$ with relatively high pressure losses for a given ε_{MC}.

e. A 1-pass intercooler is the most compact configuration but also the tallest design with the narrowest tubes. These tubes would be the most difficult to manufacture. The 1-pass configuration would also have the lowest surface area within the range of ε required. A 2-pass intercooler would be slightly shorter and heavier but twice as deep. The tubes would however be far easier to manufacture. Therefore, the 2-pass configuration is also a viable option especially for the GIRFC where more longitudinal space is available.

f. The final intercooler specifications which are the product of several design iterations are presented in Table 5.6. The preferred option is the 1-pass configuration due to the compactness of the design and weight advantage although the 2-pass is clearly viable as well. The 3-pass configuration has been rejected due to the excessive weight and more importantly size of the modules.

g. The 1-pass and 2-pass configurations are illustrated in Figure 5.37. This schematic is based on the intercooler specifications given in Table 5.6. The 1-pass configuration dimensions were established assuming the intercooler modules are placed in an upright position. In Figure 5.37 an alternate 1-pass positioning is proposed where the intercooler modules are tilted in order to obtain additional height savings. This adjustment can lower the outer radius of the 1-pass configuration thereby reducing the interference with the bypass duct and it can also simplify the header geometry thereby potentially reducing header losses. The 1-pass configuration as suggested in Figure 5.37 could eliminate the additional 180 degree bend between the intercooler and HPC which can be seen in the 2-pass configuration.

Configuration	**[-]**	1-pass	2-pass
Rows (per pass)*	**[-]**	43	24
Columns (per pass)*	**[-]**	35	20
Depth (per pass)	**[m]**	0.45	0.45
Width (per pass)	**[m]**	0.15	0.15
Tube Length (per pass)	**[m]**	0.598	0.573
Module Height (Involute Spiral)	**[m]**	0.544	0.521
Transfer Area (per pass)	**[m^2]**	20.6	11.1
Major Tube Diameter	**[m]**	0.011	0.020
Effectiveness	**[-]**	0.66	0.66
$\Delta P/P_{cold}$	**[-]**	-0.12	-0.12
$\Delta P/P_{hot}$	**[-]**	-0.05	-0.05
$E_{std,cold}$	**[W/m^2]**	351	319
$E_{std,hot}$	**[W/m^2]**	103	92
$h_{std,cold}$	**[W/m^2K]**	470	401
$h_{std,hot}$	**[W/m^2K]**	747	666
W_{cold}/W_{hot}	**[-]**	1.7	1.7

Table 5.6 – Final GISFC and GIRFC Intercooler Configuration (take-off condition)

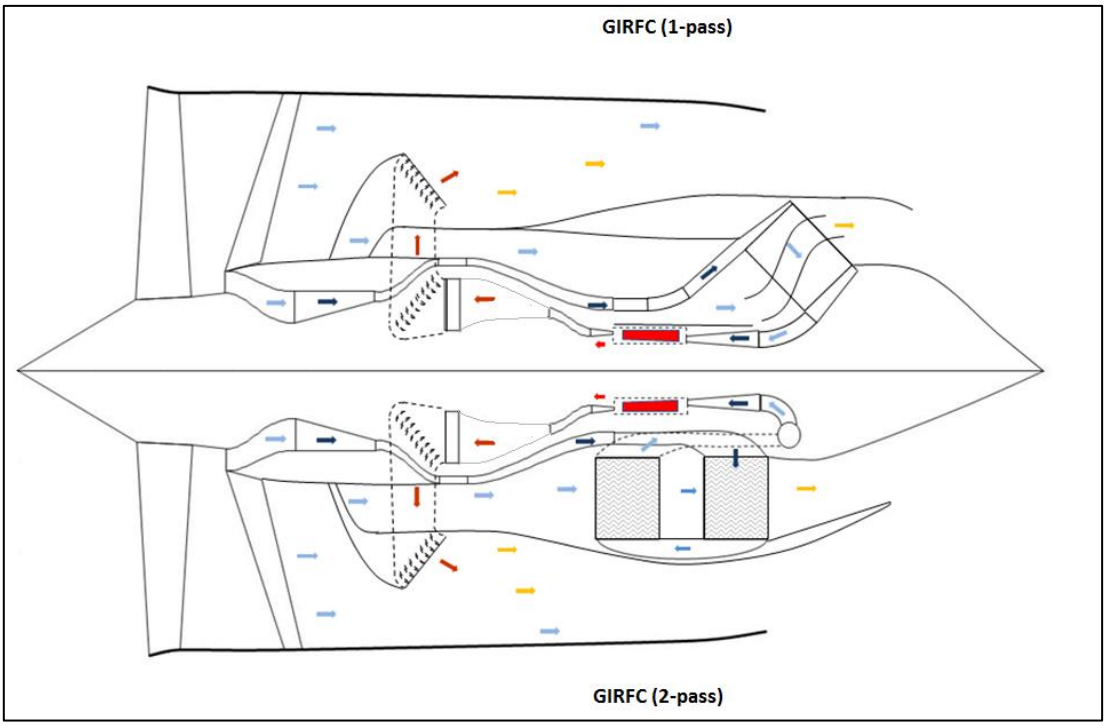

Figure 5.37 – GIRFC 1-pass and 2-pass Intercooler Configurations (Anselmi[1])

In this chapter, the evaluation of the design and performance of the intercooler module has been outlined. This evaluation allowed for the understanding of the main trade-offs in the implementation of this unit. Given this information a viable initial design was specified and integrated into the engine performance decks. Further performance studies incorporating the intercooler configuration are carried out in chapter 7 where the implication of intercooling on fuel burn and emissions is assessed.

[1] The author recognises the contribution of Eduardo Anselmi Palma, a PhD student at Cranfield University, who prepared the engine general arrangement shown in this figure. In his research Eduardo Anselmi Palma is investigating the mechanical arrangement and losses within the GIRFC concept.

6 Implication of Exhaust System Design

6.1 Nomenclature

ΔP/P	Loss in Total Pressure
A_{MC}/A_{TOC}	Nozzle Area Ratio (Mid-Cruise / Top-of-Climb)
BPR	Bypass Ratio
C_d	Discharge Coefficient
C_x	Specific Thrust Coefficient
FN	Net Thrust
FPR	Fan Tip Pressure Ratio
GIRFC	Geared Intercooled Reversed Flow Core Engine Concept
GISFC	Geared Intercooled Straight Flow Core Engine Concept
IPC	Intermediate Pressure Compressor
ISA	International Standard Atmosphere
LPT	Low Pressure Turbine
M	Mach Number
MC	Mid-Cruise
OPR	Overall Pressure Ratio
P_c/P_h	Ratio of Total Pressure in the Mixing Plane
PL/D	Perimeter x Length / Diameter of Mixing Chamber
PROOSIS	Propulsion Object Oriented Simulation Software
SFC	Specific Fuel Consumption
SFN	Specific Net Thrust
T_4	High Pressure Turbine Entry Temperature
TO	Take-Off
TOC	Top-of-Climb
TOD	Top-of-Descent
UEET	Ultra-Efficient Engine Technologies [14]
V_c/V_h	Jet Velocity Ratio

6.2 Introduction

The design of the GIRFC favours the use of a mixed exhaust system. Mixing of core and bypass streams can lead to a reduction in noise as well as gains in efficiency. Pressure losses in the mixer chute and entropy gain due to irreversibilities during mixing can, however, negate or reverse these benefits if care is not taken in the implementation of the mixer. Mixing of bypass and core streams can lead to fewer LPT stages through a reduction in FPR which is typical in a mixed flow engine. Both these aspects can contribute to a reduction in system weight. Yet a long cowl nacelle is often required to provide sufficient length for proper mixing which in itself can lead to significant weight additions. The GIRFC is unique as it allows for the mixing process to occur at a relatively forward position in the engine when compared with a typical arrangement. The bypass duct acts as the mixing chamber and must be carefully designed to minimise losses in the flows. This chapter evaluates the implication of the mixing process on the performance of the GIRFC when compared with the GISFC. In addition, these engine concepts make use of variable area nozzles for the control of the fan running line, and therefore a review of the performance of variable area nozzles is also given.

The features of the GIRFC are unique for a mixed flow engine and include a high BPR in excess of 10 as well as intercooling. The implication of these features is outlined in this chapter. The assessments carried within the scope of this research do not include detailed nacelle or mixing chamber design, and therefore a qualitative discussion is given to identify what implications these might have on the overall performance of the concepts. This chapter gives an overview of the characteritics and implications of a mixed flow exhaust. The importance and main performance characteritics of variable area bypass nozzles is also described. Finally, a performance evaluation and comparison is given for both design and off-design operation of the mixer and variable area nozzles.

6.3 Background

The exhaust system of the GIRFC includes an exhaust mixer for core and bypass streams. In addition, the cooling flow directed through the intercooler is ejected through a dedicated nozzle at the rear of the engine. The throat area of both mixed exhaust and intercooler cooling stream nozzles can be varied in order to improve the performance of the engine at off-design conditions. The implication of the variable area intercooler nozzle has already been explained in the previous section. Therefore, this chapter focuses mainly on the mixer and variable area bypass nozzle. This section provides some background which is intended to clarify the given design assumptions as well as to provide some theoretical foundation.

6.3.1 Exhaust Mixing Systems

In a mixed exhaust turbofan engine, the core stream is mixed with the bypass stream prior to ejection through a common nozzle. In a civil turbofan engine, a significant temperature ratio exists between the core and bypass streams where at the cruise condition the core stream can be as much as 2-3 times as hot as the bypass stream. The core stream is expanded to a relatively high velocity through a core nozzle. The high jet velocity of the core is detrimental to propulsive efficiency as well as a major source of noise. At the cruise condition the core nozzle is typically choked. The residual heat in the core exhaust is an unavoidable consequence of a practical Brayton cycle as well as being a function of the losses in the system. In a mixed flow engine, the waste heat is partly transferred to the bypass stream which for a realistic cycle can lead to a reduction in load and therefore losses across the fan and fan-turbine.

In a separate flow turbofan engine for a given fuel flow, BPR and fan mass flow rate, there exists an optimum bypass to core nozzle jet velocity ratio which will yield the maximum gross thrust. The ratio of bypass nozzle to core nozzle jet velocity is approximately equal to the transfer efficiency [68] and can be proven analytically for a simplified turbofan configuration which ignores the effects of duct losses. Guha [119] shows that the partial derivative of Equation (6.1) represents the condition for peak gross thrust. The partial derivative of Equation (6.2) represents the condition for minimum core energy. By equating these two derivatives as in

Equation (6.3), it is possible to find the optimum jet velocity ratio which as can be seen in Equation (6.4) is equal to the transfer efficiency.

$$F_N = \dot{m}_h\left(V_{j,h} - V_a\right) + B\dot{m}_h\left(V_{j,c} - V_a\right) \quad \textbf{(6.1)}$$

$$E_k = \frac{1}{2}\dot{m}_h\left(V_{j,h}^2 - V_a^2\right) + \frac{1}{2}\dot{m}_h\left({}^{B}/_{\eta_{KE}}\right)\left(V_{j,c}^2 - V_a^2\right) \quad \textbf{(6.2)}$$

$$\frac{\partial F_N}{\partial V_{j,h}} = \frac{\partial E_k}{\partial V_{j,h}} = 0 \quad \textbf{(6.3)}$$

$$\left({}^{V_{j,c}}/_{V_{j,h}}\right)_{op} = \eta_{KE} = \eta_{LPT}\eta_f\eta_{NB} \quad \textbf{(6.4)}$$

where:

- γ *ratio of specific heat capacities*
- η_f *fan efficiency*
- η_{KE} *transfer efficiency*
- η_{LPT} *LPT efficiency*
- η_{NB} *bypass nozzle efficiency*
- *c* *cold stream*
- *h* *hot stream*
- $\dot{m}$ *mass flow rate*
- op *optimum*
- *t* *static temperature*
- *B* *bypass ratio*
- E_k *flow kinetic energy*
- F_N *net thrust*
- V_a *flight speed*
- V_j *exhaust jet speed*

A common metric used in a mixed flow engine to determine the optimum jet velocity ratio in the mixing plane is the hot stream to cold stream ratio of total pressures. The optimum ratio of total pressures in the mixing plane is a function of the fundamental pressure losses in the mixing plane, the temperature ratio in the mixing plane and the transfer efficiency. A ratio approximately equal to unity typically yields the highest thrust for a given fuel flow [120] [121] [122]. The condition of equal total pressure in the mixing plane is also typically imposed so as not to

incur excessive off-design losses in the mixing process and so as to improve mixer stability across the operating envelope.

In the seminal work of Pearson [123], an ideal mixed flow exhaust is compared with a separate exhaust engine. Pearson [123] claims that if the efficiency of both the fan and fan-turbine are assumed to be ideal, at the condition of equal total pressures in the mixing plane there will be no thrust advantage for a mixed flow engine when compared with a separate flow engine. If ideal component efficiencies are assumed for a separate flow exhaust engine the optimum V_c/V_h will be equal to 1.0. The main advantage of a bypass engine with realistic component efficiencies is the lower SFN brought about by lower bypass jet velocity and higher mass flow which improves propulsive efficiency. Pearson [123] suggests that in a theoretical mixed exhaust jet engine, where mixing occurs at equal total pressures and zero speed in the mixing plane, no thrust advantage when compared with a separate flow exhaust engine can be achieved. By assuming that mixing occurs at zero speed, the mixing process does not suffer from any mixing losses due to momentum transfer between streams. If realistic component efficiencies are assumed, for equivalent total pressures in the mixing plane a distinct advantage can be obtained in the mixed flow case. Residual heat from the core exhaust will reduce the load across the fan and fan-turbine and hence reduce the pressure ratio and losses of each component. Pearson [123] states that the SFC superiority of a mixed exhaust is almost entirely due to the reduction in losses across these components.

Pearson [123] suggests that if a mixer is modelled as an ideal heat exchanger a thrust gain, when compared with a separate flow exhaust engine, can be obtained at a ratio of total pressure in excess of 1.0. This would occur as heat from the core stream would be transferred to the higher pressure bypass stream resulting in a useful energy gain. Although an ideal mixer can be modelled as an ideal heat exchanger, in a realistic mixer there are a number of effects which must be considered and which determine the efficacy of the design. The first loss which must be considered is fundamental to the mixing process itself. The loss represents a dissipation of kinetic energy proportional to the square of the difference of the velocities of the two streams [124]. Stratford and Williams [124] propose a formula, given in Equation (6.5), for estimating this

loss assuming incompressible flow relations, constant specific heat and equal static pressure in the mixing plane. This equation suggests that when the velocities in the mixing plane are equal, there will be no fundamental pressure loss as there is no dissipation of kinetic energy between streams. This is valid only for an incompressible flow but is a reasonable estimate for mixing at low Mach number. At equal total pressures in the mixing plane, the core velocity will exceed the bypass velocity and hence there will be a fundamental loss in pressure. At lower V_c/V_h the fundamental pressure loss will be even greater. An increase in BPR reduces the fundamental pressure loss as can be seen in Figure 6.1.

$$\frac{\Delta P}{q} = \frac{m(u-1)^2}{(1+m)(1+mu^2)} \qquad \textbf{(6.5)}$$

where:

- ΔP *fundamental pressure loss*
- q *dynamic pressure*
- m *ratio of cold stream to hot stream mass flow rates*
- u *ratio of cold stream to hot stream flow speeds*

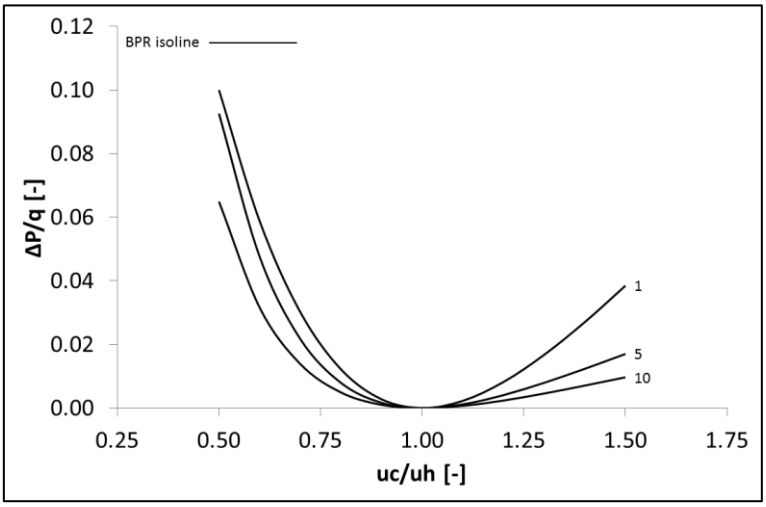

Figure 6.1 – Effect of V_c/V_h and BPR on Fundamental Pressure Loss

If ideal gases are assumed, enthalpy in the mixing process is constant while entropy increases which reduces the Gibbs free energy. This is not detrimental to engine efficiency as in a typical mixed turbofan no work is extracted from the common exhaust flow. Even assuming the composition of each fluid stream is identical, there will be an irreversible redistribution of internal energy due to the temperature difference between the flows. This is represented by the first

term on the right hand side of Equation (6.6) and of Equation (6.7). Under typical mixer conditions, the net result of these terms will be an increase in entropy. Taking into account the differences in mass flow rates, the increase in entropy due to the first term of Equation (6.7) will exceed the decrease in entropy from the first term of Equation (6.6). This increase in entropy will disappear as the temperatures of the two flows approach each other assuming equal static pressures.

There is also a difference in the fluid chemical composition of the core when compared with that of the bypass stream. The core side fluid contains the products of combustion while the bypass stream is air. The concentration of CO_2 in the core side is higher while that of O_2 is lower, and therefore the second term on the right hand side of Equation (6.6) and of Equation (6.7) must also be considered. In order to account for the entropy change due to the mixing of different gases the partial pressure of the individual constituents must be considered rather than the absolute pressure. Each of these terms will, therefore, always result in an increase in entropy as the partial pressures of the gases reduce as expansion into the mixing chamber occurs.

$$\Delta \dot{S_1} = q_{n1}\left(c_{p3}\, ln\frac{T_3}{T_1} - R_3\, ln\left(\frac{p_1'}{p}\right)\right) \qquad \textbf{(6.6)}$$

$$\Delta \dot{S_2} = q_{n2}\left(c_{p3}\, ln\frac{T_3}{T_2} - R_3\, ln\left(\frac{p_2'}{p}\right)\right) \qquad \textbf{(6.7)}$$

$$S_3 = \Delta \dot{S_1} + \Delta \dot{S_2} \qquad \textbf{(6.8)}$$

where:

- *1* — *unmixed hot stream*
- *2* — *unmixed cold stream*
- *3* — *mixed stream*
- c_{p3} — *molar heat capacity at constant pressure of mixed flow [J/(kmol K)]*
- p — *pressure [Pa]*
- p_i' — *partial pressure [Pa] (i = 1 or 2)*
- q_{ni} — *quantity flow [kmol / s] (i = 1 or 2)*
- $\dot{S}_i$ — *entropy flow [W/K] (i = 1, 2 or 3)*
- R_3 — *universal (molar) gas constant (J/(kmol K))*
- T_i — *temperature [K] (i = 1, 2 or 3)*

The gross thrust at the exit of the mixer exceeds that at the entrance of the mixer. The degree of thrust gain is a function of temperature ratio, Mach number as well as BPR [125]. A complete evaluation of the fundamental mixing equations is required to establish the gain that can be obtained from mixing core and bypass streams. Stratford and Williams [124] provide a simplified analysis of the mixing process, assuming equal total pressure in core and bypass streams, which can be used to understand some of the main influences. Stratford and Williams [124] suggest that Equation (6.9) and Equation (6.10) can be used to represent the gross thrust at the mixer exit and the thrust gain from mixing respectively. The thrust gain is with respect to the sum of the gross thrust at the hot and cold mixer entries rather than when compared with a properly configured separate flow exhaust engine. In this formula "f" refers to a function relating total to static conditions. In reality "f" is also a function of Mach number which is not the same at each mixer entry or at the mixer exit. However, for the purpose of simplification "f" can be assumed constant throughout and eliminated from the equation. Using Equation (6.11), it is possible to simplify Equation (6.10) further until a function dependant only on BPR and temperature ratio results. This is given in Equation (6.12). Figure 6.2 shows that gross thrust gain from mixing is increased as the temperature ratio between the two streams is increased. Also of interest is the fact that gross thrust peaks at low BPR while at higher BPR the gross thrust gain is substantially less.

$$M = m_3 {T_3}^{1/2} f \tag{6.9}$$

$$\Delta M = (m_1 + m_2){T_3}^{1/2} f - \left(m_1 {T_1}^{1/2} f + m_2 {T_2}^{1/2} f\right) \tag{6.10}$$

$$(m_1 + m_2)T_3 = m_1 T_1 + m_2 T_2 \tag{6.11}$$

$$\frac{\Delta M}{M} = 1 - \sqrt{\frac{T + m^2}{(1+m)(T+m)}} \tag{6.12}$$

where:

- *1,2* *unmixed streams*
- *3* *mixed stream*
- *ΔM* *gross thrust gain*
- *m* *mass flow ratio (m_2/m_1)*

- m_i *mass flow rate (i = 1, 2 or 3)*
- M *total gross thrust*
- T *temperature ratio (T_2/T_1)*
- T_i *total temperature (i = 1, 2 or 3)*

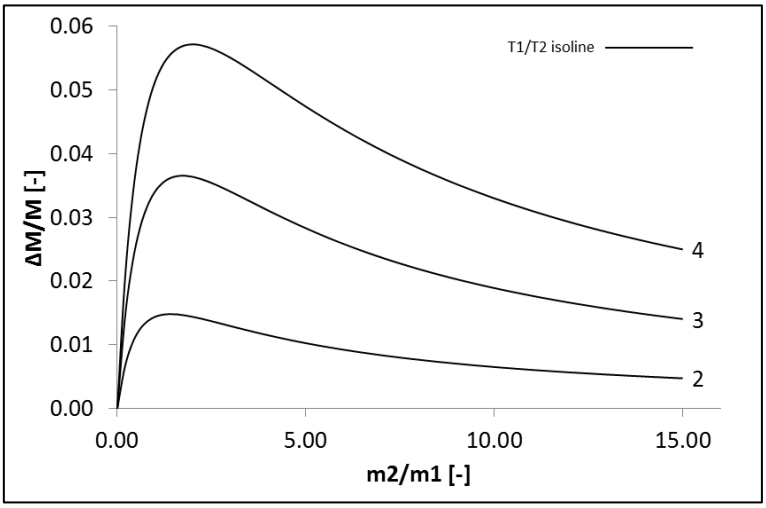

Figure 6.2 – Gross Thrust Gain from Simplified Mixing Correlation

It is difficult to interpret directly the implication of thrust gain on the overall engine performance. The thrust gain is measured with respect to the inlet of the mixer and not to an optimum separate flow configuration. The reduction of losses due to reduced fan and fan-turbine pressure ratio is not factored in here. Also as BPR is varied the FN of the engine will vary, even if the mixing thrust gain is ignored. In order to determine the benefit from mixing, an analysis taking all these factors into consideration is required.

The theoretical gain which can be achieved through mixing the core and bypass streams will in practice never be reached due to incomplete mixing of the flows. For complete mixing to occur, a mixing chamber of infinite length would be required. Mixing effectiveness, defined in Equation (6.13), is a measure of the degree of the theoretical mixing gain that can be achieved. In a real mixing chamber only a portion of the two flows entering the mixer will be mixed. Therefore, the exhaust nozzle will have three distinct streams passing through it. Specifically an unmixed core and bypass stream as well as a mixed stream.

$$\eta_{mixing} = \frac{F_{actual} - F_{unmixed}}{F_{mixed} - F_{unmixed}} \qquad \textbf{(6.13)}$$

where:

- η_{mixing} *mixing effectiveness*
- *F* *gross thrust*

There are several factors which determine the level of mixing effectiveness. Frost [122] carried out a number of experimental tests on axial chute, injection chute and annular mixer designs in order to study the mixing effectiveness and chute loss characteristics. Based on his experiments, Frost [122] proposed a simplified correlation for mixer effectiveness. This correlation is illustrated in Figure 6.3 and relates mixing effectiveness to an area interface function. This function is dependent on the length and diameter of the mixing chamber as well as the perimeter of the mixer interface. From this function it is clear that as the mixing chamber length is increased, the mixing effectiveness increases as a greater distance is allowed for the mixing process to occur. Mixing effectiveness will reduce with mixing chamber diameter for a given length and mixer perimeter. This is expected as the bypass mass flow rate, will increase quadratically with diameter while for a given perimeter, the core flow will remain the same leading to a greater quantity of bypass flow which is unmixed. The perimeter of the mixer is also critical in determining mixer performance. As the perimeter increases, the interface between the hot and cold flows increases, which increases the quantity of eddies at the mixing interface leading to better mixing.

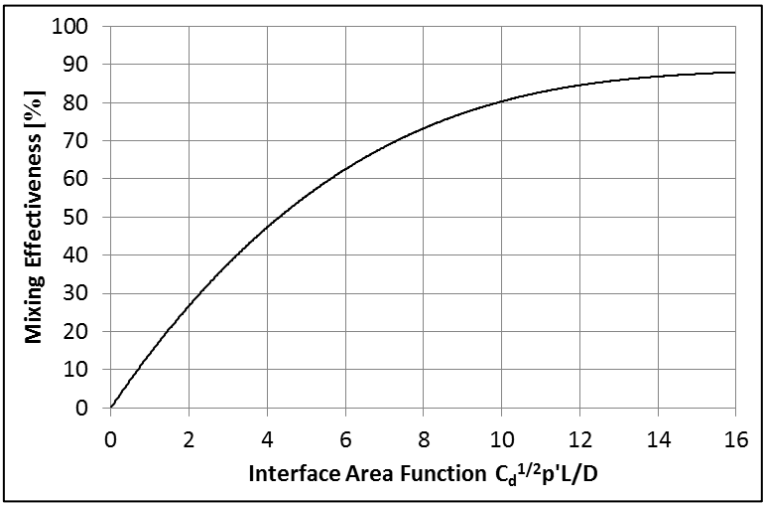

Figure 6.3 – Mixer Effectiveness Correlation (adapted from Frost [122])

Clearly, there are a number of additional losses associated with the design of the mixer. In order to achieve adequate mixing a long mixing chamber is often required which due to skin friction contributes to significant head loss. Corrugated chutes are also often used with annular mixers which again increase the mixer surface area and hence losses. Frost [122] also suggests that skin friction coefficient can vary considerably based on the design of the mixer. Injection mixers have an additional loss which is due to the radial momentum of the flow at the mixer exit. Frost [122] proposes a simplified chute loss correlation based on experimental work and it is useful for understanding the general trends in mixer design. The relationship, illustrated in Figure 6.4, includes all the loss components. However, reasonable estimates typically require the use of other more complex methods such as in Hurley et al. [126] or experimental investigations such as in Cullom et al. [127]. This typically entails detailed design work and is difficult to obtain at the conceptual design stage.

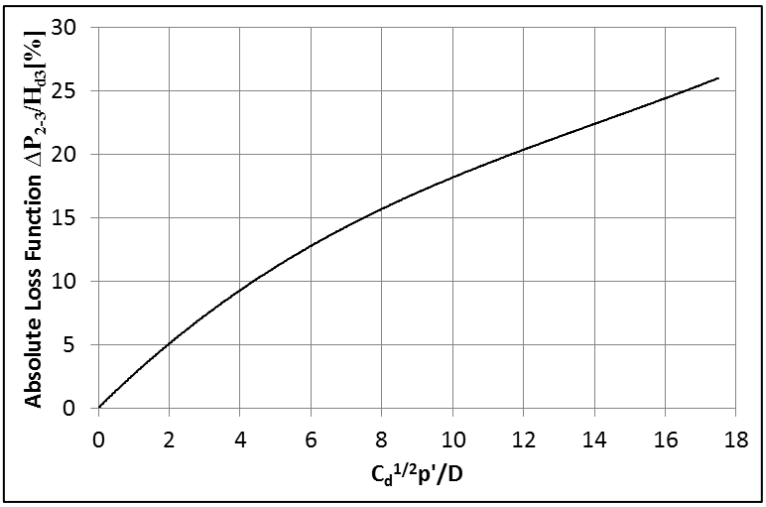

Figure 6.4 – Chute Loss Correlation (adapted from Frost [122])

6.3.2 Variable Area Bypass Nozzles

The throat area of a propulsive nozzle is typically established at a single design condition. While appropriate for this condition, at off-design, the overall engine performance can benefit from the variation of the nozzle throat area if several technical challenges can be overcome. The nozzle area, for a given inlet total temperature and pressure establishes the nozzle mass flow rate. A change in nozzle area, assuming a fixed mass flow rate, total temperature and pressure, will result in a change in back pressure if the nozzle is choked. An increase in nozzle area, under

the specified conditions, will result in a reduction in back pressure or pressure at the nozzle throat, which for a convergent nozzle is the nozzle exit. As the back pressure falls there will be an increase in the pressure difference from the fan exit to the bypass nozzle throat which will drive an increase in mass flow rate.

The fan running line is strongly affected by the variation in bypass nozzle area. For a given fan FPR, there will be an increase in fan flow capacity as the nozzle area is increased. This is represented by a shift in the operating line of the fan. Michel [128] provides a comprehensive list of the advantages of using a variable bypass nozzle. Perhaps the main advantages are:

a. The control of the fan running line position can allow for operation at regions of higher efficiency on the fan characteristic map.
b. In a separate flow exhaust engine, increasing the bypass mass flow for a given thrust allows for higher BPRs to be achieved. Therefore, for a lower SFN higher propulsive efficiency can be achieved. In a common flow exhaust engine an increase in nozzle area will affect both core and bypass flows.
c. Improved fan and propulsive efficiency can lead to lower turbine entry temperatures at the take-off condition.
d. Increasing the nozzle area will displace the fan running line away from surge. Surge margin can be a problem especially for high BPR engines which characteristically have quite shallow running lines. Zimbrick [129] suggests that for FPRs below 1.45 either variable area nozzles or variable fan geometry would be required.
e. Increasing nozzle area can allow for lower specific thrust at take-off as well as during the departure and approach phases. Experimental investigation of a sub-scale nozzle by Mabe [130] demonstrated the potential of variable area nozzles to significantly reduce noise although the given setup was not tested on an in-flight engine.

Variable area nozzles have been considered in several research papers and reports [65] [131] [132]. Daggett et al [133] outline some of the main considerations in the Ultra-Efficient Engine Technology (UEET) project [14] in which both Pratt and Whitney and General Electric engines were participants. A selection of the concepts evaluated is given in Table 6.1. Interestingly the

GE58-F2 B5 and STF1173 both had FPR approaching 1.45 but did not include a variable area nozzle. Only the STF1174 with a significantly higher BPR and an FPR of 1.32 considered the use of a variable bypass nozzle. Although it is likely that each concept would have benefitted from a variable bypass nozzle, the complexity and weight of such a system is a hindrance to its implementation. In the STF1174, a petal design was considered for the nozzle which is typical for this type of engine concept. A description of petal type variable nozzles can be found in Kurzke [73]. This type of nozzle typically suffers from leakage losses as a consequence of the spacing between adjacent petals. Pera et al. [134] suggest that a variable nozzle can weigh up to 2.75 times more than a conventional nozzle. However, nozzle weight estimation is quite specific to the nozzle design considered as well as the mechanisms required for varying the area.

	GE 90-94B	**PW 4090**	**GE 58-F2 B5**	**PW STF 1173**	**PW STF 1174**
Fan Diameter (in)	123	112.9	123.5	127.9	148.7
BPR	7.8	6.2	13.1	14.3	21.5
FPR	1.46	1.6	1.45	1.45	1.25

Table 6.1 – Main Specifications of UEET Concepts and Baselines [133]

Nozzle performance is typically described using a number of different performance coefficients. In this work a specific thrust coefficient (C_X) and a discharge coefficient (C_D) are used. C_D is the ratio of the effective to the geometric throat area while the C_X is the ratio of the effective specific thrust to ideal specific thrust. C_X reduces the nozzle gross thrust in order to account for viscous effects. C_D and C_X are dependent on nozzle pressure ratio as well as nozzle geometry. It is typical to adjust the nozzle coefficients based on the petal angle of the nozzle which in the case of a variable area nozzle is not fixed.

6.4 Methodology

The investigations carried out within this chapter deal with design point and off-design performance. In order to carry out the studies, engine performance models were constructed within the commercial engine simulation package “PROOSIS”. The standard mixer model from “PROOSIS” turbo-library was implemented. The mixer component assumes:

a. Conservation of mass flow, energy and momentum across the system boundaries.
b. No work or heat transfer across the system boundaries.
c. Equal static pressures and a fixed cold flow Mach number at the mixer entrance in order to determine the inlet and outlet flow areas.
d. Fixed inlet and outlet areas at off-design conditions.

A detailed design of the nacelle, mixer and exhaust nozzles does not form part of this thesis. Further design work regarding the dimensions and performance of these components was carried out in a separate unpublished study[1]. The mixing chamber of the GIRFC is an atypical arrangement similar to that of the Garrett ATF3 as explained in chapter 2. The main characteristics of the mixed exhaust and mixing chamber are the following:

a. The mixing chamber begins far upstream in the bypass duct. The reversed flow core arrangement re-introduces the core exhaust into the bypass stream at the interface between the IPC and LPT exit.
b. The core exhaust is discharged into the bypass stream through a number of discrete chutes. The separate chutes enable the cross-over ducting which is present in both the GIRFC and Garrett ATF3.
c. The core exhaust chutes rotate the flow through 180 degrees in order to align the core flow with bypass flow. The turning in the duct would most likely need a number of guide vanes to reduce separation at the bends.

[1] The mixing chamber model, effectiveness and losses were established by Eduardo Anselmi Palma, a PhD student at Cranfield University, and Andrew M. Rolt, a Senior Systems Specialist at Rolls-Royce plc. Their contribution is kindly acknowledged.

d. In practice, the core exhaust chutes would need to be encased by aerodynamically efficient fairings in order to reduce losses in the bypass stream.

e. Long cowl nacelles are typically required for mixed flow engines in order to provide for sufficient mixing chamber length. As the core flow enters the bypass flow so far upstream, the bypass duct need not be made much longer in order to maintain high effectiveness.

The mixer characteristics given in Table 6.2 were established in a separate study. The mixer effectiveness was calculated based on the relationships given by Frost [122] as shown in Figure 6.3. The loss estimations were based on typical skin friction factors, aerodynamic form factors for typical fairings and standard minor tube loss correlations.

Parameter	**Value**
PL/D^2 [-]	8
$\Delta P/P_{cold}$ [%]	0.3
$\Delta P/P_{hot}$ [%]	1.0
Mixer Effectiveness [%]	80

Table 6.2 – Mixing Chamber Characteristics

The nozzle calculations have also been carried out using the standard components from “PROOSIS”. For the studies in chapters 4 to 6 only three nozzle settings have been assumed corresponding to take-off, TOC (design), and cruise. The studies carried out in this and the subsequent sections rely to some extent on the geometry and the performance of these components. In order to cater for uncertainty, a rigorous sensitivity analysis has been carried out. This highlights the implication of size, weight and performance uncertainties on the final result so that the current results can be scaled given a more rigorous analysis of these components.

6.5 Evaluation

6.5.1 Selection of FPR, BPR and SFN

The configuration and sizing of the fan is very important for the performance and weight of an engine concept. In this section, only the uninstalled engine performance is explored at both the design and off-design conditions. In chapter 7, a full analysis of the engine concepts then takes into consideration the weight of the fan and other engine components. In a high BPR engine the fan provides most of the thrust while the main function of the core is to drive the fan. Therefore, it is essential that the fan and associated parameters be properly configured for the given design.

Characteristics at Fixed Fuel Flow Level

Guha [119] and Oates [135] claim that the FPR is largely dependent on SFN and only weakly affected by BPR. This relationship is even stronger for a mixed flow exhaust engine than for a separate flow exhaust engine [119]. This is true for both GISFC and GIRFC engines assuming that the designs are evaluated for a fixed fuel flow. In order to demonstrate this relationship, a constant fuel flow of 1.0 kg/s has been assumed while the mass flow through the fan has been varied between 420 kg/s and 600 kg/s at each BPR_{TOC}. In these estimations the $P_c/P_{h,TOC}$ for the GIRFC has been assumed to be equal to 1.04 (approximately equal to the optimum in terms of SFC for a mixing effectiveness of 0.8) while the $V_c/V_{h,TOC}$ for the GISFC has been assumed equal to the transfer efficiency. A fixed OPR_{TOC} of 80 has been assumed throughout. The results of the analysis are presented in Figure 6.5 and Figure 6.6. As suggested by Guha [119], the relationship between SFN and FPR is much stronger than between BPR and FPR. The FPR of the GISFC and the GIRFC is independent of the BPR for a large range of SFN. This analysis suggests that FPR can be selected somewhat independently of BPR for a given SFN. It also shows that it is the reduction in SFN which is driving a reduction in FPR rather than an increase in BPR. As expected, the GIRFC whose exhaust is mixed exhibits a lower FPR for a given SFN when compared with the GISFC whose exhaust is unmixed.

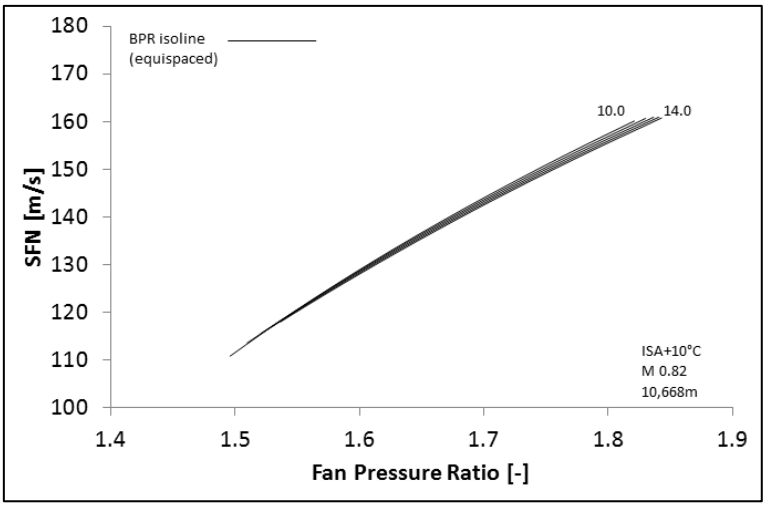

Figure 6.5 – SFN_{TOC} vs. FPR_{TOC} for the GISFC Engine (Fixed Fuel Flow)

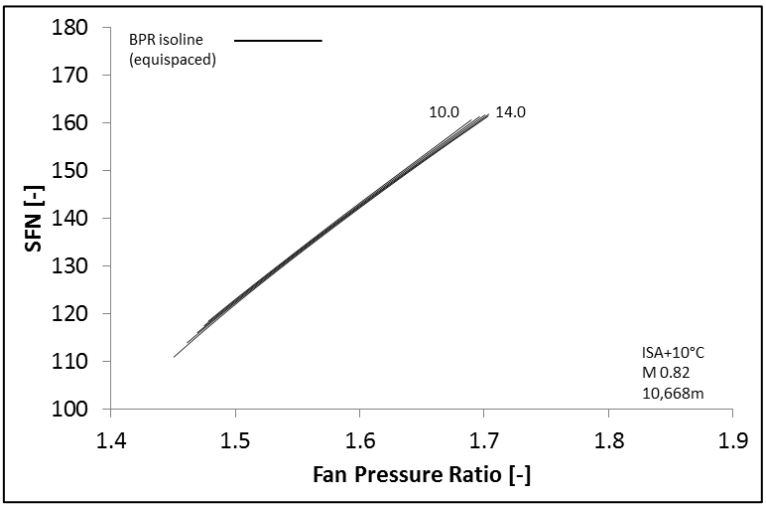

Figure 6.6 – SFN_{TOC} vs. FPR_{TOC} for the GIRFC Engine (Fixed Fuel Flow)

As the fan mass flow rate is varied, given the assumption of fixed fuel flow, the engine FN and T_4 will also vary as demonstrated in Figure 6.7 for the GISFC and in Figure 6.8 for the GIRFC. For a given BPR, T_4 decreases as the fan mass flow rate is increased. This is due to an increase in core mass flow, which for a given fuel flow and OPR results in a reduction in the temperature rise across the combustor. Similarly for a given fan mass flow rate and OPR, an increase in BPR leads to a reduction in core mass flow and an increase in the temperature rise across the combustor and thus an increase in T_4.

In both Figure 6.7 and Figure 6.8 the locus of optimum SFC is defined which for a fixed fuel flow coincides with the locus of maximum FN. Propulsive efficiency increases as fan mass flow rate

increases while SFN and FPR reduce. In order to maximise FN, BPR must increase as SFN decreases. Higher BPR is enabled by an increase in bypass mass flow rate but also by a decrease in core mass flow rate. To reduce the core mass flow rate, T_4 must be increased which also helps to maintain high thermal efficiency. For a given fuel flow and T_4 limit there is a unique optimum FN, fan mass flow rate and BPR. Therefore, for a given fuel flow, decreasing SFN should ideally be accompanied by an increase in T_4 which allows for an increase in BPR. To design the cycle for a fixed FN the fuel flow, which has been assumed constant in this case, must be adjusted.

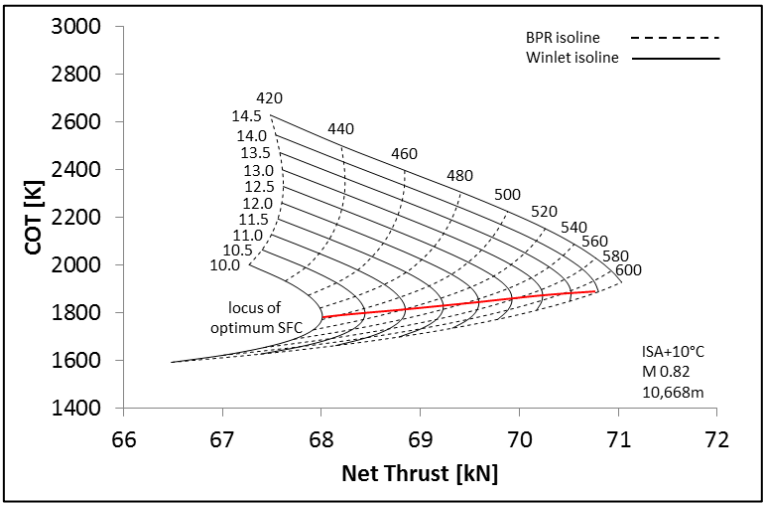

Figure 6.7 – $T_{4,TOC}$ vs. FN_{TOC} for the GISFC Engine (Fixed Fuel Flow)

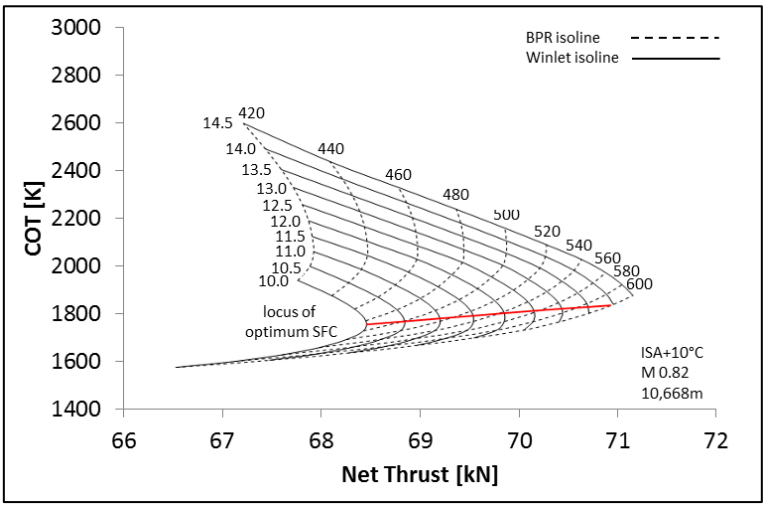

Figure 6.8 – $T_{4,TOC}$ vs. FN_{TOC} for the GIRFC Engine (Fixed Fuel Flow)

Characteristics at Fixed Thrust and T_4 Levels

The material thermal limits of the turbine nozzle guide vanes and blades limit the maximum T_4 in the combustor. In this project a $T_{4,TOC}$ of 1920K has been selected as a reasonable target for the GIRFC and GISFC engines. Given that the aircraft characteristics set the thrust requirement, it is also sensible to fix the engine design thrust level to match this level. This, of course, assumes that the aircraft thrust requirements are not scaled to account for reduced fuel burn and hence reduced take-off weight. If the FN and T_4 are fixed, for a given BPR and FPR, the fuel flow rate and fan mass flow rate will be unique. As for the fixed fuel flow case, an optimum FPR exists for minimum SFC for both GISFC and GIRFC.

Figure 6.9 and Figure 6.10 show the relationship between SFN and FPR across a range of BPRs. The sensitivity towards P_c/P_h and V_c/V_h is also shown. As for the previous case, SFN varies almost linearly with FPR and can be selected quite easily. The conditions outlined previously, namely that the GIRFC P_c/P_h will approach 1.0 at the optimum and that the GISFC will approach the transfer efficiency at the optimum, are still valid for these conditions. BPR, on the other hand, varies quite differently in this case. Figure 6.9 shows that the variation in SFN with FPR for a given BPR is far less than for the previous case. The root cause of this difference is that now fuel flow is being adjusted to maintain a constant thrust. The adjustment of fuel flow and concurrently fan mass flow results in less variation of SFN. Typically, we associate low SFN with higher efficiency. In this case, higher efficiency means that less fuel is required. For a fixed OPR and T_4 the combustor available temperature rise is also fixed. If fuel flow is reduced for a given BPR, the core and hence overall mass flow must be reduced leading to higher SFN. Therefore, the locus of minimum SFC coincides with the point of maximum SFN. The trends in Figure 6.9 for the GISFC are reflected for the GIRFC in Figure 6.10.

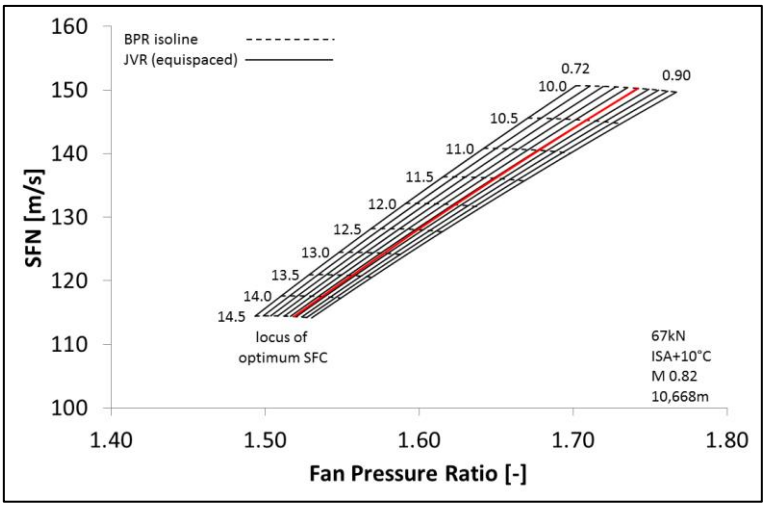

Figure 6.9 – SFN_{TOC} vs. FPR_{TOC} for GISFC (Fixed FN_{TOC} and $T_{4,TOC}$)

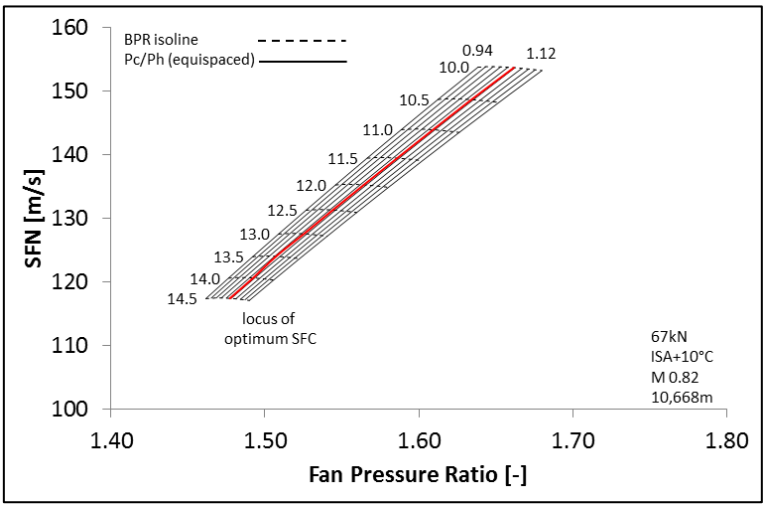

Figure 6.10 – SFN_{TOC} vs. FPR_{TOC} for GIRFC (Fixed FN_{TOC} and $T_{4,TOC}$)

Figure 6.11 and Figure 6.12 show the relationship between SFC and FPR across a range of BPRs. The characteristics shown here are much the same as for the previous charts. In this study, the polytropic efficiencies of the fan and fan-turbine have been assumed constant. For the GIRFC, the locus of optimum SFC occurs at a P_c/P_h of approximately 1.04 while for the GISFC, the optimum V_c/V_h is approximately 0.83. Clearly, these figures are applicable only to TOC. The optimum at TOC is not necessarily the optimum at the cruise condition which represents the majority of the flight. Even the characteristics at cruise change significantly between TOC and TOD. This is investigated in chapter 7.

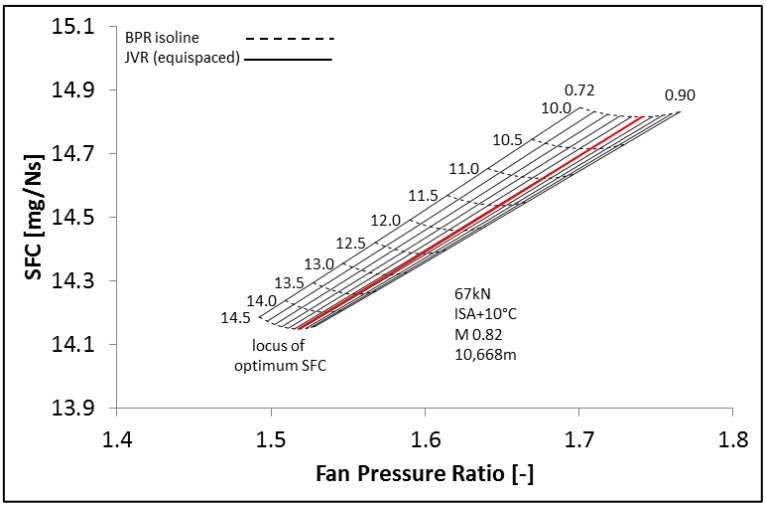

Figure 6.11 – SFC_{TOC} vs. FPR_{TOC} for GISFC (Fixed FN_{TOC} and $T_{4,TOC}$)

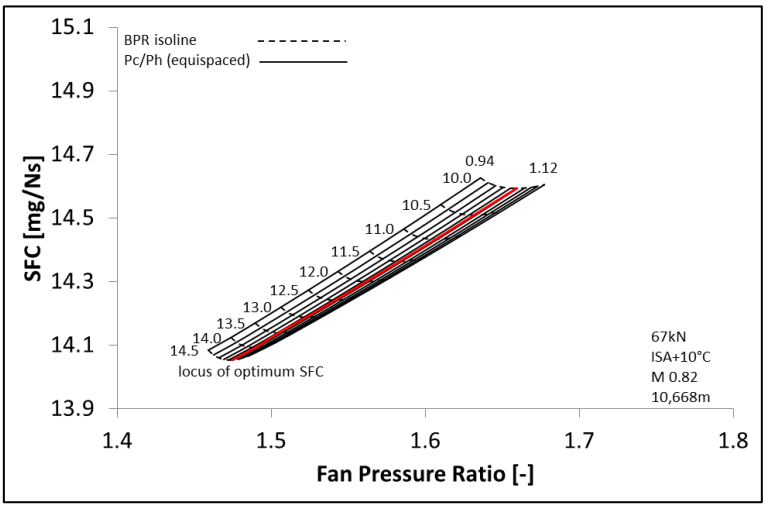

Figure 6.12 – SFC_{TOC} vs. FPR_{TOC} for GIRFC (Fixed FN_{TOC} and $T_{4,TOC}$)

The GIRFC was envisaged as a high BPR concept especially when compared with the norm for mixed flow engines. Therefore, it is relevant to consider whether mixing can still offer any thrust gain advantage. Figure 6.13 shows the relationship between the ideal mixing gain and BPR for the GIRFC. It is clear that as BPR increases there is a steady decline in mixing gross thrust gain. At BPR 14.5 the gross thrust gain is a mere 1%. This suggests that the benefit of mixing should be reduced at higher BPR.

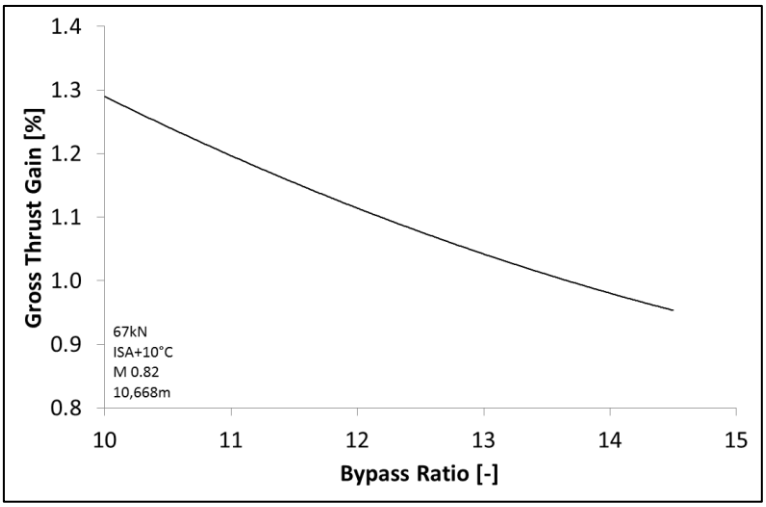

Figure 6.13 – Implication of BPR on Thrust Gain Due to Mixing

6.5.2 Implication of Mixing Effectiveness

Mixing effectiveness affects the overall efficiency of the cycle. Figure 6.14 relates SFC with FPR for different levels of mixing effectiveness and P_c/P_h. Mixing effectiveness represents a non-ideality in the system, and therefore the SFC of the GIRFC improves as the mixing effectiveness of the cycle is increased. Of more interest is the relationship between FPR and P_c/P_h in the mixing plane at different levels of effectiveness. It can be seen in Figure 6.14 that as the mixing effectiveness is increased to unity the P_c/P_h also tends to unity. The FPR in a mixed flow engine tends to be lower than for a separate flow exhaust. Higher levels of mixing effectiveness maximise this effect. This characteristic is typical for a mixed configuration and has been widely reported [122] [123]. As mixing effectiveness is reduced the ideal P_c/P_h in the mixing plane also reduces and FPR increases. As mixing effectiveness is reduced the V_c/V_h at the entry to the mixing plane increases and at zero mixing effectiveness the V_c/V_h becomes more consistent with the V_c/V_h of a separate flow engine.

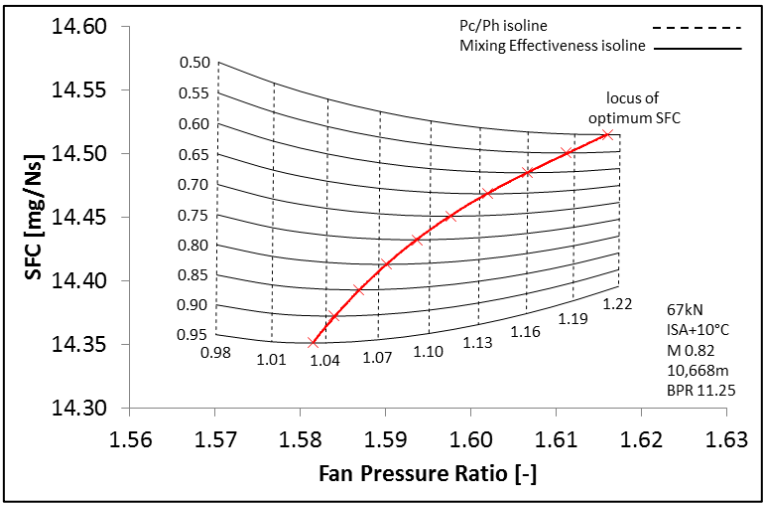

Figure 6.14 – Influence of Mixing Effectiveness on SFC_{TOC} and $P_c/P_{h,TOC}$

6.5.3 Selection of Mixing Mach Number

As stated previously, the mixing Mach number has an important effect upon the thrust gain as well as the fundamental pressure loss in the mixer. As the core Mach number is increased for a given P_c/P_h, the bypass Mach number will increase linearly. As the core Mach number increases for a given P_c/P_h, the velocity ratio in the mixing plane tends to diverge which increases the fundamental pressure loss. Therefore, it is advantageous to increase P_c/P_h and FPR when increasing the core Mach number so as to increase the bypass Mach number more rapidly and hence reduce the velocity divergence. Clearly, as P_c/P_h is increased the temperature ratio between the flows is reduced which reduces the thrust gain and increases the fan and fan-turbine pressure ratios and losses. Nevertheless, the optimum P_c/P_h increases as the Mach number increases as can be seen in Figure 6.15. The ratio of optimum bypass to core Mach number is almost constant across the given range. As can be seen in Figure 6.16 in order to minimise SFC it is clearly advantageous to reduce the mixing Mach numbers as far as possible. However, low mixing Mach numbers result in a large mixer cross-sectional area. For stability at off-design conditions it is also best to keep the mixing Mach numbers in the region of 0.4 to 0.5.

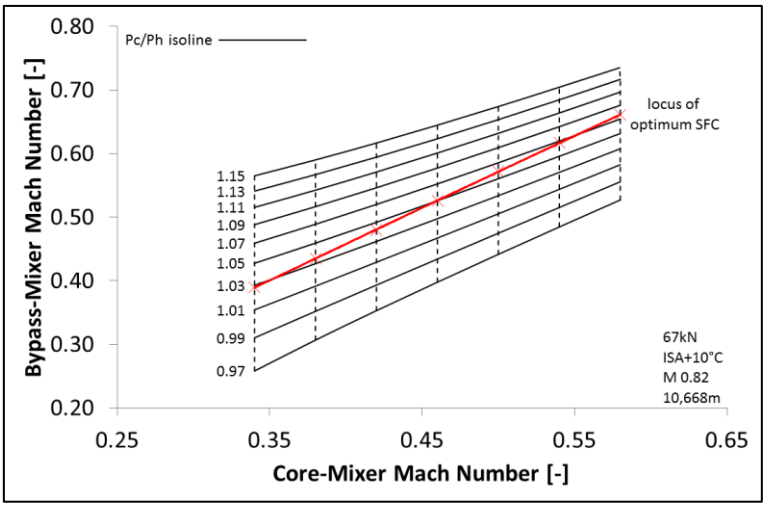

Figure 6.15 – Optimum Mixer Inlet Mach Numbers

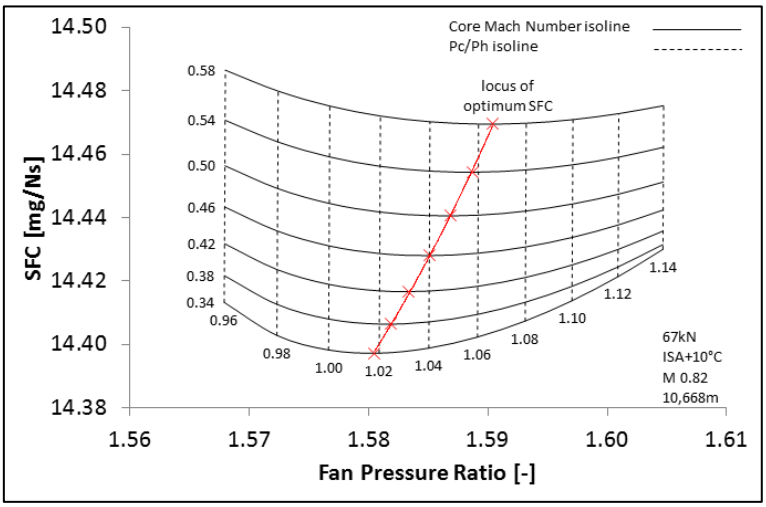

Figure 6.16 – Effect of Mixing Mach Number on SFC_{TOC}

6.5.4 Influence of Mixed Exhaust on Fan Running Line

At cruise conditions the bypass nozzle of a separate flow exhaust engine is typically choked over a large range of its operation. The running line of the fan is quite steep during cruise. For a mixed flow exhaust engine the common nozzle is also choked at most cruise conditions. In this case, however, the working line is even steeper. In a separate flow exhaust the corrected flow at the outlet of the fan is constant when the bypass nozzle is choked, but the choked mixed nozzle is fed from both core and bypass streams. Therefore, it is the combined effect of both streams which leads to choking at the nozzle. As a mixed flow engine is throttled back the core

pressure ratio falls off rapidly leading to a reduction in corrected flow. The corrected flow at the fan outlet thus increases up to the choking condition at the nozzle and therefore the fan inlet corrected flow does not fall as rapidly as for the separate flow exhaust. This characteristic can cause the fan running line to approach the locus of maximum efficiency on the fan map which can lead to improved SFC_{MC}. A variable bypass nozzle can also be used to alter the fan running line. This is evaluated in the next section. Yet, the characteristic shown in Figure 6.17 does suggest that the GIRFC would benefit less from bypass nozzle variation at cruise than would the GISFC.

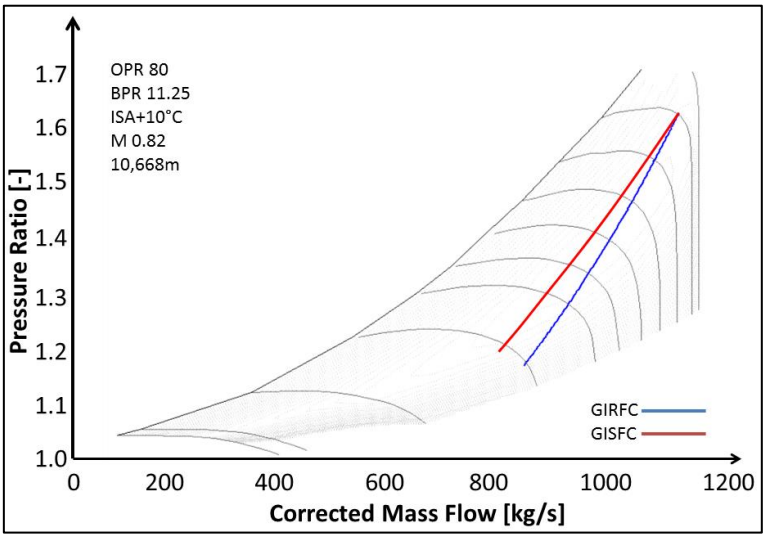

Figure 6.17 – GIRFC vs. GISFC Fan Running Line (Cruise Condition)

6.5.5 Influence of Bypass Variable Area Nozzle

Operation at Mid-Cruise

The bypass variable area nozzle also allows for optimisation of SFC_{MC}. Typically, the optimum cruise bypass nozzle area in terms of SFC_{MC} is larger than for TOC. An increase in bypass nozzle area shifts the fan running line away from surge. This allows for operation of the fan closer to the best efficiency locus on the fan map. As thrust is reduced from the TOC setting to the mid-cruise setting there is a reduction in T_4, in fan speed as well as in fan mass flow rate. The core mass flow falls off more quickly than the bypass mass flow rate leading to an increase

in BPR_{MC}. Increasing the fan nozzle area at cruise allows for even higher fan mass flow rate and a further decrease in SFN which is beneficial as well to propulsive efficiency.

The improvement in SFC_{MC} cannot be sustained even though the bypass mass flow rate continues to increase as the nozzle area is opened further. First of all, for a given fan diameter, a higher bypass mass flow rate will result in higher flow speeds in the bypass duct which leads to higher losses. Secondly, the actual fan running line will eventually overshoot the locus of best efficiency on the fan map. Therefore, the fan efficiency starts to decline at a very high nozzle aperture. In a practical sense it is also highly unlikely that a bypass nozzle area should be allowed to increase considerably as the complexity and weight of the mechanism would be excessive.

Figure 6.18 shows the effect of a variable cruise nozzle on the GISFC SFC_{MC} while Figure 6.19 shows the same relationship but for the GIRFC. It is apparent that the GIRFC optimum increase nozzle area is less than that for the GISFC. The characteristics of the fan running line for a mixed flow engine have already been outlined. Essentially, the GIRFC engine fan running line is steeper than for the GISFC due to the effects of the mixed exhaust. Therefore, a smaller change in fan running line brought about by variation of the bypass nozzle area is required to reach the optimum. The mixed flow engine therefore benefits less from a variable nozzle than does the GISFC and for this reason could possibly be excluded in order to reduce complexity, weight and cost.

Figure 6.20 shows the effect of two step changes in A_{MC}/A_{TOC} on the running line of the GISFC. It is clear that initially a large increase in fan nozzle area is required so that the fan working line can approach the best efficiency locus on the fan map. However, at low power settings where the fan speed and corrected flow are quite low, the required shift in the running line starts to reduce. This suggests that during descent, where thrust is close to the idle setting, a smaller change in nozzle area could be desirable.

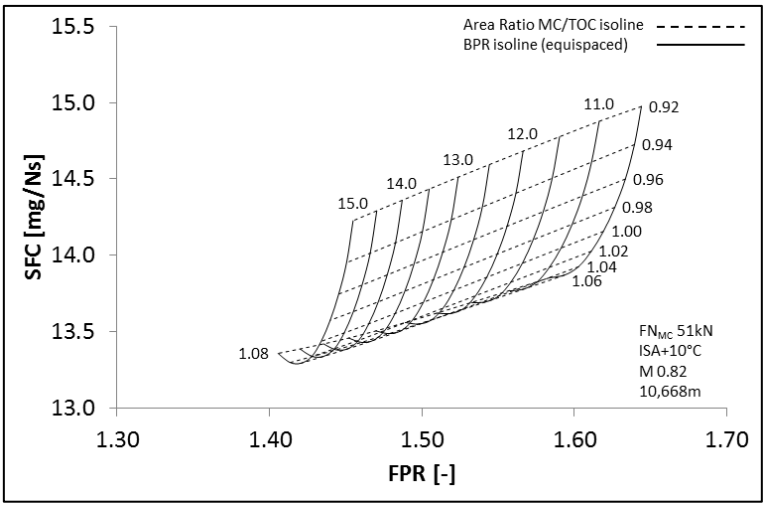

Figure 6.18 – Effect of Variable Bypass Nozzle Geometry on SFC_{MC} (GISFC)

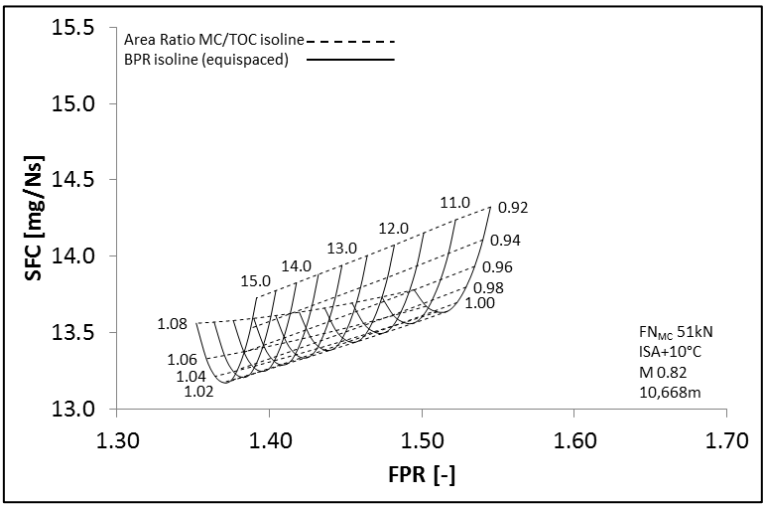

Figure 6.19 – Effect of Variable Bypass Nozzle Geometry on SFC_{MC} (GIRFC)

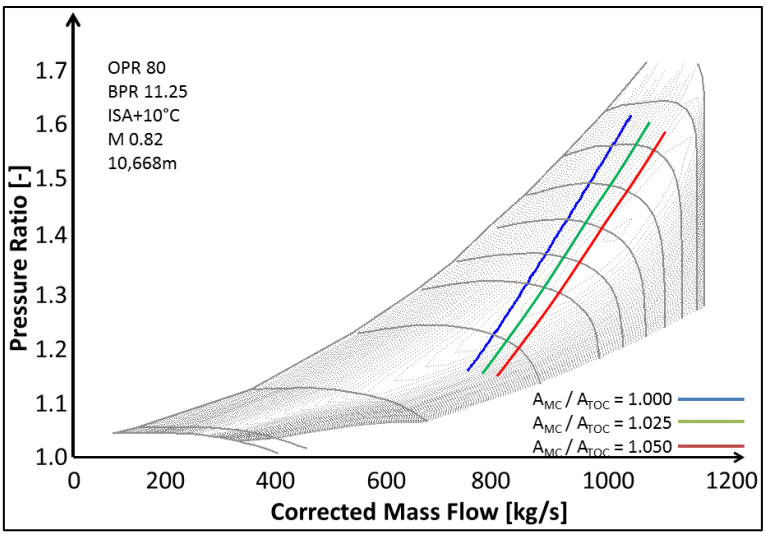

Figure 6.20 – Effect of Variable Bypass Nozzle Geometry on SFC_{MC} (GISFC)

Operation at Take-Off

Low SFN designs offer an additional benefit aside from improved propulsive efficiency. For a fixed FN_{TO} and FN_{TOC}, the $T_{4,TO}$ for a low SFN engine is lower than for a high SFN engine. For a fixed $T_{4,TO}$ and FN_{TOC}, the FN_{TO} for a low SFN engine is higher than for a high SFN engine. This relationship is illustrated in Figure 6.21 where the effect of BPR_{TOC} on FN_{TO} is explored for a fixed $T_{4,TO}$. In Figure 6.21, the BPR_{TOC} is increased from 10.5 to 15.0 for a fixed FN_{TOC} while retaining an optimum $P_c/P_{h,TOC}$ which results in a decrease in SFN_{TOC}. The thrust lapse rate with speed is larger for the low SFN designs meaning that the thrust benefit is not retained in cruise.

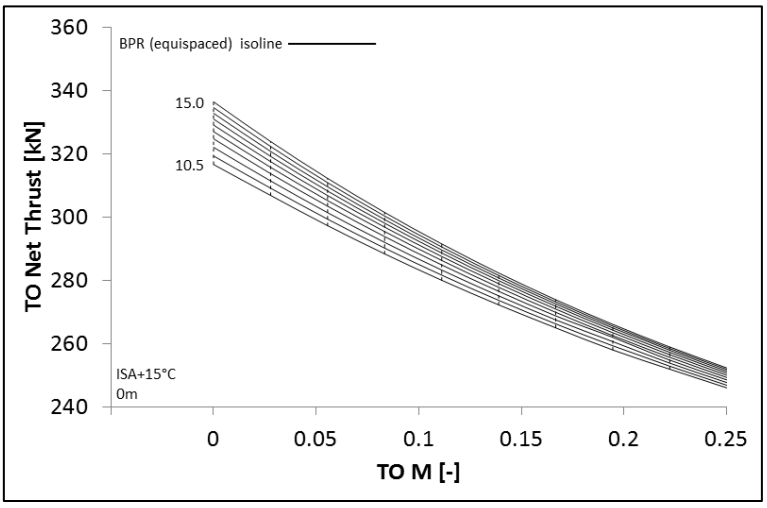

Figure 6.21 – Thrust Lapse at Varying Levels of BPR_{TOC}

An increase in bypass nozzle area can lead to a significant reduction in the required $T_{4,TO}$ as can be seen in Figure 6.22 for the GISFC and Figure 6.23 for the GIRFC. Two factors affect the $T_{4,TO}$ for a given FN_{TO}; core mass flow rate and efficiency. As can be seen in Figure 6.24, SFC_{TO} is minimised at area ratios between 1.03 and 1.10. At lower efficiency, more fuel flow is required which for a fixed core mass flow rate would result in higher T_4. However, as the bypass nozzle is opened further, the core and bypass mass flow continue to increase which helps to offset the increase in T_4. However, there is a limit beyond which the drop in efficiency becomes dominant and the T_4 starts to increase with increasing area ratio. The GISFC and the GIRFC exhibit very similar behaviour at take-off with similar reductions in T_4 with increasing nozzle area ratio. In this work, a T_4 limit of 1970K has been assumed throughout the work. This suggests that a nozzle area ratio of 1.04 for the GIRFC and 1.05 for the GISFC could be suitable for limiting the $T_{4,TO}$.

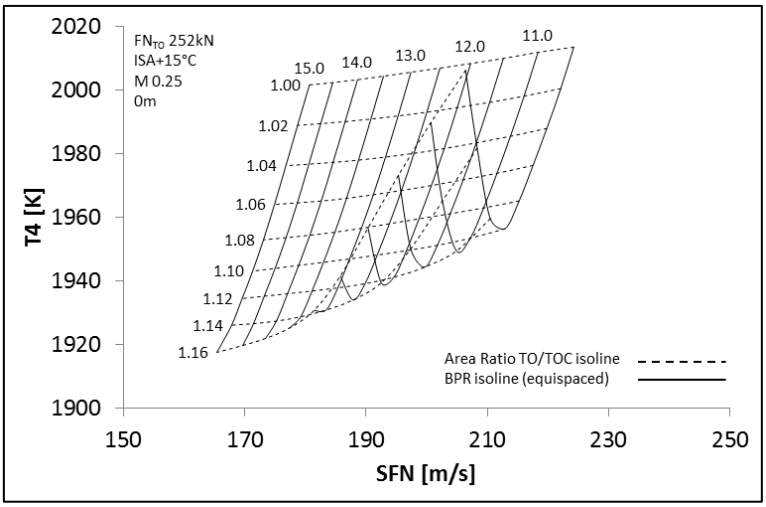

Figure 6.22 – Effect of Variable Bypass Nozzle Area on $T_{4,TO}$ (GISFC)

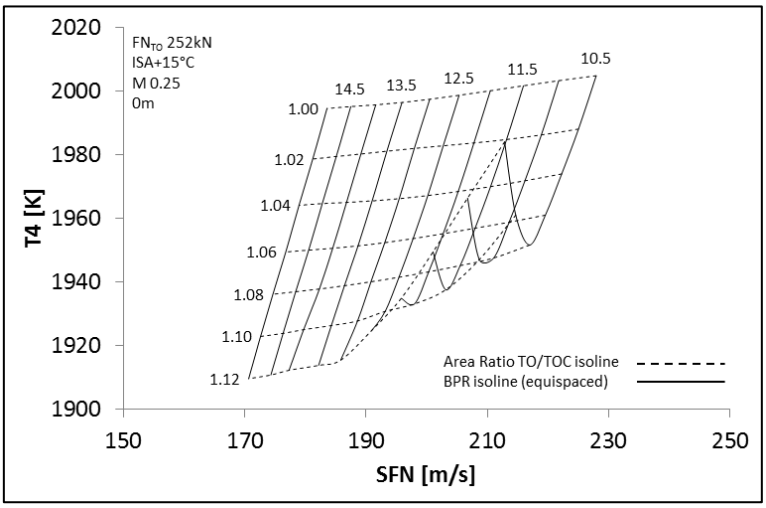

Figure 6.23 – Effect Of Variable Bypass Nozzle Area On $T_{4,TO}$ (GIRFC)

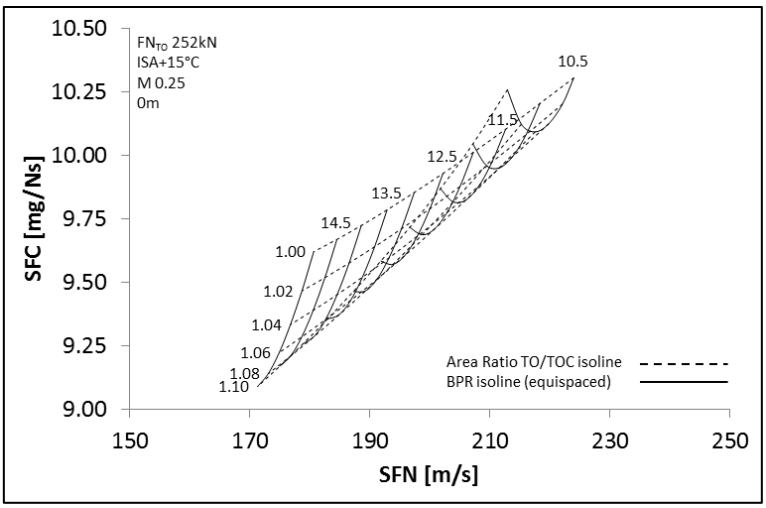

Figure 6.24 – Effect of Variable Bypass Nozzle Area on SFC_{TO} (GISFC)

6.6 Discussion and Conclusion

In this chapter, a comparison was made between the performance of the GISFC and GIRFC exhaust systems. The GIRFC incorporates a mixed exhaust and common flow bypass nozzle while the GISFC incorporates separate core and bypass nozzles. A mixed exhaust can provide a useful SFC improvement by reducing the load and therefore the losses across the fan and fan turbine. However, mixing pressure losses as well as higher parasitic losses due to the size and shape of the mixing chamber can reduce the benefits. The GIRFC is able to achieve a high mixing effectiveness with lower skin friction penalties than a conventional mixed flow engine as the mixer chutes are positioned far upstream in the bypass duct which serves as the mixing chamber, although the mixer chutes which impinge into the flow do introduce additional drag elements. The results of a separate study[1] suggest that for the GIRFC a mixing effectiveness of 0.8 could be achievable whilst maintaining reasonable bypass duct dimensions.

Variable area bypass nozzles allow the position of the fan running line to be shifted for both the GIRFC and GISFC concepts. Fan working line control allows for surge control and a useful reduction in $T_{4,TO}$ and also fan operation at improved efficiency across the entire flight envelope. The fan working line of the GIRFC is steeper due to the effects of exhaust mixing. A steeper working line is advantageous as it lies further from the surge line at take-off and closer to the locus of optimum efficiency at cruise. As a result, the GIRFC requires comparatively less bypass nozzle area variability suggesting that a simpler bypass nozzle could be considered. Although a fixed nozzle could perhaps be considered for the GIRFC, the consequent increase in T_4 would necessitate a larger intercooler which would add complexity and weight. A variable area bypass nozzle is preferable as the reduction in intercooler size is critical. Also a variable area bypass nozzle allows for a small reduction in SFC_{MC}.

[1] The mixing chamber model, effectiveness and losses were established by Eduardo Anselmi Palma, a PhD student at Cranfield University, and Andrew M. Rolt, a Senior Systems Specialist at Rolls-Royce plc. Their contribution is kindly acknowledged.

7 Evaluation and Optimisation of Concepts

7.1 Nomenclature

ΔP/P	Loss in Total Pressure
ε	Intercooler Effectiveness
A_{MC}/A_{TOC}	Nozzle Area Ratio (Mid-Cruise / Top-of-Climb)
A_{TO}/A_{TOC}	Nozzle Area Ratio (Take-Off / Top-of-Climb)
BPR	Bypass Ratio
CAEP	Committee on Aviation Environmental Protection
Dp/Foo	Units of Mass of Pollutant per Unit Thrust (g/kN)
$EINO_x$	NO_x Emission Index
EOR	End of Runway
FAR	Fuel-to-Air Ratio
FN	Net Thrust
FPR	Fan Tip Pressure Ratio
GIRFC	Geared Intercooled Reversed Flow Core Engine Concept
GISFC	Geared Intercooled Straight Flow Core Engine Concept
GTICLR	Long Range Intercooled Geared Turbofan
HP	High Pressure
HPC	High Pressure Compressor
HPT	High Pressure Turbine
IC	Intercooler
ICAO	International Civil Aviation Organization
IPC	Intermediate Pressure Compressor
IPCC	Intergovernmental Panel on Climate Change
IPT	Intermediate Pressure Turbine
ISA	International Standard Atmosphere
L/D	Lift to Drag Ratio
LDI	Lean Direct Injection
LEMCOTEC	Low Emission Core Engine Technologies
LP	Low Pressure
LPT	Low Pressure Turbine
LTO	Landing and Take-Off Cycle
M	Mach Number
MC	Mid-Cruise
NO_x	Nitrogen Oxides
OPR	Overall Pressure Ratio
P_3	Combustor Entry Pressure
P_c/P_h	Ratio of Total Pressure in the Mixing Plane
PR	Pressure Ratio
SFC	Specific Fuel Consumption
SFN	Specific Net Thrust

T_3	Combustor Entry Temperature
T_4	High Pressure Turbine Entry Temperature
TERA	Techno-Economic and Environmental Risk Analysis
TO	Take-Off
TOC	Top-of-Climb
TOD	Top-of-Descent
VAN	Variable Area Nozzle
V_c/V_h	Jet Velocity Ratio
W_c/W_h	Intercooler Cold Mass Flow to Hot Core Mass Flow Ratio

7.2 Introduction

In the previous chapters, several design features of the GISFC and GIRFC concepts were studied. However, the overall performance of the GISFC and GIRFC concepts were only loosely treated. Some reference has been made to the specific fuel consumption of each concept and how this is affected by the placement and configuration of the HP-spool, intercooler and exhaust system. Yet these components do not exist in isolation and for a good comparison to be made, each arrangement must be properly configured taking into account the special characteristics of each design. The objective of this chapter is, therefore, to make a fair comparison between the baseline TF2000, the GISFC and the GIRFC based primarily on the evaluation of mission block fuel burn which is directly proportional to the quantity of CO_2 emissions. In addition, some consideration is given to specific secondary emissions namely LTO and mission NO_x as well as contrails.

This chapter incorporates a number of novel studies including:

a. The evaluation of the block fuel burn characteristics of the TF2000, GISFC and GIRFC configurations based upon the initial specifications.
b. The optimisation of the GISFC and GIRFC cycles and the TF2000, GISFC and GIRFC cruise operation (including altitude selection and variable area nozzle control strategy) for minimum block fuel burn.
c. The optimisation of the TF2000, GISFC and GIRFC cruise operation (including altitude selection and variable area nozzle control strategy) for minimum absolute NO_x, minimum weighted NO_x and minimum persistent contrail emissions.

The organisation of this chapter is as follows: A comparison is made between the baseline TF2000 and the initial GISFC and GIRFC concepts. The objective of this comparison is to establish the performance of each engine concept prior to optimisation and to highlight differences in block fuel burn, LTO and weighted NO_x emissions, and contrails emissions. Since the GISFC and GIRFC do differ somewhat in their designs, an optimisation exercise is presented next so as to establish the limits of each design. This allows for a more justified

evaluation of the mission block fuel burn and emissions levels of each concept. In order to characterise the uncertainty in the designs a number of sensitivity studies were carried out for the GISFC and GIRFC which suggest how the design might be affected if changes to the underlying assumptions were to be made. A Monte Carlo uncertainty analysis is presented in order to suggest how the overall performance of each design might be affected by the design uncertainties. While this analysis is inherently subjective it does provide an indication of the perceived confidence in the results as well as the overall performance implications of design uncertainty. Two levels of uncertainty are presented so as to provide a confidence range rather than an absolute figure.

The aforementioned optimisations assume the minimisation of block fuel burn as the primary objective. Subsequent studies presented in this chapter focus on secondary emission types specifically NO_x and contrails. The engine cycle is not re-optimised for the reduction of cruise NO_x or contrail emissions as the value of such a strategy is limited. Therefore, without changing the cycle characteristics, different control strategies and flight profiles are then assessed for the minimisation of cruise NO_x and contrails.

7.3 Background

The focus of aero-engine optimisation is typically the minimisation of block fuel burn, LTO NO_x and noise emissions. As discussed in chapter 2, these represent the economic interests and legislative obligations of the operator and so are of major concern to the manufacturer. Although an in depth treatment of noise for this class of engines could certainly be of interest, the development of the tools and methods necessary for a proper evaluation of this emission type are outside the scope of this dissertation. Block fuel burn and LTO NO_x emissions are however treated in this chapter.

LTO NO_x emissions as well as low altitude ozone formation can be detrimental to health due to respiratory impairment, as well as to the environment, due to vegetation damage and acid rain. Aircraft are however unique as they emit NO_x pollutants also at high altitude. The IPCC [6] recognises that tropospheric NO_x alters the chemical composition of the atmosphere through

changes to tropospheric concentrations of ozone (O_3) and methane (CH_4). There is some ambiguity as to the effect of these species on global warming. Indeed, even the underlying chemistry is not fully understood which has led to much scientific research into the area. Faber et al. [136] describe some of the chemical principles underlying the relevant tropospheric reactions. Sausen et al. [137], in an update to the IPCC report on climate change [6], claim that O_3 leads to positive radiative forcing while CH_4 leads to negative radiative forcing as can be seen in Figure 7.1. The degree to which ozone (O_3) and methane (CH_4) contribute to global warming and how this relates to CO_2 is difficult to judge as the lifetime, reaction rates and distribution of the different species can be quite different and can lead to different local and global effects. Regional non-uniformities do however play an important and as yet not fully understood role. Detailed atmospheric circulation and chemistry modelling and emission metrics are beyond the scope of this study and would require a dedicated treatise. Rather this work is limited to providing an indication of how different design choices can affect NO_x emissions without assessing their larger environmental impact.

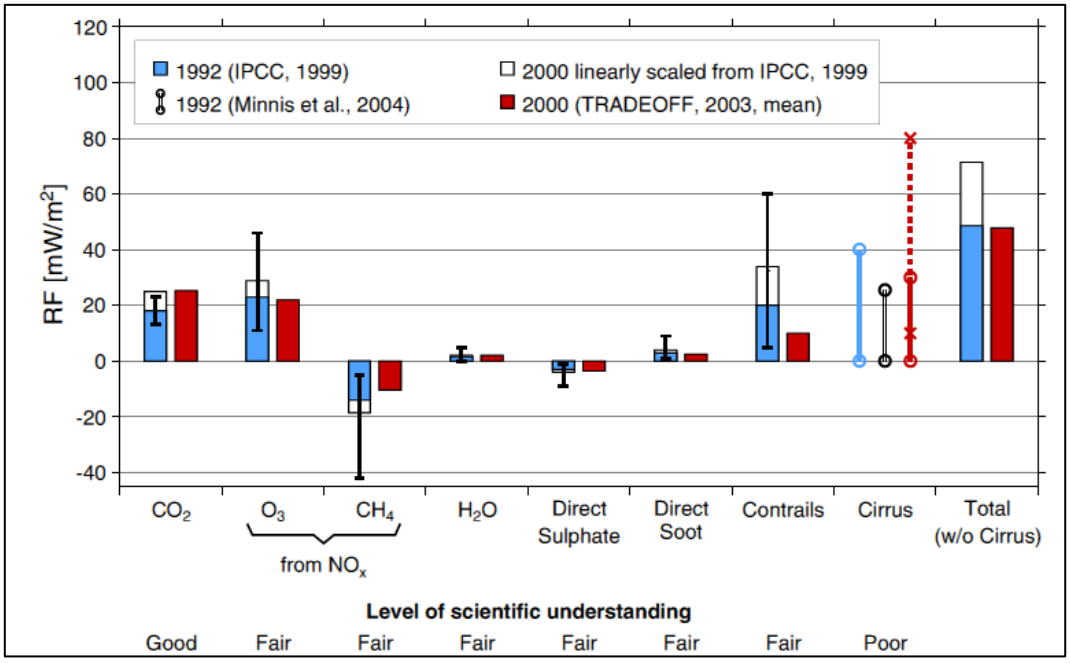

Figure 7.1 – Radiative Forcing from Aviation (from Sausen [137])

The aforementioned reports [6] [137] have also highlighted the importance of contrails on global warming. Contrails or condensation trails are thin line-shaped ice clouds [138] that, under the

right conditions, form in the wake of an aircraft. Contrails form when water vapour in the exhaust plume becomes supersaturated [139] [140]. Particulate emissions and to some extent particles in the atmosphere serve as condensation nuclei leading to the formation of ice or mixed-phase clouds. Without these condensation nuclei water vapour would exist in a supercooled state down to about 235K below which spontaneous freezing would occur [141]. Two types of contrails can be formed; persistent contrails that evaporate only after some hours and non-persistent contrails that evaporate almost immediately [138]. Persistent contrails can only exist in an environment which is supersaturated with respect to a surface of ice but subsaturated with respect to a surface of water. Given these conditions, in a mixed-phase cloud water droplets rapidly evaporate while on the other hand, ice-particles tend to grow through vapour deposition. Clearly, persistent contrails are of main concern as the effects of non-persistent contrails are short lived. Schuman [139] also points out that there are two sources of contrails. Those, as already described, that are engine related but also aerodynamic contrails caused by the pressure drop and near adiabatic cooling that occurs over an aircraft wing. As aerodynamic contrails do not persist in the atmosphere they are not considered in this dissertation.

Contrails are believed to reflect incoming solar radiation which leads to negative radiative forcing. On the other hand, contrails are believed to trap outgoing long-wave radiation emitted from the Earth and atmosphere which leads to a positive radiative forcing. It is believed that contrails lead to a net warming of the atmosphere as is demonstrated in Figure 7.1. Understanding the net effect of contrails is also a difficult proposition. Contrails emissions can persist in the atmosphere for hours. In addition, depending on regional weather conditions, linear contrails cover can spread over vast expanses. For this reason, a good understanding of upper air weather patterns is necessary for understanding the global effect of contrails. While no attempt has been made to understand the global effect of contrail emissions the research presented focusses on how the given concepts could encourage the formation of contrails.

7.4 Methodology

The performance of the integrated engine and aircraft was evaluated over a typical long range mission for an A330 type aircraft. The main mission phases include the taxi, take-off, initial climb, en-route, final descent and landing phases. The aircraft block fuel typically includes the taxi fuel, trip fuel, contingency fuel, alternate fuel, final fuel reserve, additional fuel and extra fuel. The relevant fuel planning parameters are given in Table 7.1 and are based on European Commission Regulation (EC) No 8/2008 [142]. No extra fuel has been assumed while the trip fuel is calculated through an iterative procedure which determines the actual fuel burn based upon the engine performance at each mission phase. The main mission range and cruise speed are defined in Table 7.1. The baseline trajectory is also presented in Figure 7.2.

Parameter	Unit	Value
Taxi Time	min	20
Contingency Fuel / Trip Fuel	%	5
Final Reserve Fuel (240kts, 1500ft)	min	30
Additional Fuel (240kts, 1500ft)	min	15
Range	km	5543
Cruise Speed	M	0.82

Table 7.1 – Mission Planning Assumptions

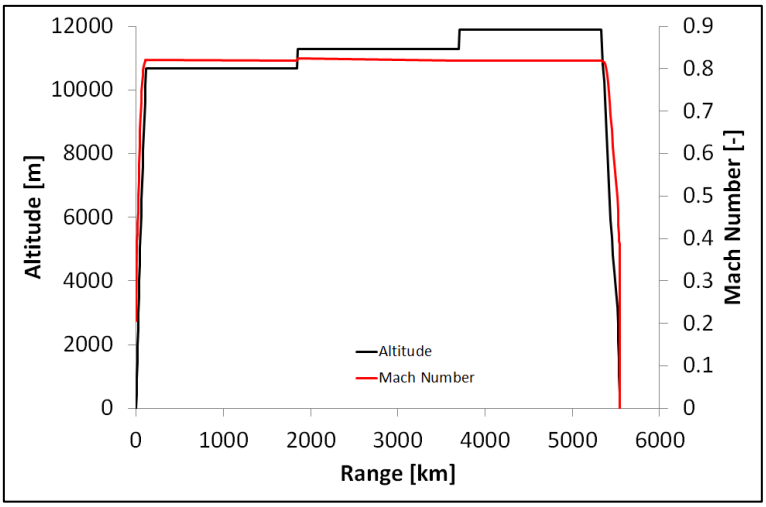

Figure 7.2 – Baseline Trajectory

TOC was assumed to correspond to the engine primary design point. The conditions at TOC are equivalent to the maximum climb rating in Table 7.2. The Take-Off (EOR) point was also

used to check the $T_{4,TO}$. The $T_{4,TOC}$ was assumed equal to 1920K while the $T_{4,TO}$ (both static and EOR) was limited to 1970K. The T_4 limits ensure that the material integrity of the hot section is not compromised. The mid-cruise point is used only for comparison and the engine is optimised based on the entire mission performance. The mid-cruise condition is, however, fairly representative of the mission as a whole and is, therefore, a useful reference point. The customer bleed flow and power offtake at 10668m were assumed to be 1.85 lb/s and 123 kW respectively. At take-off, zero customer bleed and 157kW of power offtake were assumed. The turbine cooling bleed flows were scaled from previous designs in order to maintain similar metal temperatures. The ICAO ratings are used to obtain data for LTO emission prediction. The ICAO 100% thrust is equivalent to the FN_{TO} at standstill and ISA+15°C. This is assumed to occur at the same T_4 as the EOR condition. Further details regarding the aircraft performance model are presented in Appendix B.

Thrust Rating	**Altitude [m]**	**Mach [-]**	**∆ISA [°C]**	**Thrust [lbf]**
Take-Off (End-of-Runway)	0	0.25	15	56670
Maximum Climb	10668	0.82	10	15140
Mid-Cruise	10668	0.82	10	14290
ICAO 100%	0	0	0	$1.00xTO_{static}$
ICAO 85%	0	0	0	$0.85xTO_{static}$
ICAO 30%	0	0	0	$0.30xTO_{static}$
ICAO 7%	0	0	0	$0.07xTO_{static}$

Table 7.2 – Engine Thrust Ratings

Mission block fuel burn and CO_2 emissions can be readily estimated from the thrust, time and SFC profiles of the engine aircraft system. A CO_2 emission index of 3.19kg CO_2 / kg fuel can be used to estimate the block CO_2 emissions of the aircraft. Predicting NO_x emissions is considerably more difficult. NO_x emissions, as stated previously, can be divided into two distinct categories; LTO NO_x emissions and cruise NO_x emissions. Typical LTO NO_x values can be obtained for existing aero-engines from the ICAO emissions databank [(28)]. In order to estimate the LTO emission factor given in the emission databank, the engine is tested at the sea-level thrust settings as suggested in Table 7.2. The thrust settings are representative of take-off (0.7mins), climb (2.2mins), approach (4.0mins) and taxi/ground idle (26mins). The final value of

LTO NO_x emissions is then factored up based on the number of engine tests carried out where a higher number of tests increases confidence and results in a lower correction factor. While this method is useful for understanding the emission potential of existing aero-engines at set points it does not allow for the estimation of NO_x emissions at other conditions or for other engines. Chandrasekaran and Guha [143] outline the main options available for the prediction of NO_x emissions and suggest that these fall under five main categories, specifically:

a. Correlation based methods.
b. P_3-T_3 methods.
c. Fuel-flow methods.
d. Simplified physics models.
e. High fidelity simulations.

There are inherent advantages and disadvantages to each technique. In the absence of empirical data, simplified physics models and high fidelity simulations are perhaps the most accurate of the simulation techniques. These techniques are, however, complex, computationally expensive, time consuming and require detailed proprietary knowledge of the combustor geometry and flow characteristics. This level of fidelity is inappropriate and impractical for the research carried out within the scope of this dissertation which relies mainly on data available only at the conceptual design stage. On the other hand fuel-flow methods as well as the P_3-T_3 method rely upon reference data typically sourced from the ICAO emissions databank [28] for the estimation of NO_x emissions. Two common fuel flow methods are the Boeing fuel-flow method 2 [144], and the DLR fuel-flow methods [145]. Chandrasekaran and Guha [143] as well as Norman et al. [146] suggest that fuel flow methods are perhaps the most easily implemented method for estimating cruise NO_x as they rely on only external parameters such as ambient temperature and pressure as well as Mach number which are then used to correct reference $EINO_x$ values estimated at reference conditions. Nonetheless, Norman et al. [146] suggest that comparison of fuel flow method predictions with tests carried out in an altitude facility for a conventional combustor suggest a 10% scatter in the predicted results. These predictions are even less suitable for other combustor types.

The P_3-T_3 method is similar to the fuel flow methods in that it corrects reference NO_x values taken at reference conditions. However, the corrections are carried out based on reference values at the inlet to the combustor; specifically the P_3, T_3 and humidity values. The corrections rely on a number of exponents. These exponents are combustor specific and can only be established through testing of the combustor in question. As a result, the application of the P_3-T_3 method is significantly more challenging than the fuel-flow methods. Norman et al. [146] suggest that in the absence of actual information regarding the combustor in question, a standard set of exponents can be assumed. Without manufacturer data it is difficult to ascertain which method, fuel-flow or P_3-T_3, will give the most reasonable results. Certainly, with good knowledge of the exponents the P_3-T_3 should provide a better estimate. Additional details regarding the P_3-T_3 method and its implementation can be found in Appendix E.

Another major problem with the implementation of the P_3-T_3 method is the reliance upon reference values from the ICAO databank [28]. While for the TF2000 the reference values for the Trent 700 can be assumed, this is certainly not the case for the GISFC or GIRFC. Correlation based methods provide a possible solution to this problem. Typically, such methods rely on a characteristic equation or set of equations which are derived from empirical data obtained through combustor testing. Correlation based equations typically incorporate a number of variables related to the conditions at the entry to or within the combustor such as P_3, T_3 or FAR to mention but a few. Chandrasekaran and Guha [143] as well as Tsalavoutas et al. [147] provide a detailed comparison of several common methods available in literature. Of course, the main problem with all of these methods is that they are combustor specific. If the combustor type is changed than the methods are no longer applicable. For this reason Tsalavoutas et al. [147] show that there is a large dispersion in the predictions which can be obtained from these types of methods. Tsalavoutas et al. [147] do suggest a method for correcting these correlation types for the specific combustor in question. However, scaling the correlations as suggested by Tsalavoutas et al. [147] requires specific combustor test data which is not typically available in the public domain. The GISFC and GIRFC incorporate an LDI combustor. NO_x emissions from LDI combustors have been investigated in NEWAC [12] by Calantuoni et al. [148] as well as separately by NASA [149] [150] [151] [152]. In NEWAC [12] a correlation for predicting LDI emissions was

proposed, as suggested in Kyprianidis [52]. This correlation is however proprietary and could only been used for validation. The correlation from NASA [152] is the only widely published empirically derived characteristic and was investigated in the context of the NASA Ultra Efficient Engine Technology Project [149]. Based on the capabilities of the available methods, the absolute NO_x emissions have been calculated in the following way:

a. The reference LTO NO_x emissions at the given ICAO thrust levels for the TF2000 have been assumed equal to those listed in the ICAO emission databank [28].
b. The reference LTO NO_x emissions at the given ICAO thrust levels for the GISFC and GIRFC have been estimated using the NASA [152] correlation.
c. Cruise NO_x emissions have been estimated using the P_3-T_3 method. Given the uncertainty in the selection of the pressure exponent, two exponent levels have been selected; 0.4 and 0.2. The former corresponds to a typical combustor characteristic while the latter corresponds to a lean burning combustor (although not necessarily an LDI combustor).

Unlike LTO NO_x, cruise NO_x can have serious consequences for global warming. As already alluded to in the previous section, cruise NO_x can result in a positive radiative forcing. However, the altitude at which the cruise NO_x is emitted is a major factor in determining the severity of the given NO_x emission. It is quite difficult to gauge the radiative forcing impact of NO_x emissions at different altitudes. Eurocontrol [153] suggests that a series of weighting factors can be applied at different altitudes. These weighting factors, adapted from the work of Köhler et al. [154], can be applied to the absolute NO_x value at the corresponding altitude in order to have a better appreciation of the severity of the NO_x emissions for a single flight. The overall weighted NO_x emissions level calculated through such an exercise is not a measure of radiative forcing but rather a basis for comparing the impact of distinct flights. Therefore, in this study the cruise NO_x is estimated in three steps. First the LTO NO_x is estimated. The P_3-T_3 method is then used to estimate the absolute NO_x for each flight segment. Finally, the weighting factors from Eurocontrol [153] are used to establish a weighted NO_x value. The weighted NO_x is therefore a function of the combustor type and flight profile. The optimisation exercise carried out for the

minimisation of cruise NO_x has been carried out for both absolute and weighted NO_x emissions. Further details regarding the specific correlations used are given in Appendix E.

Contrails are also considered in this dissertation as they are perceived to be an important emission source. The conditions under which contrails are formed have already been outlined in the previous section and a detailed description of the contrails prediction tool is given in Appendix D. The impact of contrails on radiative forcing is difficult to assess. Unlike for NO_x, the effect of contrails is short lived as contrails tend to dissipate within hours. The relative impact of contrail emissions is also highly dependent on weather patterns. In addition, the likelihood of contrail formation depends significantly on the atmospheric conditions including temperature and humidity at the cruise altitudes. Accordingly, local conditions must be taken into consideration when predicting the formation of contrails and no general rule relating only to the engine or aircraft performance can be applied.

In this dissertation, the impact of contrails has not been assessed as to do so would entail the consideration of fleet behaviour and regional or global weather patterns which fall outside the scope of this work. Rather the impact of the current concepts on contrail formation is evaluated. In addition, the cruise altitudes of each concept are optimised in order to minimise contrail emissions. The business case flight model assumes a typical 5400km route. In order to study the contrail characteristics an actual city-pair trajectory of similar length had to be selected. The city-pair for this study, which is for a London to New York flight, was chosen arbitrarily and the route is depicted in Figure 7.3. The atmospheric conditions along this flight route were obtained from Kalnay et al. [155]. The atmospheric data is based upon atmospheric conditions on the 1st of January 2012 and the 1st of July 2012. The relevant atmospheric data is shown in Appendix D.

Figure 7.3 – London to New York Flight Trajectory [156]

Clearly, this scenario is extremely limited and results from this study cannot be used to extrapolate the regional or global implications of contrails on radiative forcing. The test case is, however, useful as it does allow for the understanding of how different levels of engine efficiency affect the total length of contrails formed and the height at which these contrails are formed for a specific flight. In addition to assessing the length of contrails formed along a specific route, the contrail prediction tool is also used to assess at which altitudes these contrails are most likely to form. This is accomplished in a more generic way through the use of an Appleman diagram such as the one shown in Figure 7.4. The Appleman diagram shows the critical temperatures required for contrail formation at various pressure altitudes and humidities. For a given atmospheric pressure, only an atmospheric temperature which falls below the applicable iso-humidity line will allow for contrail formation. This diagram is useful for assessing how the critical temperature required for contrail formation changes with engine efficiency. A complete description of the contrail model is given in Appendix D.

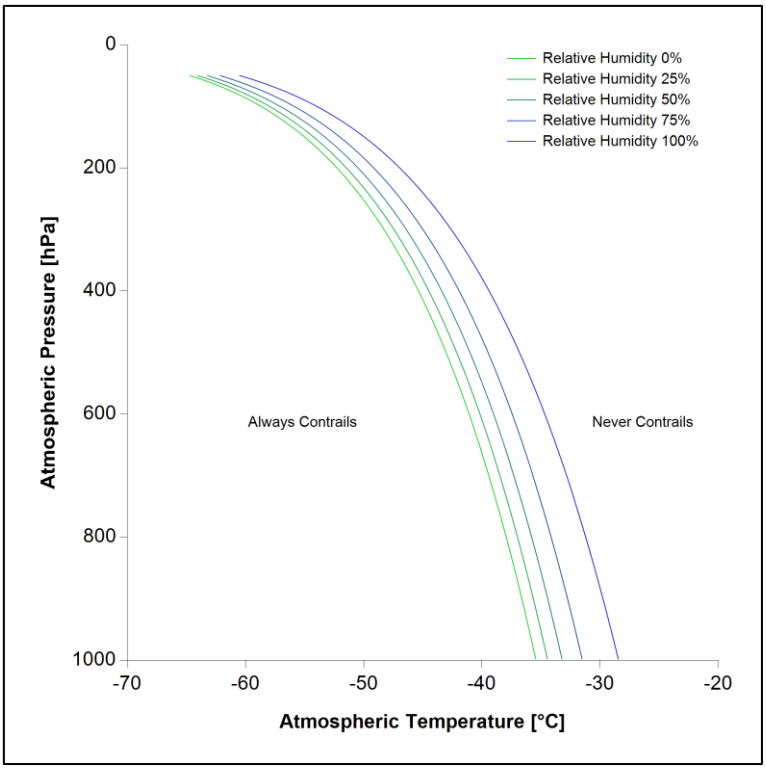

Figure 7.4 – Typical Appleman Diagram

7.5 Baseline and Initial Concept Evaluation

The objective of this section is to compare the mission performance of the initial GISFC with that of the GIRFC concept. The baseline TF2000 mission performance is also presented as it is representative of the level of technology in the year 2000. The initial GISFC and GIRFC concepts are based on the GTICLR manufacturer specifications as established during the NEWAC [12] project. These specifications were updated for a later entry-into-service in 2025 where the original GTICLR was targeted for a 2020 entry-into-service. A comparison between the baseline TF2000, the initial GISFC and the initial GIRFC configurations is given in Table 7.3. The initial GISFC and GIRFC specifications have not been optimised and are based upon previous designs explored in NEWAC [12]. The main differences between the baseline TF2000 and the initial GISFC and GIRFC concepts are:

a. The initial GISFC and GIRFC OPR far exceed that of the TF2000. The high OPR is made possible by a significant increase in T_4, intercooling, higher component efficiencies and improved material temperature limits.
b. The initial GISFC and GIRFC SFN and consequently FPR are far lower than that of the TF2000. A number of factors contribute to the consideration of lower SFN. A geared fan allows for a significant increase in fan diameter. The gearbox alleviates the speed mismatch between the fan and LPT and hence allows for improved fan and LPT efficiency. The increase in BPR from the TF2000 level to the initial GISFC and GIRFC level is achieved not only through an increase in bypass mass flow rate but also through a significant increase in T_4 which allows for a reduction in core mass flow rate. The increase in T_4 is especially necessary as the OPR is also significantly higher for the GISFC and GIRFC.
c. The IPC-HPC worksplit in the initial GISFC and GIRFC favours the HPC. This is in part due to the higher efficiency of the HPC but also due to the effects of intercooling. A more equal worksplit is preferred in the TF2000 which does not incorporate an intercooled core.
d. The TF2000 combustor is assumed similar to that of the Trent 772. Therefore, the LTO NO_x data from the ICAO databank [28] have been adopted for this configuration. On the other hand, the GISFC and GIRFC concepts assume an advanced LDI combustor which is

necessary to limit NO_x emissions at high OPR. The LTO NO_x levels for the GISFC and GIRFC have, therefore, been estimated using a correlation from Tacina et al. [152] which is more representative of this combustor type.

e. The GISFC and GIRFC incorporate variable area bypass nozzles. This allows for control of the fan running line so that higher fan cruise efficiency can be achieved. The incorporation of such nozzles also allows for the offset of take-off T_4 and an increase in surge margin.

The main performance characteristics of the TF2000, GISFC and GIRFC, based upon the initial specifications, are given in Table 7.3. It is clear that both the SFC_{MC} for both the GISFC and GIRFC are significantly lower than for the TF2000 with a 15.7% and 16.8% improvement respectively. This is brought about both by an increase in thermal efficiency due to higher OPR and improved component efficiency as well as an increase in propulsive efficiency due to lower SFN. The propulsive efficiencies of the GISFC and GIRFC are similar but the thermal efficiency of the GIRFC is higher. The thermal efficiency advantage of the GIRFC is due to the effects of the mixed exhaust which slightly reduce the losses across the fan and LPT as well as higher HPC and HPT efficiency due to reduced over-tip leakage losses. The GIRFC, aside from having lower SFC, is also lighter. The reduction in engine weight is mainly due to the reduction in the fan and LPT weight as well as due to a reduction in HP-spool size. The GIRFC saves 1.52% in block fuel burn with respect to the GISFC.

The TF2000, GISFC and GIRFC have different characteristics in terms of their potential for contrail formation. Figure 7.5 shows an Appleman diagram comparing the likelihood of contrail formation for the TF2000 and the GIRFC at different altitudes and atmospheric conditions. The cruise efficiencies listed in Table 7.3 were assumed in this diagram. It is clear that for a given atmospheric pressure and humidity, the GIRFC would create persistent contrails at higher temperatures than would the TF2000. This increases the likelihood of contrail formation but also changes the flight level at which contrails are likely to form. Given that the contrails for the GIRFC can form at higher temperatures, it is implicit that the altitude at which the contrails can form will be lower.

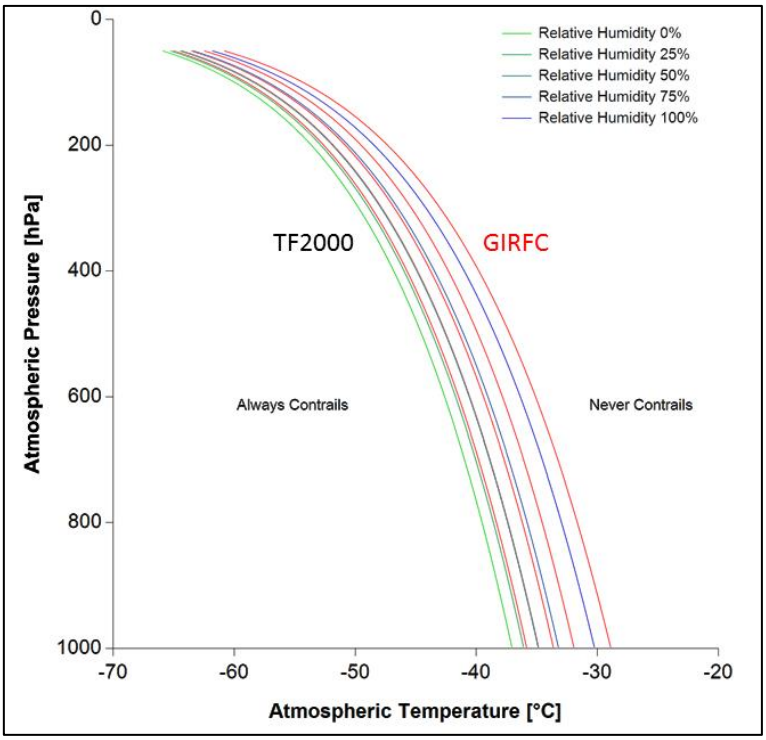

Figure 7.5 – Appleman Diagram (baseline TF2000 vs. initial GIRFC)

Higher engine efficiency results in a steeper contrail mixing line which can lead to higher contrail emissions. Therefore, it is expected that the GISFC and GIRFC concepts, for a given mission, would create greater lengths of contrail than the TF2000. For the January test case the GISFC and GIRFC cause about 820km of additional non-persistent contrails when compared with the TF2000. For the July test case the GISFC produces 566km of additional non-persistent contrails while the GIRFC produces 610km of additional non-persistent contrails when compared with the TF2000. As expected, the GIRFC has the worst contrail signature due to the fact that it is the most efficient engine of the three.

In terms of persistent contrails there is little or no difference between the three concepts for the January test. The atmospheric conditions for the January test case were significantly colder than for the July test case. In the January test case, humidity levels which allowed for persistent contrails were accompanied in all cases by temperatures below the critical level. In the July test case, where the average temperatures were a good deal warmer, humidity levels which allowed for persistent contrail formation did not necessarily coincide with temperatures below the critical level. As the GISFC and GIRFC engines are more efficient than the TF2000 the associated

critical temperatures for contrail formation are higher, and therefore resulted in more frequent persistent contrail formation. Consequently, in the July test case the GIRFC exhibited the worst persistent contrail signature. The GISFC contrail emissions were reduced by 13km while the TF2000 contrail emissions were reduced by a further 266km. Figure 7.6 and Figure 7.7 show where contrails were formed during the mission flown by the TF2000 engine. The characteristic is similar for the GISFC and GIRFC and hence has not been repeated. For the January test case shown in Figure 7.6, non-persistent contrails are present through much of the flight. However, persistent contrails only form in regions of high relative humidity. For the July test case shown in Figure 7.7, persistent contrails only form over a short period in a region of high humidity. In July, warmer air temperatures significantly limit the formation of contrails.

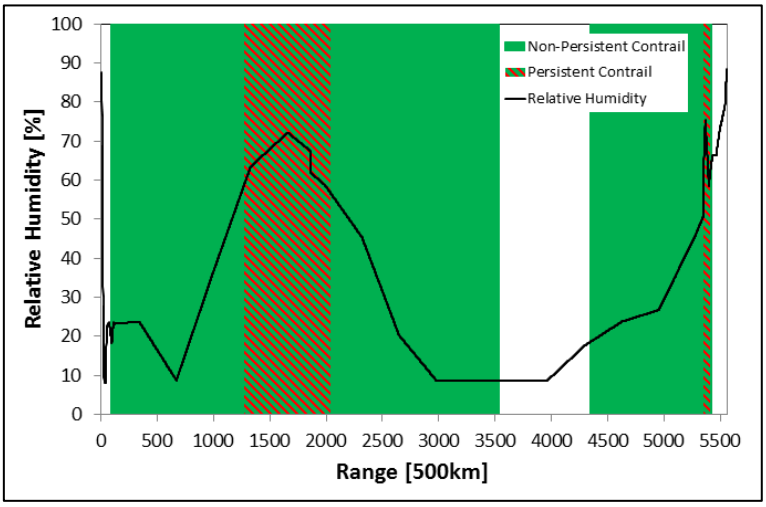

Figure 7.6 – Contrail Occurrence during Cruise for TF2000 (January)

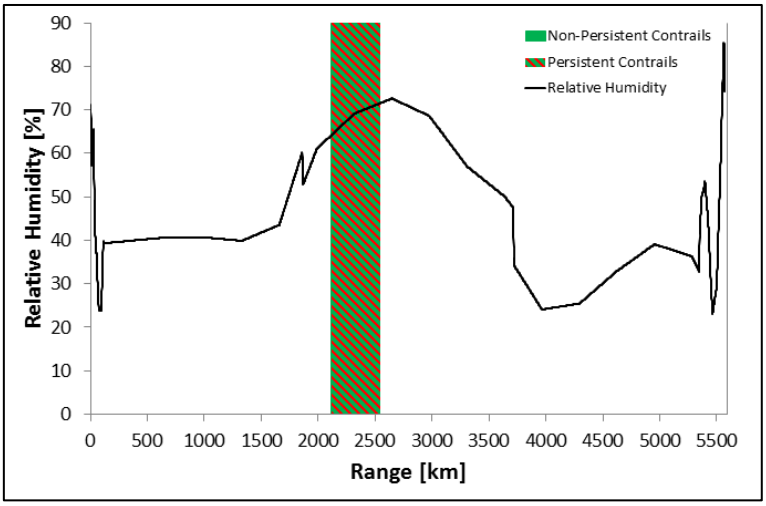

Figure 7.7 – Contrail Occurrence during Cruise for TF2000 (July)

It is expected that higher OPR designs should result in higher NO_x levels due to higher T_3 levels. However, the initial GISFC and GIRFC configurations demonstrate lower LTO NO_x levels than does the TF2000 which is of much lower OPR. The main factor behind this improvement is the change in combustor type. The LDI combustor results in far lower NO_x emissions than does the standard TF2000 combustor. The efficiencies of the GISFC and GIRFC are also higher than for the TF2000 which leads to lower fuel burn for a given thrust profile and hence less opportunity for NO_x formation. In addition, the GISFC and the GIRFC also benefit from intercooling which lowers the T_3 considerably. The T_3 of the GIRFC is also lower due to the higher efficiency HPC which means that the LTO NO_x of the GIRFC is even lower than that of the GISFC. When comparing the GISFC and GIRFC with the TF2000, the combination of these factors results in an overall reduction in LTO NO_x of 51.2% and 52.5% respectively. The LTO NO_x levels are shown in Figure 7.8. The absolute and weighted NO_x emissions for the GISFC and the GIRFC also show marked reductions when compared with those of the TF2000. In this case, the mission profile has been assumed identical, and therefore the NO_x weighting is identical in each case.

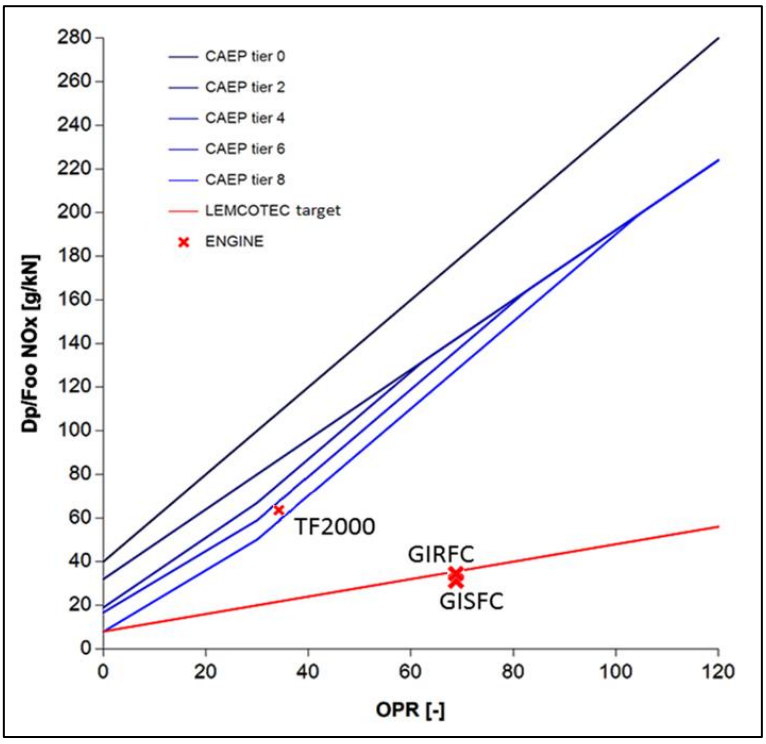

Figure 7.8 – LTO NO_x Comparison (baseline TF2000 vs. initial GISFC vs. initial GIRFC)

Parameter	Operating Point	Units	TF2000	GISFC	GIRFC
OPR	TOC	-	38.17	80	80
SFN	TOC	m/s	190	146	150
BPR	TOC	-	4.85	11.25	11.25
FPR	TOC	-	1.8	1.67	1.63
IPC PR	TOC	-	5.2	4.5	4.5
HPC PR	TOC	-	4.4	13.70	13.70
Intercooler W_c/W_h	TOC	-	-	1.50	1.50
T_4	TOC	K	1654	1920	1920
Intercooler Effectiveness	TOC	-	-	0.6	0.6
SFN	MC	m/s	150	111	115
SFC	MC	mg/Ns	16.28	13.73	13.55
BP Nozzle A_{MC}/A_{TOC}	MC	%	100.0	105.0	102.5
Intercooler Effectiveness	MC	-	-	0.57	0.57
BP Nozzle A_{TO}/A_{TOC}	TO	%	100	105.0	102.5
T_4	TO	K	1717	1947	1958
Intercooler Effectiveness	TO	-	-	0.67	0.67
Δ Engine + Nacelle Weight	-	%	ref	+27.0	+23.5
Absolute NO_x n=0.4 / 0.2	-	kg	424 / 468	294 / 320	270 / 296
Δ Weighted NO_x n=0.4 / 0.2	-	%	ref / ref	-38.8/-39.6	-45.4/-46.0
LTO NO_x (Dp/Foo)	-	g/kN	66.6	32.5	31.6
Persistent Contrails (Jan)	-	km	804	804	804
Persistent Contrails (Jul)	-	km	419	685	698
Non-Persistent Contrails (Jan)	-	km	4487	5306	5308
Non-Persistent Contrails (Jul)	-	km	419	985	1029
Δ Block Fuel Burn	-	%	ref	-18.5	-19.7
Δ Block Fuel Burn (vs. GISFC)	-	%	n/a	ref	-1.52

Table 7.3 – Baseline TF2000, Initial GISFC and Initial GIRFC Concept Comparison

7.6 Cycle Optimisation for Minimum Block Fuel Burn

The trends presented in the last section are only valid for the TF2000, GISFC and GIRFC based on the initial specifications. Further optimisation of the designs is necessary to improve the fuel burn characteristics. However, changes to the cycle can have important effects not only on block fuel burn, but also on NO_x and, to a lesser degree, contrails. The TF2000 is based on the specifications of an existing engine, and is therefore assumed to be representative of year 2000 technology. The initial GISFC and GIRFC specifications are based upon manufacturer specifications for a similar concept investigated in NEWAC [12]. However, the GISFC and GIRFC, in a number of parametric studies outlined in this thesis, have demonstrated the potential for further design improvements. The GISFC and GIRFC architectures also differ, and therefore each concept needs to be optimised independently in order to identify the optimum configuration. As a result, the objective of this section is to optimise the GISFC and GIRFC cycles for minimum fuel burn. The TF2000 engine is again adopted as the baseline configuration in this study.

7.6.1 Method and Assumptions

The optimisation was carried out primarily for the GISFC and GIRFC. Two numerical optimisation tools were used and, as explained in chapter 3, form part of the SIMULIA Isight Suite [53]. A simulated annealing method, suitable for global optimisation problems, was used to approximate the optimum configurations. A Downhill-Simplex method was then used to refine each concept. The optimisation was carried out for a single objective; the minimisation of fuel burn. The optimisation variables are listed in Table 7.4 while the constraints are listed in Table 7.5. The optimisation variables consist of design point cycle parameters, control parameters and trajectory parameters.

The control parameters regulate the intercooler effectiveness and bypass nozzle area during cruise. The trajectory parameters determine the flight profile during cruise. A step-cruise was used for each concept, and therefore the cruise altitudes were included as optimisation variables. For consistency, the TF2000 cruise altitudes were also optimised. Only the cruise phase altitudes were optimised as these were found to have the largest impact upon the final

result. In order to optimise the climb and descent phases, air traffic control constraints would also need to be respected. Air traffic control constraints were not considered in this work, and therefore the baseline climb and descent profiles were maintained. The cruise speeds were not modified so as minimise changes to the mission time. The climb phase control variables were assumed to maintain the TOC setting. For the descent phase, the nominal bypass nozzle area and cruise intercooler effectiveness were maintained.

The problem constraints included the time to height, block time and take-off distance for both the design and business mission. The optimisation was carried out assuming fixed thrust levels and a fixed aircraft platform, and therefore these constraints were not violated during the optimisation routine. The fan diameter constraint has been imposed so as to limit installation, weight and manufacturing challenges and is representative of standard limits established within LEMCOTEC. The $T_{4,TO\ EOR}$ limit is imposed to guarantee material integrity.

Variable Name	**Units**	**Lower Limit**	**Upper Limit**
TOC OPR	[-]	80	100
TOC IPC PR	[-]	3	6
TOC Mixer P_c/P_h	[-]	0.95	1.05
TOC fully expanded V_c/V_h	[-]	0.65	0.95
TOC intercooler W_c/W_h	[-]	1.1	1.55
TO bypass nozzle area (A_{TO}/A_{TOC})	[-]	1.0	1.05
1st cruise intercooler effectiveness ($\varepsilon_{MC}/\varepsilon_{TO}$)	[-]	0.8	1.0
2nd cruise intercooler effectiveness ($\varepsilon_{MC}/\varepsilon_{TO}$)	[-]	0.8	1.0
3rd cruise intercooler effectiveness ($\varepsilon_{MC}/\varepsilon_{TO}$)	[-]	0.8	1.0
1st cruise bypass nozzle area (A_{MC}/A_{TOC})	[-]	1.0	1.1
2nd cruise bypass nozzle area (A_{MC}/A_{TOC})	[-]	1.0	1.1
3rd cruise bypass nozzle area (A_{MC}/A_{TOC})	[-]	1.0	1.1
Top-of-climb altitude (TOC)	[m]	9500	12500
Top-of-descent altitude (TOD)	[m]	9500	12500

Table 7.4 – Optimisation Variables

Constraint Name	Units	Lower Limit	Upper Limit
Business time to height	[min]	-	20
Design time to height	[min]	-	30
Business block time (gate-to-gate)	[min]	-	400
Design take-off distance	[km]	-	2.5
Fan diameter	[m]	-	3.1
$T_{4,TO\ EOR}$	[K]	-	1970

Table 7.5 – Constraints

7.6.2 Optimisation Results

The results of the optimisation study carried out for the baseline TF2000, the GISFC and the GIRFC are presented in Table 7.6. Both the GISFC and the GIRFC benefit from a significant increase in OPR with respect to the baseline TF2000. The OPR of the GISFC and of the GIRFC tend to higher values than for the initial estimates where the blade heights are still quite reasonable. In the case of the GIRFC, which has characteristically longer HPC and HPT blades than the GISFC, a higher optimum OPR is found before the over-tip leakage losses become dominant. The OPR of the GIRFC is 151% higher than for the TF2000 while the OPR of the GISFC is only 127% higher than for the TF2000. When compared with the TF2000, the higher OPR, lower component losses and the mixed exhaust (in the case of the GIRFC) contribute to a significant increase in thermal efficiency. The GISFC and the GIRFC also benefit from significantly lower SFN when compared with the TF2000 which is beneficial to propulsive efficiency. The optimum SFN_{TOC} for both the GISFC and GIRFC are approximately 39.5% lower than that of the TF2000. This is reflected by a significant increase in the BPR of each design which was found to exceed 14.8 at TOC. Although the optimum SFN of the GIRFC is equal to that of the GISFC, the FPR is nevertheless lower due to the effects of the mixed exhaust.

The intercooler effectiveness at TOC was found to lie at around 60% for a limiting intercooler W_c/W_h of 1.5. At cruise a much reduced intercooler effectiveness of 53% was found to be optimum. The bypass nozzle area was also optimised for operation at cruise. It was found that the GIRFC only required an average of a 2% change in nozzle area while the GISFC benefitted

from 4% change in nozzle area. This is expected as the working line of a mixed flow engine is typically steeper than for a separate flow engine which means that a smaller deviation of the bypass nozzle is required for the fan running line to be displaced to the fan map locus of optimum efficiency. At take-off it was found that the relatively high design intercooler effectiveness and bypass A_{TO}/A_{TOC} were adequate for retaining the $T_{4,TO}$ below the required limit. Both engines exhibit a significant increase in weight when compared with the baseline TF2000 as well as when compared with the initial GISFC and GIRFC specifications. This is mainly driven by the increase in fan diameter and consequently weight and similarly significant increases in LPT weight. The block fuel burn reduction for the GISFC and GIRFC concepts, when compared with the baseline TF2000, is 20.0% and 21.4% respectively. The block fuel burn reduction for the optimised configurations is an additional 1.6-1.8% lower than for the initial concept specifications. The LTO NO_x of the GIRFC is now 9% higher than that of the GISFC. Although the efficiency of the GIRFC is higher than that of the GISFC, the OPR and hence the T_3 has also increased significantly.

The optimum block fuel burn trajectory of the TF2000 engine is shown in Figure 7.9. To minimise block fuel burn, L/D must be maximised at cruise. Both lift and drag are dependent on angle of attack and the maximum L/D occurs at a specific angle of attack. At a given flight condition, the angle of attack must, however, be selected according to the required lift which in cruise is approximately equal to the aircraft weight. Flight speed and atmospheric density both influence the angle of attack for maximum L/D. Therefore, for a given lift requirement there is an optimum flight speed or altitude (corresponding to atmospheric density) which will yield the optimum angle of attack and the maximum L/D. In this case a fixed Mach number has been assumed which sets the flight speed at a given altitude, and therefore only the variation of altitude is available for maximising the L/D. As the aircraft becomes lighter the lift requirement reduces and the angle of attack for maximum L/D also changes. To reach the optimum L/D the flight altitude must be increased as shown in Figure 7.9. The optimum cruise altitudes of the GISFC and GIRFC are slightly higher as the fuel load is lower in each case.

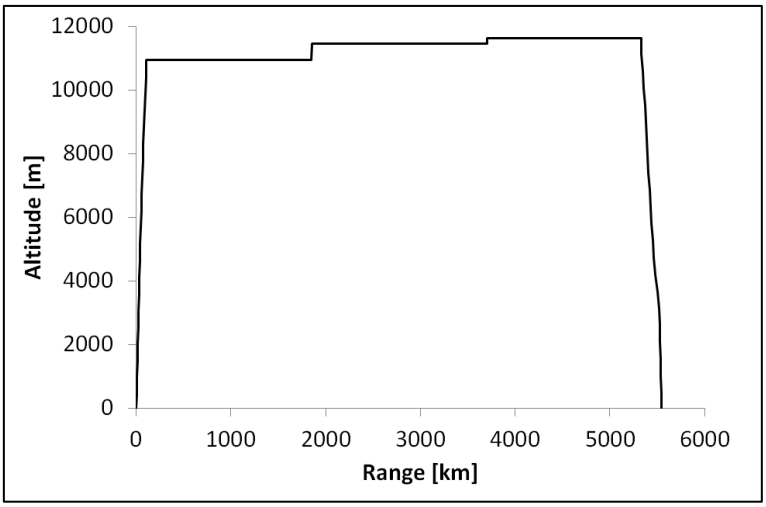

Figure 7.9 – Optimal Trajectories (based on TF2000 data)

The HP-spool designs presented in chapter 4 were reliant upon the initial specifications for both the GISFC and the GIRFC which assume an OPR of 80 and a BPR of 11.25. The optimisation of each concept clearly introduces changes to the core thermo-fluid characteristics, to the component pressure ratios as well as to the disc stress profiles. Consequently, the initial HP-spool designs are not representative of the final GIRFC and GISFC designs. For this reason, several HP-spool design iterations were carried out throughout the course of this research. The final HP-spool designs for both the GISFC and GIRFC are presented in Figure 7.10.

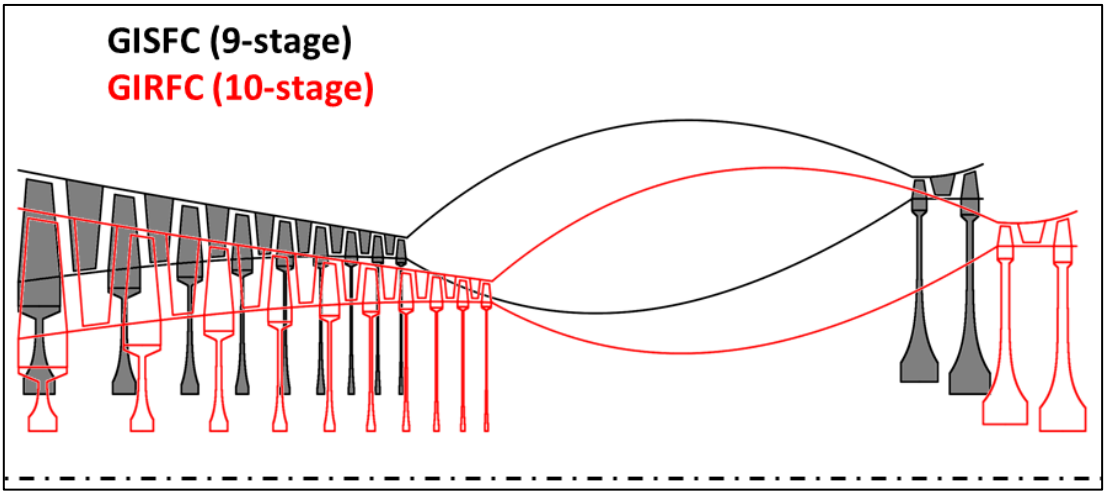

Figure 7.10 – Comparison HP-Spools for Optimised GISFC and GIRFC

Due to the higher pressure ratio across the GIRFC HPC, the stage count for this component has been increased from 9 to 10 in order to maintain similar levels of stage loading. The GISFC

OPR and work split have not changed significantly and therefore 9 stages have been retained. The size-effect curves for these two components, shown in Figure 7.11 and Figure 7.12, are almost identical to those presented in chapter 4 for a 9-stage HPC and a 2-stage HPT as the initial assumptions regarding stage loading coefficients, flow coefficients and stage geometry have been retained for both HPC and HPT. The last stage blade heights of the HPC and the first stage blade heights of the HPT are very similar. For both concepts there is a minimum blade height below which over-tip leakage losses become critical. In both cases over-tip leakage losses decrease efficiency by about 0.2-0.3%. The critical HPC and HPT blade heights are reached in the GIRFC at higher OPR than for the GISFC. Further decreases in blade height beyond the current levels would result in a rapid decrease in component efficiency.

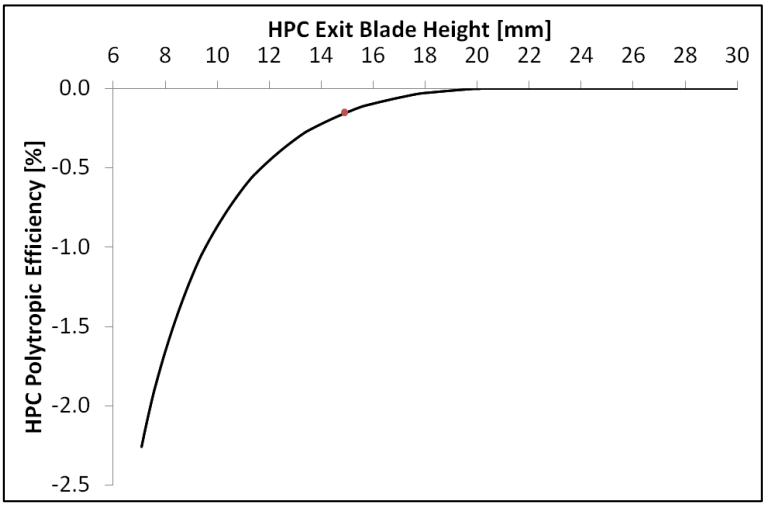

Figure 7.11 – HPC Polytropic Efficiency Variation with Blade Height

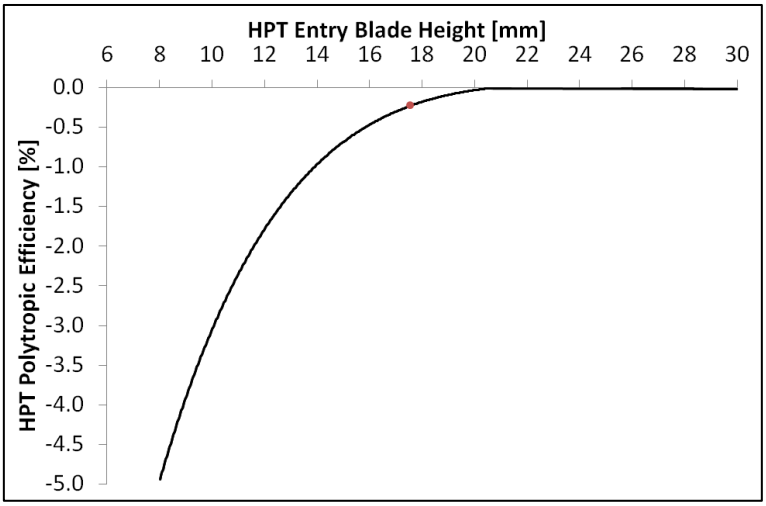

Figure 7.12 – HPT Polytropic Efficiency Variation with Blade Height

Parameter	Operating Point	Units	TF2000	GISFC	GIRFC
OPR	TOC	-	38.17	84.3	95.8
SFN	TOC	m/s	190	114.5	114.5
BPR	TOC	-	4.85	14.9	14.8
FPR	TOC	-	1.8	1.50	1.45
IPC PR	TOC	-	5.2	4.5	4.57
HPC PR	TOC	-	4.4	14.8	16.6
Intercooler W_c/W_h	TOC	-	-	1.5	1.5
T_4	TOC	K	1654	1920	1920
Intercooler effectiveness	TOC	-	-	0.6	0.6
SFN	MC	m/s	150	87.8	88.2
SFC	MC	mg/Ns	16.28	13.2	13.0
BP nozzle A_{MC}/A_{TOC}	MC	%	100.0	106.0	102.0
Intercooler effectiveness	MC	-	-	0.53	0.53
BP nozzle A_{TO}/A_{TOC}	TO	%	100.0	105.0	105.0
T_4	TO	K	1717	1939	1947
Intercooler effectiveness	TO	-	-	0.67	0.67
Δ Engine + nacelle weight	-	%	ref	+45.0	+41.0
LTO NO_x (Dp/Foo)	-	g/kN	66.5	32.6	35.54
Δ Block fuel burn	-	%	ref	-20.4	-21.6
Δ Block fuel burn (vs. GISFC)	-	%	n/a	ref	-1.65

Table 7.6 – Comparison of Optimum TF2000, GISFC and GIRFC Configurations

7.7 Operation for Minimum Emissions

In the previous section the performance of the baseline TF2000 and fuel optimal GISFC and GIRFC were compared. Currently mission NO_x emissions and contrail emissions are unregulated, and therefore it is perhaps premature to design engines for minimum NO_x or minimum contrail emissions. Indeed, the previous comparisons suggest that minimising contrail emission through cycle changes would be a costly strategy in terms of the fuel burn penalty. However, the baseline TF2000 and the fuel-optimal GISFC and GIRFC have a number of additional variables which could be used to reduce secondary emissions. These variables include the mission profile definition and also, in the case of the fuel-optimal GISFC and GIRFC, the control strategy of the variable area nozzles. That being so, in this section two trade-offs are considered. The first trade-off presented is between fuel burn and NO_x while the second is between fuel burn and contrail formation length.

7.7.1 Method and Assumptions

The optimisation was carried out for the baseline TF2000 and the fuel-optimal GISFC and GIRFC. The cruise was defined through the use of three control points each of which were used to define the intercooler and variable area nozzle scalars for the fuel-optimal GISFC and GIRFC. A step-cruise was once again assumed where the altitude at each control point was taken as a variable. As for the previous optimisation, only the cruise phase altitudes were optimised. Based on the NO_x weighting scheme, below 9200m the effects of NO_x are negligible. Therefore, there is little advantage in optimising the climb or descent phases for minimum weighted NO_x. Similarly, contrails are not formed at low altitudes as the ambient conditions are too warm. There is little to be gained, therefore, from optimising the climb and descent phases for minimum contrail emissions. The cruise speeds were also not altered so as to minimise the changes to the flight time. The $T_{4,MC}$ is a function of the thrust requirement which, for a given speed and altitude, is constant. The cruise thrust is updated at each finite segment as the aircraft weight reduces as fuel is consumed. A multi-objective numerical optimisation tool was used to perform the required trade-off as explained in chapter 3. A global optimisation package was used to suggest an optimal Pareto front describing the best strategy for the minimisation of

fuel-burn and NO_x as well as a second Pareto front describing the best strategy for the minimisation of fuel-burn and contrail length. The optimisation variables are listed in Table 7.7 and the constraints in Table 7.8.

Variable Name	Units	Lower Limit	Upper Limit
1st cruise intercooler effectiveness ($\varepsilon_{MC}/\varepsilon_{TO}$)	[-]	0.8	1.0
2nd cruise intercooler effectiveness ($\varepsilon_{MC}/\varepsilon_{TO}$)	[-]	0.8	1.0
3rd cruise intercooler effectiveness ($\varepsilon_{MC}/\varepsilon_{TO}$)	[-]	0.8	1.0
1st cruise bypass nozzle area (A_{MC}/A_{TOC})	[-]	1.0	1.1
2nd cruise bypass nozzle area (A_{MC}/A_{TOC})	[-]	1.0	1.1
3rd cruise bypass nozzle area (A_{MC}/A_{TOC})	[-]	1.0	1.1
Top-of-climb altitude	[m]	9500	12500
Intermediate Cruise Altitude	[m]	9500	12500
Top-of-descent altitude	[m]	9500	12500

Table 7.7 – Optimisation Variables

Constraint Name	Units	Lower Limit	Upper Limit
Business block time (gate-to-gate)	[min]	-	400
Design take-off distance	[km]	-	2.5

Table 7.8 – Optimisation Constraints

7.7.2 Optimisation Results – NO_x vs. Block Fuel Burn

The optimum block fuel burn, weighted NO_x and absolute NO_x solutions are summarised in Table 7.9 to Table 7.11. The trade-off between weighted NO_x and block fuel burn are shown in Figure 7.13 for the TF2000, GISFC and GIRFC. The fuel burn advantage of the GISFC with respect to the TF2000 and the fuel burn advantage of the GIRFC with respect to the GISFC are clear and are in line with the results presented in the previous section.

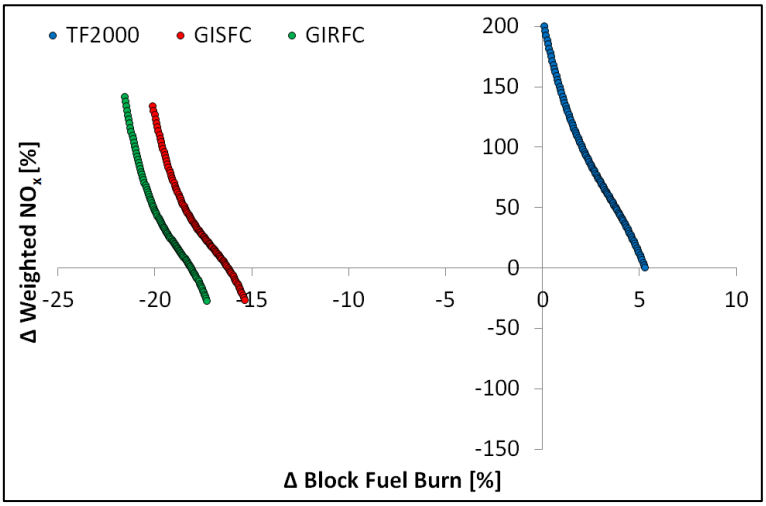

Figure 7.13 – Trade-Off: Weighted NO_x vs. Block Fuel Burn Optimal Strategies

From Figure 7.14, it is clear that the trade-off between weighted NO_x and block fuel burn is strongly linked with the way in which the aircraft and engine are operated. The weighted NO_x of each engine is 55-70% lower for the minimum weighted NO_x solutions when compared with the minimum block fuel burn solutions. Upon first consideration, one would expect the weighted NO_x emissions to reduce with block fuel burn. However, the cruise altitudes selected have a strong effect upon the weighted NO_x emission characteristics where higher altitudes lead to a higher NO_x penalty in line with the weighting scheme outlined in the previous section. As can be seen in Figure 7.14, it was found that an altitude of about 9500m resulted in the lowest weighted NO_x emissions. The optimisation routine was not allowed to select altitudes below 9500m. Weighted NO_x emissions are also reduced through an increase in intercooler effectiveness when compared with the effectiveness level for the optimal fuel burn solution. It was found that a 13-14% increase in intercooler effectiveness was required to reach the minimum weighted cruise NO_x emissions when compared with the minimum fuel burn operation. The block fuel burn

penalty associated with the minimum weighted NO_x solution was found to be in the order of 4.5-5.5%.

Figure 7.14 also shows the trajectory for minimum absolute NO_x emissions. As stated previously, NO_x emissions do not have a uniform effect on the environment across a range of altitudes. Nevertheless, it is interesting to note how the weighted and absolute NO_x trajectories differ. The minimum absolute NO_x trajectory follows closely the minimum block fuel burn trajectory but with a few differences. The minimum absolute NO_x trajectory occurs at a level cruise altitude. As the aircraft gets lighter, due to fuel being consumed, the required lift also reduces. In turn the induced drag and hence thrust reduces. A decrease in thrust results in a decrease in T_3 which reduces absolute NO_x. In the optimum block fuel burn solution, the climb phases during the step-cruise are carried out at higher thrust settings. This leads to higher temperatures in the combustor which also results in instances of higher NO_x emissions. Therefore, it was found that to reduce the absolute NO_x emissions it is preferable to adopt a level cruise altitude rather than a step-cruise. For minimising absolute NO_x emissions a 14-15% increase in effectiveness is also found to be beneficial. While this results in higher fuel consumption it also allows for a significant reduction in T_3 and hence NO_x emissions. The block fuel burn penalty associated with the adoption of the minimum absolute NO_x strategy is less than 1%.

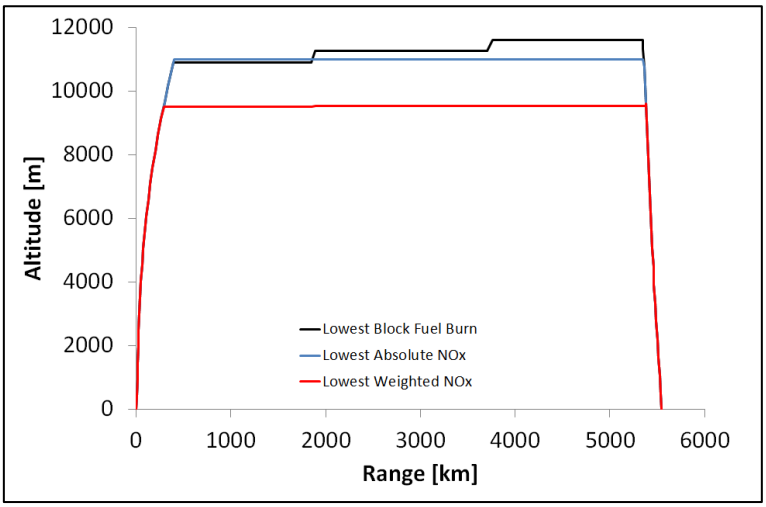

Figure 7.14 – Optimal Trajectories (based on TF2000 data)

Variable Name	Units	TF2000	GISFC	GIRFC
Mean cruise intercooler effectiveness ($\varepsilon_{MC}/\varepsilon_{TO}$)	[-]	-	0.81	0.80
Mean cruise bypass nozzle area (A_{MC}/A_{TOC})	[%]	-	1.06	1.01
Top-of-climb altitude (TOC)	[m]	10962	11046	11050
Top-of-descent altitude (TOD)	[m]	11624	11750	11760
Weighted NO_x emissions	[%]	ref	-23.80	-20.08
Absolute NO_x emissions	[%]	ref	-22.78	-18.58
Block fuel burn	[%]	ref	-20.34	-21.57

Table 7.9 – Block Fuel Burn Optimum (w.r.t. Optimum Block Fuel TF2000 Solution)

Variable Name	Units	TF2000	GISFC	GIRFC
Mean cruise intercooler effectiveness ($\varepsilon_{MC}/\varepsilon_{TO}$)	[-]	-	0.94	0.94
Mean cruise bypass nozzle area (A_{MC}/A_{TOC})	[%]	-	1.04	1.01
Top-of-climb altitude	[m]	9511	9501	9535
Top-of-descent altitude	[m]	9539	9556	9586
Weighted NO_x emissions	[%]	-67.70	-79.82	-76.32
Absolute NO_x emissions	[%]	5.50	-18.38	-15.20
Block fuel burn	[%]	5.44	-15.26	-17.03

Table 7.10 – Weighted NO_x Optimum (w.r.t. Optimum Block Fuel TF2000 Solution)

Variable Name	Units	TF2000	GISFC	GIRFC
Mean cruise intercooler effectiveness ($\varepsilon_{MC}/\varepsilon_{TO}$)	[-]	-	0.95	0.95
Mean cruise bypass nozzle area (A_{MC}/A_{TOC})	[%]	-	1.04	1.01
Top-of-climb altitude	[m]	10999	10909	10922
Top-of-descent altitude	[m]	11000	10990	10999
Weighted NO_x emissions	[%]	-2.67	-27.06	-22.80
Absolute NO_x emissions	[%]	-1.30	-25.68	-21.02
Block fuel burn	[%]	0.28	-19.48	-20.73

Table 7.11 – Absolute NO_x Optimum (w.r.t. Optimum Block Fuel TF2000 Solution)

7.7.3 Optimisation Results – Contrails vs. Block Fuel Burn (January)

The trade-off between persistent contrail emissions and block fuel burn for the TF2000, GISFC and GIRFC is shown in Figure 7.15. The block fuel burn results are in line with those presented in the previous sections. As can be seen also in Table 7.12, the block fuel burn penalty for the minimum persistent contrails solutions when compared with the minimum block fuel burn solutions is about 0.44-0.58% for each concept.

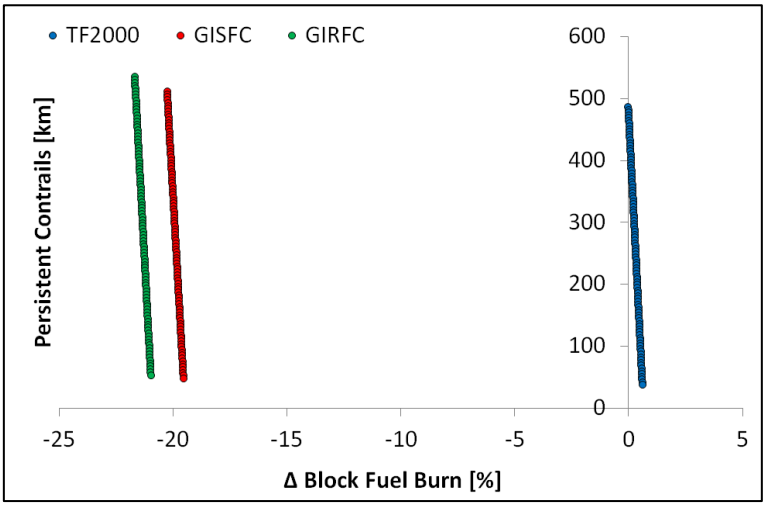

Figure 7.15 – Trade-Off: Persistent Contrails vs. Block Fuel Burn Optimal Strategies

Variable Name	Units	TF2000	GISFC	GIRFC
Mean cruise intercooler effectiveness ($\varepsilon_{MC}/\varepsilon_{TO}$)	[-]	-	0.80	0.80
Mean cruise bypass nozzle area (A_{MC}/A_{TOC})	[%]	-	1.07	1.03
Top-of-climb altitude	[m]	11868	11867	11881
Top-of-descent altitude	[m]	11814	11892	11788
Persistent contrail emissions	[%]	-90.3	-89.9	-90.3
Block fuel burn	[%]	0.58	0.46	0.44

Table 7.12 – Persistent Contrail Optimum (w.r.t Optimum Block Fuel Burn Solutions)

For the January test case, the optimum trajectory for minimum contrail emissions is higher than that for minimum block fuel burn as can be seen in Figure 7.16. At higher altitudes the atmosphere is drier which makes persistent contrail formation less likely. In Figure 7.16, the optimal trajectories are shown superimposed over the vertical humidity profile. It can be seen that at a range of about 1500km the humidity is relatively high even at the altitude required for minimum block fuel burn. The trajectory for minimum contrails avoids this region by flying at a

higher altitude. At TOD there is also a region of high humidity which leads to persistent contrail formation. In the third cruise segment, where the humidity is lower, the flight altitude drops down to a level closer to the optimum fuel burn trajectory. Descents are not typically considered during the cruise phase even though, in this case, it is beneficial. The block fuel burn penalty is slightly higher for the TF2000 as the change in mean altitude for this concept is greater. The GISFC and GIRFC require a lighter fuel load and hence adopt slightly higher cruise altitudes for minimum block fuel burn.

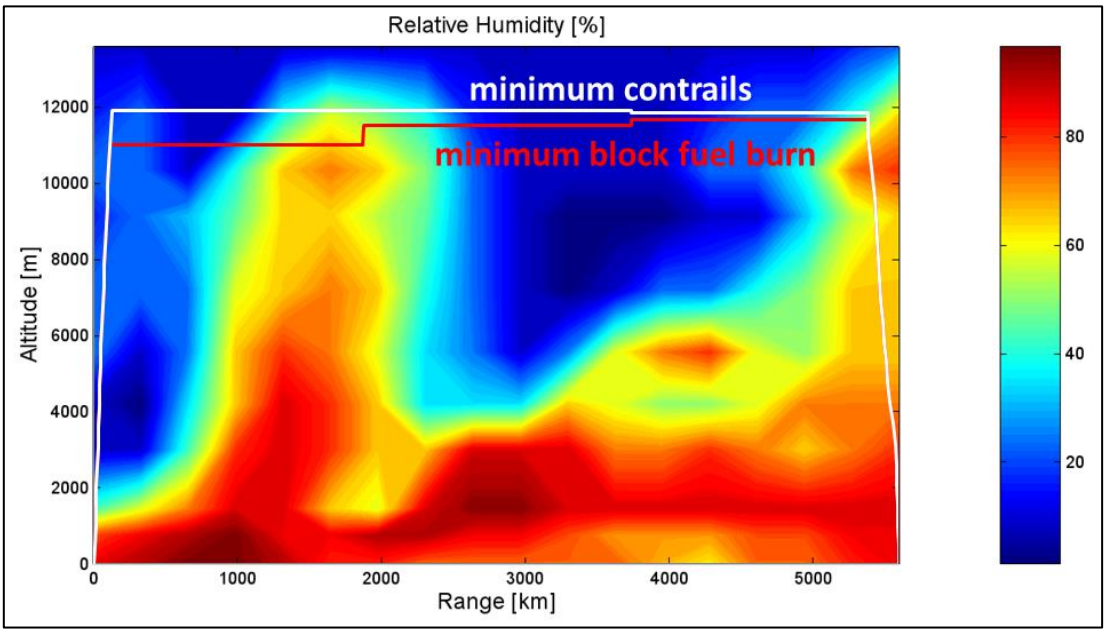

Figure 7.16 – Optimal Trajectories based on TF2000 Data (January)

Noppel et al. [(157)] carried out a similar investigation for a London to New York route. In Noppel et al. [(157)], rather than selecting a specific set of atmospheric conditions, the route was described according to the probability of contrail formation at different altitudes for a given month. In this study, lateral diversions were also considered. There are significant similarities between the results presented in this section and those described by Noppel et al. [(157)]. Specifically, Noppel et al. [(157)] demonstrated that an increase in altitude to 12000m was necessary to reduce contrail emissions and also that a 0.5% penalty in fuel burn was required for a significant reduction in the probability of contrail formation. The strategy for contrail avoidance suggested in this dissertation fits the more general strategy proposed by Noppel et al. [(157)].

7.7.4 Optimisation Results – Contrails vs. Block Fuel Burn (July)

A multi-objective optimisation was also carried out for the July test case. As demonstrated for the baseline cases, the contrail formation for the July test case is far more limited due to higher mean ambient temperatures. In the multi-objective optimisation it was found that no contrails were formed at the optimum block fuel burn trajectory. The trajectory which yielded the minimum block fuel burn was previously found to lie higher than the assumed baseline trajectory for the TF2000, GISFC and GIRFC. Given the higher altitude, it was found that contrail formation was eliminated at the optimum block fuel burn trajectory for all the engines considered. That being so, given the atmospheric conditions assumed, no block fuel burn penalty was encountered. Figure 7.17 shows the optimum fuel burn trajectory for the July test case. Only the TF2000 trajectory has been plotted as the GISFC and GIRFC minimum block fuel burn trajectories are only slightly higher at the start of the cruise phase.

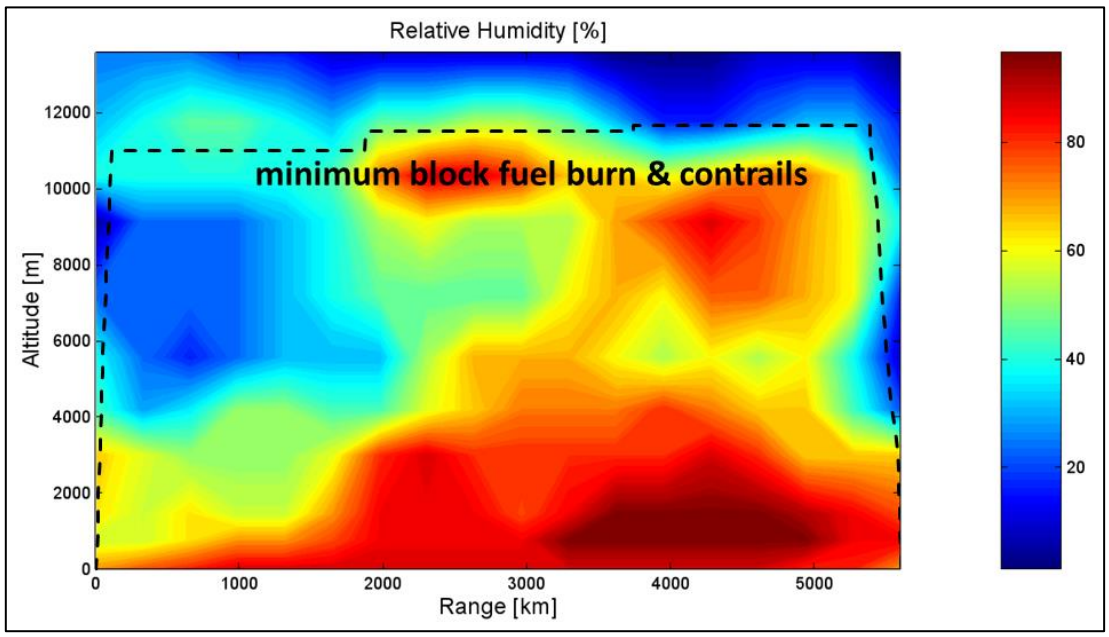

Figure 7.17 – Optimal Trajectories based on TF2000 Data (July)

7.8 Uncertainty Analysis

The results presented in this section rely on a number of model input parameters which inevitably, at the conceptual design stage, are subject to a degree of uncertainty. This uncertainty can compromise the validity of the predicted results, and therefore needs to be characterised. As part of the uncertainty analysis several sensitivity studies have been carried out. The objectives of the sensitivity analyses are:

a. To quantify uncertainty in the block fuel burn and weighted NO_x emissions predictions.
b. To provide a set of sensitivity coefficients. Given a known input perturbation, these coefficients can then be used to correct the predicted results.

The sensitivity studies are useful for gauging how uncertainty in individual parameters can affect the outcome of the problem. However, sensitivity studies as implemented in this section do not give a true measure of uncertainty. A definite measure of uncertainty is not possible to achieve at the conceptual design level. Nevertheless, in chapter 3, a methodology for the estimation of uncertainty is outlined. The resulting technique is inherently subjective, and therefore should only be used to gauge the degree of confidence in the design rather than to define an absolute uncertainty level. In this section, this method has been used to highlight the relative uncertainty between the GISFC and GIRFC designs. As the two concepts are based upon different architectures, different levels of uncertainty exist within the component performance estimates of each design.

7.8.1 Method and Assumptions

Two types of sensitivity analysis are presented in this section. A differential sensitivity analysis is presented to investigate the effect of small perturbations in the design point parameters on block fuel burn and weighted cruise NO_x. The input perturbations have been restricted to ±0.25% and are, therefore, only valid in the local area around the nominal value. The nominal value in this case is the optimum fuel burn configuration. Each response is a non-dimensional partial derivative relating the percentage change in block fuel burn or weighted NO_x to the

percentage change in the input parameter. The result of this sensitivity study is a response surface which can be used to ascertain the effect of small changes in the input values.

The difficulty with such a differential sensitivity study is that it does not reflect different levels on uncertainty in the input parameters. For example, the uncertainty in the intercooler duct pressure loss estimates is far larger than the uncertainty in the shaft mechanical efficiency. A differential sensitivity study can, therefore, lead to undue importance being attributed to specific responses. This drawback is addressed by a second sensitivity analysis where responses are evaluated based on more realistic input uncertainty ranges.

Finally, a Monte-Carlo analysis is presented. This has been used only to highlight uncertainties which are related to the specific differences between the GISFC and GIRFC. The GISFC bypass duct and core exhaust are relatively conventional while the GIRFC has a mixed exhaust with core-exhaust mixer chutes fed by multiple C-ducts. The intercooler positioning in the GIRFC is also very different from that of the more conventional GISFC which leads to higher uncertainty. Both designs suffer from uncertainty in the HP-spool design as at high OPRs the blade height will be quite small in both cases. Relatively high efficiency is assumed for the HPC and HPT and the improvement in efficiency of these components vis-à-vis existing technology is not great. Therefore, the assumed uncertainty in these values is quite small. One of the factors yielding the highest uncertainty is engine weight. Weight estimates made using techniques applicable at the early stages of design are notoriously inaccurate. For the GIRFC this is even more so as the design incorporates an unusual general arrangement whose weight is even harder to predict. Table 7.13 lists the main uncertainties which differentiate the GISFC and GIRFC together with the perceived uncertainty level based upon the aforementioned characteristics.

Parameters	GISFC	GIRFC
Bypass duct pressure loss	Low	Medium
Exhaust duct pressure loss	Low	Medium
Intercooler hot inlet header pressure loss	Medium	High
Intercooler hot outlet header pressure loss	Medium	High
Intercooler cold inlet header pressure loss	Medium	High
Intercooler cold inlet header pressure loss	Medium	High
Engine weight	High	Very High
HPC polytropic efficiency	Very Low	Very Low
HPT polytropic efficiency	Very Low	Very Low
Mixer effectiveness	n/a	Low

Table 7.13 – Perceived Parameter Uncertainty Level

In order to quantify the uncertainty that exists when comparing the GISFC and GIRFC concepts based upon the perceived uncertainty level, it is necessary to assign a confidence interval to each parameter. Table 7.14 lists the confidence intervals which have been assumed for each level of uncertainty. The lowest parameter uncertainty relates to turbomachinery efficiency and pressure losses in the intercooler matrix. The expected improvement in HPC and HPT efficiency from projects such as LEMCOTEC with respect to previous NEWAC [(12)] targets is only around 1-2%. In this research an average of 1% improvement has been assumed and thus the confidence interval suggested in Table 7.14 represents the failure or success of a given technology or study to deliver the full improvement.

On the other side of the spectrum, the estimation of engine weight is subject to a large degree of uncertainty. This is reflected by the confidence limits listed in Table 7.14 which represent typical weight estimation uncertainty levels as suggested by Lolis [(158)]. The intercooler header losses were estimated based on previous work carried out in NEWAC [(12)]. No published confidence levels can be found for these components. However, given that the GISFC resembles the NEWAC [(12)] engine, it is assumed that relatively low uncertainty is related to the losses within these ducts. The GIRFC, due to its significantly different header designs, is

therefore assumed to have higher uncertainty. Similarly there are no published confidence intervals relating to the performance of a mixer. Mixer effectiveness is largely dominated by the cowl length. Therefore, much of the uncertainty can be assumed to exist within the weight rather than the effectiveness parameter. Nevertheless, a low uncertainty level has been assumed as there will surely be variation between the estimated effectiveness and the operating effectiveness especially at off-design conditions.

As stated in chapter 3, the estimation of uncertainty at the conceptual design level is inherently subjective. The actual confidence intervals are difficult to ascertain and so two confidence levels have been outlined where the low confidence level assumes an additional 50% expansion of the confidence interval. This is intended to show the sensitivity of the given assumptions. In Kirby et al. [59], uncertainty in conceptual design is also investigated. As in this case, the absence of appropriate magnitudes for forecasting technology uncertainty led to the consideration of several different input distributions so as to build up a spectrum of design uncertainty based on different assumptions. Although this study would have benefitted from such an approach, given that the current simulations are relatively computationally expensive, only two cases could be considered.

Parameter Uncertainty	**Units**	**Confidence Interval ($\Delta P_{2\sigma}$ / P×100)**	
		High	**Low**
Very low	%	±0.50	±0.75
Low	%	±2.50	±3.75
Medium	%	±5.00	±7.50
High	%	±7.5	±11.25
Very high	%	±10.00	±15.00

Table 7.14 – 95% Parameter Confidence Interval at Different Levels of Uncertainty

7.8.2 Differential Sensitivity Analysis

Figure 7.18 and Figure 7.19 show the most significant block fuel burn and weighted NO_x responses. From Figure 7.18, it is clear that uncertainty in parameters affecting the performance of the fan and the bypass are the most critical. The following trends can be observed:

a. The response to a perturbation in the mechanical efficiency of the LP-shaft or fan gearbox is far stronger than the response to a perturbation in the mechanical efficiency of the HP-shaft.
b. The response to a perturbation in the polytropic efficiency of the LPT or fan and fan gearbox is somewhat stronger than the response to a perturbation in the polytropic efficiency of the HPC, HPT or IPC. The response to a perturbation in the HPC and HPT polytropic efficiency is still quite strong due to significant power losses across these high pressure ratio components.
c. The response to a perturbation in the ΔP/P in the bypass duct is far stronger than the response to a perturbation in either the ΔP/P of the intercooler headers or in the ΔP/P of the core ducting. The core ducting response is not shown in Figure 7.18 as it is quite small. This is again expected as losses in the bypass duct, given a BPR in excess of 14, affect a much larger quantity of fluid than do the core or intercooler ducting. The W_c/W_h of the intercooler is approximately 1.5 which means that even the cold side of the intercooler has a much lower flow rate than the bypass duct.

In Figure 7.18 it is also clear that a perturbation in the allowable blade metal temperature of the HPT has a much bigger effect on the performance than does a similar perturbation in the LPT. The cooling mass flow for the HPT must be taken from the exit of the HPC while for the LPT it is taken from the front stages of the HPC. Therefore, given that the HPT cooling flow is hotter, a change in the allowable HPT metal temperature will result in a bigger change in cooling mass flow rate which in turn will result in a larger variation in HPC compressor work. The responses to perturbations in engine system weight and mixer effectiveness are also given in Figure 7.18. While these are significant, they are difficult to assess as no similar parameter exists for comparison.

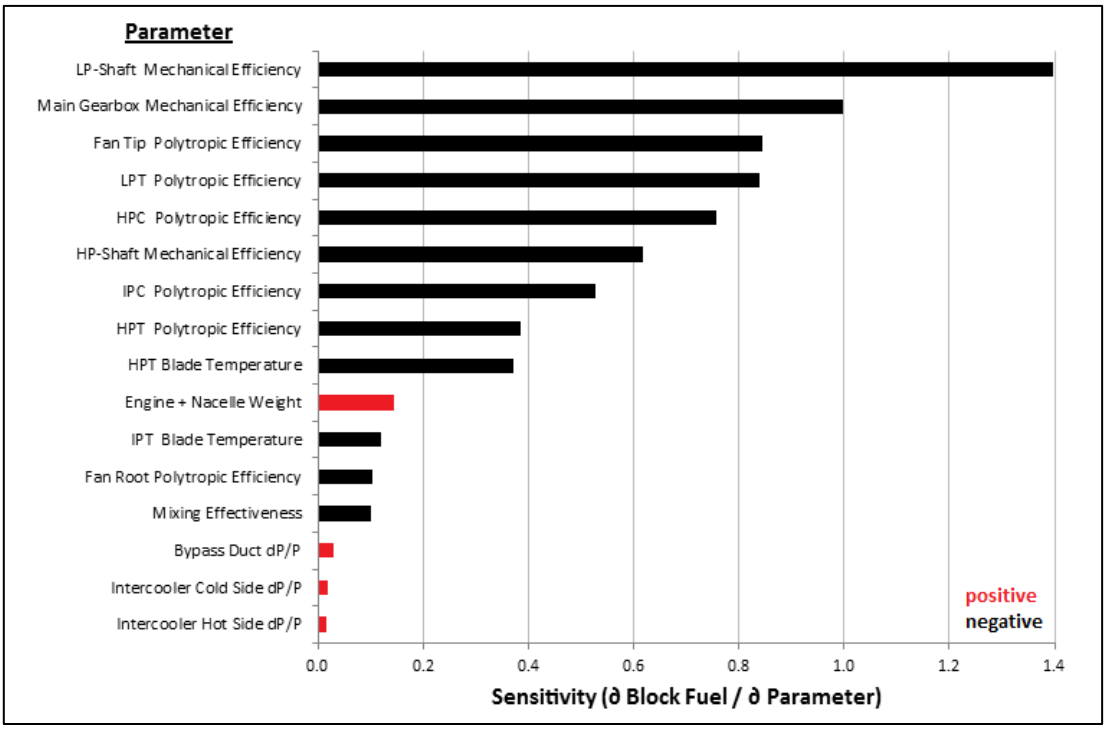

Figure 7.18 – Differential Sensitivity Analysis for Block Fuel Burn (GIRFC)

Weighted NO_x emissions are proportional to fuel flow and therefore the weighted NO_x responses shown in Figure 7.19, are similar to the block fuel burn responses shown in Figure 7.18 but there are some key differences which are useful to appreciate. NO_x emissions are highly dependent on the temperatures within the combustor and so perturbations which result in a change in combustor temperature result in a stronger response. This is clear in Figure 7.19 where perturbation in HPC and IPC efficiency show a stronger response than do perturbation in fan efficiency. Moreover, perturbations in intercooler hot side pressure losses show a stronger response than do pressure losses in the bypass duct. As the losses increase prior to the combustor, the temperature in the combustor will increase and the fuel burn will increase which both lead to higher NO_x emissions.

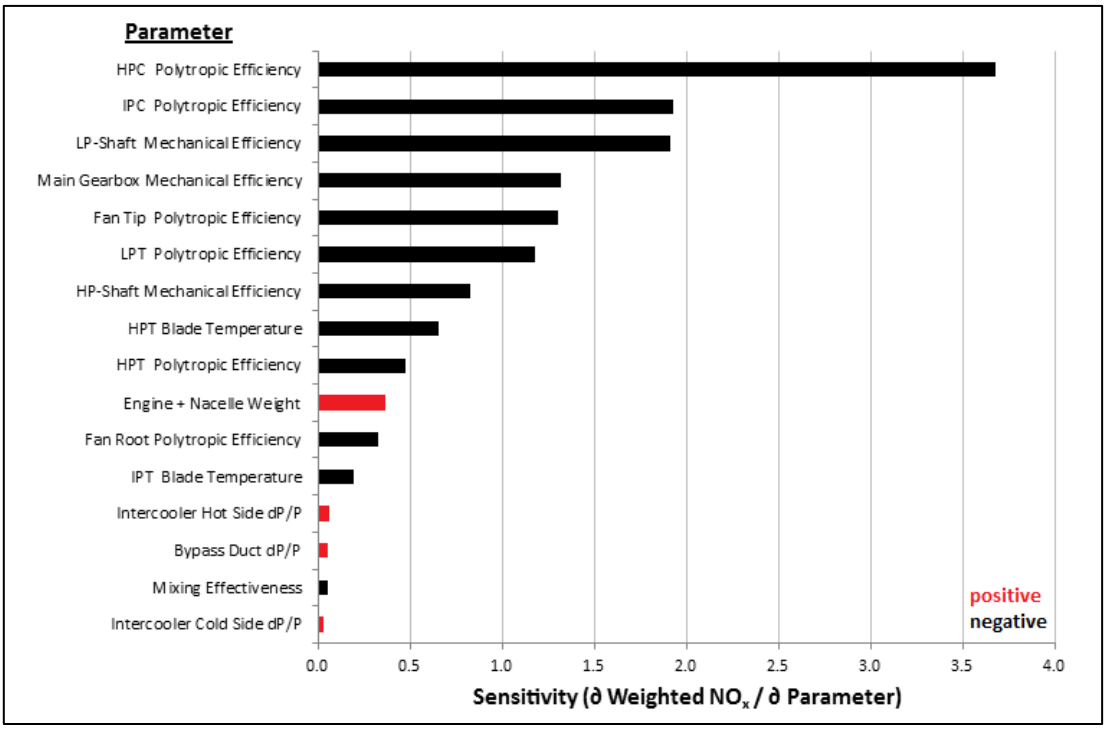

Figure 7.19 – Differential Sensitivity Analysis for Weighted Cruise NO_x (GIRFC)

7.8.3 Range Based Sensitivity Analysis

The sensitivity analysis carried out in the previous section does not take into account the level of uncertainty in the input parameters, and therefore must be interpreted carefully. In this section, the block fuel burn and weighted NO_x responses are presented based upon more realistic variations in the input parameters.

Figure 7.20 and Figure 7.21 show the sensitivity of block fuel burn and weighted NO_x emissions to variations in component weight. The heaviest components in the GISFC and the GIRFC are the LPT, fan and nacelle, and therefore for a given input perturbation these exhibit the strongest responses. A 20% increase in the weight estimation of the nacelle would account for more than a 1.5% increase in block fuel burn. In the most severe case, the uncertainty in the block fuel burn estimate arising from uncertainty in the weight estimation alone, could negate the fuel savings of the GIRFC when compared with the GISFC but it is unlikely that for example the weight estimates for the GIRFC are understated while those of the GISFC are not. Much of the architecture of the GISFC is similar to that of the GIRFC. That being the case, the relative

uncertainty between the weight predictions of the two designs would be in reality lower. In this case, the weighted NO_x responses largely mirror the block fuel burn responses.

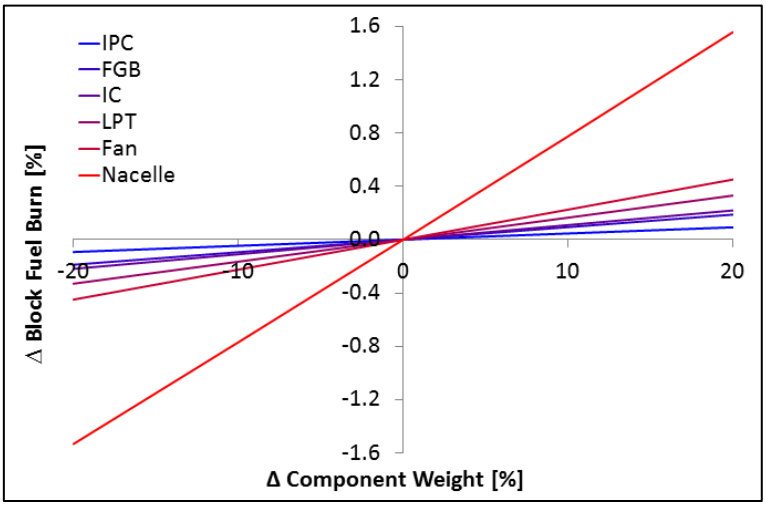

Figure 7.20 – Block Fuel Burn Sensitivity to Component Weight

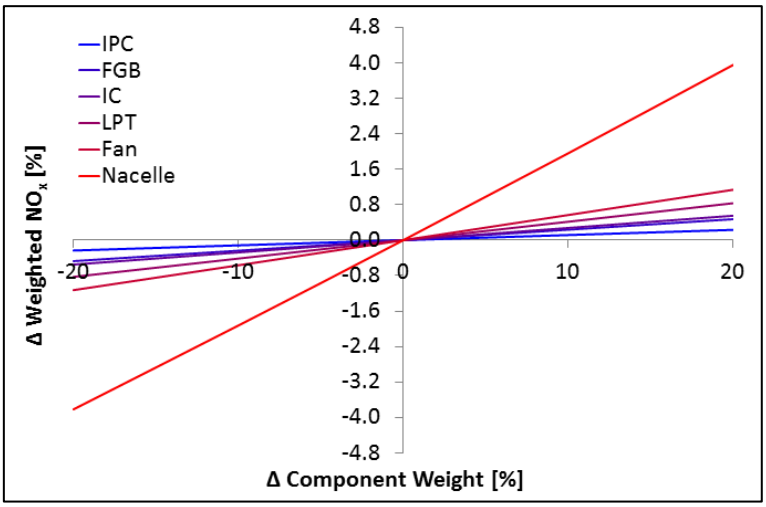

Figure 7.21 – Weighted NO_x Sensitivity to Component Weight

Figure 7.22 and Figure 7.23 show the sensitivity of block fuel burn and weighted NO_x emissions to variations in HPT and LPT blade metal temperatures. As discussed in chapter 2, material thermal capabilities have improved over the years. Thermal barrier coatings have allowed for higher turbine entry temperatures and higher turbine material temperatures. In recent years, there has been approximately a 12K per year increase in material thermal limits [(26)]. Further significant strides will be difficult to achieve and so for the GISFC and GIRFC a modest 1.5% increase in metal temperature with respect to the NEWAC [(12)] GIRFC specification has been

assumed. A ±0.5% variation in metal surface temperature represents about ±1 year scatter when compared with the historical trend. As outlined previously, changes to the HPT metal temperature are dominant and for a 0.5% decrease in material thermal limits, a 0.25% block fuel burn penalty is incurred. The weighted NO_x variation again follows that of the block fuel burn.

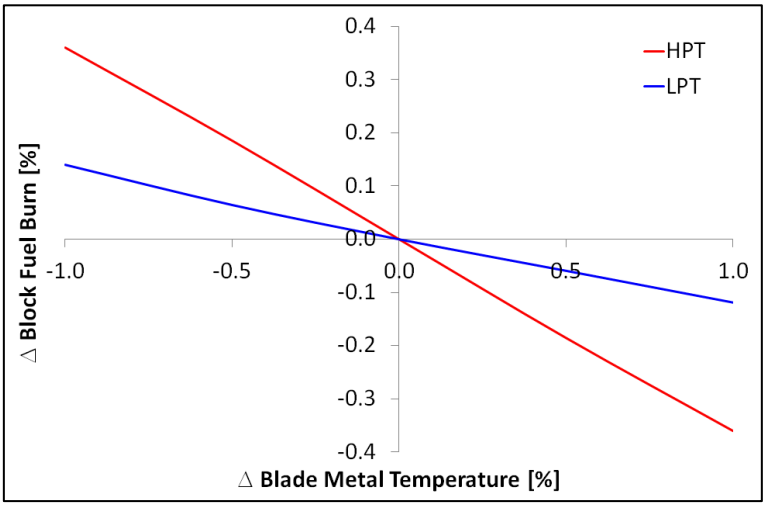

Figure 7.22 – Block Fuel Burn Sensitivity to Blade Metal Temperature

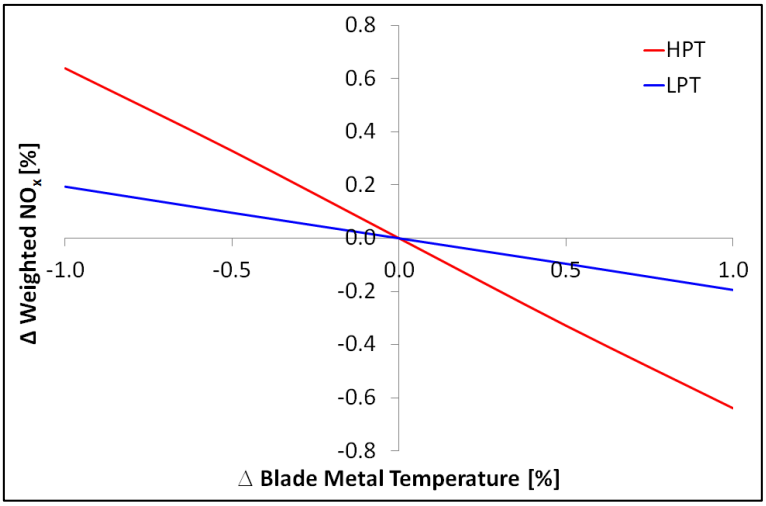

Figure 7.23 – Weighted NO_x Sensitivity to Blade Metal Temperature

Figure 7.24 and Figure 7.25 show the sensitivity of block fuel burn and weighted NO_x emissions to variations in pressure losses within the engine core and bypass. Variations in the bypass duct loss, the core exhaust duct loss and the intercooler matrix losses were found to cause the dominant block fuel burn responses. The block fuel burn response to losses in the intercooler headers were also evaluated but were found to be less significant than those given in Figure

7.24 and Figure 7.25. For the GIRFC, the bypass duct serves as a mixing chamber and the core exhaust duct serves as a mixing chute. Given the irregular geometry of these components, a ±10% variation in the nominal values is considered. The bypass and core exhaust duct losses for the GISFC have been compared with manufacturer data for a similar engine concept and are, therefore, more certain.

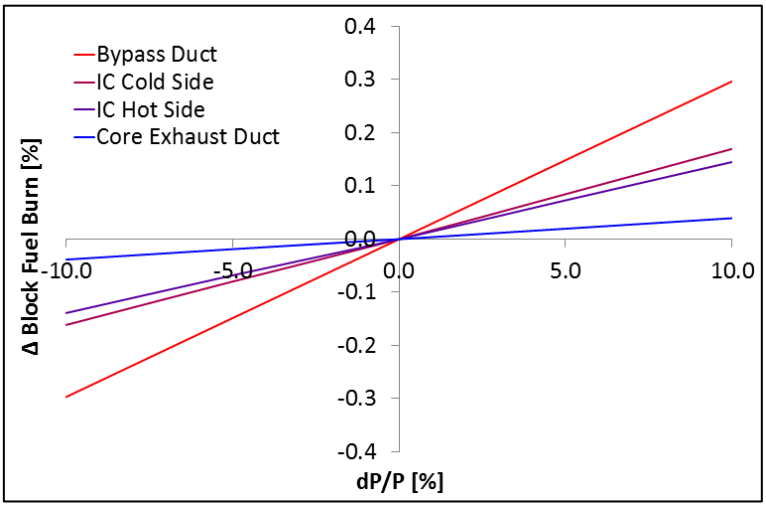

Figure 7.24 – Block Fuel Burn Sensitivity to ΔP/P

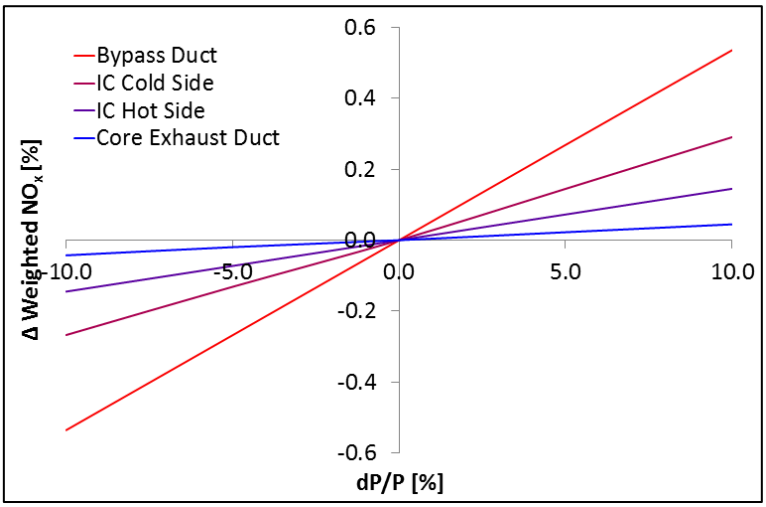

Figure 7.25 – Weighted NO_x Sensitivity to ΔP/P

Figure 7.26 and Figure 7.27 show the sensitivity of block fuel burn and weighted NO_x emissions to variations in component polytropic efficiency. The component polytropic efficiencies were based upon the targets outlined in LEMCOTEC and historical trends from Grönstedt [93]. Given these assumptions, an average improvement in polytropic efficiencies of 1% with respect to

previous NEWAC [12] targets was assumed. The component designs are similar for the GISFC and GIRFC, and therefore, the relative uncertainty is low. As demonstrated in the previous section, the weighted NO_x emissions response to changes in IPC and HPC efficiency is relatively stronger than the block fuel burn response due to changes in both the fuel burn and combustor entry conditions.

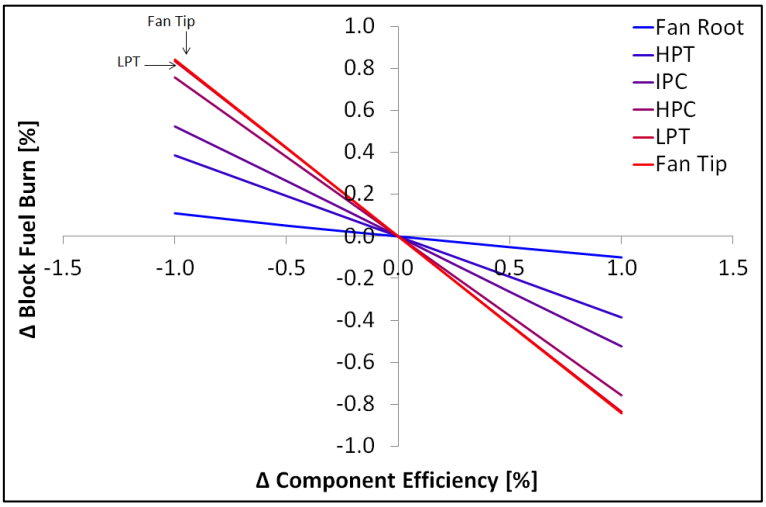

Figure 7.26 – Block Fuel Burn Sensitivity to Component Polytropic Efficiency

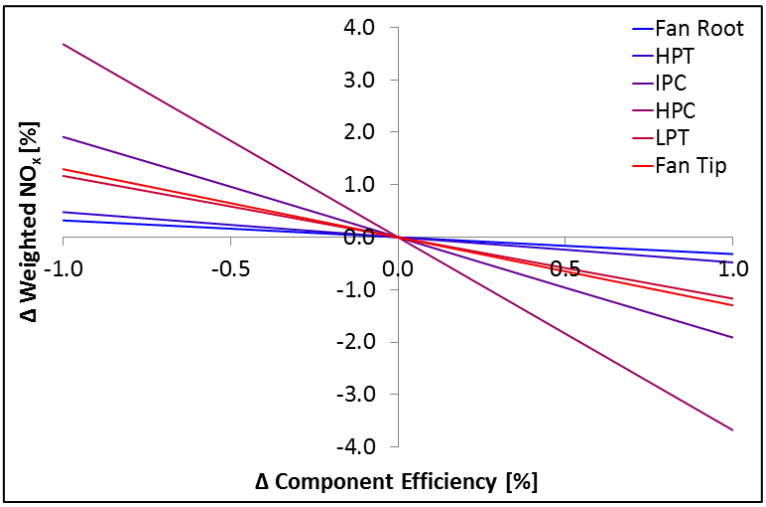

Figure 7.27 – Weighted NO_x Sensitivity to Component Efficiency

7.8.4 Monte Carlo Analysis

The results of the Monte-Carlo analysis are presented in Figure 7.28 and Figure 7.29. The standard deviation in the results is listed in Table 7.15. The standard deviation in the results for the GISFC is lower than for the GIRFC. The confidence in GISFC parameter inputs is higher because the architecture is more conventional and hence is based to a greater degree on existing designs. The standard deviation at the high uncertainty level is approximately 1.5 times that at the low uncertainty level which is equivalent to the assumed ratio of high to low input uncertainty. This suggests output uncertainty varies linearly with different levels of uncertainty for the current input set. This is reflected as well in the sensitivity studies carried out in the previous section.

Standard Deviation	**Low Uncertainty**	**High Uncertainty**
GISFC Block Fuel Burn (with respect to mean) [kg]	148	224
GIRFC Block Fuel Burn (with respect to mean) [kg]	200	300
GISFC Weighted NO_x (with respect to mean) [kg]	73700	110813
GIRFC Weighted NO_x (with respect to mean) [kg]	96667	144979

Table 7.15 – Standard Deviation in Block Fuel Burn and Weighted NO_x

The distributions in Figure 7.28 represent the variation in block fuel burn for the GISFC and GIRFC based on the low uncertainty assumption while the distributions presented in Figure 7.29 represent the variation in block fuel burn for the high uncertainty assumptions. The mean values in each case represent the optimum block fuel burn scenario discussed in the previous sections. From Figure 7.28 and Figure 7.29 it is apparent that the GIRFC will not necessarily demonstrate a reduction in block fuel burn when compared with the GISFC as suggested by the previous analysis. It is clear that there is significant overlap between the predicted results of the GISFC and GIRFC configurations for both the low and high uncertainty scenarios.

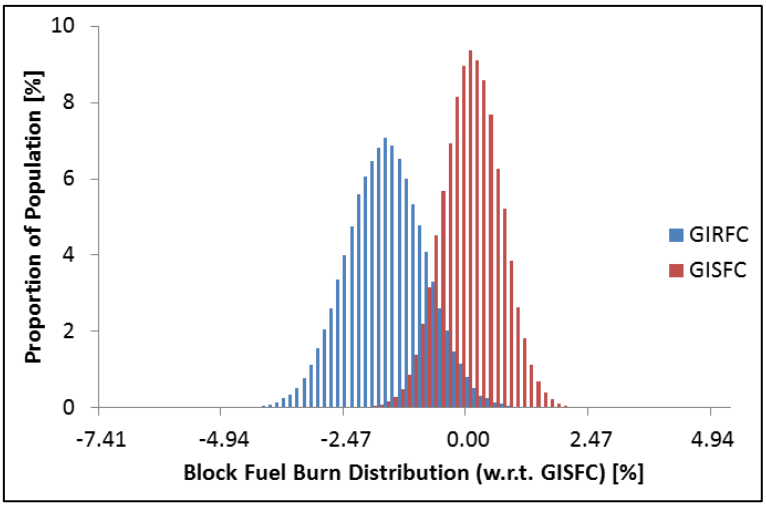

Figure 7.28 – Comparison of GISFC and GIRFC Block Fuel Burn Distribution

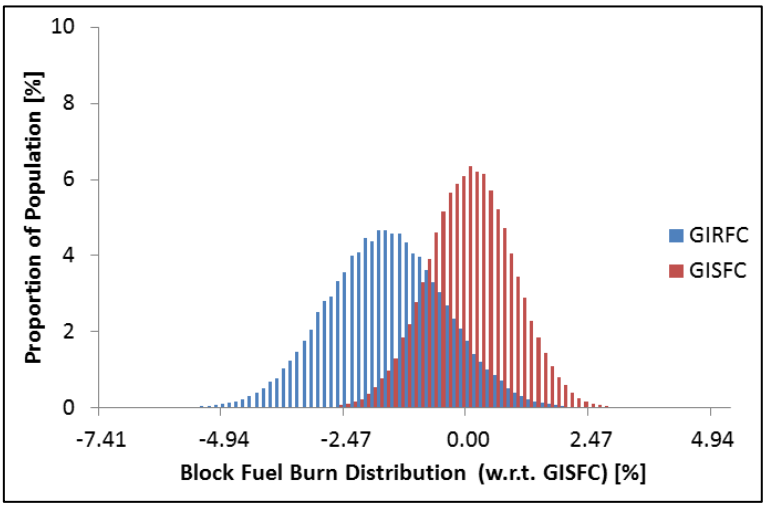

Figure 7.29 – Comparison of GISFC and GIRFC Block Fuel Burn Distribution

The distributions in Figure 7.30 represent the variation in weighted NO_x for the GISFC and GIRFC based on the low uncertainty assumption while the distributions presented in Figure 7.31 represent the variation in weighted NO_x for the high uncertainty assumptions. Unlike for block fuel burn, the GISFC has lower weighted NO_x emissions than does the GIRFC (assuming the optimum block fuel burn operating condition). Again, given the assumed levels of input uncertainty, it is conceivable that the GIRFC could have lower weighted NO_x emissions than the GISFC although this is unlikely.

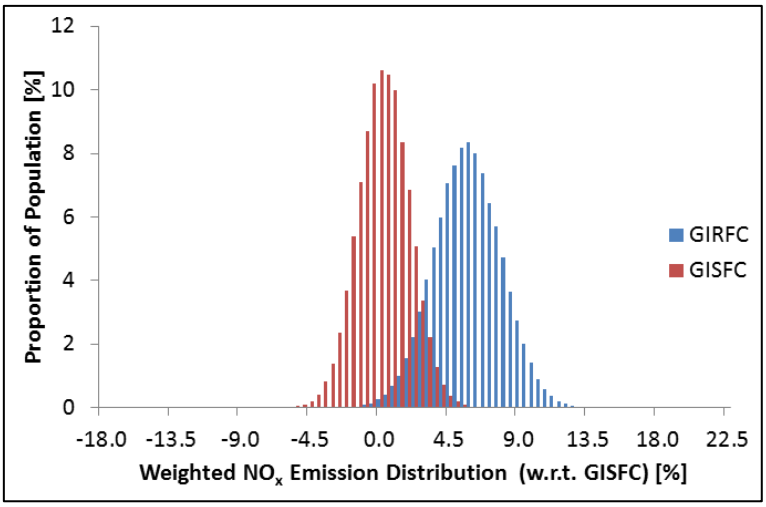

Figure 7.30 – Comparison of GISFC and GIRFC Weighted NO_x Distribution

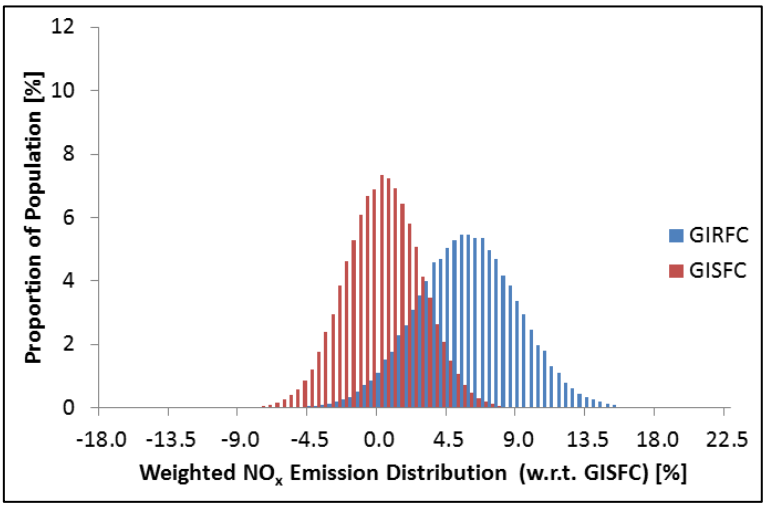

Figure 7.31 – Comparison of GISFC and GIRFC Weighted NO_x Distribution

Figure 7.32 shows the probability that the GIRFC will achieve a given level of improvement over the GISFC given the assumed levels of input uncertainty. The probability that the mean improvement will be achieved is about 50%. This is expected given that the input uncertainty was assumed to be normally distributed and given also the linearity of the combined responses. Clearly, the probability that the GIRFC block fuel burn is lower than that of the GISFC by a given margin increases as the margin is reduced. The probability that the GIRFC block fuel burn will exceed that of the GISFC by any degree is around 85%-95%. Thus, it is highly unlikely that the GISFC block fuel burn actually be lower than that of the GIRFC. Figure 7.33 shows the same relationship for weighted NO_x emissions although in this case the arguments are in favour of the GISFC.

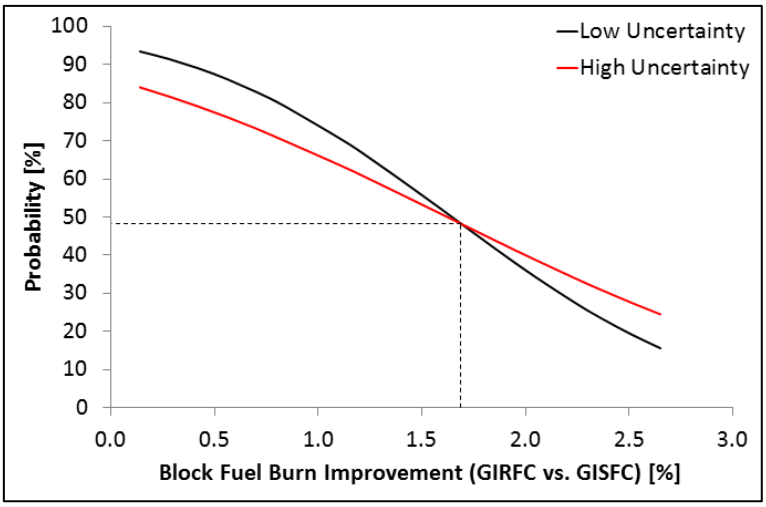

Figure 7.32 – Confidence in GIRFC Block Fuel Burn Advantage

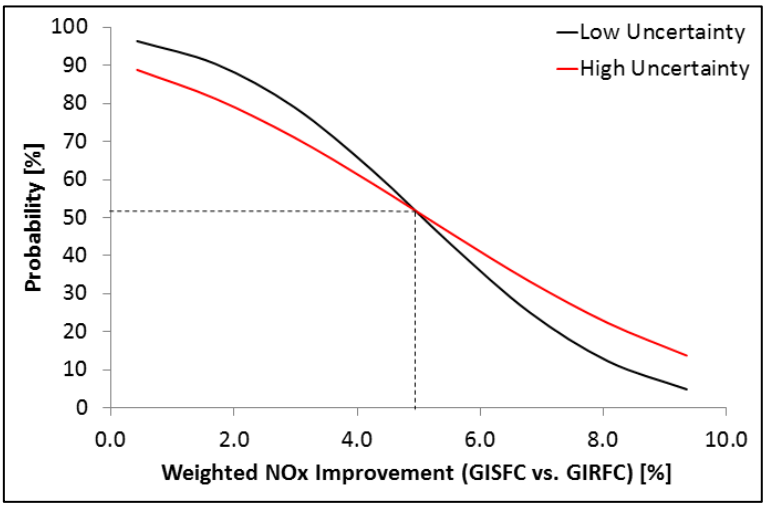

Figure 7.33 – Confidence in GISFC Weighted NO_x Advantage

7.9 Discussion and Conclusion

In this chapter, it was found that the optimum GISFC configuration can deliver a 20% reduction in block fuel burn with respect to the TF2000. The GIRFC can deliver an additional 1.65% reduction in block fuel burn with respect to the GISFC. The optimum GISFC and GIRFC both benefit from very low SFN and high OPRs. The GIRFC benefits from higher OPR than does the GISFC due to the design of the HP-spool which improves the thermal efficiency. The improved thermal efficiency is due in part to the exhaust mixing. Both concepts benefit from high intercooler effectiveness which is reduced at cruise to minimise losses. The GIRFC variable area bypass nozzle need only be varied by about 2% to achieve the optimum cruise operating line while the GISFC requires an additional 4% freedom. From an efficiency perspective alone, the GIRFC would not suffer greatly if the variable area bypass nozzle were removed. This would also reduce the complexity and weight of the design. The impact on the GISFC would be far greater. The variable area bypass nozzle was found to be very effective in reducing the take-off T_4 in both cases. Without the variable area bypass nozzle a larger intercooler would have been necessary for both the GISFC and GIRFC. For minimum block fuel burn, a step-cruise was found to be ideal.

The TF2000, GISFC and GIRFC operations were also optimised for minimum absolute NO_x emissions, minimum weighted NO_x emissions and minimum contrail emissions. The optimum cruise altitude for minimum weighted NO_x was found to be 9500m to which the optimisation was restricted. It was also found that higher intercooler effectiveness tends to reduce both weighted and absolute NO_x emissions through a reduction in combustor temperatures. High intercooler effectiveness at cruise is however detrimental to block fuel burn. The block fuel burn penalty for minimum weighted NO_x was found to be in the order of 5%.

The cruise phase flight altitudes of the TF2000, GISFC and GIRFC were also optimised for minimum persistent contrail emissions. The first test case considered a London to New York flight occurring in the month of January. It was found that an increase in altitude was required to avoid humid regions and therefore prevent persistent contrail formations. By increasing the mean latitude to just below 11900m the contrail emissions in terms of length were reduced by

around 90% for each concept. The block fuel burn penalty for this trajectory change was about 0.44-0.58%. The block fuel burn penalty is more serious for the TF2000 as the altitude change and fuel load are greater. For the July test case it was found that no change was required to the optimal fuel burn trajectory as this already resulted in the minimum contrail emissions. For the nominal trajectory it was found that the GIRFC formed contrails over larger distances than did the GISFC and to a greater degree the TF2000. This is due to the fact that the efficiency of the GIRFC exceeds that of the other engines which tends to aggravate contrail emissions. It is important to note that this study only considered contrail emissions in terms of length of contrails formed. A more efficient engine uses less fuel and therefore its exhaust should contain less water vapour. The relationship between length of contrails, density of contrails and radiative forcing could be an interesting area for future research. This would, however, require the consideration of weather patterns and contrail dispersion.

The uncertainty analysis shows, that assuming reasonable levels of uncertainty, the GIRFC block fuel burn is less than that of the GISFC to a high degree of confidence, and yet maintaining an adequate margin in that improvement is more challenging. The uncertainty in the predicted inputs in the GIRFC design is higher than for the GISFC. Given the responses proposed in this chapter, it is possible to understand the implication of deviations from the nominal configuration. Perhaps the most critical uncertainty is related to the weight of the designs and to the losses in the fan, LPT and bypass. Especially for the GIRFC, where the architecture of the engine is quite unconventional, the weight is very difficult to predict without a detailed mechanical analysis. The interaction of the fan and mixer as well as losses in the bypass duct are also difficult design points that need to be addressed at a higher level of fidelity in order to increase confidence in the design.

8 Conclusions and Recommendations

8.1 Nomenclature

BPR	Bypass Ratio
DDISFC	Direct Drive Intercooled Straight Flow Core Concept
FN	Net Thrust
FPR	Fan Tip Pressure Ratio
GIRFC	Geared Intercooled Reversed Flow Core Engine Concept
GISFC	Geared Intercooled Straight Flow Core Engine Concept
HP	High Pressure
HPC	High Pressure Compressor
HPT	High Pressure Turbine
IPC	Intermediate Pressure Compressor
LDI	Lean Direct Injection
LPT	Low Pressure Turbine
LTO	Landing and Take-Off Cycle
MC	Mid-Cruise
NO_x	Nitrogen Oxides
OPR	Overall Pressure Ratio
P_c/P_h	Ratio of Total Pressure in the Mixing Plane
SFC	Specific Fuel Consumption
SFN	Specific Net Thrust
T_4	High Pressure Turbine Entry Temperature
TO	Take-Off
TOC	Top-of-Climb
V_c/V_h	Jet Velocity Ratio
W_c/W_h	Intercooler Cold Mass Flow to Hot Core Mass Flow Ratio

8.2 Summary

This thesis delivers an original contribution to knowledge by comparing the design, performance, and fuel burn and emission characteristics of a novel GIRFC with those of a conventional GISFC concept. Intercooled turbofan cycles allow higher overall pressure ratios to be reached which gives rise to improved thermal efficiency. In addition, intercooling allows core size to be reduced which facilitates higher bypass ratios. The GIRFC concept is similar to the NEWAC [12] intercooled aero engine concepts but includes a reversed flow core and a mixed exhaust similar to the Garrett ATF3 engine. The GIRFC concept was conceived in order to overcome some of the limitations encountered with previous generations of intercooled aero-engine designs. These limitations included high over-tip leakage losses which limited OPR as well as increased pressure losses and weight due to the intercooler. A full description of these concepts together with a discussion of the main trends in aero-engine design and development has been given in chapter 2.

As has been explained in chapter 3, the sizing and evaluation of the GIRFC was restricted to a level of fidelity expected at the conceptual design stage. The scope of this thesis did not extend to preliminary component design or the detailed evaluation of any single feature. Rather this dissertation evaluated the feasibility of the given concept in order to determine whether it could be a viable option for further design and research effort. The principal features of the GIRFC which were explored in this dissertation were related to:

a. The design and performance on the HP-spool which has been explored in chapter 4.
b. The design and performance of the intercooler matrix which has been explored in chapter 5.
c. The performance implications of the exhaust system design, taking into account the effects of exhaust mixing and variable area nozzle control, which has been explored in chapter 6.

The performance characteristics of both the GISFC and GIRFC concepts have been evaluated in chapter 7 with a special emphasis on the estimation and comparison of mission block fuel burn. The secondary emission characteristics, including contrail, LTO NO_x and cruise NO_x emissions were also assessed for each concept. In chapter 7, the engine cycles have been

optimised for minimum fuel burn. The engine operation and cruise trajectory were also optimised for minimum contrail, LTO NO_x, weighted NO_x and absolute NO_x emissions. A sensitivity analsyis of the main parameters was also carried out within chapter 7. A novel uncertainty evaluation method was also implemented in chapter 7. This was used to guage the uncertainty in the predicted fuel burn advantage and weighted NO_x disadvantage for the GIRFC when compared to the GISFC.

8.3 Main Outcomes

8.3.1 HP-Spool Analysis

The HP-spool design for a GIRFC was compared with the HP-spool design for a DDISFC and with the HP-spool design for a GISFC. As the GIRFC has no inner concentric shafts it was found that the HPC and HPT disc bore diameters, disc heights and mean blade diameters could be significantly reduced when compared to the DDISFC or the GISFC. The reduction in mean blade diameter of the GIRFC was shown to lead to an increase in the HPC and HPT blade heights of 26% with respect to the GISFC and of 45% with respect to the DDISFC for a given flow area. The stage loading was maintained constant in each case leading to a 21% and 31% increase in the HP-spool speed of the GIRFC with respect to the GISFC and DDISFC respectively.

For both the HPC and the HPT a set of size effect curves were derived. These showed that below a critical blade height the component efficiency falls rapidly due to over-tip leakage losses. With an HPC exit and HPT entry blade height of 15mm and 17mm respectively, the DDISFC component dimensions were shown to be already at this critical juncture. The GISFC with an HPC exit and HPT entry blade height of 17mm and 19mm respectively and the GIRFC with an HPC exit and HPT entry blade height of 22mm and 25mm respectively were found to have fairly conservative HP-spool dimensions. This suggested that the GISFC and to a greater degree the GIRFC could sustain high efficiency at even lower core size. This in turn indicated that both concepts could benefit from higher OPR without incurring excessive over-tip leakage loss penalties.

8.3.2 Intercooler Analysis

The dimensions and configuration of the intercooler matrix strongly affect the performance of the component, and therefore were examined in detail. The intercooler performance was also evaluated under different operating conditions. The GIRFC HP-spool is compact, and therefore the intercooler inner diameter and hence width could be reduced more than those of the GISFC. It was found that for the given configurations there was, however, little advantage in reducing the intercooler module widths below 0.15m as narrower modules would result in larger overall dimensions and weight. Therefore, the ideal radial position for the intercooler in both the GISFC and GIRFC was found to be quite similar.

A 1-pass intercooler was found to be the most compact but tallest configuration. A 2-pass intercooler configuration, for equivalent effectiveness and pressure losses, was found to be slightly shorter, heavier and twice as long in the axial direction. Although the 1-pass design would be more compact it would be the more difficult to manufacture given its narrow tube dimensions. In the GIRFC either configuration would be feasible but a more detailed header design could perhaps lead to a preferred option based upon installation challenges.

The intercooler is positioned between the IPC and HPC. A high IPC pressure ratio favours high intercooler effectiveness while a low IPC pressure ratio favours lower HPC work. The IPC-HPC work split was found to favour high work across the HPC where for the GISFC and GIRFC configuration an IPC pressure ratio of about 4.3-4.6 and a pressure ratio exponent of about 0.39-0.43 were found to be ideal. It was found that the intercooler should ideally be sized for the take-off condition and that a high intercooler $W_c/W_{h,TO}$ of about 1.7 should be maintained in order to reduce $T_{4,TO}$. A reduction in intercooler $W_c/W_{h,MC}$, through a contraction of the intercooler variable nozzle area, was found to improve SFC_{MC} by up to 1% through a reduction in intercooler matrix pressure losses. A high $W_c/W_{h,TOC}$ was also found to be beneficial as it led to a reduction in the design core size which enabled higher BPR. This led to a decrease in the absolute mass flow rate through the intercooler at cruise and thus a reduction in the pressure losses at cruise for a given effectiveness.

8.3.3 Exhaust System Analysis

In the GIRFC arrangement the core exhaust is mixed into the bypass stream. The mixing occurs in the bypass duct and the common flow is subsequently exhausted through a single nozzle. The mixer chutes in the GIRFC are positioned far upstream in the bypass duct, and therefore allow for considerable length for proper mixing to occur. It has been suggested in a separate study[1], that the GIRFC can deliver a mixing effectiveness of as much as 80% while causing additional pressure drops of 0.3% and 1% in the mixer cold and hot side respectively. In this work, it was shown that if ideal mixing is assumed a P_c/P_h of 1.0 results in the optimum SFC. However, as the mixing effectiveness is reduced the optimum P_c/P_h increases steadily. For a mixing effectiveness of 80% the P_c/P_h was found to lie in the region of 1.02 to 1.05 (depending on the mixing Mach number). The FPR of the GIRFC was also found to be less than that of the GISFC. The reduction in FPR allows for a reduction in the fan and fan-turbine load which in turn reduces the losses across these components thus contributing to better SFC.

Both the GISFC and GIRFC concepts make use of a variable area bypass nozzle to regulate the operation of the fan. It was found in this work that, for both concepts, the variable area bypass nozzle was able to:

a. Increase the surge margin at take-off.
b. Reduce the $T_{4,TO}$ for both concepts.
c. Improve the SFC_{MC} by shifting the fan working line towards the locus of optimum efficiency.

The fan working line of the GIRFC was found to be steeper than that of the GISFC due to the effects of the mixed exhaust. This means that the fan working line, without the use of a variable area nozzle, operates closer to the locus of optimum efficiency than that of the GISFC. Therefore, it is concluded that a variable area nozzle is of less benefit for the GIRFC in cruise than it is for the GISFC.

---

[1] The mixing chamber model, effectiveness and losses were established by Eduardo Anselmi Palma, a PhD student at Cranfield University, and Andrew M. Rolt, a Senior Systems Specialist at Rolls-Royce plc. Their contribution is kindly acknowledged.

8.3.4 Evaluation and Optimisation of Concepts

In chapter 7, the block fuel burn and secondary emission characteristics of an A330 type aircraft were evaluated incorporating first the TF2000 which is based on the Trent 772, then the GISFC concept and finally the GIRFC concept. The GISFC and GIRFC concepts were optimised in order to identify the configurations which resulted in the minimum block fuel burn. The optimisation routine included the regulation of two variable area nozzles for minimum minimum fuel burn at cruise. Following are the main conclusions drawn from this study:

a. The GIRFC delivers a 1.65% reduction in block fuel burn with respect to the GISFC.
b. Intercooling allows for the size, weight and exhaust jet velocity of the core to be reduced. For an optimum V_c/V_h and fixed FN, the FPR and SFN are also reduced which benefits propulsive efficiency. The optimum GISFC and GIRFC both benefit from an SFN of approximately 114.5m/s and a BPR in excess of 14.7. The FPR of the GIRFC is 1.45 compared with that of the GISFC which is 1.50. The reduction in FPR is possible due to the effects of a mixed exhaust.
c. The GIRFC and the GISFC benefit from high OPRs of 84.3 and 95.8 respectively. The OPR of the GIRFC is significantly higher than that of the GISFC due to the design of the HP-spool as suggested in chapter 4. It was shown that the efficiency of the HPC and HPT of each concept could be maintained down to a blade height of 15mm and 17mm respectively. Given that the GIRFC mean diameter is less than that of the GIRFC the critical blade height was reached at a higher OPR.
d. The SFC advantage of the GIRFC over the GISFC is due to improved thermal efficiency. The GIRFC thermal efficiency advantage is due to higher OPR and the benefits of mixing. The GIRFC block fuel burn advantage is due to the SFC improvement as well as due to a reduction in engine system weight when compared with the GISFC.
e. Both concepts benefit from high intercooler effectiveness at TO and TOC. At cruise both concepts benefit from a significant reduction in intercooler W_c/W_h which reduces effectiveness but also reduces the intercooler matrix pressure losses.

f. Both concepts benefit from a high bypass nozzle area at take-off in order to limit T_4 and hence reduce the intercooler size. To optimise SFC at cruise, the GIRFC requires a 2% increase in nozzle area with respect to TOC. The GISFC requires an additional 4% increase. The GIRFC could perhaps be designed without a variable area bypass nozzle which would result in less complexity and nozzle weight. However, without a variable area bypass nozzle the $T_{4,TO}$ would need to be controlled through intercooling alone, and therefore might require a larger and heavier intercooler.

The secondary emission characteristics of the TF2000, GISFC and GIRFC engines were also assessed and compared in chapter 7. At the condition for minimum block fuel burn the NO_x characteristics demonstrated the following trends:

a. The absolute NO_x emissions of the GISFC and GIRFC concepts, based on a complete mission, were 23% and 19% less than those of the TF2000. The main cause of the reduction can be attributed to the LDI combustor design and to the reduction in fuel burn.
b. The weighted NO_x trends, based on a complete mission, follow the absolute NO_x trends given the similar flight profiles for minimum block fuel burn.
c. The LTO NO_x emissions of the GISFC and GIRFC are significantly lower than for the TF2000 again due to the assumed combustor technology and reduced fuel burn and in spite of the significant increase on OPR. Due to its higher OPR, the LTO NO_x of the GIRFC was found to be slightly higher than that of the GISFC at 35.5g/kN compared to 32.6g/kN.

Based on a complete mission, the cruise flight altitudes of the TF2000, GISFC and GIRFC as well as the operation of the GISFC and GIRFC variable area bypass and intercooler nozzles were optimised for minimum absolute NO_x and minimum weighted NO_x. Given these conditions the following trends were observed:

a. Operation for minimum weighted NO_x requires that the minimum cruise altitude be adopted. The assumed weighting scheme suggests that the impact of NO_x is lower at low altitudes. For minimum weighted NO_x, it was found that a 10% increase in intercooler effectiveness was beneficial as it reduced the combustion temperatures. A 60% reduction in weighted

NO_x was achieved when compared with the optimum fuel burn trajectory and operation. The decrease in weighted NO_x was achieved in spite of an increase of more than 3% in absolute NO_x. The absolute NO_x increased due to an increase in fuel burn and due to elevated T_4 levels which were required to sustain higher thrust at low altitude cruise. The optimum weighted NO_x flight profile resulted in a 4.5% to 5.5% fuel burn penalty.

b. Operation for minimum absolute NO_x requires a cruise altitude similar to that for minimum fuel burn. For minimum fuel burn it was found that a step cruise profile should be adopted. However, for minimum absolute NO_x it was found that a relatively constant cruise altitude should be maintained in order to avoid high combustion temperatures during the climb phase of a step cruise. For minimum absolute NO_x emissions it was found that a 10% increase in intercooler effectiveness was beneficial as it reduced combustion temperatures. When compared with the optimum fuel burn trajectory, the optimum absolute NO_x trajectory resulted in a fuel burn penalty of less than 1% but resulted in an absolute NO_x reduction of more than 1% when compared with the minimum block fuel solutions.

The cruise flight altitudes of the TF2000, GISFC and GIRFC as well as the operation of the GISFC and GIRFC variable area bypass and intercooler nozzles were also optimised for minimum persistent contrail emissions based on a complete mission. Given these conditions the following trends were observed:

a. Engine efficiency and ambient conditions determine whether contrails are formed. If the ambient temperature is close to the critical temperature for contrail formation then engine efficiency can determine effect the likelihood of contrail formation. If the ambient air temperature is distant from the critical temperature for contrail formation than engine efficiency is unlikely to play a key role. If a contrail is formed, its persistence is then a function of the ambient conditions only.

b. For the TF2000, GISFC and GIRFC (assuming the initial engine specifications and trajectory) non-persistent contrails were more prevalent as engine efficiency improved. For the January test case, given cold conditions, the GISFC and GIRFC created an additional 800km of non-persistent contrails while for the July test case, given warmer conditions, an

additional 600km of non-persistent contrails were produced. Persistent contrails were found to form only in regions of very high humidity.

c. For the January test case (assuming the initial engine specifications and trajectory) the amount of persistent contrails formed was very similar for the TF2000, GISFC and GIRFC. In this case, given the colder atmospheric conditions, the regions which allowed for persistence all coincided with flight segments where contrails were formed. Therefore, no difference between the three concepts could be observed in terms of the length of contrails formed.

d. For the July test case (assuming the initial engine specifications and trajectory) the TF2000, given far lower engine efficiency, actually produced 39% less persistent contrails than the GISFC or GIRFC. Given the warmer atmospheric conditions, in this case, the regions which allowed for persistence did not all coincide with flight segments where contrails formed. The probability of persistence was higher for the GISFC and GIRFC given the better engine efficiency leading to higher persistent contrail formation.

e. For the January test case, (assuming the fuel burn optimum engine specifications) the lowest persistent contrail signature was obtained by adopting a high cruise altitude of just below 11900m. This cruise altitude resulted in a 90% reduction in contrail emissions and a 0.5% increase in block fuel burn when compared with the minimum fuel burn trajectory. At high altitude the air is sufficiently dry to eliminate contrail formation. The residual persistent contrails were formed in this case during the initial descent phase where relatively humid atmospheric conditions were present.

f. For the July test case, (assuming the fuel burn optimum engine specifications) the minimum fuel burn and minimum persistent contrail trajectories were almost identical. The atmospheric conditions were on the whole warmer in this case and therefore the humidity levels at the cruise altitude required for minimum fuel burn did not result in persistent contrail formation.

8.4 Limitations and Possible Areas for Future Research

The research presented in this thesis was carried out with the aim of determining the feasibility of a new turbofan concept. The GIRFC appears to deliver a significant block fuel burn advantage over the GISFC concept. The feasibility of the GIRFC will however depend on a number of factors. First of all, the promise of the GIRFC is largely dependent on block fuel burn savings. Currently, the rising cost of fuel and environmental concerns favour efficient aero-engine concepts. This is likely to be the case in the foreseeable future. There are of course a number of aspects which have not been assessed with regards to the reversed flow core concept. Clearly the design is somewhat radical and therefore its actual implementation would carry greater risk than a more conventional engine design. The risk is related both to technology failure where the concept might not meet its stated goals and also development costs. There are of course several competing designs of which the intercooled engine is only one. Each of these concepts carries a risk comparable with that of the GIRFC and would need to be assessed and compared carefully prior to moving forward with an engine design. The uncertainty analysis methodology presented in this thesis is a useful tool for comparing competing concepts. Coupled with a full TERA analysis suite this could easily be extended to compare economic and environmental risks.

The scope of the thesis did not extend to preliminary or detailed design and did not address every component within the engine, instead focussing on the HP-spool, intercooler and exhaust system. The investigations related to the quantification of mission fuel burn and emissions were also restricted to a limited set of test cases where in all cases a simplified mission was assumed. In this thesis, these restrictions were put in place so as to focus on the critical elements of the research required for an initial assessment of the GIRFC concept. In order to build upon the research carried out in this thesis the following activities, which could provide further insight into the GIRFC design and performance, are recommended.

8.4.1 Detailed Mechanical Design

The results presented in this thesis rely upon a suite of interdisciplinary models and tools. During this research it was verified that the level of fidelity of the models was sufficient for

conceptual design work. Moving forward, this research could benefit from higher fidelity investigations. Broadly speaking there is scope for more detailed structural evaluations. The GIRFC configuration incorporates a number of less common design features such as cross-over ducting, an isolated HP-spool and an intercooler which are positioned in the rear engine section. The structural components required to sustain the loads in this part of the engine should be investigated. In addition, the mechanical design of the intercooler and IPC to HPC ducts should be evaluated further and could even be considered for use as a structural component to brace the HP-spool. The mechanical design of the HP-spool and LP-spool also deserve further consideration. The reversed LPT in the GIRFC will set up particular high axial loads, and therefore careful bearing design is necessary. The HP-spool, given its compactness and high rotational speed, should also be designed to a higher level of fidelity taking into consideration whirling speeds, bearings, drive-arms, cooling passages and a complete stress system. The variable area intercooler nozzle and variable area bypass nozzle mechanical design is also an interesting area which could benefit from further research in order to establish practical limits with regards to the change in nozzle area. The LP-system including fan, LPT and gearbox have not been treated in detail in this thesis. Clearly, the mechanical design of these components and also of the nacelle and mixer system will have major implication for the weight of the engine. As suggested in this dissertation, the weight estimation module adapted for this work is subject to a high degree of uncertainty. More detailed mechanical design and material selection could result in a more accurate weight estimate for this concept. Weight has an important effect on block fuel burn and certainly a major increase in the weight of the GIRFC with respect to the GISFC could not be tolerated.

8.4.2 Detailed Aerodynamic Design

The evaluation of the GIRFC concept could also benefit from detailed aerodynamic design. The main components which could benefit from improved aerodynamic characterisation are the exhaust mixer and nacelle, the intercooler headers and the HP-spool. The mixer performance was established in this thesis based on a generic mixer correlation. However, the mixer design is atypical due to the arrangement of the mixer chutes and therefore the accuracy of the

performance estimates would benefit from higher fidelity research into this area. The cross-over ducting which delivers hot exhaust to the mixer passes by the IPC to HPC ducting. The potential impact of heat leakage between the two sides should also be assessed as it could possibly increase the temperature of the core flow prior to intercooling which would reduce the efficiency of the engine. As suggested in this dissertation, the design of the intercooler headers is a challenging aspect of the design. Standard header correlation cannot be used to accurately predict the losses in these components. Qualitatively it can be deduced that the GIRFC should allow for less severe inlet and outlet headers and thereby reduce losses with respect to the GISFC. This aspect of the research would, therefore, benefit from detailed computational and experimental verification. The HPC and HPT size effects at both design and off-design conditions could also be more rigorously addressed through detailed computational and experimental investigation. More detailed aerodynamic investigations would allow for increased accuracy in the estimation of component efficiencies and reduce the uncertainty level that exists when comparing the GIRFC with the GISFC.

8.4.3 Higher Fidelity Modelling and Simulation

It has already been suggested that the weight estimation tool could benefit from an improved understanding of the engine structure. The weight tool is a component based method which relies on empirical correlations. These correlations would benefit from a modern revision in order to accommodate the use of new materials and techniques. While the weight of the novel components within the GIRFC has been accounted for, a more accurate estimation based on detailed design of these components would be beneficial. Ideally the prototyping of key components, such as the intercooler could also help define the associated performance and weight.

The NO_x emissions model estimates the NO_x emissions of an LDI combustor. Clearly, the design and testing of a combustor specifically designed for the type of engine considered in this thesis is required in order to improve the NO_x prediction. Importantly, it is necessary to have more accurate information about how the combustor behaves at altitude and at varying fuel to air ratios. The contrail studies carried out in this thesis are extremely reliant upon atmospheric

conditions. Higher resolution atmospheric data as well as a much wider base of test cases would provide further insight into the implication of engine design on contrail formation. The engine cycle optimisations in this thesis were all carried out with the objective of minimising fuel burn. As the scientific community's understanding of the trade-off between CO_2, NO_x, contrails and other emissions improves, future research could evaluate the GIRFC and GISFC based on minimum environmental impact.

8.5 Conclusion

The primary objective of this research was to compare the GIRFC with a more conventional GISFC concept. The results of this research suggest that the GIRFC, which benefits from higher OPR and a mixed exhaust can deliver a 1.65% improvement in block fuel burn. The GIRFC does however suffer from slightly higher LTO NO_x and cruise NO_x. Under some circumstances the GIRFC, due to its higher efficiency, exhibits slightly higher contrail emissions than similar in-service engines which in this dissertation were represented by the conventional TF2000. However, when compared with the GISFC the difference in contrail emissions is negligible. The results presented in this work also suggest that higher fidelity component modelling as well as improved weight estimation should be the next areas to be addressed in subsequent research efforts. The GIRFC appears to be a good candidate for further research given its advantageous block fuel burn characteristics with respect to the more conventional GISFC.

Appendices

Appendix A Engine Models

A.1 Nomenclature

ΔP/P	Loss in Total Pressure
BPR	Bypass Ratio
FN	Net Thrust
FPR	Fan Pressure Ratio
GIRFC	Geared Intercooled Reversed Flow Core Engine Concept
GISFC	Geared Intercooled Straight Flow Core Engine Concept
GTICLR	Geared Intercooled Long Range Engine Concept from NEWAC
HP	High Pressure
HPC	High Pressure Compressor
IPC	Intermediate Pressure Compressor
ISA	International Standard Atmosphere
LDI	Lean Direct Injection
LEMCOTEC	Low Emission Core Engine Technologies
LP	Low Pressure
M	Mach Number
MC	Mid-Cruise
OPR	Overall Pressure Ratio
PR	Pressure Ratio
PROOSIS	Propulsion Object Oriented Simulation Software
SFC	Specific Fuel Consumption
T_4	High Pressure Turbine Entry Temperature
TERA	Techno-Economic and Environmental Risk Analysis
TO	Take-Off
TOC	Top-of-Climb

A.2 Overview

As part of this research, several engine models were developed in order to estimate the thermodynamic behaviour of different turbofan concepts. The engine modelling activities were carried out in three phases. First, the evaluation, selection and enhancement of the available engine modelling techniques were undertaken. Second, a number of baseline engine models were created and validated against available data. Finally, engine models were created which describe the behaviour of the concepts under investigation. Several engine simulation tools have been used successfully at Cranfield University to model the behaviour of turbofan engines both at a conceptual level and also at higher levels of fidelity. Of note are EVA [52], Cranfield University's Turbomatch and PROOSIS [60]. EVA [52] was used to model the long range engines within NEWAC [12]. This code, while quite sophisticated, was not available for this research. PROOSIS [60] was selected over Turbomatch as it offered more flexibility in terms of problem definition and design. The PROOSIS [60] development environment also facilitated the enhancement of the standard turbo-library as well as the creation of new components.

The capabilities of the PROOSIS [60] turbo-library were compared with the capabilities of EVA [52] and as a consequence several enhancements were made to the PROOSIS [60] turbo-library bleed model, intercooler component, flow splitter, flow mixer, duct component and fan component. A limitation identified in PROOSIS was the instability of the design point calculation. Typically a design point solution is found using a gradient based root-finding algorithm such as a Newton-Raphson method or a Brayton method. The success of these types of algorithms is highly dependent on the quality of the initial solution estimate. To overcome this limitation, a proportional correction strategy was designed and employed in order to obtain design point calculations from relatively generic initial estimates while taking into account large numbers of variables. While this did not allow for the same convergence rate as a gradient based root-finding algorithm it did provide good stability which is necessary for TERA type optimisation studies where the engine definition changes significantly throughout the optimisation.

A.3 The RFC70 Model

The RFC70 engine model represents a Garrett ATF3-6A type engine. The Garrett ATF3-6A is the only reversed flow core turbofan engine in operation. Therefore, this engine was modelled in order to understand the difficulties and challenges which could be encountered with this unique engine type. This engine model was not used in the parametric or TERA type studies performed in this dissertation but served as an initial validation case for the engine simulation tools. The main characteristics of the Garret ATF3 are listed below:

a. Single-stage fan
b. 5-stage axial intermediate-pressure compressor
c. Single-stage centrifugal high-pressure compressor
d. Reverse-flow annular combustor
e. Single-/3-/2- stage high-/fan-/low pressure turbine
f. Mixed-flow exhaust

The main thrust ratings of the Garrett ATF3 are given in Table A.3.1, the maximum permissible temperatures in Table A.3.2 and the SFC levels in Table A.3.3. The remaining information required for the RFC70 model is found in Table A.3.4 which was partly compiled from the referenced sources and partly estimated based on typical component performance for a 1970's type engine.

Condition	FN (kN)
Take-Off (Sea-Level, ISA)	24.2
Cruise (12,200m, M0.8)	5.10
Maximum Continuous (Sea-Level, ISA)	22.6
Flight Idle (Sea-Level, ISA)	3.29

Table A.3.1 – Garrett ATF3 Thrust Ratings [(91) (159)]

Condition	Interstage Turbine Temperature (°C)
Take-Off (5-minute)	1010
Take-Off (5-second transient)	1020
Maximum Continuous	970
Starting	1010
Starting (5-second transient)	1020

Table A.3.2 – Garrett ATF3 Temperature Limits [159]

Condition	SFC (mg/Ns)
Take-Off (Sea-Level, ISA)	14.25
Cruise (12,200m, M0.8)	22.83

Table A.3.3 – Garrett ATF3 SFC [159]

Component	Parameter	Value
Fan	Pressure Ratio	1.55
LPC	Pressure Ratio	5.8
HPC	Pressure Ratio	2.55
Burner	Pressure Loss (ΔP/P)	0.034
	Combustion Efficiency	0.995
Mixing Chute Duct	Pressure Loss (ΔP/P)	0.02
Mixer	Mixing Mach Number	0.4

Table A.3.4 – RFC70 Additional Model Data [159]

The RFC70 engine model was validated with empirical data related to the performance of the Garrett ATF3-6A at the top-of-climb and mid-cruise conditions. Gunston [91] contains the most detailed information about the performance of the ATF3-6A. The discrepancies between the reference data and the model data are all below 1% even at the off-design condition. It is important to point out that the value of this comparison is limited. It does suggest reasonable agreement between the behaviour of the reference engine and model at the given conditions. However, a more complete data set would be required to build a model beyond this level of fidelity.

Parameter	Cruise (Mach 0.8, 12200m)			Take-Off (Mach 0.0, 0m)		
	From Reference	From Model	Error %	From Reference	From Model	Error %
BPR	2.52	2.52	0.00	-	2.78	n/a
FAN PR	-	1.59	n/a	1.50	1.49	-0.67
IPC PR	-	6.19	n/a	5.50	5.49	-0.18
HPC PR	-	2.67	n/a	2.60	2.61	0.38
FN [N]	5100	5100	0.00	24200	24179	-0.08
SFC [mg/Ns]	22.83	22.69	0.60	14.25	14.35	0.71

Table A.3.5 – RFC70 Model Validation

A.4 The TF2000 Model

The TF2000 engine model is based on the Rolls-Royce Trent 772 engine. The Rolls-Royce Trent 772 engine is the reference large turbofan engine for the year 2000 in studies such as NEWAC [(12)] and LEMCOTEC. Therefore, this engine was modelled in order to serve as a baseline for comparison when studying the novel intercooled engine cycles in this research. This engine model was not re-optimised as it was considered to represent the state-of-the-art for the year 2000. Detailed cycle data for this concept is given in chapter 2 and chapter 7 but the main characteristics are listed below:

a. Single-stage fan
b. 8-stage axial intermediate-pressure compressor
c. 6-stage axial high-pressure compressor
d. Annular combustor
e. 1-/1-/4- stage high-pressure /intermediate-pressure /fan- turbine
f. Mixed-flow exhaust

The TF2000 model was validated against reference data provided by the manufacturer. The TF2000 model is intended to show the capability of the engine modelling tools and procedures to capture the technology level and features of an in-service turbofan engine. Figure A.4.1 shows the comparison between a selection of manufacturer thermodynamic data and the equivalent model predicted values. The maximum error is below 2.5% while the mean error is approximately 1%.

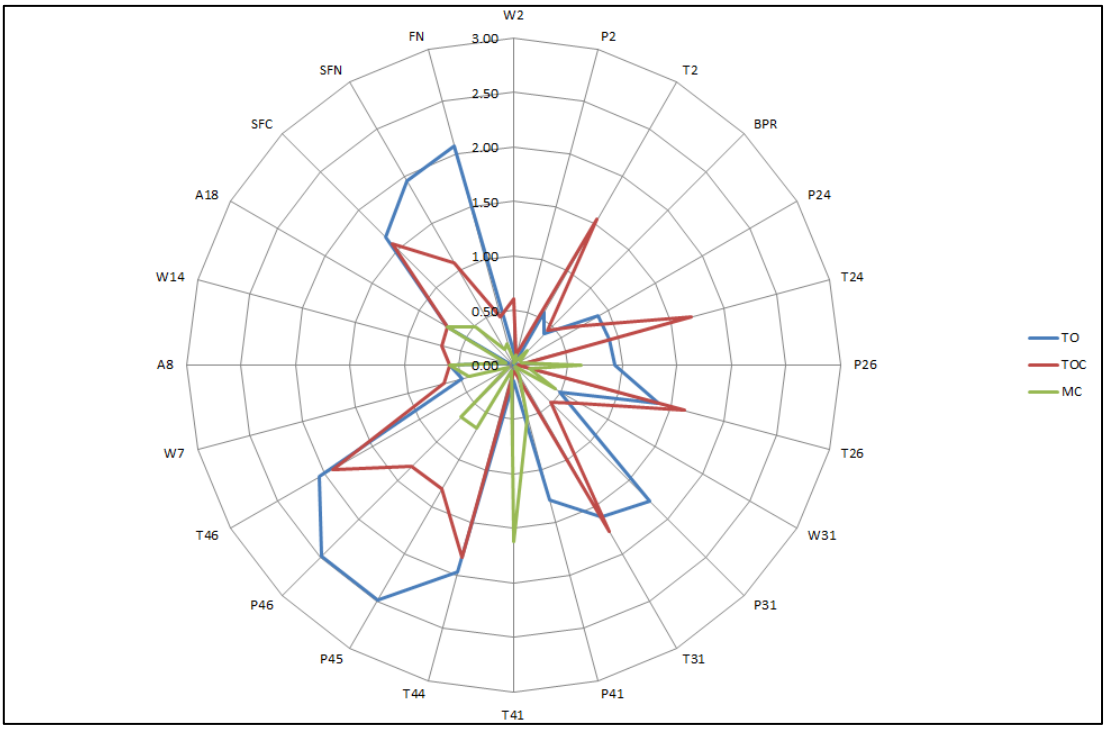

Figure A.4.1 – TF2000 Reference vs. Model Error

A.5 The NEWAC GTICLR

The GTICLR was a concept considered in NEWAC [12]. Currently, there are no intercooled engines in service, and therefore the GTICLR model data from NEWAC [12] was the only reasonable baseline for comparison. The main characteristics of the GTICLR are listed below:

a. Single stage geared fan

b. 7-stage intermediate pressure compressor

c. Intercooled core

d. 9-stage high pressure compressor

e. LDI combustor

f. 2-/4- stage high-pressure /fan- turbine (2-spool)

g. Separate Flow Exhaust

h. Variable area intercooler nozzles

The main specifications of the GTICLR engine are listed in Table A.5.1 for the TOC, MC and TOC conditions. These specifications were established in NEWAC [12] and are based upon data provided by the manufacturer.

Parameter	Units	TOC	MC	TO
FPR	-	1.52	1.48	1.53
IPC PR	-	4.72	4.70	4.54
HPC PR	-	12.70	10.60	11.50
Intercooler Effectiveness	-	0.66	0.61	0.71
T_4	K	1920	1650	1970
OPR	-	79.2	63.8	67.0
SFN	m/s	135	105	209
BPR	-	12.5	11.2	11.6
SFC	mg/Ns	15.8	14.3	10.3
FN	kN	67.3	51.2	252.0

Table A.5.1 – GTICLR Model Specifications

As part of the NEWAC [12] project the GTICLR was modelled using EVA [52]. In this thesis, the GTICLR concept was re-modelled in order to validate the ability of the available tools and methods to represent an intercooled turbofan concept. The GTICLR model in this dissertation was created with the PROOSIS library. The new GTICLR engine model was not re-optimised within this thesis. Rather an updated GISFC model was produced based on the GTICLR but more representative of the expected state-of-the-art in the year 2025. Figure A.5.1 compares a selection of manufacturer thermodynamic data against the equivalent values predicted by the current GTICLR. The maximum error is below 3.0% in all cases while overall the mean error is approximately 1%.

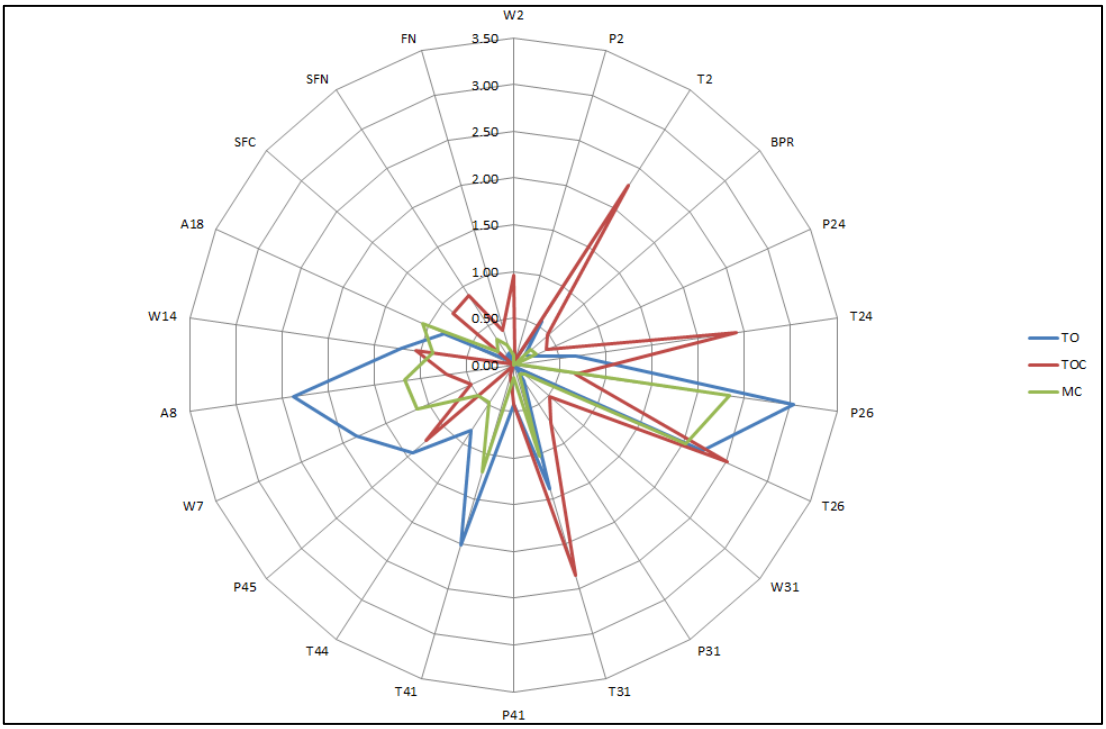

Figure A.5.1 – GTICLR Reference vs. Model Error

A.6 The Initial GISFC and GIRFC Concepts

The main engine concepts which were modelled in this dissertation include a 2-spool GISFC and 2-spool GIRFC. The architecture of the initial GISFC engine is based on the NEWAC [(12)] GTICLR engine which has already been described. The initial GIRFC concept was conceived in order to overcome some of the limitations identified with the NEWAC [(12)] GTICLR engine. Detailed cycle data for the GISFC and GIRFC concepts is given in chapters 0 to 7. The main characteristics of the GISFC and GIRFC are listed below:

a. Single-stage geared fan / 7-stage IPC / 9-stage HPC

b. Intercooled core

c. LDI combustor

d. 2-/4- stage high-pressure /fan- turbine

e. Separate Exhaust [GISFC] / Mixed Exhaust [GIRFC]

f. Straight Flow Core [GISFC] / Reversed Flow Core [GIRFC]

g. Variable area bypass and intercooler nozzles

Appendix B Aircraft Performance Model

B.1 Nomenclature

DATCOM	Data Compendium
ESDU	Engineering Sciences Data Unit
MTOW	Maximum Take-Off Weight
SFC	Specific Fuel Consumption
TERA	Techno-Economic and Environmental Risk Analysis
TOW	Take-Off Weight

B.2 Overview

An aircraft performance model was required in order to study the ramifications of engine design and performance on the mission characteristics of an A330-200 type aircraft. The aircraft modelling activities were divided into two stages. The first stage involved the evaluation and re-development of an existing aircraft performance code. The second phase of the project entailed the validation of the model based on the global objectives. The main objectives of the model were:

a. The determination of the fuel burn profile for a given mission.
b. The determination of the flight time and range of a discrete number of flight segments.
c. The estimation of the aircraft performance both during taxi, take-off and landing.

The aircraft performance model used in this project was a re-development of an in-house Cranfield University tool called HERMES [160]. Different versions of HERMES were used in the VITAL [10] [11] and NEWAC [12] projects in addition to being widely used for both MSc and PhD work within the Department of Power and Propulsion at Cranfield University. Several key limitations were identified which led to the following modifications:

a. A rework of the drag build-up method in order to account for different forms of drag.
b. A lift calculation module was introduced. The introduction of a lift model introduced the ability to account for non-level flight, angle-of-attack and Mach number.
c. New take-off and landing modules were implemented.
d. New numerical techniques were introduced to manage the increased complexity of the lift and drag modules.
e. A state calculation module was introduced in order to allow for the specification of flight speed and range in several different forms.
f. A mission design module was introduced in order to evaluate flight phases individually and to increase the flexibility of the mission definition.
g. A simplified input and output strategy was employed to cater for any mission type.

h. A complete rework of the code was implemented in order to cater for the additional features and to reduce redundancy and unnecessary complexity.

The objective of this thesis was not to develop new methods for modelling the performance of a commercial aircraft. Therefore, a survey of existing modelling techniques was carried out. There are several texts which describe the performance of aircraft including Anderson [161], Jenkinson [162], Raymer [48], Roskam [163] and Torenbeek [164]. One of the most detailed preliminary design methods for evaluating aircraft performance is perhaps contained within the digital DATCOM tool [165]. ESDU[1] also provides many correlations for the prediction of aerodynamic performance. The original HERMES tool was based on the work of Jenkinson [162]. However, it is difficult to find any work in the public domain which describes the validity of this method. The Roskam, DATCOM and ESDU methods are very complex and given the input data requirements were not feasible within the scope of this thesis. Several authors have used the method from Raymer [48] for modelling aircraft performance including Becker et al. [166] and Gur et al. [167]. In Becker et al. [166], a detailed comparison is made between the drag prediction methods of Raymer [48], Torenbeek [164] and Hoerner [168]. The Raymer [48] method was found to compare well with the Hoerner [168] method and to a lesser degree with the Torenbeek [164] method. Given its wide use, the Raymer [48] method has been applied in this thesis and the fundamental components which have been implemented are summarised in the next section. The take-off and landing performance is based on the method suggested by Anderson [161].

B.2.1 Theory

In this section the fundamental equations used for modelling aircraft performance are presented. The aircraft performance model estimates the take-off, flight and landing performance separately. The main flight is further subdivided into several finite segments where for each segment the fundamental equations are solved. The take-off and landing performance is modelled using characteristic equations representative of the entire phase.

[1] The IHS ESDU aerodynamic series contains detailed aerodynamic data regarding aerofoils, wings, bodies, flaps and controls. These can be obtained via subscription from www.esdu.com

During the flight phases, the aircraft is modelled as a steady state point mass. The model considers only vertical flight profiles and angular motion is not considered as the model does not aim to capture transient behaviour which typically occurs over short periods. The fundamental form of the lift and drag equations are shown in Equation (B.2.1) and Equation (B.2.2). Both the lift and drag depend on the estimation of the lift and drag coefficient which form the basis of the aerodynamic module in the aircraft model.

$$L = qSC_L \quad \textbf{(B.2.1)}$$

$$D = qSC_D \quad \textbf{(B.2.2)}$$

$$q = {}^{1}/_{2}\,\rho v^2 \quad \textbf{(B.2.3)}$$

where:

- ρ *air density*
- v *true air speed*
- C_L *lift coefficient*
- C_D *drag coefficient*
- D *drag*
- L *lift*
- q *dynamic viscosity*
- S *reference surface area*

In a commercial aircraft, both the main wing and the tail surface have a lift component. According to Raymer [48], the lift coefficient of the main wing can be estimated according to Equation (B.2.4) which is dependent on a lift-curve slope. For a cambered wing, at zero-angle of attack there is a positive lifting force. In Equation (B.2.4), this is brought about by the α_{0L} term which is the angle of attack required to bring about zero-lift force and is always negative. The angle of attack, which is one of the factors which determines the lift for the main wing, must be adjusted for the tail plane in order to account for downwash from the main wing. In the aircraft model this is taken into account through the use of Equation (B.2.5) and Equation (B.2.6).

$$C_L = (\alpha + i_w - \alpha_{0L})\frac{dC_L}{d\alpha} \quad \textbf{(B.2.4)}$$

$$C_{Lh} = (\alpha_h - \alpha_{0Lh})\frac{dC_{Lh}}{d\alpha} = (\alpha + i_h - \epsilon - \alpha_{0Lh})\frac{dC_{Lh}}{d\alpha} \quad \textbf{(B.2.5)}$$

$$\alpha_h = (\alpha + i_w)\left(1 - \frac{d\epsilon}{d\alpha}\right) + (i_h - i_w) \quad \textbf{(B.2.6)}$$

where:

- α *angle of attack*
- α_{0L} *angle of attack for zero lift from the main wing*
- α_{0Lh} *angle of attack for zero lift from the horizontal stabiliser*
- $\frac{dC_L}{d\alpha}$ *lift-curve slope for the main wing*
- $\frac{dC_{Lh}}{d\alpha}$ *lift-curve slope for the horizontal stabiliser*
- ϵ *downwash angle*
- i_w *main wing incidence angle*
- i_h *horizontal stabiliser incidence angle*
- C_L *lift coefficient for the main wing*
- C_{Lh} *lift coefficient for the horizontal stabiliser*

According to Raymer [48] and also DATCOM [165], the lift-curve slope for a subsonic wing can be estimated according to Equation (B.2.7) and is valid up to the drag divergence Mach number. Similar definitions for the lift-curve slope can also be found in several references including Ojha [169] and Asselin [170]. This equation is derived primarily from lifting line theory, but also accounts for compressibility through the use of the 2D Prandtl-Glauert factor and wing sweep.

$$\frac{dC_L}{d\alpha} = \frac{2.\pi.A}{2 + \sqrt{4 + \frac{A^2\beta^2}{\eta^2}\left(1 + \frac{\tan^2\Lambda}{\beta^2}\right)}}\left(\frac{S_{exposed}}{S_{ref}}\right)F \quad \textbf{(B.2.7)}$$

$$\beta^2 = 1 - M^2 \quad \textbf{(B.2.8)}$$

$$\eta = \frac{\beta C_{l\alpha}}{2\pi} \approx 0.95 \quad \textbf{(B.2.9)}$$

$$F = 1.07\left(1 + \frac{d}{b}\right)^2 \quad \textbf{(B.2.10)}$$

where:

- $\frac{dC_L}{d\alpha}$ *lift-curve slope for the main wing*
- Λ *wing sweep at the thickest chord location*
- η *aerofoil efficiency*
- b *wingspan*

- *d* *fuselage diameter*
- *A* *aspect ratio*
- *F* *fuselage lift factor*
- *M* *Mach number*
- *S* *surface area*
- $C_{l\alpha}$ *lift coefficient*
- C_{Lh} *lift coefficient for the horizontal stabiliser*

Aircraft drag includes parasitic and lift-induced components. The minimum drag of a cambered wing occurs at a positive value of lift. The lift-induced drag should, therefore, be defined according to Equation (B.2.11). For wings of moderate camber it can be assumed that the $C_{Dm} \approx C_{Do}$ [48]. The zero-lift drag coefficient was calculated using a drag build up method.

$$C_D = C_{Dm} + C_{Di} \qquad \textbf{(B.2.11)}$$

$$C_{Di} = \frac{(C_L - C_{Lm})^2}{\pi A e} \qquad \textbf{(B.2.12)}$$

where:

- *e* *Oswald efficiency*
- *A* *aspect ratio*
- C_D *drag coefficient*
- C_{Dm} *minimum drag coefficient*
- C_{Di} *induced drag coefficient*
- C_L *lift coefficient*
- C_{Lm} *minimum lift coefficient*

The general form of the drag build up method used in this model can be described according to Equation (B.2.13). The zero-lift drag coefficient is dependent on a skin-friction coefficient and a form-factor which accounts for pressure-drag. The general form of the equation also takes into account interference effects between components, such as the effect of the nacelle wake on the wing. In addition, the equation makes corrections for miscellaneous drag components (such as drag due to the deployment of either the flaps, the spoiler or the landing gear) and drag due to leakage and protruberances.

$$C_{Do} = \frac{\sum\left(C_{fc} F F_c Q_c S_{wet,c}\right)}{S_{ref}} + C_{D,misc} + C_{D,L\&P} \qquad \textbf{(B.2.13)}$$

where:

- C_{Do} *zero-lift drag coefficient*
- C_{fc} *component skin friction coefficient*
- $C_{D,misc}$ *miscellaneous drag coefficient*
- $C_{D,L\&P}$ *leakage and protuberance drag coefficient*
- FF_c *component form factor*
- Q_c *component interference factor*
- S *wetted area*

As sugested by Raymer [48] , the skin friction coefficient is dependant on Reynolds number and can be described according to Equation (B.2.14) for laminar flow and according to Equation (B.2.15) for turbulent flow. Turbulent flow is typically present over most of the aircraft wetted surface.

$$C_f = \frac{1.328}{\sqrt{R}} \qquad \textbf{(B.2.14)}$$

$$C_f = \frac{0.455}{(\log_{10} R)^{2.58}(1 + 0.144M^2)^{0.65}} \qquad \textbf{(B.2.15)}$$

$$R = \frac{vl}{\nu} \qquad \textbf{(B.2.16)}$$

where:

- ν *kinematic viscosity*
- l *length*
- v *velocity*
- C_f *skin friction coefficient*
- M *Mach number*
- R *Reynolds number*

Several authors propose form factors for the estimation of parasitic drag. Becker et al. [166] carried out a comparison between different sets of form factors and found the set proposed by Raymer [48] to be consistent with those from other leading researchers. The form factors from Raymer [48] are also widely used and accepted in academic work and hence have been implemented in this thesis. These form factors are shown in Equations (B.2.17) to (B.2.19) and are dependent on the geometry of the components. Equation (B.2.17) is the form factor for the wing or tail; Equation (B.2.18) is for the fuselage; Equation (B.2.19) is for the nacelle.

$$F = \left[1 + \frac{0.6}{x/c}\left(\frac{t}{c}\right) + 100\left(\frac{t}{c}\right)^4\right][1.34M^{0.18}(\cos\Lambda_m)^{0.28}] \quad \textbf{(B.2.17)}$$

$$FF = \left(1 + \frac{60}{f^3} + \frac{f}{400}\right) \quad \textbf{(B.2.18)}$$

$$FF = \left(1 + \frac{0.35}{f}\right) \quad \textbf{(B.2.19)}$$

$$f = \frac{l}{d} = \frac{l}{\sqrt{(4/\pi)A_{max}}} \quad \textbf{(B.2.20)}$$

where:

- Λ_m *sweep of the maximum thickness line*
- x/t *thickness to chord ratio of the aerofoil*
- x/c *chordwise location of the aerofoil maximum thickness*
- *l length*
- *d fuselage maximum diameter*
- A_{max} *maximum frontal projected area*
- *M Mach number*

The aircraft model takes into account four other components of parasitic drag which are grouped under the miscellaneous drag term. As recommended by Raymer [48], these include the drag due to the upsweep of the fuselage as given in Equation (B.2.21); the drag due to the landing gear (when deployed) as given in Equation (B.2.22); the drag due to the the flaps (when deployed) as given in Equation (B.2.23); and the drag due to the the spoilers (when deployed) as given in Equation (B.2.24). These equations are simple estimates for the increase in drag that can be expected due to these components. A rigorous miscellaneous drag estimate would require the use of detailed experimental data specific to the aircraft type which in this dissertation were not available. Although no specific relationship was found, Raymer [48] suggests that, in order to account for the leakage and protruberance drag, the parasitic drag shoud be increased by 2% to 5%.

$$C_{D,us} = 3.83u^{2.5}A_{max} \quad \textbf{(B.2.21)}$$

$$C_{D,lg} = 0.00157W_{lg}^{0.73} \quad \textbf{(B.2.22)}$$

$$C_{D,f} = F_{flap}\left(\frac{C_f}{C}\right)\left(\frac{S_f}{S_{ref}}\right)(\delta_{flap} - 10) \quad \textbf{(B.2.23)}$$

$$C_{D,sp} = [0.139 + .419(M - 0.161)^2]A_{base} \quad \textbf{(B.2.24)}$$

where:

- Λ_m *sweep of the maximum thickness line*
- t/c *thickness to chord ratio of the aerofoil*
- x/c *chordwise location of the aerofoil maximum thickness*
- *u upsweep angle*
- *d fuselage maximum diameter*
- A_{base} *frontal projected area*
- A_{max} *maximum fuselage frontal projected area*
- *C aerofoil chord length*
- $C_{D,us}$ *drag coefficient due to the fuselage upsweep angle*
- $C_{D,lg}$ *drag coefficient due to the landing gear*
- $C_{D,f}$ *drag coefficient due to the flaps*
- $C_{D,sp}$ *drag coefficient due to spoiler*
- C_f *flap chord length*
- *S surface area*
- W_{lg} *landing gear weight*

Becker et al. [166] present a method for estimating the effects of compressibility on the drag of a commercial aircraft. This additional drag, also known as wave drag, is typically only accounted for beyond the drag divergence Mach number where many of the equations presented above reach their limit of applicability. However, Becker et al. [166] show that compressibility plays a small role beyond a critical Mach number which is, however, below the drag divergence Mach number. According to Becker et al. [166], the drag divergence Mach number can be esitmated according to the Korn equation extended with simple sweep theory as shown in Equation (B.2.25). The critical Mach number can then be estimated according to Equation (B.2.26) and finally the drag rise can be estimated using Lock's fourth power law shown in Equation (B.2.27). Within the proximity of the ground (at less than half the wing span above the ground), the drag will be reduced due to in-ground effects. The effective drag due to lift can be estimated according to Equation (B.2.28).

$$M_{dd} = \frac{\kappa_A - \frac{C_l}{10\cos^2\Lambda_{0.5}} - \frac{t/c}{\cos\Lambda_{0.5}}}{\cos\Lambda_{0.5}} \quad \textbf{(B.2.25)}$$

$$M_{cr} = M_{dd} - \sqrt[3]{\frac{0.1}{80}} \quad \textbf{(B.2.26)}$$

$$C_{dw} = \begin{matrix} 0 & (if\ M < M_{cr}) \\ 20\ (M - M_{cr})^4 & (if\ M \geq M_{cr}) \end{matrix} \quad \textbf{(B.2.27)}$$

$$\frac{K_{effective}}{K} = \frac{33\left(\frac{h}{b}\right)^{1.5}}{1 + 33\left(\frac{h}{b}\right)^{1.5}} \quad \textbf{(B.2.28)}$$

where:

- $\Lambda_{0.5}$ *mid-wing sweep*
- κ_A *Korn factor*
- t/c *thickness to chord ratio of the aerofoil*
- *b* *wingspan*
- *h* *altitude*
- *u* *upsweep angle*
- C_{dw} *drag rise coefficient*
- C_l *lift coefficient*
- *K* *drag due to lift*
- *M* *Mach number*
- M_{cr} *critical Mach number*
- M_{dd} *divergence drag Mach number*

Take-off performance is estimated according to the procedure outlined in Anderson [161]. The take-off is assumed to consist of two stages; the first an acceleration from stationary to lift-off velocity which is termed “ground roll” and then a pull-up manoeuvre to a given obstacle clearance height. The ground roll distance can be estimated according to Equation (B.2.29) where the thrust, lift and drag are estimated at 70% of the lift-off velocity which is estimated according to Equation (B.2.30).

$$s_g = \frac{W{V_{LO}}^2}{2g[T - D - \mu_r(W - L)]_{0.7V_{LO}}} + NV_{LO} \quad \textbf{(B.2.29)}$$

$$V_{LO} = 1.1V_{stall} \quad \textbf{(B.2.30)}$$

where:

- μ_r *coefficient of rolling resistance*
- *g* *acceleration due to gravity*
- s_g *ground roll distance*
- *D* *aircraft drag*
- *L* *aircraft lift*
- *N* *constant (3 for large aircraft)*
- *T* *engine total thrust*
- *W* *aircraft weight*
- V_{LO} *lift-off velocity*
- V_{stall} *stall velocity*

During the pull up manoeuvre the velocity must be increased from 1.1 V_{stall} to 1.2 V_{stall} at the obstacle clearance height [161]. This results in an average velocity of 1.15 V_{stall}. The ground distance required for the obstacle clearance can be found from Equation (B.2.31) which is dependent on the radius of the pull-up manoeuvre and the required climb gradient to meet the obstacle height clearance requirement.

$$s_a = R \sin \theta_{OB} \quad \textbf{(B.2.31)}$$

$$\theta_{OB} = \cos^{-1}\left(1 - \frac{h_{OB}}{R}\right) \quad \textbf{(B.2.32)}$$

$$R = \frac{(1.15V_{stall})^2}{g(n-1)} \quad \textbf{(B.2.33)}$$

where:

- θ_{OB} *obstacle clearance angle*
- *g* *acceleration due to gravity*
- h_{OB} *obstacle height*
- *n* *load factor (1.19)*
- s_a *ground distance covered while airborne to clear obstacle*
- *R* *pull-up turn radius*
- V_{stall} *stall velocity*

A similar calculation can be made for the landing manoeuvre. In this case, the approach velocity is assumed to be 1.3 V_{stall} and the touchdown velocity is assumed to be 1.15 V_{stall} [161]. The flare velocity is taken as the mean of the approach and touchdown velocities; therefore 1.23 V_{stall}. The approach is assumed to begin from 50ft above the ground. The approach gradient can be

estimated according to Equation (B.2.34), the flare radius according to Equation (B.2.35) and flare height according to Equation (B.2.36). Given this information, it is possible to estimate both the approach distance and the flare distance as can be seen in Equation (B.2.37) and Equation (B.2.38) respectively. Finally the ground roll distance can be estimated according to Equation (B.2.39) which again assumes that the thrust, lift and drag are estimated at 70% of the touchdown velocity. The thrust term allows for reverse thrust and the frictional coefficient assumes braking action.

$$\sin\theta_a = \frac{1}{L/D} - \frac{T}{W} \qquad \textbf{(B.2.34)}$$

$$R = \frac{{V_f}^2}{(n-1)g} \qquad \textbf{(B.2.35)}$$

$$h_f = R(1-\cos\theta_a) \qquad \textbf{(B.2.36)}$$

$$s_a = \frac{50 - h_f}{\tan\theta_a} \qquad \textbf{(B.2.37)}$$

$$s_f = R\sin\theta_a \qquad \textbf{(B.2.38)}$$

$$s_g = NV_{td} + \frac{W{V_{td}}^2}{2g}\left[\frac{1}{T_{rev} + D + \mu_r(W-L)}\right]_{0.7V_{td}} \qquad \textbf{(B.2.39)}$$

where:

- θ_a *obstacle clearance angle*
- μ_r *coefficient of rolling resistance*
- g *acceleration due to gravity*
- h_f *flare height*
- s_a *approach distance*
- s_f *flare distance*
- s_g *ground roll distance*
- D *aircraft drag*
- L *aircraft lift*
- N *time increment for free roll (1-3s)*
- R *flare turn radius*
- T_{rev} *engine thrust (reversed)*
- W *aircraft weight*
- V_f *flare velocity*
- V_{td} *touchdown velocity*

B.3 Model Structure

A simplified schematic of the aircraft performance model is given in Figure B.3.1. The aircraft model relies upon engine performance data which is supplied by the engine performance models within the TERA framework. The aircraft performance model also requires detailed aircraft geometric data which in this dissertation has been obtained from Jenkinson [162] for the A330 aircraft. The aircraft model also requires the definition of the flight trajectory. The flight trajectory can be defined in a number of ways but in this dissertation, each segment node has been defined using Mach number, altitude and thrust level.

The aircraft model further sub-divides the input flight segments so as to increase the problem resolution. The take-off performance is calculated first based upon the method described in the previous section. Then for each flight sub-segment a Newton-Raphson algorithm is used to find the thrust, time and pitch angle required to meet the sub-segment trajectory objectives. The lift and drag coefficients are estimated based on the initial sub-segment flight conditions. If the thrust is an input, as was the case is this dissertation, then the thrust variable is switched off and only the flight time and pitch are used as control variables. After the final flight segment has been resolved, the model then estimates the landing performance based on the method presented in the previous section. Given the stated variable set, it is not possible to know the total amount of fuel required for the mission and the descent range. Therefore, an additional iteration is required in order to adjust the initial fuel load and the cruise length so that the correct range and take-off weight can be determined.

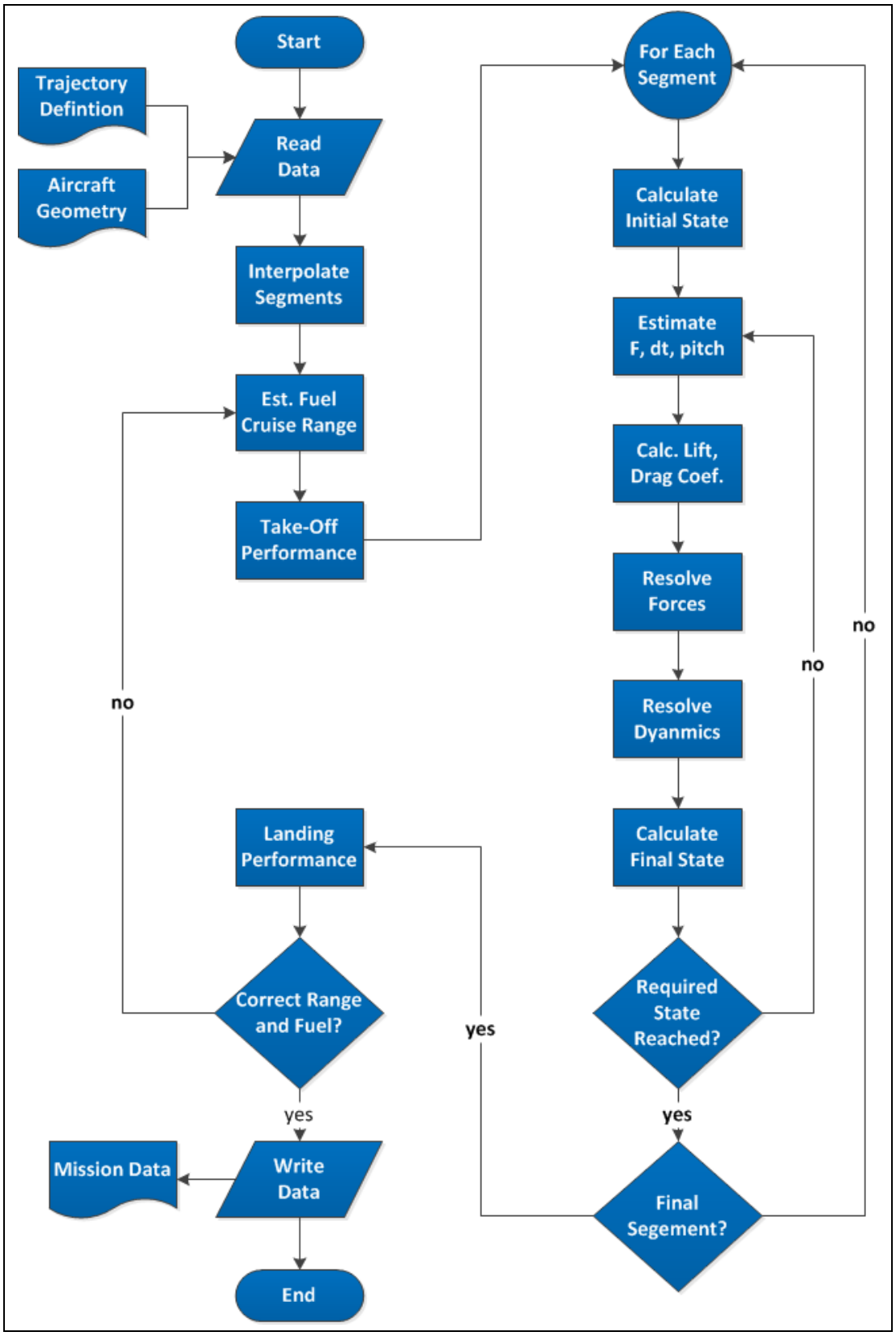

Figure B.3.1 – Simplified Schematic of Aircraft Model

B.4 Validation

The validation of the aircraft model was carried out only for an A330-200 type aircraft. It is important to remember that this model is also dependent on the validity of the accompanying engine model. For these validation cases the TF2000 engine model was used to provide the required engine related information such as SFC for a given thrust demand. Laskaridis [160] describes the use of a payload-range diagram as a suitable validation strategy. The criteria upon which the payload diagram was defined for this case are outlined in Jenkinson [162]. The results are shown in Figure B.4.1. The maximum error in block fuel burn is 1.5%.

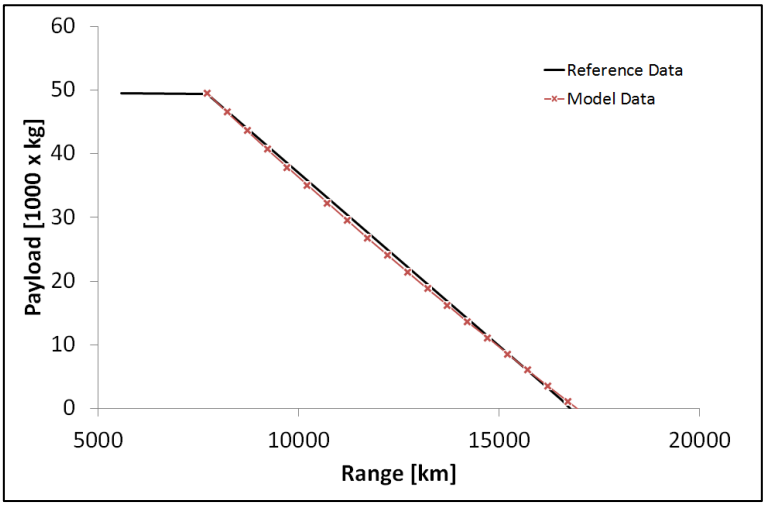

Figure B.4.1 – Comparison of Actual and Model Payload-Range Diagram

The second validation activity carried out was a comparison with block fuel burn values from four actual A330-200 flights described in Aircraft Commerce [171]. The information reported in Aircraft Commerce [171] is summarised in Table B.4.1. As can be seen in Figure B.4.2 the maximum error in block fuel burn was found to be less than 1.0% when comparing the model predictions against the actual mission data.

Payload [kg]	MTOW [kg]	Actual TOW [kg]	Block Fuel [kg]	Block Time [s]	Range [km]
25300	233040	175404	23709	18060	3889
25300	233040	179509	27598	20520	4482
25300	233040	210634	57093	39180	8982
25300	233040	215338	61575	41520	9556

Table B.4.1 – Validation Data from Aircraft Commerce [171]

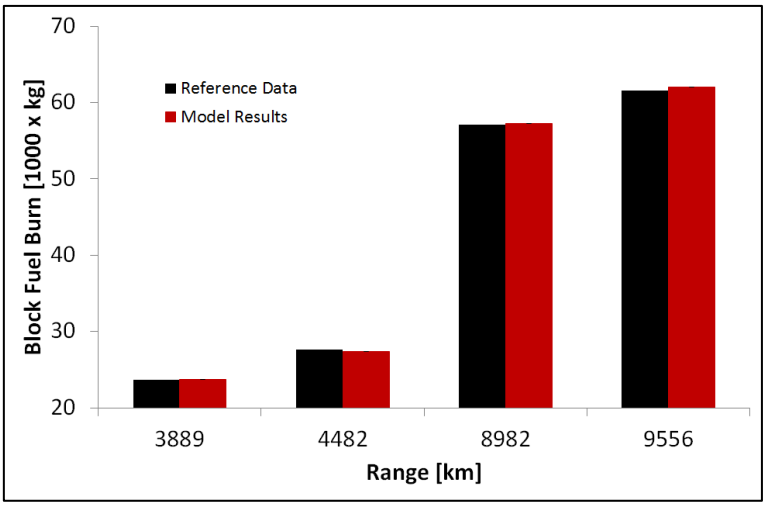

Figure B.4.2 – Comparison of Actual and Model Typical Mission Block Fuel

Kyprianidis [52] suggests that the validation of aircraft and equivalent engine model can be performed by assessing the optimality of the engine matching to the mission. It is typical for the engine to be designed to achieve optimum fuel burn per passenger kilometre for the business case scenario pertaining to the given aircraft type. The business case range for the A330 is approximately 5500km. As shown in Figure B.4.3, the aircraft model's optimum transport efficiency is also at about 5500km which suggests that the aircraft and engine are properly matched.

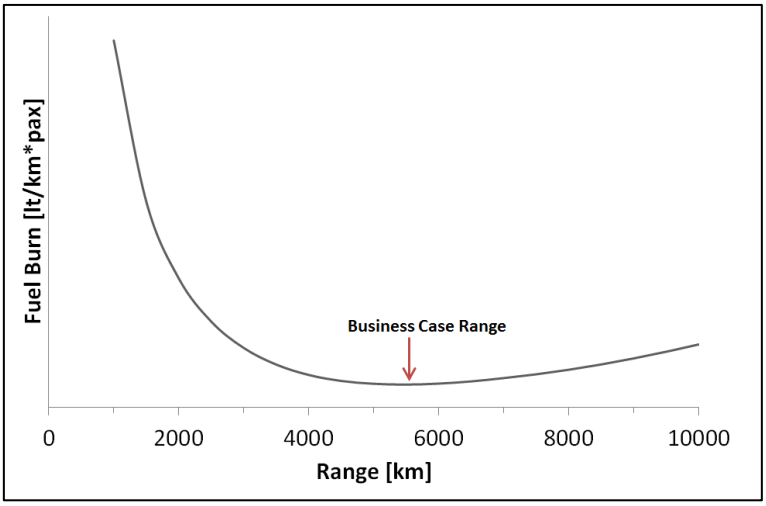

Figure B.4.3 – A330 Model Transport Efficiency

In each validation case there is some ambiguity in the definition of the trajectory. However, the relatively low validation uncertainty suggests that the model can nonetheless be applied with confidence at the conceptual design level of fidelity.

Appendix C Preliminary Engine Weight Estimation Model

C.1 Nomenclature

BPR	Bypass Ratio
DDICLR	Direct Drive Intercooled Long Range Engine Concept from NEWAC
GISFC	Geared Intercooled Straight Flow Core Engine Concept
GIRFC	Geared Intercooled Reversed Flow Core Engine Concept
GTICLR	Geared Intercooled Long Range Engine Concept from NEWAC
HP	High Pressure
OPR	Overall Pressure Ratio
TERA	Techno-Economic and Environmental Risk Analysis
TO	Take-Off
TOC	Top-of-Climb
WATE	Weight Analysis of Turbine Engines
WEICO	Weight and Cost Analysis of Turbine Engines

C.2 Description

A preliminary engine weight estimation model was developed in order to study the implications of design choices on engine weight. The weight modelling activity was carried out in two stages. In the first stage, the development of a conceptual engine weight estimation tool was undertaken. The second stage involved the validation of the weight model against existing information for a number of test engines. The main objective of the weight estimation model was to give an approximation for engine system weight based upon the thermal and fluid characteristics of an engine.

Several weight estimation tools are described in literature. Perhaps the most renowned are the WATE tool [(172)] and the WEICO tool which was used in NEWAC [(12)]. Neither WATE nor WEICO were available for this project and so a different approach was sought. Jackson [(173)], following a review of preliminary weight estimation techniques, found the method of Sagerser et al. [(174)] to be best suited for the preliminary estimation of engine weight. No recent alternative was found, and therefore the method of Sagerser et al. [(174)] formed the basis of the weight estimation in this thesis. The basic weight estimation strategy had to be augmented with other weight estimation techniques for components not included in the original Sagerser et al. [(174)] method. These are presented in the following section.

C.3 Theory

A component based approach was used for the estimation of engine weight within this research. A summary of the weight estimation methods chosen for each component group is presented below.

Fan Weight Estimation (based on Sagerser et al. [174] *method)*

The fan system weight which includes the weight of the fan, fan stator and fan duct is estimated according to Equation (C.3.1). In this method, fan weight largely depends on stage count, fan diameter and aspect ratio. It is suggested also that solidity and tip-speed affect the weight of the fan, and therefore should be included. There are a number of limitations related to this correlation. Firstly, the empirical data used in this method did not consider fan diameters beyond 2.6m. Secondly, modern materials could possibly reduce the weight of the fan beyond what this equation might suggest. However, in the absence of more recent data the standard form of the equation has been retained.

$$W_f = K_f {D_t}^{2.7} \frac{N}{AR_{x,r}^{0.5}} \left[\frac{\sigma_t}{\sigma_{t,ref}}\right]^{0.3} \left[\frac{U_t}{U_{t,ref}}\right]^{0.3} \qquad \textbf{(C.3.1)}$$

where:

- σ_t *fan solidity at the tip (reference value of 1.25)*
- $AR_{x,r}$ *average aspect ratio of rotor*
- *Dt fan diameter*
- K_f *fan weight proportionality factor (reference value of 135)*
- *N number of stages*
- U_t *fan tip speed (reference value of 350m/s)*
- W_f *mass of the fan*

Compressor Weight Estimation (based on Sagerser et al. [174] *method)*

The compressor weight includes the weight of the rotor blades, discs, seals, stator blades and casing. Compressor weight is largely a function of mean diameter, number of stages, tip-speed, as well as compressor length. In this study, the maximum stage loading was obtained from trends suggested in Grönstedt [80]. Equation (C.3.2) and Equation (C.3.3) relate compressor length to mean inlet diameter while Equation (C.3.4) is used for the estimation of compressor weight. The component inlet and outlet Mach numbers and hub-to-tip ratios have been estimated according to trends defined in Grönstedt [80], based on HP-spool designs carried out in this thesis and from annulus design work carried out by Anselmi[1].

$$ {L_c}/{D_{m,1}} = 0.2 + \left(0.234 - 0.218\left[\frac{D_{h,1}}{D_{t,1}}\right]\right)N \qquad \textbf{(C.3.2)} $$

$$ {L_c}/{D_{m,1,ref}} = 0.2 + 0.081N \qquad \textbf{(C.3.3)} $$

$$ W_c = K_c\overline{D_m}^{2.2}N^{1.2}\left[\frac{U_t}{U_{t,ref}}\right]^{0.5}\left[1 + \frac{{L_c}/{D_{m,1}}}{{L_c}/{D_{m,1,ref}}}\right] \qquad \textbf{(C.3.4)} $$

where:

- $\overline{D_m}$ *average mean diameter*
- $D_{m,1}$ *mean diameter of 1st stage*
- $D_{h,1}$ *hub diameter of 1st stage*
- $D_{t,1}$ *tip diameter of 1st stage*
- K_c *compressor weight proportionality factor (reference value of 24.2)*
- L_c *length of compressor*
- N *number of stages*
- U_t *tip speed (reference value of 335m/s)*
- W_c *mass of the compressor*

[1] Eduardo Anselmi Palma, a PhD student at Cranfield University, is investigating in his PhD the mechanical arrangement and losses within the GISFC and GIRFC concept.

Turbine Weight Estimation (based on Sagerser et al. [174] *method)*

The turbine weight includes the weight of the rotor blades, discs, seals, stator blades and casing. In this method turbine weight is a function of mean diameter, stage count and tip-speed. In this study, the maximum stage loadings in accordance with the recommendations outlined in Grönstedt [80] were assumed. The component inlet and outlet Mach numbers and hub-to-tip ratios have been estimated according to trends defined in Grönstedt [80], based on HP-spool designs carried out in this thesis and from annulus design work carried out by Anselmi[1].

$$W_t = K_t \overline{D_m}^{2.5} N \overline{U_m}^{0.6} \qquad \textbf{(C.3.5)}$$

where:

- $\overline{D_m}$ *average mean diameter*
- K_t *turbine weight proportionality factor (reference value of 24.2)*
- N *number of stages*
- $\overline{U_m}$ *average mean blade speed*
- W_t *mass of the turbine*

Combustor Weight Estimation (based on Sagerser et al. [174] *method)*

The combustor weight is taken to include the weight of the inner and outer casing, liner and fuel nozzles. In this method, combustor weight is mainly a function of the combustor mean diameter. Sagerser et al. [174] were not able to establish the effect of combustor pressure or length due to non-uniformities in reported combustor weights.

$$W_b = K_b \overline{D_m}^{2.0} \qquad \textbf{(C.3.6)}$$

where:

- $\overline{D_m}$ *average mean diameter*
- K_b *combustor weight proportionality factor (reference value of 390)*
- W_b *mass of the combustor*

[1] Eduardo Anselmi Palma, a PhD student at Cranfield University, is investigating in his PhD the mechanical arrangement and losses within the GIRFC concept.

Weight of Structure (based on Sagerser et al. [174] *method)*

Sagerser et al. [174] do not propose specific correlations for the remainder of the structure which includes the engine mounts, bearings, bearing supports, shafts, inner wall of fan duct and transition sections. However, it is suggested in this method that as a first estimate it can be assumed that the weight of the component already described should be scaled up by a factor of 1.18 to cater for these elements.

Intercooler Weight Estimation (based on Onat and Klees [175] *method)*

Sagerser et al. [174] do not provide a weight estimation method for an intercooler. Therefore, a method proposed by Onat and Klees [175] has been adopted for this work. The method forms part of the NASA WATE-2 code. The heat exchanger weight estimation for a fixed type intercooler is based on Equation (C.3.7). This equation is limited to the estimation of the intercooler matrix weight. Specific relationships for the estimation of header and intercooler structural weight were not found. Therefore, a correction factor was used to account for the additional weight as a function of the matrix weight. In this method, it is suggested that the casings, mounting hardware and manifolds could double the weight of the heat exchanger. The wall thickness of the tubes was established based on a limit hoop stress.

$$W_{ic} = k_{ic}\rho N_t L_t \pi (R_o^2 - R_i^2) \qquad \textbf{(C.3.7)}$$

where:

- ρ *tube material density*
- k_{ic} *proportionality factor to account for structural weight*
- L_t *length of intercooler tubes*
- N_t *number of intercooler tubes*
- R_i / R_o *internal / external tube diameter*
- W_{ic} *mass of the intercooler*

Gearbox Weight Estimation (based on Pera et al. [134] method)

Pera et al. [134] provide a simple method, shown in Equation (C.3.8), for the estimation of planetary gearbox weight. In this equation the gearbox weight is shown to be proportional to the input torque. The gearbox weight is also determined by the gear ratio.

$$W_{gb} = k_{gb} Q K_w \qquad \textbf{(C.3.8)}$$

where:

- Q *input torque (Nm)*
- K_{gb} *gearbox weight proportionality factor (recommended value of 0.001129)*
- K_w *weight factor (≈2 for a planetary gearbox and gear ratio of 3)*
- W_{gb} *mass of the gearbox*

Nacelle Weight Estimation (based on Beltramo et al. [176] method)

The nacelle weight estimation method is based on a scaling procedure from Beltramo et al. [176]. The method relies upon the scaling of an existing nacelle based on critical nacelle dimensions. The baseline nacelle dimensions were obtained from the results of the NEWAC [12] project where engine concepts of similar size and type were studied. The main nacelle dimensions were estimated according to Equations (C.3.9) to (C.3.10). The weight of each nacelle section was then calculated according to Equations (C.3.11) to (C.3.15).

$$D_f = \left(\frac{D_f}{L_i}\right) L_i = \left(\frac{D_f}{L_f}\right) L_f = \left(\frac{D_f}{L_{ex}}\right) L_{ex} = \left(\frac{D_f}{L_{tr}}\right) L_{tr} \qquad \textbf{(C.3.9)}$$

$$D_{ft} = \left(\frac{D_{ft}}{L_c}\right) L_c \qquad \textbf{(C.3.10)}$$

$$W_f = 1.9 \times \left(\pi \times \left(3.28084\ L_f\right) \times \left(3.28084 \times D_f\right)\right) \times 0.45 \qquad \textbf{(C.3.11)}$$

$$W_c = 1.9 \times \left(\pi \times (3.28084\ L_c) \times \left(3.28084 \times D_{ft}\right)\right) \times 0.45 \qquad \textbf{(C.3.12)}$$

$$W_i = \left(2.5 + 0.02388 \times \left(3.28084 \times D_f \times 12\right)\right) \times \left(\pi \times (3.28084 \times L_i) \times \left(3.28084 \times D_f\right)\right) \times 0.45 \qquad \textbf{(C.3.13)}$$

$$W_{ex} = \left(2.5 + 0.03630 \times \left(3.28084 \times D_f \times 12\right)\right) \times \left(\pi \times (3.28084 \times L_{ex}) \times \left(3.28084 \times D_f\right)\right) \times 0.45 \qquad \textbf{(C.3.14)}$$

$$W_{tr} = \left(0.218 \times \left(3.28084 \times D_f \times 12\right)\right) \times \left(\pi \times (3.28084 \times L_{tr}) \times \left(3.28084 \times D_f\right)\right) \times 0.45 \quad \textbf{(C.3.15)}$$

where:

- *c* *core cowl*
- *ex* *exhaust*
- *f* *fan*
- *ft* *fan turbine*
- *i* *intake*
- *tr* *translating part (adjustable geometry for thrust reverser / variable nozzle)*
- *D* *diameter*
- *L* *length*
- *W* *nacelle weight*

C.4 Model Structure

The model structure for the preliminary weight estimation tool is shown in Figure C.4.1. The main inputs required by the model include Mach numbers, mean diameters at component interfaces as well as tip-velocities. Thermodynamic data is required from the engine models in order to estimate annulus areas and stage numbers. The weight estimation of each component is carried out individually except for interdependencies related to the shaft rotational speed. The output file contains the weight breakdown, main dimensions and total engine weight.

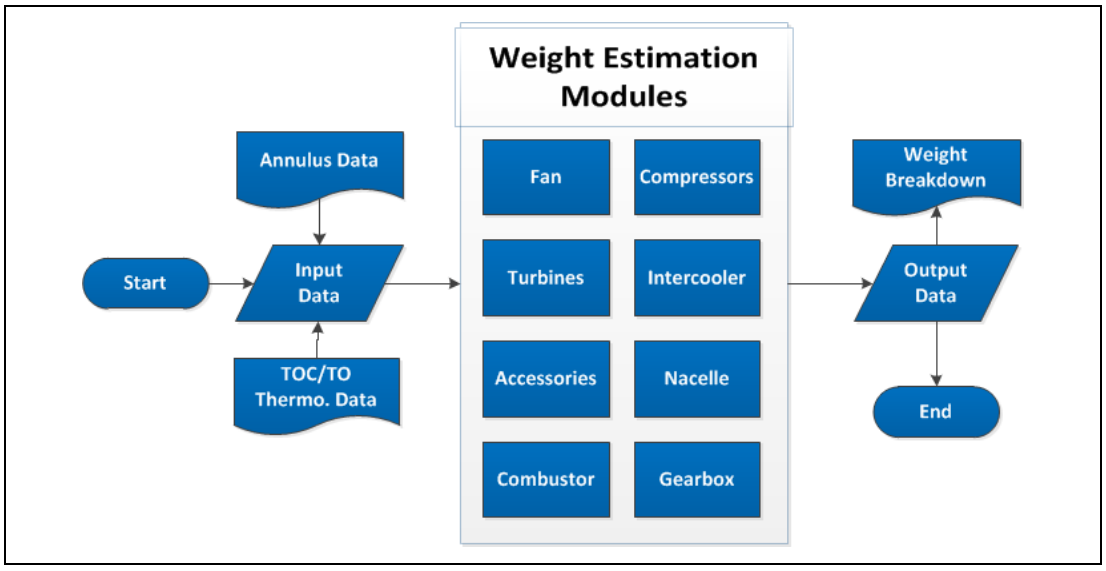

Figure C.4.1 – Simplified Schematic of the Weight Estimation Tool

C.5 Validation

In order to confirm the ability of this model to meet the stated objectives, the weight of three test engines were estimated. The engine types evaluated included the Trent 772, the NEWAC [12] DDICLR and the NEWAC [12] GTICLR. The Trent 772 was chosen in order to assess an existing engine type. As no in-service intercooled engine exists, the NEWAC [12] DDICLR and GTICLR were chosen in order to assess novel features such as intercooling, gearing and high OPRs and BPRs. The original weight estimates for these two engines were made using WEICO.

Table C.5.1 shows a comparison between the actual weight of the engines or concept engines and the weight predicted by the current model. Sagerser [174] claims that the methods presented can lead to a prediction with less than ±10% error. A similar claim is made by Onat and Klees [175] for the WATE-2 tool. However, Lolis et al. [158] suggest that the actual error in these types of estimates can be as large as ±20%. The maximum error in the weight estimates presented in Table C.5.1 is only 6.2% which suggests that the tool is well calibrated to the given engine types. It must be stated, however, that the sample size is quite small and that the DDICLR and GTICLR comparisons were made against the prediction of another model which itself cannot be validated. The large uncertainty in this prediction is taken into account in this thesis.

	Reference Weight	**Predicted Weight**	**Error**
	[kg]	**[kg]**	**%**
Trent 772 (actual)	4785*	4743*	-0.9
NEWAC [12] DDICLR (model)	7059	6993	-0.9
NEWAC [12] GTICLR (model)	7365	6906	-6.2
**not including nacelle*			

Table C.5.1 – Comparison of Reference Engine and Model Predicted Weight

Appendix D Contrail Prediction Model

D.1 Nomenclature

esi	Saturation Pressure Over a Surface of Ice
esw	Saturation Pressure Over a Surface of Water
CIMO	Commission for Instruments and Methods of Observation
ITD	Integrated Technology Developer
SGO	Systems for Green Operations

D.2 Description

A contrail prediction model was developed in order to study the implications of engine design choices and trajectories on contrail emissions. The initial contrail prediction modelling was carried out as part of the CleanSky SGO ITD. The first version of the contrail prediction model was created in collaboration with Pervier[1]. A second version of the tool was created for use in the research effort and is outlined in this section. The development of the tool was carried out in three phases. First, version 1.0 of the tool was built. Secondly, version 1.0 was validated and documented. Finally, the tool was re-built, its capabilities enhanced and the model was then re-validated to ensure that the changes had not compromised its capabilities. Version 2.0 of the contrail prediction tool was intended to deliver the following capabilities:

a. To predict the formation of contrails and persistent contrails for discreet flight segments.
b. To estimate the overall length of contrails and persistent contrails formed.
c. To generate an Appleman diagram for the identification of critical temperatures for contrail formation across a range of pressure altitudes.

A detailed survey of the various existent theories on contrail formation as well as the main methods for predicting the formation of contrails is given in Shull [(139)]. The basis for much of the work done in contrail forecasting is based on the original work of Appleman [(177) (cited in (139))]. Schrader [(178) (179)] however proposes a useful methodology for determining whether contrails will be formed. This methodology is directly related to the efficiency of the engine as well as the atmospheric conditions which makes it ideal to use within cycle comparisons.

D.3 Theory

The exhaust plume of an aircraft engine contains unsaturated water vapour which is liberated during the combustion phase. The wake of the engine is composed of the exhaust plume as well as ambient air. Mixing occurs rapidly in the engine wake, and therefore can be assumed to

[1] H. Pervier was a PhD student at Cranfield University during the development phase of the Contrails Prediction Model. His contribution towards the contrail prediction tool is kindly acknowledged.

occur adiabatically and isobarically. Assuming constant specific heat capacity in the wake, the specific humidity of the exhaust plume decreases linearly with temperature [140] [180] . The contrail factor, shown in Equation (D.3.1), is defined as the ratio between the moisture content and temperature change in the engine plume.

$$\mathrm{C} = c_p \frac{\Delta q}{\Delta h_p} \qquad \textbf{(D.3.1)}$$

where:

- c_p *specific heat capacity of air at constant pressure*
- h_p *mass specific plume enthalpy*
- q *vapour / air mass ratio*
- C *contrail factor*

For a given temperature, if the specific humidity decreases linearly then so does the partial pressure of vapour as can be seen in Equation (D.3.2). The contrail factor can, therefore, be used to define the mixing line gradient as shown in Equation (D.3.3) [140]. The mixing line gradient relates the change in vapour partial pressure to the change in temperature.

$$\frac{\mathrm{e}}{\mathrm{p}} = q \frac{\mathrm{R}_{air}}{\mathrm{R}_{H_2O}} = \frac{\mathrm{q}}{\varepsilon} \qquad \textbf{(D.3.2)}$$

$$G = \frac{\Delta e}{\Delta T} = \frac{\mathrm{p}}{\varepsilon}\mathrm{C} \qquad \textbf{(D.3.3)}$$

where:

- ε *ratio of H_2O to air gas constants (0.622)*
- e *vapour pressure*
- p *ambient pressure*
- q *vapour to air mass ratio*
- C *contrail factor*
- G *mixing line slope*
- R *gas constant*
- T *vapour temperature*

If during the mixing process the exhaust plume becomes saturated (or supersaturated) with respect to a water surface, then a contrail will form. In order to determine whether the mixing results in saturation of the exhaust plume, it is useful to plot the mixing line as well as the

vapour saturation curves on a hygrometric chart. As described by Vomel [181], there are several relationships which approximate saturation pressure over a surface of water or ice at different ambient temperatures. For the initial formulation of this study, two different relationships were used. Both the Goff Gratch equations as well as the CIMO equations are widely used, and therefore were thought appropriate for counter verification.

$$\log_{10} e_w = \left[-7.90298\left(\frac{T_s}{T}-1\right)\right] + \left[5.02808\left(\frac{T_s}{T}\right)\right] - \left[1.3816\mathrm{e}^{-7} \times 10^{11.344\left(1-\frac{T}{T_s}\right)} - 1\right] + \left[8.1328\mathrm{e}^{-3} \times 10^{-3.49149\left(\frac{T_s}{T}-1\right)} - 1\right] + [\log_{10} e_s] \quad \textbf{(D.3.4)}$$

Goff Gratch Vapour Saturation Pressure over a Surface of Water

$$\log_{10} e_i = \left[-9.09718\left(\frac{T_0}{T}-1\right)\right] - \left[3.56654\ \log_{10}\left(\frac{T_0}{T}\right)\right] + \left[0.876793\left(1-\frac{T}{T_0}\right)\right] + [\log_{10} e_o] \quad \textbf{(D.3.5)}$$

Goff Gratch Vapour Saturation Pressure over a Surface of Ice

$$e_w = 6.112e^{\frac{17.62T}{243.12+T}} \quad \textbf{(D.3.6)}$$

CIMO Vapour Saturation Pressure over a Surface of Water

$$e_i = 6.112e^{\frac{22.46T}{272.62+T}} \quad \textbf{(D.3.7)}$$

CIMO Saturation Pressure over a Surface of Ice

where:

- e_w *vapour saturation pressure over a surface of water*
- e_i *vapour saturation pressure over a surface of ice*
- e_s *vapour saturation pressure at steam point (1013.25hPa)*
- e_o *vapour saturation pressure at ice point (6.1173hPa)*
- T *vapour temperature*
- T_o *vapour saturation temperature at ice point (273.16K)*
- T_s *vapour saturation temperature at steam point (273.15K)*

There is little variance between the two relationships as can be seen in Figure D.3.1. However, the Goff-Gratch equations have been widely used in contrail prediction work and were, therefore, used in this dissertation.

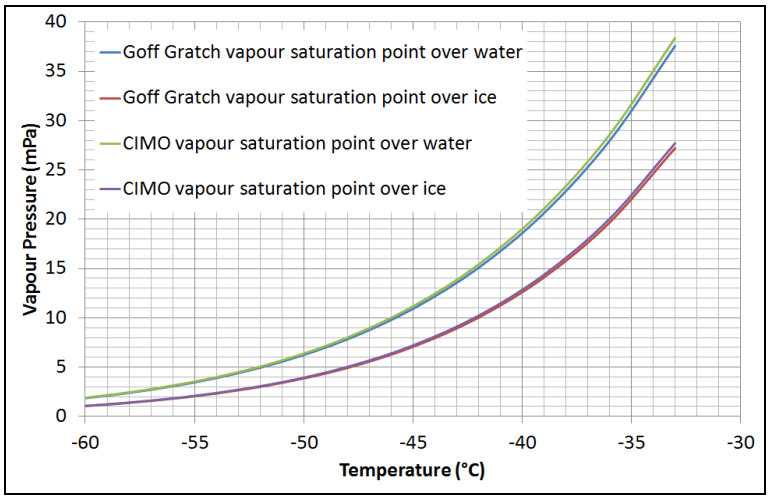

Figure D.3.1 – Vapour Saturation Curves

Figure D.3.1 shows a number of mixing lines superimposed on a hygrometric chart. If the mixing line crosses the vapour saturation (w.r.t. a surface of water) a contrail is likely to form. In such a case the exhaust plume becomes super-saturated and water droplets are likely to form. Particulate emissions and to some extent particles in the atmosphere serve as condensation nuclei leading to the formation of ice or mixed-phase clouds. Without these condensation nuclei, water vapour would exist in a supercooled state down to about 235K below which spontaneous freezing would occur [(141)]. Given these conditions, in a mixed-phase cloud water droplets rapidly evaporate while, on the other hand, ice-particles tend to grow through vapour deposition in what is known as a Wegener–Bergeron–Findeisen process [(182)]. Two types of contrails can be formed; persistent contrails that evaporate only after hours and non-persistent contrails that evaporate almost immediately [(138)]. Persistent contrails can only exist in an environment which is supersaturated with respect to a surface of ice but subsaturated with respect to a surface of water. This is demonstrated in Figure D.3.3. Clearly, persistent contrails are of main concern as the effects of non-persistent contrails are short lived.

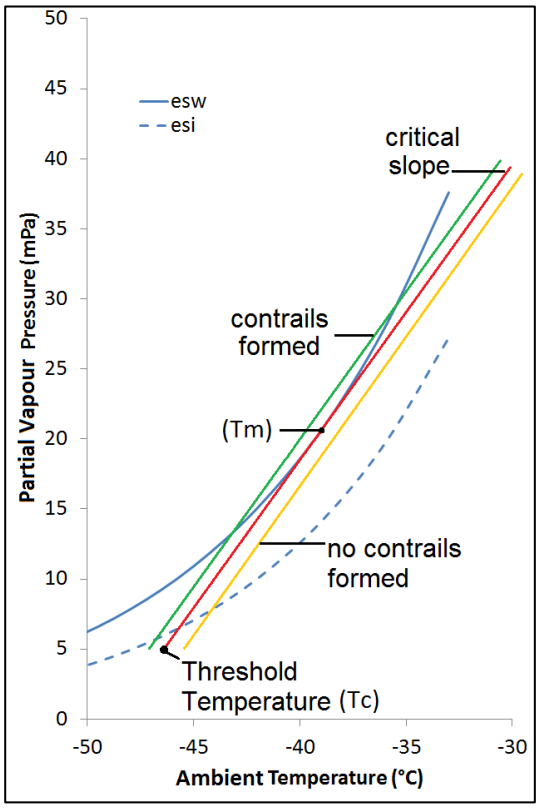

Figure D.3.2 – Contrail Mixing Lines

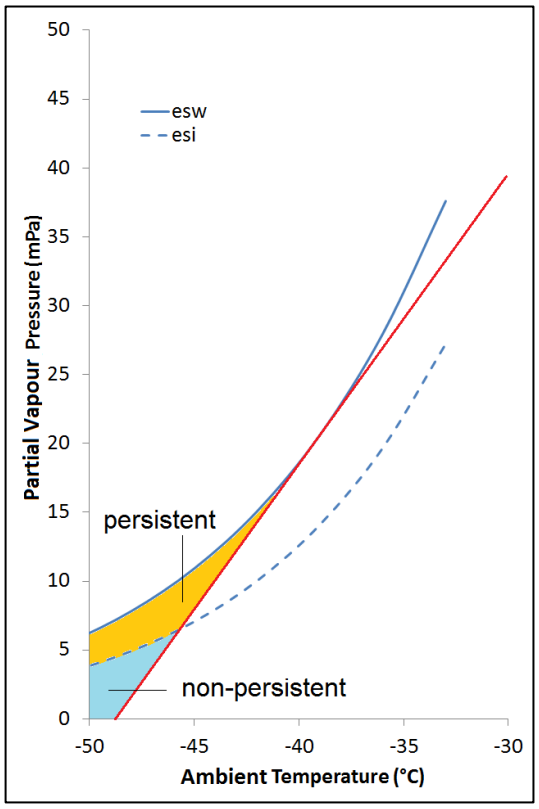

Figure D.3.3 – Contrail Formation Region

The critical mixing line is tangent to the vapour saturation curve, as can be seen in Figure D.3.2. If the actual mixing line slope is greater than that of the critical mixing line then a contrail will form. If the actual mixing line slope is less than that of the critical mixing line, then the mixing line will not cross the vapour saturation curve and hence no contrail will form. The slope of the mixing line is, therefore, a very important parameter when trying to predict the formation of contrails. The simplest method for estimating the slope of the mixing line is by using standard values for the contrail factor. Appleman [(177)] recommends the use of a contrail factor equal to 0.0336 g/kg/K. However, as the contrail factor is dependent on the engine exhaust conditions, Peters [(183)] suggests that a contrail factor of 0.030 g/kg/K be used for non-bypass engines, 0.034 g/kg/K for low-bypass engines and 0.039 for high-bypass engines. These methods are clearly not robust enough to capture the differences in contrail factor between similar engine concepts. Even Peters [(183)] only provides three possible contrail factors. Schuman [(178)] [(179)] provides an alternative method for estimating the mixing slope and the contrail factor. Schuman [(178)] [(179)] suggests that the contrail factor is dependent on engine overall propulsion efficiency.

Clearly, heat addition to the exhaust plume is directly a function of engine efficiency as can be seen in Equation (D.3.8). Useful energy from the fuel is dissipated in the wake of the aircraft. Residual energy is converted into waste heat in the core exhaust. It is assumed that rapid and complete mixing of the core and bypass gases occurs in the engine wake whether it is a separate or mixed flow engine. Given Equation (D.3.2) and Equation (D.3.8), it is possible to arrive at Equation (D.3.9). In Equation (D.3.9), the mixing line slope is a function of engine efficiency rather than a pre-defined contrail factor. In this way, coupled with an engine model it is possible to estimate a more realistic mixing line gradient.

$$q_{net} m_{fuel}(1-\eta_0) = c_p m_{air} \Delta T \qquad \textbf{(D.3.8)}$$

$$G = \frac{\Delta e}{\Delta T} = \left(\frac{p\,\Delta q}{\varepsilon}\right)\frac{c_p m_{air}}{q_{net} m_{fuel}(1-\eta_0)} = \frac{c_p\, EI_{H_2O}\, p}{q_{net}\,(1-\eta_0)\,\varepsilon} \qquad \textbf{(D.3.9)}$$

where:

- ε *ratio of molar masses of water vapour and air (equivalent to 0.622)*
- η_o *overall propulsive efficiency*
- c_p *specific heat capacity of the air*
- m *mass flow*
- p *ambient pressure at the given flight level*
- q_{net} *combustion heating value*
- EI_{H_2O} *emission index of water vapour in the engine exhaust*
- T *temperature*

The critical mixing line is tangent to the vapour saturation curve and passes through the point corresponding to the ambient temperature and ambient vapour pressure. In order to determine the gradient of the critical mixing line an iterative procedure is required. Contrails are formed if the gradient of the mixing line exceeds that of the critical mixing line. Another method for predicting the formation of contrails is by assuming that the mixing line as defined in Equation (D.3.9) is the critical mixing line. Then by using Equation (D.3.10) and Equation (D.3.11), a critical or threshold temperature can be found. The critical or threshold temperature is the ambient temperature at which the given mixing line would be critical. If the ambient temperature is below the critical temperature, then contrails are formed as the mixing line would cross the saturation curve.

$$T_m = -46.46 + 9.43\ln(G - 0.053) + 0.720[\ln(G - 0.053)]^2 \quad \textbf{(D.3.10)}$$

$$T_c = T_m - \frac{\left[e_{sat,T_m} - U e_{sat\ T_c}\right]}{G} \quad \textbf{(D.3.11)}$$

where:

- e_{sat} *saturation pressure*
- G *mixing line slope*
- T_c *critical temperature*
- T_m *tangent point temperature*

D.4 Computational Representation

The contrail prediction model flowchart is shown in Figure D.4.1. The model consists of two distinct parts. The first is concerned with the estimation of the total length of contrail and persistent contrails produced for an entire mission. The input data includes the required engine performance characteristics and trajectory definition. The data is interpolated in order to increase the spatial resolution. Then the critical and actual missing lines for each segment are estimated so that it can be determined if a contrail is likely to form. This procedure is repeated for each segment. The second part of the model generates the data required for the Appleman diagram. The engine performance for a single cruise point is assumed and then for a range of altitudes and humidity levels the mixing line and threshold temperatures are estimated. Finally the output module generates:

a. An Appleman diagram.
b. A detailed list containing the contrail predictions for each segment at the resolution used in the interpolation.
c. A prediction summary containing the total length of non-persistent contrails and the total length of persistent contrails formed.

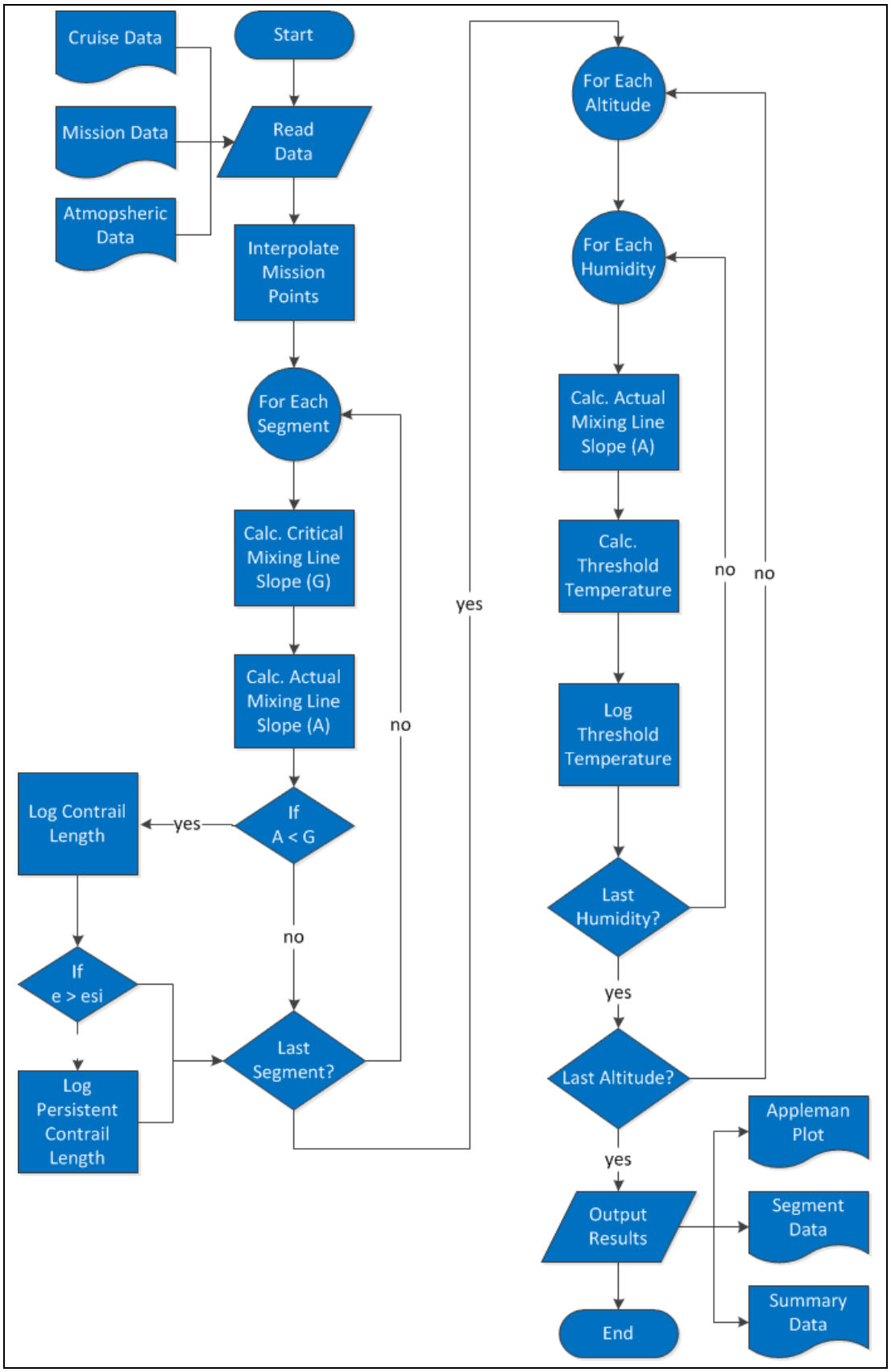

Figure D.4.1 – Contrail Prediction Model Flowchart

D.5 Validation

The validation of this model was carried out against data found in Shull [139]. This work contains data gathered from the observation of actual aircraft at different altitudes and includes typical atmospheric conditions and contrail observations. Shull [139] also carries out a comparison of these actual observations with predictions from the Air Force Weather Agency JETRAX Contrail Forecast Model. Therefore, this data provided the possibility to benchmark the model created for this work against a sophisticated third party tool in addition to assessing its ability to predict the formation of contrails based on actual observations. A summary of the result is given Table D.5.1.

Number of Data Points	236
Number of Contrail Observations	141
Number of No Contrail Observations	95
Number of Contrail Predictions	117
Number of No Contrail Predictions	119
Hit Rate	81%

Table D.5.1 – Results Summary for Contrail Model Validation

The contrail prediction tool gives good results, correctly predicting formation or absence of contrails 81% of the time based on available data. Shull [139] reports that other algorithms such as those based on Schrader [140] and Schuman [178] give hit rates of 79% and 81% respectively. This places the current algorithm well in the same field of accuracy. This is hardly surprising considering that the current model is based largely on the work of Schuman [178]. The JETRAX algorithm [183] gives better results with a hit rate of above 84% in some cases.

D.6 Baseline Atmospheric Data (Route: London – New York)

The contrail prediction tool relies on atmospheric data for the prediction of contrail emissions. In this thesis standard atmospheric data from Kalnay et al. [155] was obtained for a London to New York trajectory where the shortest route between the two cities was assumed. An extract of the data is illustrated in the following figures. Only two dates were considered: the 1st of January 2012 (12:00) and the 1st of July 2012 (12:00). The data is presented at 11 pressure altitudes.

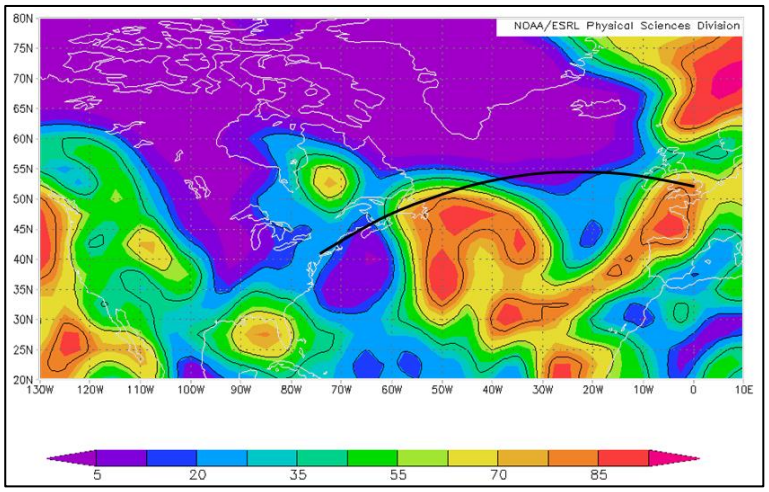

Figure D.6.3 – Relative Humidity at 250hPa (01/01/2012 12:00)

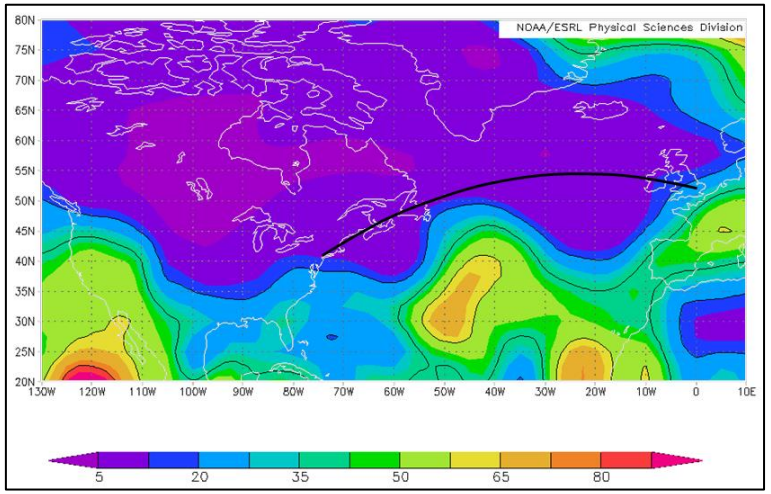

Figure D.6.1 – Relative Humidity at 150hPa (01/01/2012 12:00)

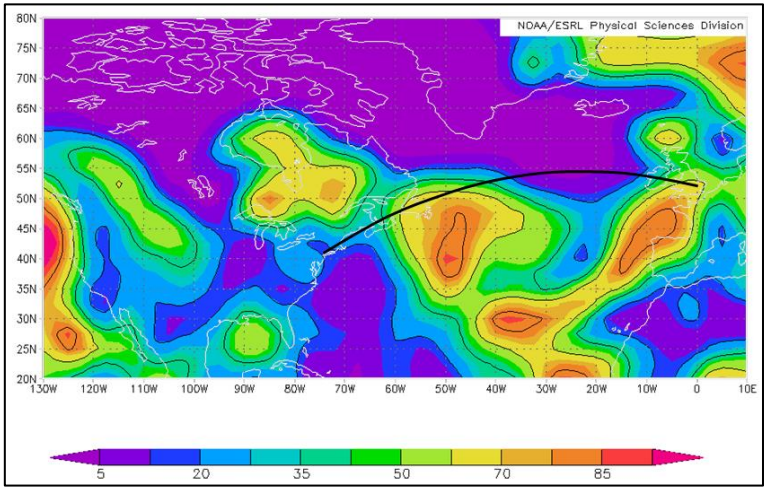

Figure D.6.4 – Relative Humidity at 300hPa (01/01/2012 12:00)

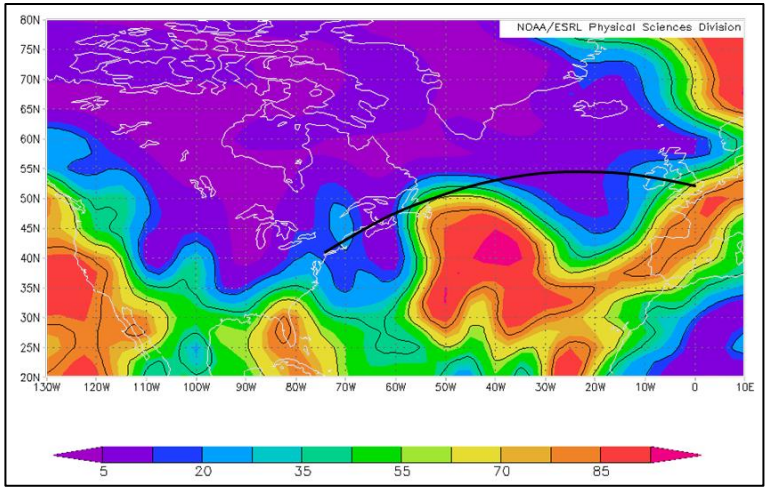

Figure D.6.2 – Relative Humidity at 200hPa (01/01/2012 12:00)

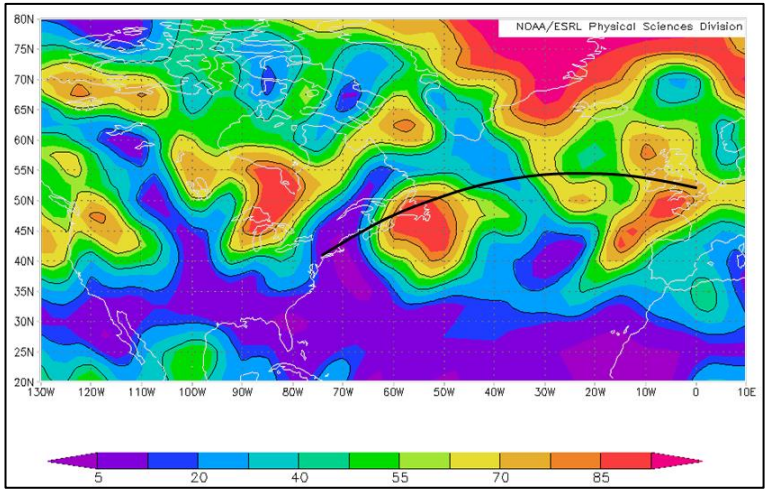

Figure D.6.7 – Relative Humidity at 600hPa (01/01/2012 12:00)

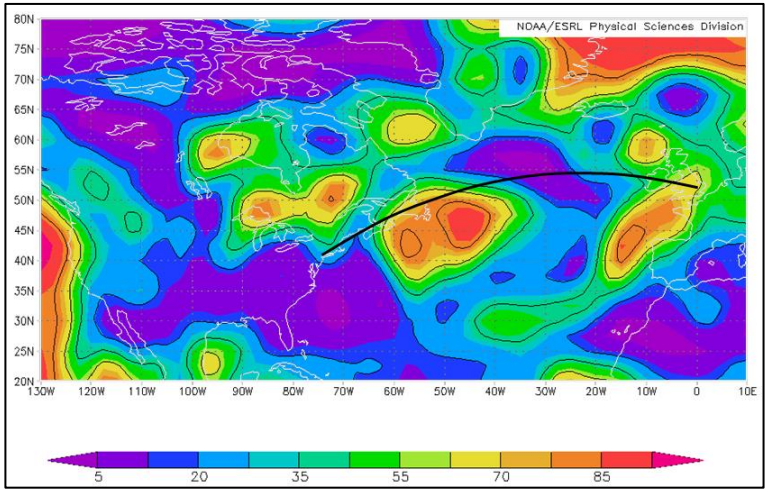

Figure D.6.5 – Relative Humidity at 350hPa (01/01/2012 12:00)

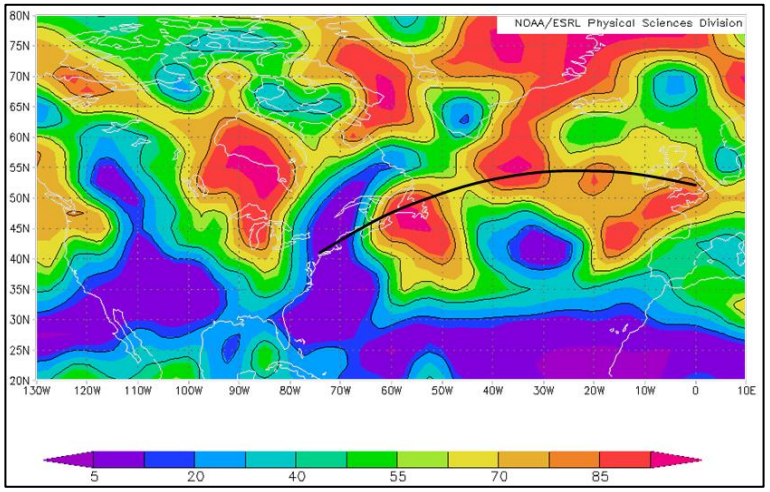

Figure D.6.8 – Relative Humidity at 700hPa (01/01/2012 12:00)

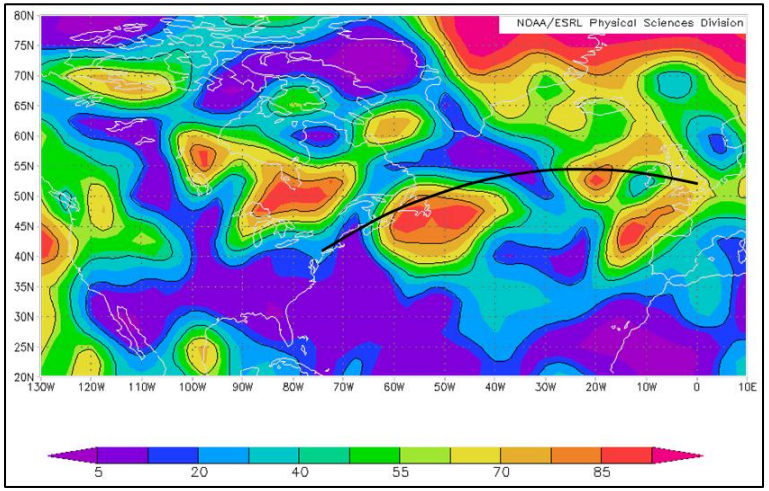

Figure D.6.6 – Relative Humidity at 400hPa (01/01/2012 12:00)

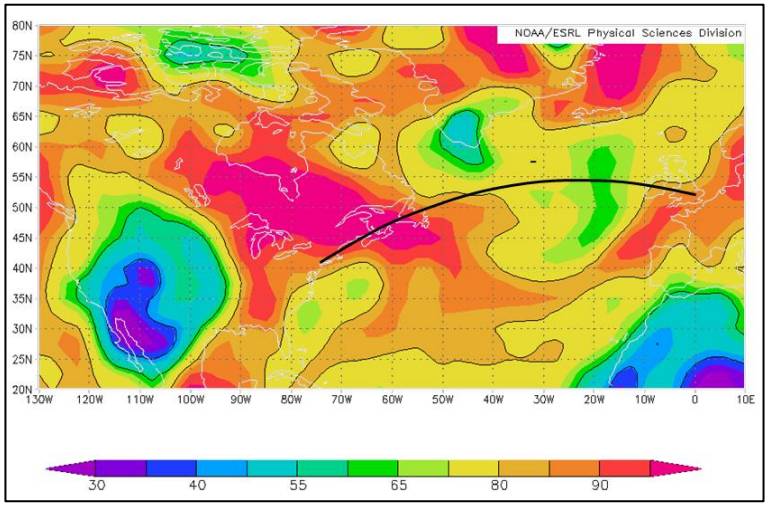

Figure D.6.11 – Relative Humidity at 1000hPa (01/01/2012 12:00)

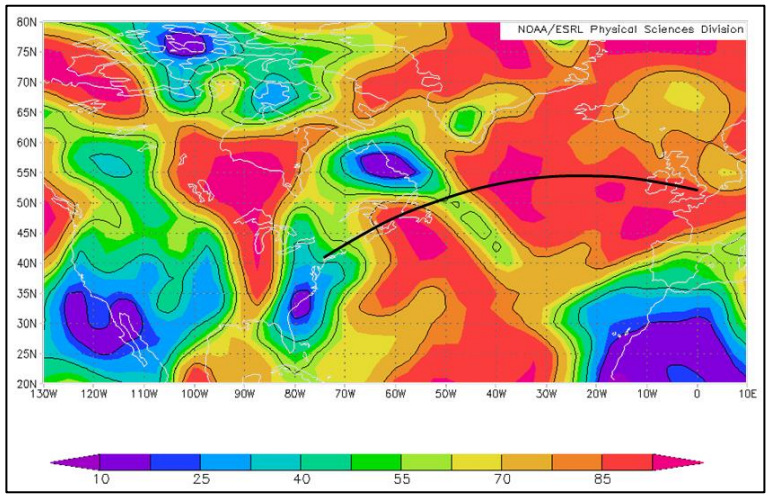

Figure D.6.9 – Relative Humidity at 850hPa (01/01/2012 12:00)

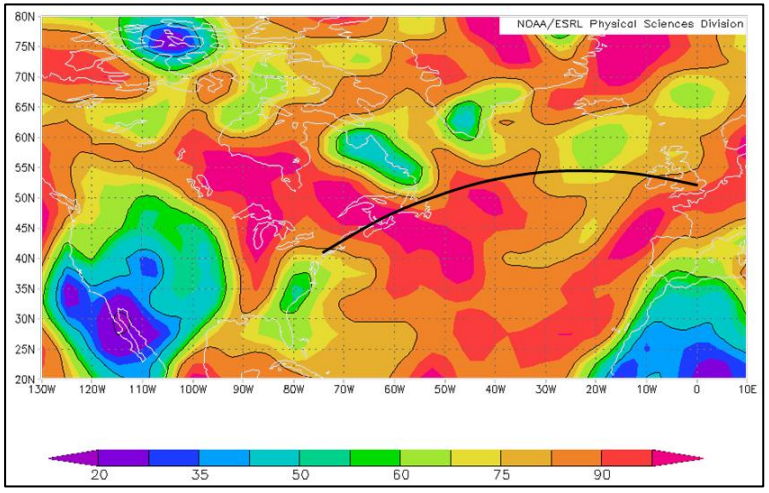

Figure D.6.10 – Relative Humidity at 925hPa (01/01/2012 12:00)

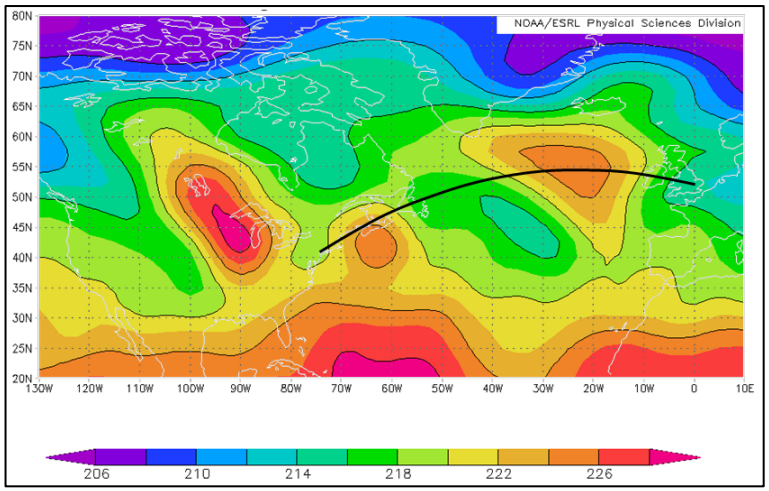

Figure D.6.14 – Ambient Temperature at 250hPa (01/01/2012 12:00)

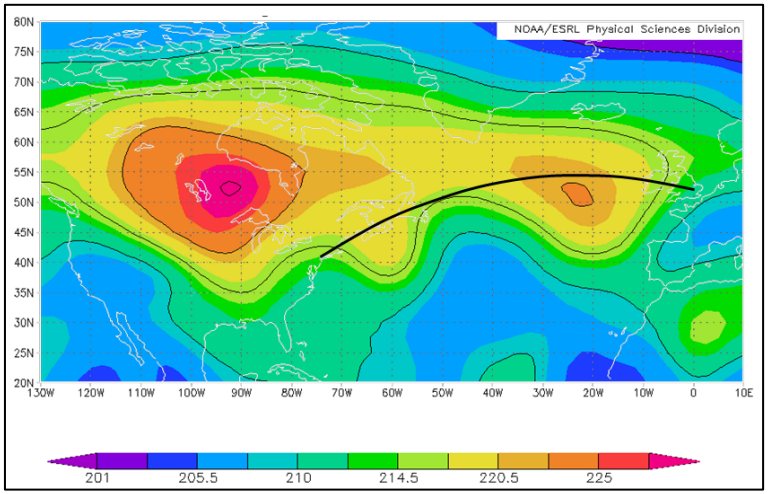

Figure D.6.12 – Ambient Temperature at 150hPa (01/01/2012 12:00)

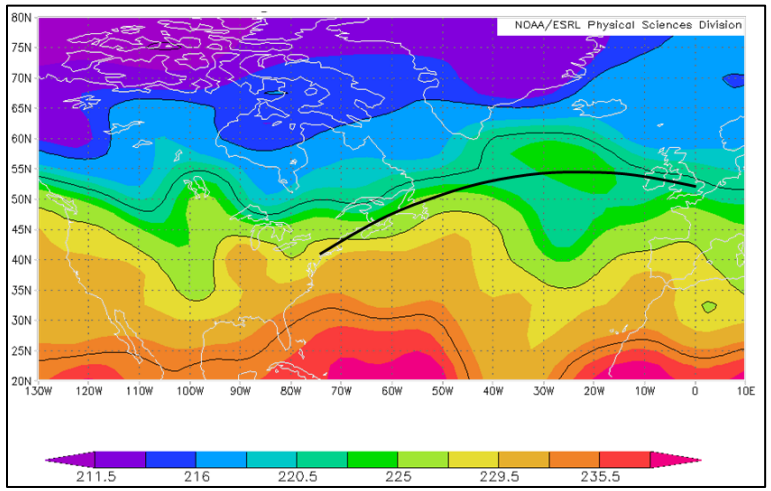

Figure D.6.15 – Ambient Temperature at 300hPa (01/01/2012 12:00)

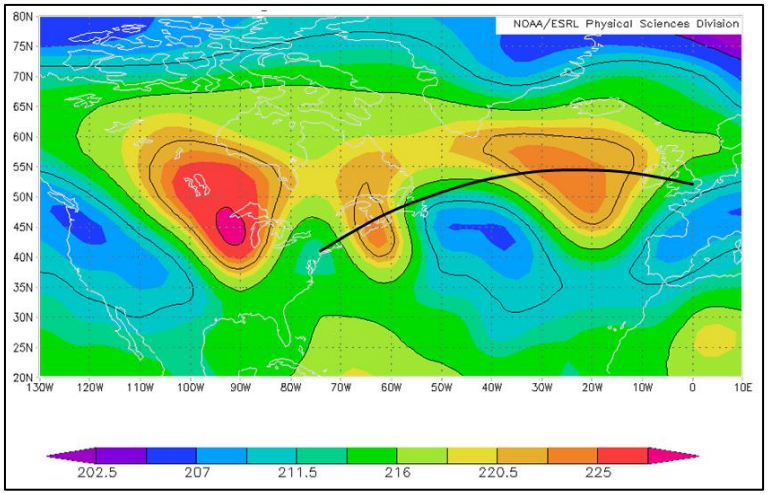

Figure D.6.13 – Ambient Temperature at 200hPa (01/01/2012 12:00)

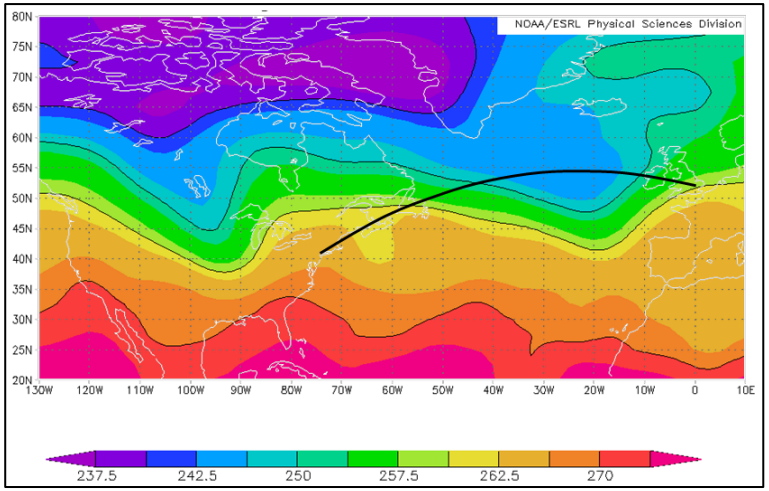

Figure D.6.18 – Ambient Temperature at 600hPa (01/01/2012 12:00)

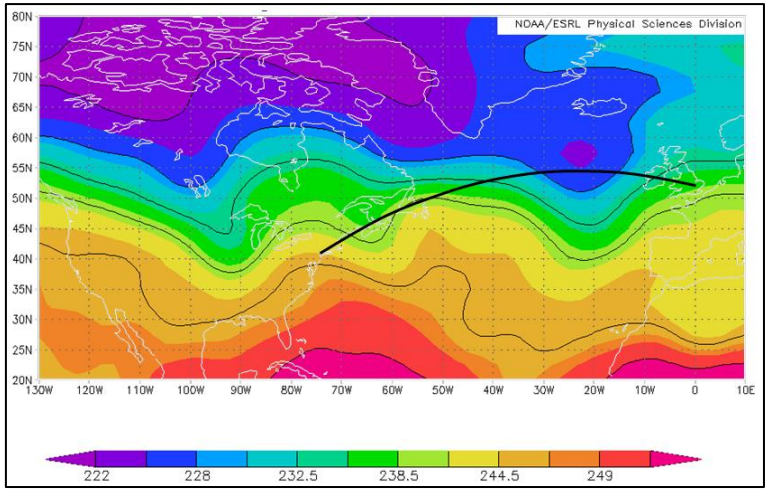

Figure D.6.16 – Ambient Temperature at 350hPa (01/01/2012 12:00)

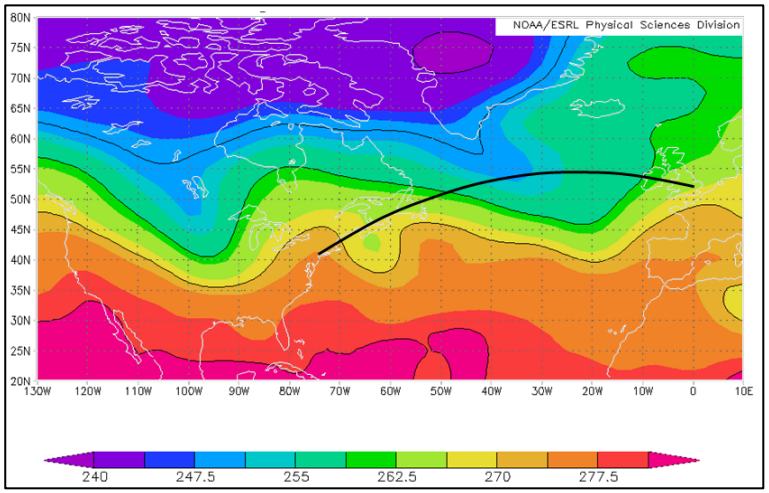

Figure D.6.19 – Ambient Temperature at 700hPa (01/01/2012 12:00)

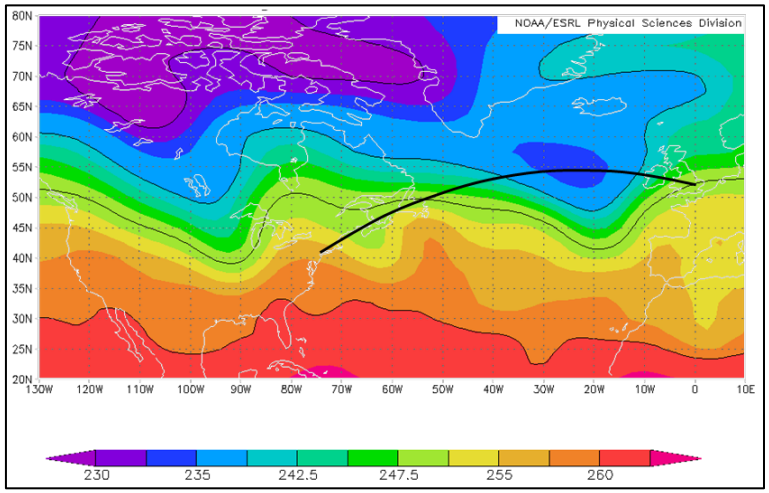

Figure D.6.17 – Ambient Temperature at 400hPa (01/01/2012 12:00)

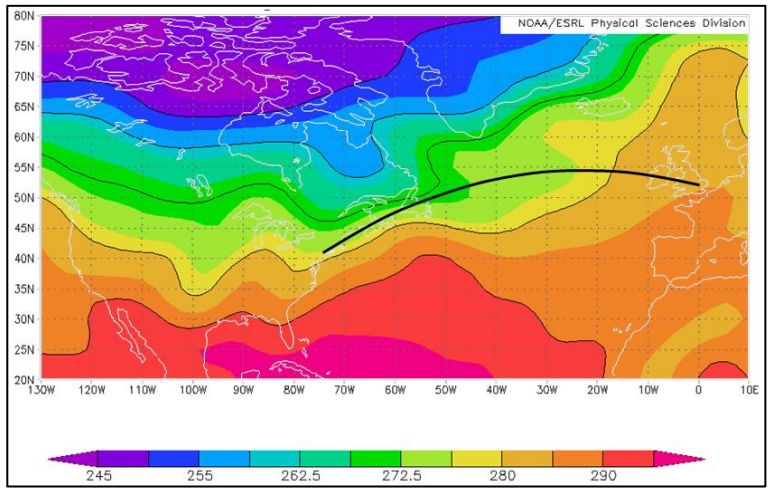

Figure D.6.22 – Ambient Temperature at 1000hPa (01/01/2012 12:00)

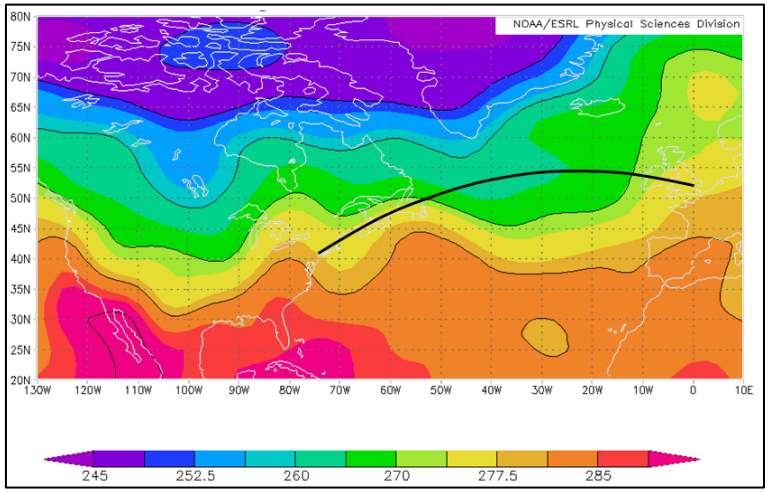

Figure D.6.20 – Ambient Temperature at 850hPa (01/01/2012 12:00)

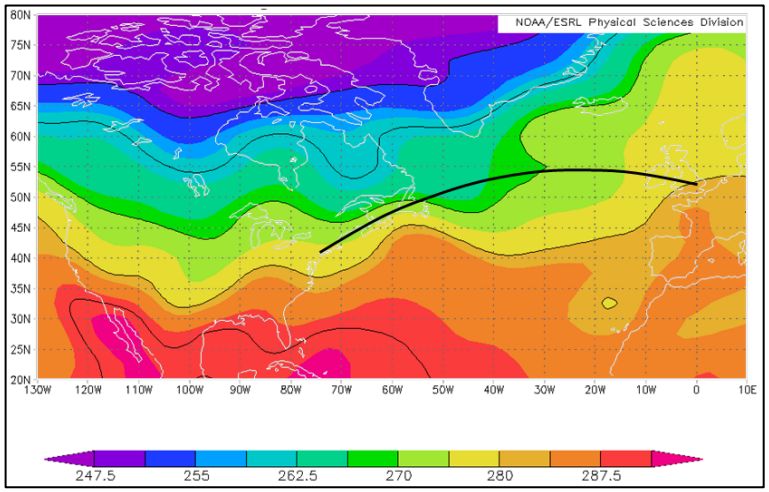

Figure D.6.21 – Ambient Temperature at 925hPa (01/01/2012 12:00)

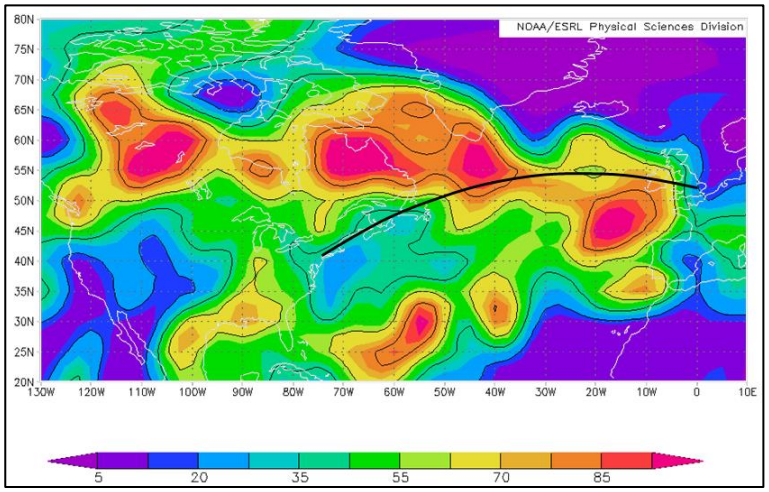

Figure D.6.25 – Relative Humidity at 250hPa (01/07/2012 12:00)

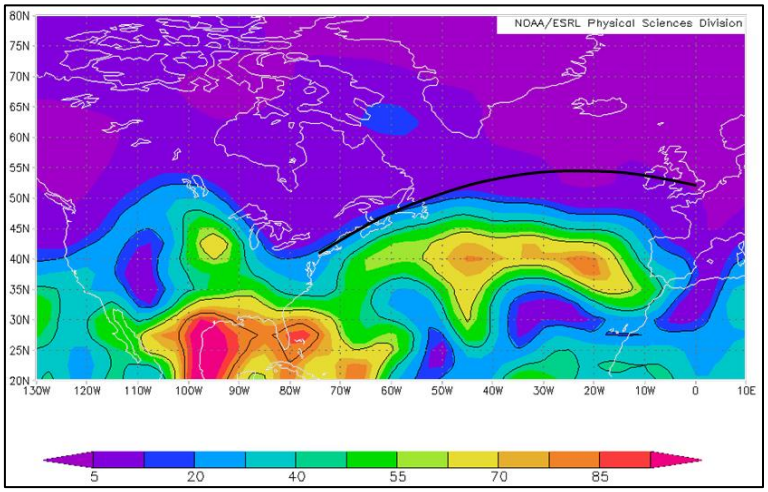

Figure D.6.23 – Relative Humidity at 150hPa (01/07/2012 12:00)

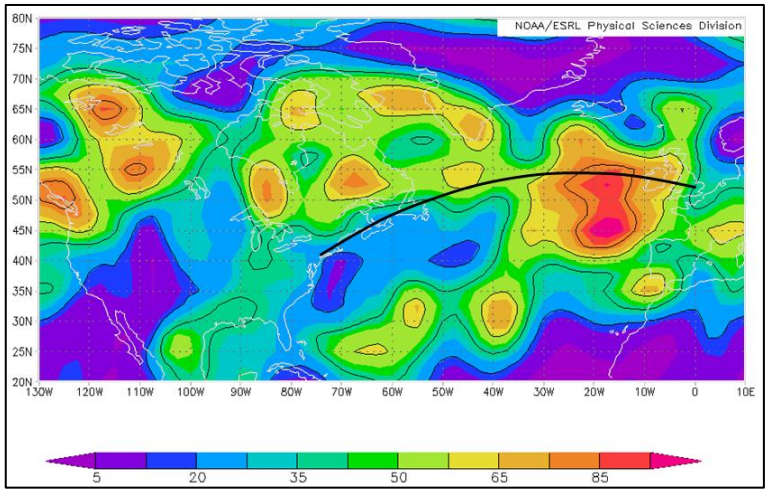

Figure D.6.26 – Relative Humidity at 300hPa (01/07/2012 12:00)

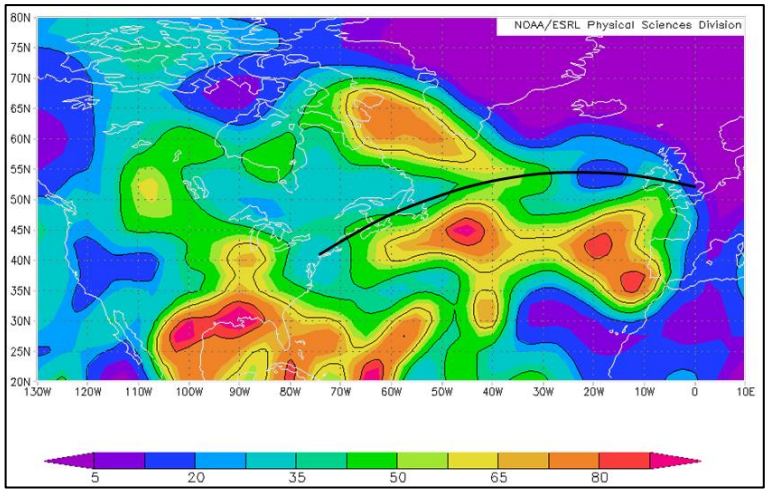

Figure D.6.24 – Relative Humidity at 200hPa (01/07/2012 12:00)

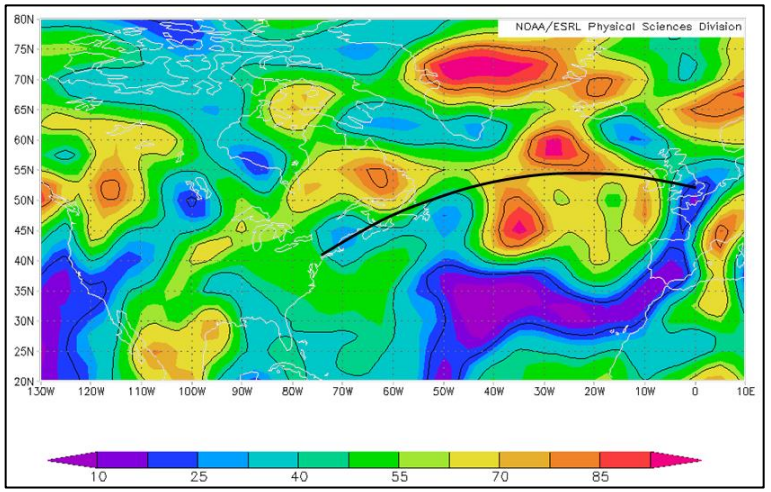

Figure D.6.29 – Relative Humidity at 600hPa (01/07/2012 12:00)

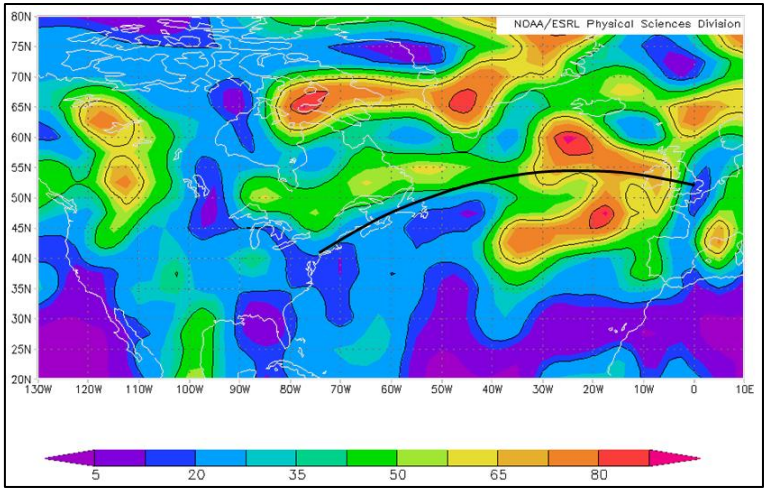

Figure D.6.27 – Relative Humidity at 350hPa (01/07/2012 12:00)

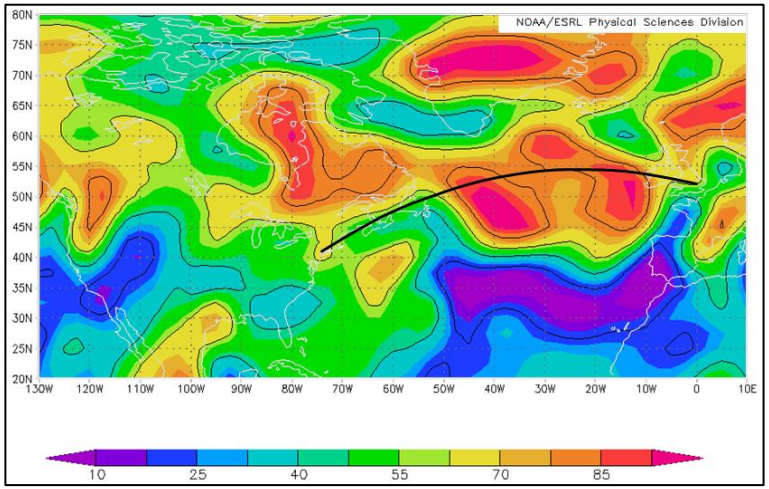

Figure D.6.30 – Relative Humidity at 700hPa (01/07/2012 12:00)

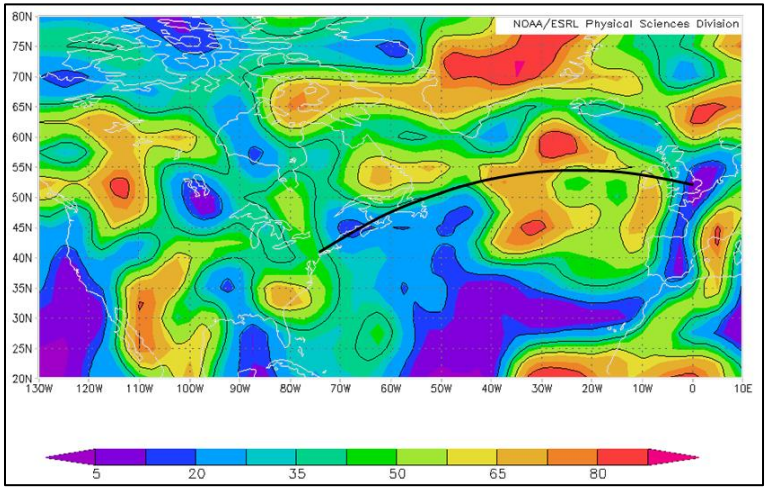

Figure D.6.28 – Relative Humidity at 400hPa (01/07/2012 12:00)

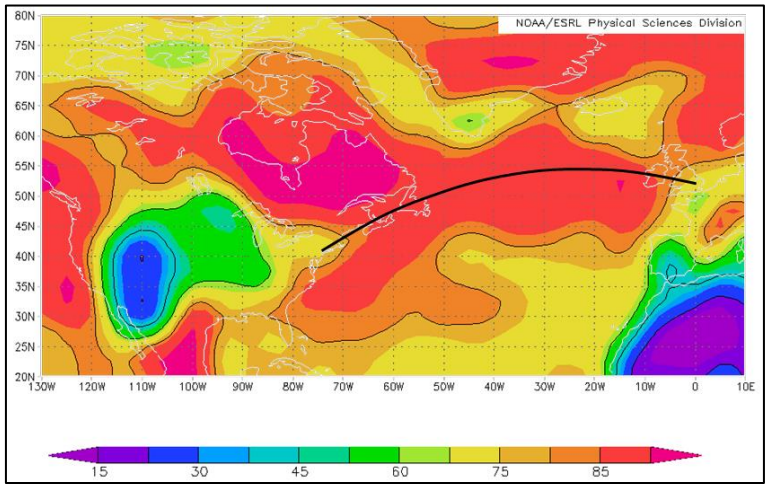

Figure D.6.33 – Relative Humidity at 1000hPa (01/07/2012 12:00)

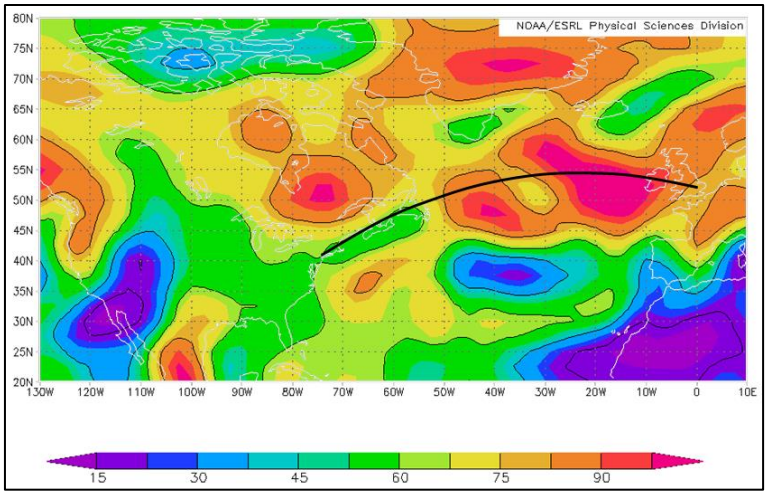

Figure D.6.31 – Relative Humidity at 850hPa (01/07/2012 12:00)

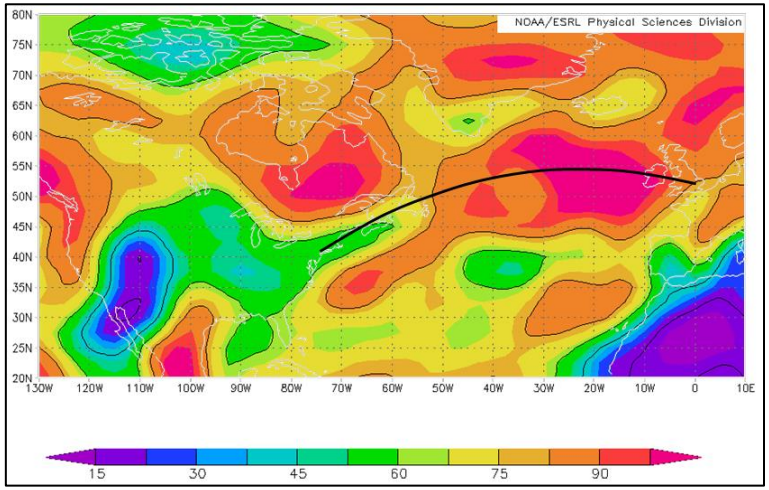

Figure D.6.32 – Relative Humidity at 925hPa (01/07/2012 12:00)

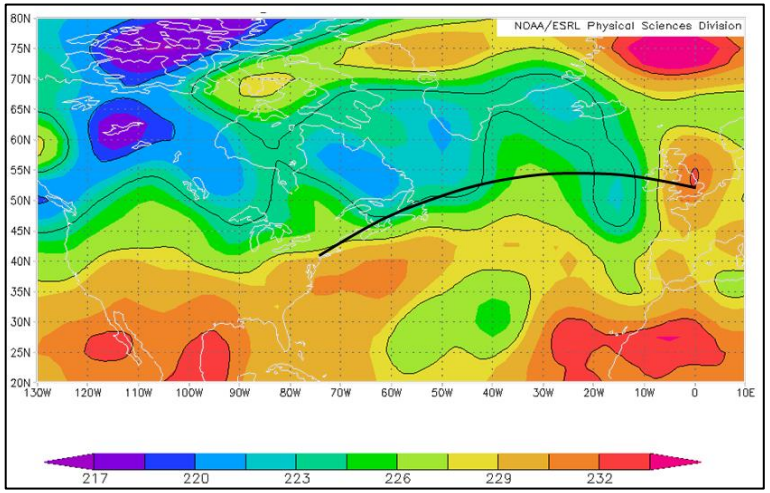

Figure D.6.36 – Ambient Temperature at 250hPa (01/07/2012 12:00)

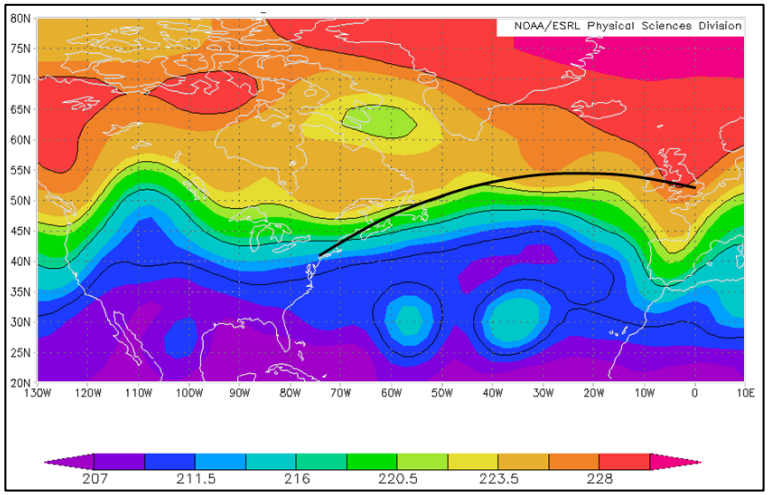

Figure D.6.34 – Ambient Temperature at 150hPa (01/07/2012 12:00)

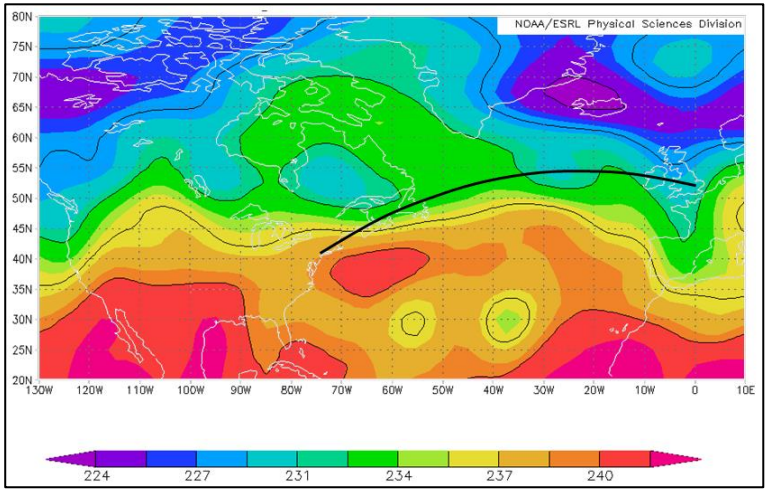

Figure D.6.37 – Ambient Temperature at 300hPa (01/07/2012 12:00)

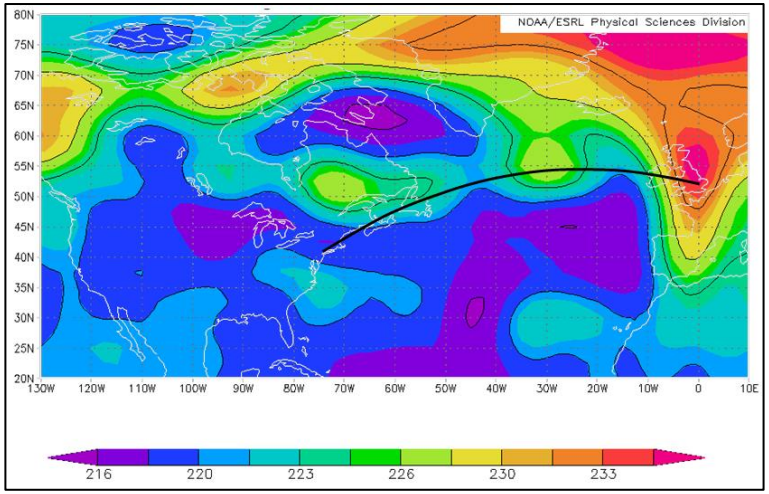

Figure D.6.35 – Ambient Temperature at 200hPa (01/07/2012 12:00)

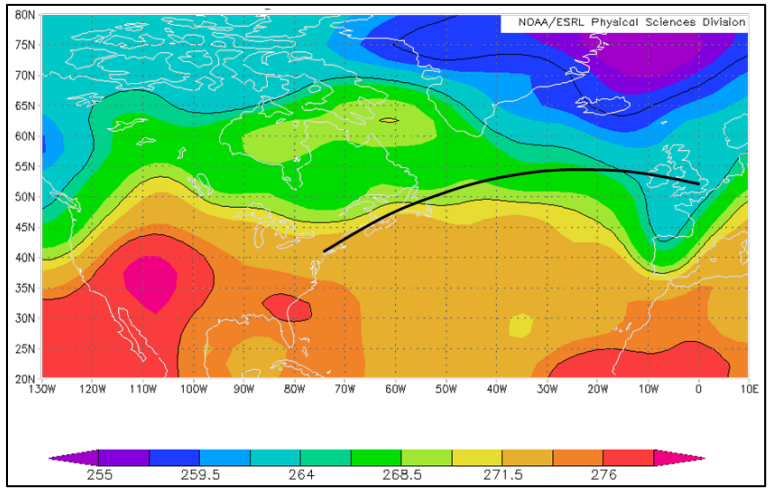

Figure D.6.40 – Ambient Temperature at 600hPa (01/07/2012 12:00)

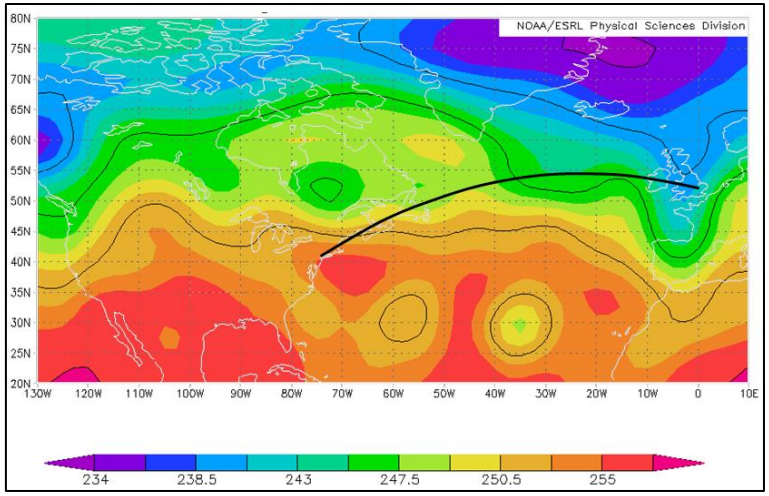

Figure D.6.38 – Ambient Temperature at 350hPa (01/07/2012 12:00)

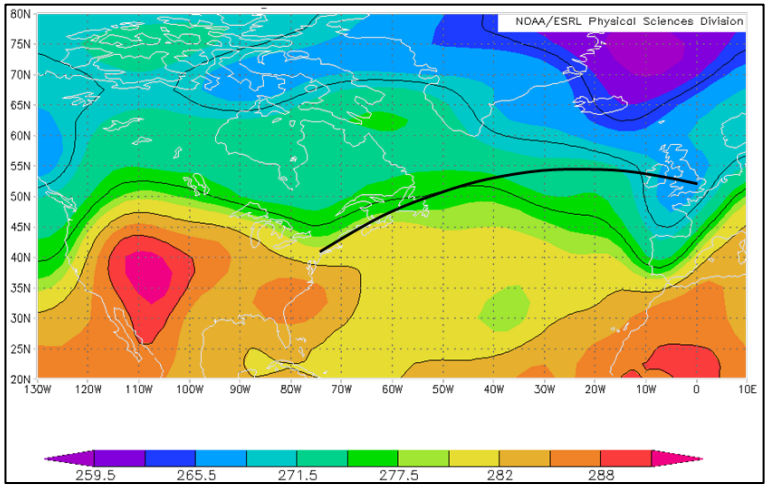

Figure D.6.41 – Ambient Temperature at 700hPa (01/07/2012 12:00)

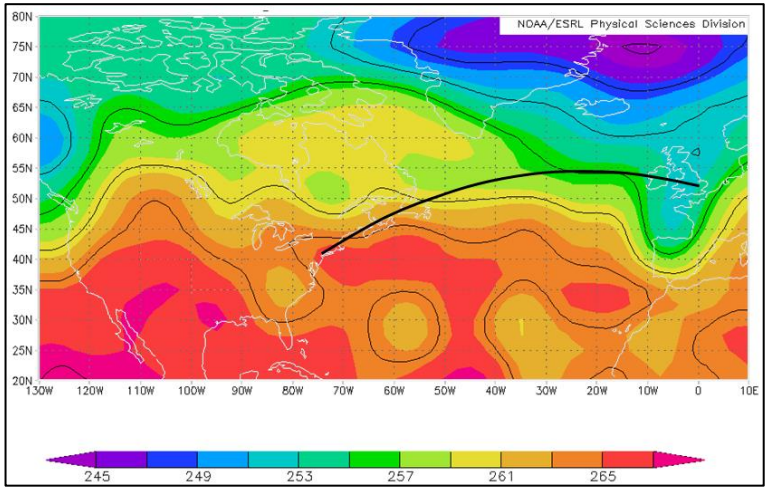

Figure D.6.39 – Ambient Temperature at 400hPa (01/07/2012 12:00)

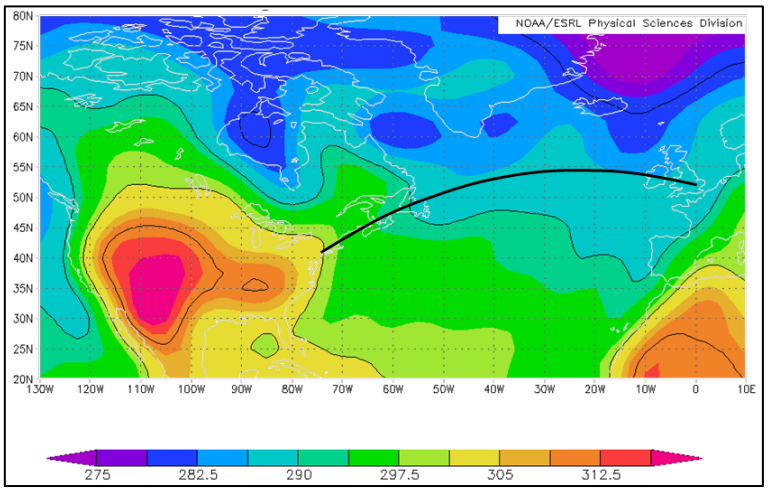

Figure D.6.44 – Ambient Temperature at 1000hPa (01/07/2012 12:00)

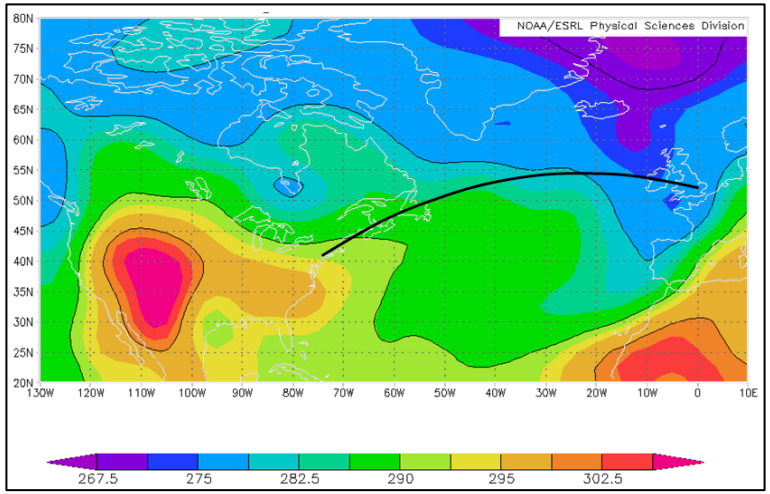

Figure D.6.42 – Ambient Temperature at 850hPa (01/07/2012 12:00)

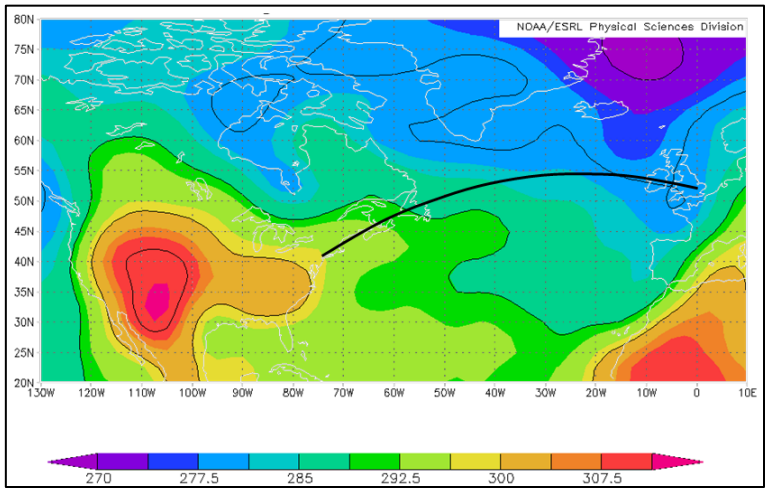

Figure D.6.43 – Ambient Temperature at 925hPa (01/07/2012 12:00)

Appendix E NO_x Emissions Model

E.1 Nomenclature

Dp/Foo	Units of Mass of Pollutant per Unit Thrust (g/kN)
$EINO_x$	NO_x Emission Index
FAR	Fuel-to-Air Ratio
GIRFC	Geared Intercooled Reversed Flow Core Engine Concept
GISFC	Geared Intercooled Straight Flow Core Engine Concept
GTICLR	Geared Intercooled Long Range Engine Concept from NEWAC
ICAO	International Civil Aviation Organization
LDI	Lean Direct Injection
LTO	Landing and Take-Off Cycle
P3	Combustor Entry Pressure
T3	Combustor Entry Temperature
TO	Take-Off

E.2 Description

A NO_x prediction model was developed in order to study the implications of design choices on both LTO and cruise NO_x emissions. At the core of this tool are a number of simple NO_x correlations. The development of new NO_x prediction methods is beyond the scope of this dissertation and was not attempted. Unlike for the previously described models, the scope for model validation in this case was very limited. The correlations which have been used were validated by the respective researchers to which appropriate references are given. Strict verification of the model was carried out to ensure that the correlations were correctly implemented. The objectives of the NO_x prediction tool are:

a. To predict the LTO NO_x, absolute NO_x and weighted NO_x values for a given set of input thermodynamic data.
b. To generate an LTO NO_x chart for comparison with the LTO NO_x certification levels.

E.3 Theory

A comparison between different NO_x emission prediction strategies is given in chapter 7, and therefore shall not be repeated in this section. However, a general description of the specific correlations used is presented. The TF2000 engine model is based upon the specifications of the Trent 772. The TF2000 combustor is also assumed to have the same characteristics as that of the Trent 772. Reference LTO NO_x values for the Trent 772 combustor taken at the four main ICAO certification points can be found in the ICAO emissions databank [28]. Table E.3.1 lists the relevant reference points.

ICAO Rating	EI NO_x [g/kg]
Idle	5.74
Approach	10.68
Climb-Out	32.66
Take-Off	43.60

Table E.3.1 – Trent 772 LTO NO_x Reference Values [28]

These reference points are useful for determining the LTO NO_x emissions of the TF2000 engine but cannot be used on their own to determine the altitude NO_x emissions of this engine. The P_3-T_3 method has proved to be one of the most reliable methods for estimating altitude NO_x emissions based on ground level NO_x reference values [136] [146]. The reference condition is established at the correct T_3 from existing engine test data obtained at ground level. For existing in-service engine types this type of data can be found in the ICAO emissions databank [28] as shown for the Trent 772. The P_3-T_3 correlation is given in Equation (E.3.1) and is dependent on P3, FAR and humidity as well as two exponents. The exponents are engine specific and without proprietary engine data cannot be accurately defined although Norman et al. [146] do provide a guideline for using the P_3-T_3 method when accurate information about the combustor cannot be obtained. Norman et al. [146] suggest that FAR was found to vary by about 10% between ground level and cruise for a given T_3. For a conventional combustor it was found that this level of variation only weakly affected the NO_x emission level. Therefore, the FAR term can be ignored and "m" can be assumed equal to 0. However, Norman et al. [146] point out that lean burn technology could be very sensitive to a 10% change in FAR and therefore might necessitate the use of a different value of "m". The P_3 term on the other hand was found to strongly affect the level of NO_x at altitude. The "n" exponent value of 0.4 was found by Norman et al. [146] to yield the best accuracy in the prediction of NO_x emission levels at altitude when compared with data obtained in an altitude test facility for a range of civil aero engines. The error in the predicted value was found to be in the range of ±11% but Norman et al. [146] also suggest that for some of the lean burn combustors a lower value of "n" would improve the accuracy of the prediction. The lowest value suggested for "n" was 0.2.

$$EINO_{x_{fl}} = EINO_{x_{sl}} \left(\frac{P_{3fl}}{P_{3sl}}\right)^{n} \left(\frac{FAR_{fl}}{FAR_{sl}}\right)^{m} e^{19(h_{sl}-h_{fl})} \qquad \textbf{(E.3.1)}$$

where:

- *h* *relative humidity*
- *fl* *flight level condition*
- *sl* *sea level condition*
- *$EINO_x$* *emission index of nitrogen oxides*
- *FAR* *fuel-to-air ratio*
- *P_3* *combustor inlet pressure*

While for the TF2000 engine it was possible to use the ICAO emissions databank [28] reference data, this was not the case for the GIRFC and GISFC engines where an LDI type combustor is assumed. As already stated in chapter 7, the only publically available correlations for LDI combustor emission are those published by the NASA Glenn Research Centre [150] [151] [152]. The most recent correlation, which was established through combustor rig-testing, is that proposed by Tacina et al. [152] and is given in Equation (E.3.2). Comparison with proprietary data[1] shows that Equation (E.3.2) yields similar trends and magnitudes in terms of LTO NO_x emissions for the engine types considered. No suitable data was found to compare cruise NO_x emissions. Therefore, the P_3-T_3 method was retained for the estimation of NO_x at altitude. However, two levels of the "n" exponent were considered in order to show how the final prediction might be affected by different technology assumptions.

$$EINO_x = 0.104e^{\left({}^{T_3}/_{185}\right)} FAR^{1.32} {P_3}^{0.68} \left(\frac{\Delta P}{P_3}\right)^{-0.36} \qquad \textbf{(E.3.2)}$$

where:

- ΔP *combustor pressure loss [kPa]*
- $EINO_x$ *emission index of nitrogen oxides [g/kg]*
- *FAR* *fuel-to-air ratio [-]*
- P_3 *combustor inlet pressure [kPa]*
- T_3 *combustor inlet temperature [K]*

As explained in chapter 7, the severity of NO_x emissions is not the same at every altitude. In this thesis, a weighting factor from Köhler et al. [154] has been applied to account for the variation in NO_x severity. The overall weighted NO_x can be estimated according to Equation (E.3.3) while the weighting factors suggested by Köhler et al. [154] are repeated in Table E.3.2. The weighted NO_x values allow for the trade-off between different engine concepts and different trajectories based on weighted NO_x values.

[1] Proprietary data obtained from research carried out by Rolls-Royce Deutschland, Avio and Turbomeca within the NEWAC (12) project. Correlations were made available by Rolls-Royce Deutschland based on combustor rig test results for the LTO conditions of advanced engine concepts including the GTICLR.

$$Wighted\ NO_x = \sum_{i=0}^{n} (Absolute\ NO_x \times f) \qquad \textbf{(E.3.3)}$$

where:

- *f* *weighting factor*
- *n* *number of segments*

Min. Altitude (m)	Max. Altitude (m)	Weighting factor (f)
14173	14783	113
13564	14173	43
12954	13564	15
12344	12954	29
11735	12344	21
11125	11735	23
10516	11125	16
9906	10516	8
9296	9906	4
Below 9296		0

Table E.3.2 – Cruise NO_x Weighting Factors (Köhler et al. [154])

E.4 Model Structure

The NO_x estimation model schematic is given in Figure E.4.1. The data required by the NO_x model includes thermodynamic parameters from the engine model including P_3, T_3, FAR and fuel flow rate. It also requires atmospheric data including atmospheric pressure, temperature and humidity as well as trajectory information including for each flight segment the segment flight time and altitude. For the LTO NO_x estimation similar information is required for the four ICAO certification points.

The model procedure is straightforward. The $EINO_x$ is estimated at each ICAO certification point followed by the estimation of the NO_x Dp/Foo value which allows for the evaluation and benchmarking of the LTO NO_x. The mission NO_x is then estimated iteratively for each mission segment. The absolute NO_x emission for each segment is estimated as described in the previous section. The weighted NO_x value is then established based on the flight altitude and the weighting factors outlined in the previous section. At each iteration the total NO_x and

weighted NO_x values are updated. Finally, given the information generated by the model, both a summary report and detailed report are prepared by the model. In addition the LTO chart is generated automatically by the model where both the engine LTO NO_x and certification limits are presented.

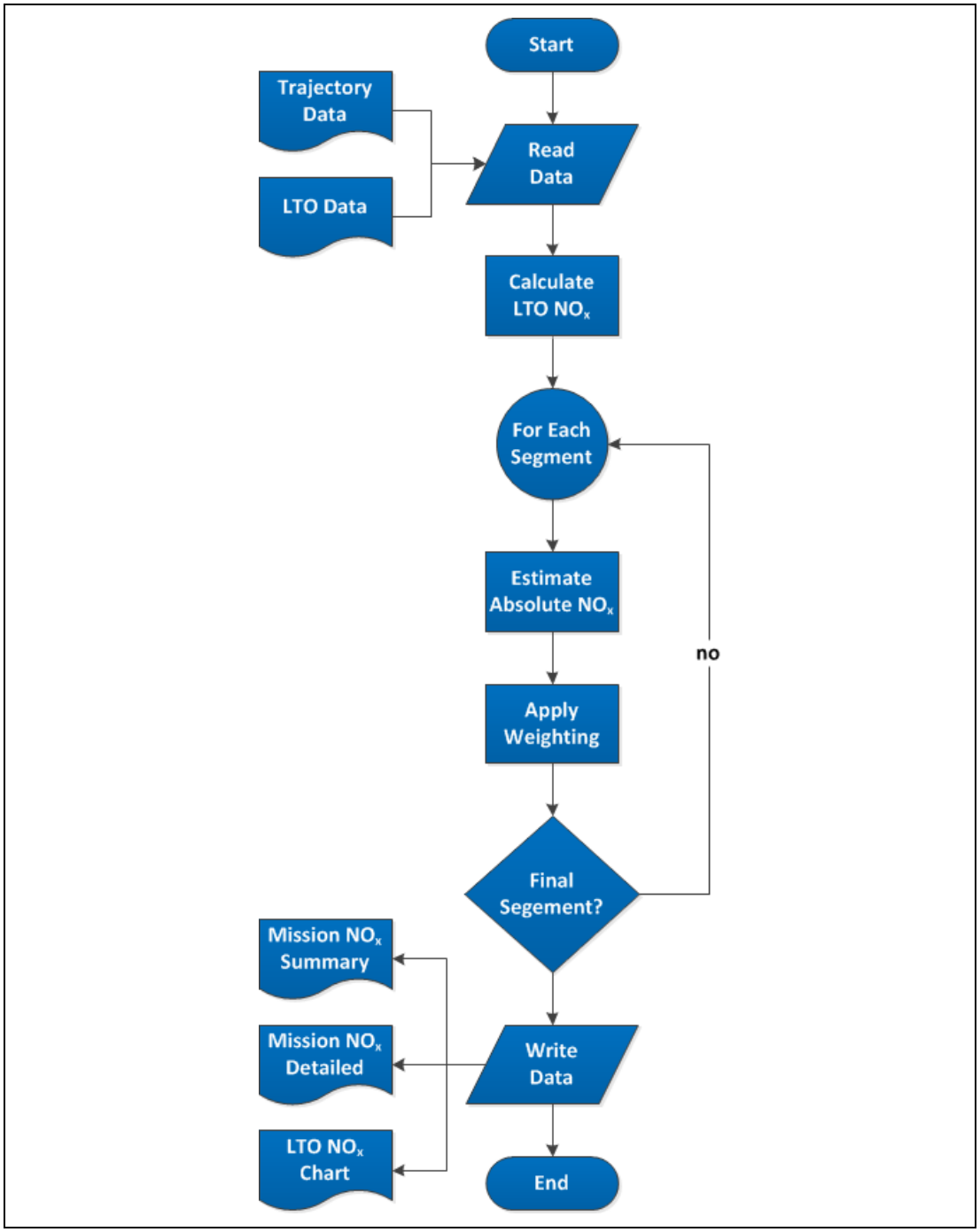

Figure E.4.1 – NO_x Estimation Model Schematic

References

1. Birch NT. 2020 Vision: The Prospects for Large Civil Aircraft Propulsion. In Proceedings of the 22nd International Congress of Aeronautical Science; 2000; Harrogate, UK. p. 111.1-9.

2. Airbus. Navigating the Future: Global Market Forecast 2011-2030. Blagnac, France: Airbus; 2011.

3. Boeing. Current Market Outlook 2013–2032. Seattle, Washington: Boeing; 2013.

4. Rolls Royce plc. Rolls Royce Market Outlook. [Online]. Los Angeles [cited 2013 October 15. Available from: http://www.rolls-royce.com/civil/about/market_outlook/.

5. Penner JE, Lister DH, Griggs DJ, Dokken DJ, McFarland M. Special Report on Aviation and the Global Atmosphere Geneva, Switzerland: Cambridge University Press; 1999.

6. Pachauri RK, Reisinger A. Synthesis Report. Contribution of Working Groups I, II and III to the Fourth Assessment Report of the Intergovernmental Panel on Climate Change. Geneva, Switzerland: IPCC; 2007.

7. International Civil Aviation Organization. Aviation and Climate Change: Environmental Report. Montréal, Québec, Canada: ICAO; 2010.

8. Environmental Protection Agency. Control of Air Pollution From Aircraft and Aircraft Engines; Emission Standards and Test Procedures; Final Rule. Federal Register. 2012 June; 77(117).

9. Advisory Council for Aeronautics Research in Europe. ACARE Key Findings. [Online]. [cited 2013 October 15. Available from: http://www.acare4europe.org/html/sra1_key_findings.asp.

10. Korsia JJ. VITAL - European R&D Programme for Greener Aero-Engines (ISABE-2009-1114). In Proceedings of the 19th International Symposium on Air Breathing Engines; 2009; Montreal, Canada.

11. Goutines M. Main Achievements of VITAL (enVIronmenTALly Friendly Aero Engine). In Proceedings of the 6th European Aeronautics Days; 2012; Madrid, Spain. p. 184-189.

12. Wilfert G, Sieber J, Rolt A, Baker N, Touyeras A, Colantuoni S. New Environmental Friendly Aero Engine Core Concepts (ISABE 2007-1120). In Proceedings of 18th International Symposium on Air Breathing Engines; 2007; Beijing, China.

13. Darecki M, Edelstenne C, Enders T, Fernandez E, Hartman P, Herteman JP, et al. Flightpath 2050: Europe's Vision for Aviation. Luxembourg: European Commision; 2011. Report No.: ISBN: 978-92-79-19724-6.

14. Shaw RJ. NASA's Ultra-Efficient Engine Technology (UEET) Program / Aeropropulsion Technology Leadership for the 21st Century. In Proceedings of the 22nd Congress of the International Council of the Aeronautical Sciences (ICAS); 2000; Harrogate, UK.

15. Brown N, Gupta M, Jefferies R, Maurice L. The US Strategy for Tackling Aviation Climate Impacts. In Proceedigns of the 27th Congress of the International Council of the Aeronautical Sciences (ICAS); 2010; Nice, France.

16. Rolt AM, Baker NJ. Intercooled Turbofan Engine Design and Technology Research in the EU Framework 6 NEWAC Programme (ISABE-2009-1278). In Proceedings of the 19th International Symposium on Air Breathing Engines 2009; 2009; Montreal, Canada: Curran Associates, Inc.

17. Howse M. Rolls-Royce and Gas Turbines. In Proceedings of the 16th International Symposium on Air Breathing Engines; 2003; Cleveland, Ohio, USA.

18. Solomon S, Qin D, Manning M, Chen Z, Marquis M, Averyt KB, et al. Climate Change 2007: The Physical Science Basis. New York, USA: International Panel on Climate Change (IPCC); 2007. Report No.: ISBN 978-0-521-70596-7.

19. Lunbladh A, Donnerhack S, Giuliani F, Gronstedt T. Future Innovative Cores for Commerical Engines. In XIX International Symposium on Air Breathing Engines 2009 (ISABE 2009) ; 2009; Montreal: Curran Associates, Inc.

20. Kurzke J. About Simplifications in Gas Turbine Performance Calculations (GT2007-27620). In Proceedings of ASME Turbo Expo 2007: Power for Land, Sea and Air; 2007; Montreal, Canada.

21. Riegler C, Bichlmaier C. The Geared Turbofan Technology–Opportunities, Challenges and Readiness Status. In Proceedings of the First CEAS European Air and Space Conference; 2007; Berlin, Germany.

22. Kyprianidis KG, Gronstedt T, Ogaji S, Pilidis P, Singh R. Assessment of Future Aero-engine Designs With Intercooled and Intercooled Recuperated Cores. Journal of Engineering for Gas Turbines and Power. 2010 September; 133(1): p. 011701.1-10.

23. Koff BL. Gas Turbine Technology Evolution: A Designers Perspective. Journal of Propulsion and Power. 2004 July-August; 20(4): p. 577–595.

24. Saravanamuttoo HI, Rogers GFC, Cohen H. Gas Turbine Theory. 5th ed. Harlow, Essex: Pearson Education Limited; 2001.

25. MIT OpenCourseWare. Efficiencies of A/C Engines. [Online]. [cited 2013 October 15. Available from: http://ocw.mit.edu/ans7870/16/16.unified/propulsionS04/UnifiedPropulsion3/UnifiedPropulsion3.htm.

26. Singh R. Chairman's Address: Civil Aero Gas Turbines: Technology and Strategy. Cranfield, UK: IMechE Prestige Lecture - Post Nubes Lux: Aerospace Propulsion; 2001.

27. Ruffles PC. The Future of Aircraft Propulsion. Proceedings of the Institution of Mechanical Engineers, Part C: Journal of Mechanical Engineering Science. 2000 January; 214(1): p. 289-305.

28. International Civil Aviation Organization (ICAO). Aircraft Engine Emissions Databank. [Online]. [cited 2013 October 15. Available from: http://easa.europa.eu/environment/edb/aircraft-engine-emissions.php.

29. Federal Aviation Authority (FAA). Type Certificates. [Online]. [cited 2012 October 15. Available from: http://www.faa.gov/.

30. Lefebrve AH, Ballal DR. Gas Turbine Combustion 3rd Edition Boca Raton, Florida: CRC Press; 2010.

31. Wilfert G, Kriegl B, Wald L, Johanssen O. CLEAN-Validation of a GTF High Speed Turbine and Integration of Heat Exchanger Technology in an Environmental Friendly Engine Concept (ISABE-2005-1156). In Proceedings of the 17th International Symposium on Airbreathing Engines; 2005; Munich.

32. Shinmyo T, Okamoto K, Teramoto S, Nagashima T. Feasibility Study on Intercooled Turbofan Engines (ISABE-2011-1319). In Proceedings of the 20th International Symposium on Air Breathing Enignes; 2011; Gothenburg, Sweden.

33. Lundbladh A, Sjunnesson A. Heat Exchanger Weight and Efficiency Impact on Jet Engine Transport Applications (ISABE-2003-1122). In Proceedings of the 16th International Symposium on Air Breathing Engines; 2003; Cleveland, Ohio, USA.

34. Xu L, Tomas G. Design and Analysis of an Intercooled Turbofan Engine. Journal of Engineering for Gas Turbines and Power. 2010 August; 132(11): p. 114503.1-4.

35. Min JK, Jeong JH, Ha MY, Kim KS. High Temperature Heat Exchanger Studies for Applications to Gas Turbines. Journal of Heat and Mass Transfer. 2009 December; 46(2): p. 175-186.

36. Rolt A, Kyprianidis K. Assessment of New Aeroengine Core Concepts and Technologies in the EU Framework 6 NEWAC Programme. In Proceedigns of the 27th Congress of the International Council of the Aeronautical Sciences (ICAS); 2010; Nice, France: ICAS.

37. Grönstedt T, Kyprianidis K. Optimisation of the Intercooled Turbofan Engine (GT2010-22519). In Proceedings of ASME Turbo Expo 2010: Power for Land, Sea and Air; 2010; Glasgow, UK.

38. Larsson L, Grönstedt T, Kyprianidis K. Conceptual Design and Mission Optimisation for a Geared Turbofan and an Open Rotor Configuration (GT2011-46451). In Proceedings of ASME Turbo Expo 2011; 2011; Vancouver, Canada.

39. Walker D, Regunath G, Carrotte J, Denman P, Rolt A. Aerodynamic Design of the Core Duct System for an Intercooled Aero Engine (ISABE-2011-1256). In Proceedings of the 20th International Symposium onAirbreathing Engines; 2011; Gothenburg, Sweden: ISABE.

40. Walker D, Carrotte JF, Rolt AM. Duct Aerodynamics for Intercooled Aero Gas Turbines: Constraints, Concepts and Design Methodology (GT2009-612). In Proceedings of ASME Turbo Expo 2009: Power for Land, Sea and Air; 2009; Orlando, Florida, USA.

41. Walker D, Carrotte J, Denman P, Rolt A. Aerodynamic Design of the Cooling Flow Duct System for an Intercooled Aero engine (ISABE-2011-1257). In Proceedings of the 20th International Symposium on Airbreathing Engines; 2011; Gothenburg, Sweden.

42. Hirst M. Garrett ATF 3 - A Power Unit for the Next Generation of Business Jets. Flight International. 1979 July 14: p. 108-112.

43. Van Nimwegen RR. Design Features of the Garrett ATF3 Turbofan Engine. In Proceedings of the National Aeronautic and Space Engineering and Manufacturing Meeting; 1971; Los Angeles, California, USA.

44. Evans JC. ATF3 Online Museum. [Online].; 2008 [cited 2011 November 10. Available from: http://www.atf3.org/ATF3_Online_Museum.html.

45. Flightglobal. Flightglobal Cutaways. [Online]. [cited 2012 October 15. Available from: http://www.flightglobal.com/cutaways/.

46. Norris JW, Epstein A, Roberge GD, Costa MW, Berryann AP, Kupratis DB, inventors; Reversed-Flow Core for a Turbofan with a Fan Gear Drive System. United States patent US 2011/0056208 A1. 2011 March 10.

47. Fielding JP. Introduction to Aircraft Design Cambridge: Cambridge University Press; 1999.

48. Raymer DP. Aircraft Design: A Conceptual Approach 4th Edition. 4th ed. Reston, Virginia, USA: AIAA; 2006.

49. Mattingly JD, Heiser WH, Pratt DT. Aircraft Engine Design. 2nd ed. Reston, Virginia, USA: AIAA; 2002.

50. Stricker JM. The Gas Turbine Engine Conceptual Design Process - An Intergated Approach. In Proceedings of the RTO AVT Symposium on “Design Principles and Methods for Aircraft Gas Turbine Engines"; 1998; Toulouse, France.

51. Ogaji S, Pilidis P, Hales R. TERA - A Tool for Aero-Engine Modelling and Management. In Proceedings of the 2nd World Congress on Engineering Asset Management and 4th International Conference on Conditiion Monitoring; 2007; Harrogate, UK.

52. Kyprainidis K. Multi-disciplinary Conceptual Design of Future Jet Engine Systems. PhD Thesis. Cranfield, UK: Cranfield University, Department of Power and Propulsion; 2010.

53. Dassault Systemes. Isight & the SIMULIA Execution Engine. [Online]. [cited 2013 October 15. Available from: http://www.3ds.com/products-services/simulia/portfolio/isight-simulia-execution-engine.

54. Simulia. Simulia Homepage. [Online]. [cited 2013 October 15. Available from: http://www.3ds.com/products/simulia/overview/.

55. Hills RG, Trucano TG. Statistical Validation of Engineering and Scientific Models: Background. Albuquerque, New Mexico: Sandia National Laboratories; 1999. Report No.: SAND99-1256.

56. Robinson S. Simulation: The Practice of Model Development and Use Chichester, West Sussex: John Wiley & Sons Ltd; 2007.

57. Sargent RG. Verification and Validation of Simulation Models. In Proceedings of the 1998 Winter Simulation Conference; 1998; Washington DC, USA.

58. Law AM. Simulation Modelling and Analysis. 4th ed. New York, New York, USA: McGraw-Hill; 2007.

59. Kirby MR, Mavris DN. Forecasting Technology Uncertainty in Preliminary Aircraft Design (1999-01-5631). In Proceedings of the World Aviation Conference; 1999; San Francisco, California, USA.

60. Bala A, Sethi V, Gatto EL, Pachidis V, Pilidis P. PROOSIS – A Collaborative Venture for Gas Turbine Performance Simulation using an Object Oriented Programming Schema (ISABE-2007-1357). In Proceedings of the 18th International Symposium on Air-breathing Engines; 2007; Beijing, China.

61. Denton JD. The 1993 IGTI Scholar Lecture: Loss Mechanisms in Turbomachines. Journal of Turbomachinery. 1993 October; 115(4): p. 621-656.

62. Koch CC. Loss Sources and Magnitudes in Axial-Flow Compressors. Journal of Engineering and Power. 1976 July; 98(3): p. 411-424.

63. Eltis EM, Wilde GL. The Rolls-Royce RB 211 Turbofan Engine. James Clayton Lecture, IMechE Proceedings. 1974; 188(37/74): p. 549-575.

64. Jacobsson D, Lundbladh A, Nilsson M, Ore S, Rolt A. The Lightweight Integration of Intercoolers to the Turbofan Engine (ISABE-1498-1506). In Proceedings of 20th International Symposium on Airbreathing Engines; 2011; Gothenburg, Sweden.

65. Guynn MD, Berton JJ, Fisher KL, Haller WJ, Tong MT, Thurman DR. Engine Concept Study for an Advanced Single-Aisle Transport. Hampton, Virginia, USA: NASA; 2009. Report No.: TM-2009-215784.

66. Glassman AJ. User Manual for the Updated Computer Code for Axial-Flow Compressor Conceptual Design. Cleveland, Ohio: NASA; 1992. Report No.: CR-189171.

67. Philpot MG. Practical Considerations in Designing the Engine Cycle in: Steady and Transient Performance Prediction of Gas Turbine Engines. Lecture Series. AGARD; 1992. Report No.: 183.

68. Kurzke J. Aero-Engine Design: A State of the Art. Lecture Series. von Karman Institute for Fluid Dynamics; 2002-2003.

69. Schreiber HA, Steinert W, Sonoda T, Arima T. Advanced High-Turning Compressor Airfoils for Low Reynolds Number Condition — Part II: Experimental and Numerical Analysis. Journal of Turbomachinery. 2004 October; 126(4): p. 482-492.

70. Schaffler A. Experimental and Analytical Investigation of the Effects of Reynolds Number and Blade Surface Roughness on Multistage Axial Flow Compressors. Journal of Engineering for Power. 1980 January; 102(1): p. 5-12.

71. DiOrio AG. Small Core Axial Compressors for High Efficiency Jet Aircraft. MSc Thesis. Cambridge, Massachusetts, USA: Massachusetts Institute of Technology; 2012.

72. Riegler C, Bauer M, Kurzke J. Some Aspects of Modeling Compressor Behavior in Gas Turbine Performance Calculations. Journal of Turbomachinery. 2000 February; 123(2): p. 372-378.

73. Kurzke J. GasTurb Details 5. User Manual. Aachen, Germany: Gasturb; 2007.

74. Locq D, Caron P. On Some Advanced Nickel-Based Superalloys for Disk Applications (AL03-01). Journal AerospaceLab. 2011 November;(3).

75. Barack WN, Domas PA. An Improved Turbine Disk Design To Increase Reliability of Aircraft Jet Engines. Cincinnati, Ohio, USA: NASA; 1976. Report No.: CR-135033.

76. Ummiti MB, Sitram N, Prasad BVSSS. Computational Investigation of Effect of Axial Spacing on Blade Row Interaction in a 1 1/2 Stage Axial Flow Turbine. Engineering Applications of Computational Fluid Mechanics. 2009 March; 3(1): p. 56-70.

77. Restemeier M, Jeschke P, Guendogdu Y, Gier J. Numerical and Experimental Analysis of the Effect of Variable Blade Row SPacing in a Subsonic Axial Turbine. In Proceedings of ASME Turbo Expo 2011: Power for Land, Sea and Air; 2011; Vancouver, British Columbia, Canada.

78. Sanghi V, Kumar SK, Sundararajan V, Sane SK. Preliminary Estimation of Engine Gas-Flow-Path Size and Weight. Journal of Propulsion and Power. 1998 March-April; 14(2): p. 208-214.

79. Purohit K, Sharma CS. Design of Machine Elements. 1st ed.: PHI Learning; 2009.

80. Grönstedt T. Conceptual Aero Engine Design Modelling - Engine Sizing. Course Notes. Gothenburg, Sweden: Chalmers University of Technology; 2011.

81. Tong MT, Halliwell I, Ghosen LJ. A Computer Code for Gas Turbine Engine Weight Estimation and Disk Life Estimation. In Proceedings of ASME TurboExpo 2002: Power for Land, Sea and Air; 2002; Amsterdam, Netherlands.

82. Gutzwiller DP. Automated Design, Analysis, and Optimization of Turbomachinery Disks. MSc Thesis. Cincinatti, Ohio, USA: University of Cincinatti; 2008.

83. Gutzwiller DP, Turner MG. Rapid Low Fidelity Turbomachinery Disk Optimization. Advances in Engineering Software. 2010 February; 41(5): p. 779–791.

84. Malkin I. Design and Calculation of Steam-Turbine Disk Wheels. Transactions of the American Society of Mechnical Engineers. 1934; 56(8): p. 585-600.

85. Ersavas F. Multidisciplinary Conceptual Design of a Transonic High Pressure Compressor. MSc Thesis. Gothenburg, Sweden: Chalmers University of Technology; 2011. Report No.: ISSN 1652-8557.

86. Gean MC. Elevated Temperature Fretting Fatigue of Nickel Based Alloys. PhD Thesis. Ann Arbor, Michigan, USA: Purdue University; 2008. Report No.: UMI: 3343977.

87. Shamblen CE, Allen RE, Walker FE. Effect of Processing and Microstructure on René 95. Jouranl of Metallurgical Transactions A. 1975 November; 6(11).

88. Smith CW. Aircraft Gas Turbines New York: John Wiley & Sons. Inc.; 1956.

89. Sawyer JW. Sawyer's Gas Turbine Engineering Handbook (Volume 1). 2nd ed.: Gas Turbine Engineering Publications Inc.; 1972.

90. Faragher JS, Antoniou RA. Preliminary Finite Element Analysis of a Compressor Disk in the TF30 Engine. Melbourne, Australia: Defence Science and Technology Organisation, Airframes and Engines Division; 2000. Report No.: DSTO-TR-0915.

91. Gunston B. Jane's-Aero Engines: Jane's Information Group; 2000.

92. Mathias DM. Fundamentals of Turbine Design. In Logan EJ, Roy R, editors. Handbook of Turbomachinery. New York: Marcel Dekker Inc.; 2003. p. 312-366.

93. Grönstedt T. Conceptual Aero Engine Design Modelling - Efficiency Prediction. Course Notes. Gothenburg: Chalmers University of Technology; 2011.

94. Lakshminarayana B. Methods of Predicting the Tip Clearance Effects in Axial Flow Turbomachinery. Journal of Basic Engieering. 1970 September; 92(3): p. 467-480.

95. Sitram N, Lakshminarayana B. End Wall Flow Characteristics and Overall Performance of an Axial Flow Compressor Stage. Washington D.C., USA: NASA; 1983. Report No.: CR-3671.

96. Montella F, van. Buijtenen JP. A Simplified Method to Evalaute the Impact of Component Design on Engine Performance (GT2007-28051). In Proceedings ASME Turbo Expo 2007: Power for Land, Sea and Air; 2007; Montreal, Canada.

97. Ciofalo M, Piazza ID, Stasiek JA. Investigation of Flow and Heat Transfer in Corrugated-Undulated Plate Heat Exchangers. Journal of Heat and Mass Transfer. 2000 September; 36(5): p. 449-462.

98. Stasiek J, Collins MW, Ciofalo M, Chien PE. Investigation of Flow and Heat Transfer in Corrugated Passages - I. Experimental Results. Journal of Heat and Mass Transfer. 1996 January; 39(1): p. 149-164.

99. Ciofalo M, Stasiek J, Collins MW. Investigation of Flow and Heat Trasfer in Corrugated Passages - II. Numerical Simulations. Journal of Heat and Mass Trasfer. 1996 January; 39(1): p. 165-192.

100. Kwan PW, Gillespie DRH, Stieger RD, Rolt AM. Minimising Loss in a Heat Exchanger Installation for an Intercooled Turbofan Engine (GT2011-45814). In Proceedings of ASME Turbo Expo 2011; 2011; Vancouver, Canada.

101. Kwan PW. Flow Management in Heat Exchanger Installations for Intercooled Turbofan Engines. D.Phil Thesis. Oxford, UK: University of Oxford; 2011.

102. Doo JH, Ha MY, J.K. Min RS, Rolt A, Son C. Theoretical Prediction of Longitudinal Heat Conduction Effect in Cross-Corrugated Heat Exchanger. International Journal of Heat and Mass Transfer. July 2012; 55(15-16): p. 4129-4138.

103. Doo JH, Ha MY, Min JK, Stieger R, Rolt A, Son C. An Investigation of Cross-Corrugated Heat Exchanger Primary Surfaces for Advanced Intercooled-Cycle Aero Engines (Part-I: Novel Geometry of Primary Surface). International Journal of Heat and Mass Transfer. 2012 September; 55(19-20): p. 5256-5267.

104. Doo JH, Ha MY, Min JK, Stieger R, Rolt A, Son C. An Investigation of Cross-Corrugated Heat Exchanger Primary Surfaces for Advanced Intercooled-Cycle Aero Engines (Part-II: Design Optimization of Primary Surface). International Journal of Heat and Mass Transfer. 2013 June; 61: p. 138-148.

105. Fukui K, Kawakami Y, Okamoto K, Shinmya T. Compact Heat Exchangers for Intercooled Turbofan Engines (ISABE-2011-1603). In Proceedings of 20th International Symposium on Airbreathing Engines; 2011; Gothenburg, Sweden.

106. Utriainen E, Sundén B. Evaluation of the Cross Corrugated and Some Other Candidate Heat Transfer Surfaces for Microturbine Recuperators. Journal of Engineering for Gas Turbines and Power. 2000 September; 124(3): p. 550-560.

107. Guerra RO. Parametric Study of a Compact Intercooler for a Reverse Flow Core Intercooled Turbofan Engine Concept. MSc Thesis. Cranfield, UK: Cranfield University, Departmen of Power and Propulsion; 2013.

108. Kays WM, London AL. Compact Heat Exchangers. 3rd ed. Florida: Krieger Publishing Company; 1998.

109. Zhao X, Grönstedt T, Kyprianidis KG. Assessment of the Performance Potential for a Two-Pass Cross Flow Intercooler For Aero Engine Applications (ISABE-2013-10266). In Proceeedings of the 21st International Symposium on Airbreathing Engines; 2013; Busan, South Korea.

110. Hausen H. Heat Transfer in Counterflow Parallel Flow and Cross Flow. 1st ed. New York: McGraw-Hill; 1983.

111. Holman JP. Heat Transfer. 9th ed. New York: McGraw-Hill; 2002.

112. Khan WA, Culham JR, Yovanovich MM. Convection heat transfer from tube banks in crossflow: Analytical approach. International Journal of Heat and Mass Transfer. 2006 December; 49(16): p. 4831–4838.

113. Hammock GL. Cross-Flow, Staggered-Tube Heat Exchanger Analysis for High Enthalpy Flows. MSc Thesis. Knoxville, Tennessee, USA: University of Tennessee; 2011.

114. Zukauskas A. Convective Heat Transfer in Cross Flow. In Kakac S, Shah RK, Aung. W. Handbook of Single-Phase Convective Heat Transfer. New York: Wiley-Interscience Puplication; 1987.

115. Gnielski V. New Equations for Heat and Mass Transfer in TurbUlent Pipe and Channel Flow. International Journal of Chemical Engineering. 1976; 16(2): p. 359-368.

116. Jakob M. Flow Resistance in Cross Flow of Gases over Tube Banks. Transaction of the American Society of Mechanical Engineers. 1938; 60: p. 384-386.

117. Haaland SE. Simple and Explicit Formulas for the Friction in Turbulent Pipe Flow. Journal of Fluids Engineering. 1983 March; 105(1): p. 89-90.

118. Hermann R, Burbach T. Strömungswiderstand und Wärmeübergang in Rohren Leipzig: Akad. Verlagsges.; 1930.

119. Guha A. Optimum Fan Pressure Ratio for Bypass Engines with Separate or Mixed Exhaust Streams. Journal of Propulsion and Power. 2001 September; 17(5): p. 117-1122.

120. Sanghi V, Lakshmanan BK. Optimum Mixing of Core and Bypass Streams in High-Bypass Civil Turbofan. Journal of Power and Propulsion. 2002 August; 18(4): p. 907-911.

121. Millhouse PT, Kramer SC, King PI, Mykytka EF. Identifying Optimal Fan Compressor Pressure Ratios for the Mixed-Stream Turbofan Engine. Journal of Power and Propulsion. 2000 February; 16(1): p. 79-86.

122. Frost TH. Practical Bypass Mixing Systems for Fan Jet Aero Engines. The Aeronautical Quarterly. 1966 May;: p. 141-160.

123. Pearson H. Mixing of Exhaust and By-pass Flow in a By-pass Engine. Journal of the Royal Aeronauticla Society. 1962 August; 66: p. 528-530.

124. Stratford BS, Williams JG. A Simplified Treatment of Losses for One-Dimensional Mixing Between Hot and Cold Gas Streams at Constant Pressure and Low Velocity. London, UK: Ministry of Aviation, Aeronautical Research Council; 1963. Report No.: C.P. No. 686.

125. Rayee T, Verstraete D, Hendrick P. Development of a Mixer Model to Compare Mixed and Unmixed HBPR Turbofans. In 44th AIAA/ASME/SAE/ASEE Joint Propulsion Conference & Exhibit; 2008; Hartford, Connecticut, USA. p. 4502-4508.

126. Hurley JF, l'Anston L, Wilson CA. Design of an Exhuast Mixer Nozzle for the AVCO Lycoming Queit Clean General Aviation Turbofan (QCGAT). Washington D.C., USA: NASA; 1978. Report No.: CR-159426.

127. Cullom R, Bobula GA, Burkardt LA. Mixing Effectiveness Test of an Exhaust Gas Mixer in a High Bypass Turbofan at Altitude. In Proceedings of the 7th Joint Propulsion Conference; 1981; Colorado Springs, Colorado, USA.

128. Michel U. The Benefits of Variable Area Fan Nozzles on Turbofan Engines. In Proceedings of the 49th AIAA Aerospace Sciences Meeting; 2011; Orlando, Florida, USA.

129. Zimbrick RA, Colehour JL. Investigation of Very High Bypass Ratio Engines for Subsonic Transports. Journal of Propulsion and Power. 1990; 6(4): p. 490-496.

130. Mabe J. Variable Area Jet Nozzle for Noise Reduction using Shape Memory Alloy Actuators. Journal of the Acoustical Society of America. 2008 May; 123(5): p. 3871-3871.

131. Guynn MD, Berton JJ, Fisher KL, Haller WJ, Tong MT, Thurman DR. Refined Exploration of Turbofan Design Options for an Advanced Single-Aisle Transport. Hampton, Virginia, USA: NASA; 2011. Report No.: TM-2011-216883.

132. Guynn M, Berton J, Fisher K, Haller W, Tong M, Thurman D. Analysis of Turbofan Design Options for an Advanced Single-Aisle Transport Aircraft. In Proceedings of the 9th AIAA Aviation Technology, Integration, and Operations Conference (ATIO); 2009; Hilton Head, South Carolina, USA.

133. Daggett DL, Brown ST, Kawai RT. Ultra-Efficient Engine Diameter Study. Washington D.C., USA: NASA; 2003. Report No.: CR-2003-212309.

134. Pera RJ, Onat E, Klees. GW, Tjonnel E. A Method to Estimate Weight and Dimensions of Aircraft Gas Turbine Engines-Final Report. Washington D.C., USA: NASA; 1977. Report No.: CR 1351 70.

135. Oates G. Performance Estimation for Turbofan with and without Mixers. Journal of Propulsion and Power. 1985 June; 1(3): p. 252-256.

136. Faber J, Greenwood D, Lee D, Mann M, Leon PMd, Nelissen D, et al. Lower NOx at Higher Altitudes - Policies to Reduce the Climate Impact of Aviation NOx Emission. Delft, Netherlands:; 2008. Report No.: Publication number: 08.7536.32.

137. Sausen R, Isaksen I, Grewe V, Hauglustaine D, Lee DS, Myhre G, et al. Aviation Radiative Forcing in 2000: An Update on IPCC (1999). Meteorologische Zeitschrift. 2005 August; 14(4): p. 555-561.

138. Noppel FG. Contrail and Cirrus Cloud Avoidance Technology. PhD Thesis. Cranfield, UK: Cranfield University, Department of Power and Propulsion; 2007.

139. Shull JD. A Validation Study of the Air Force Weather Agency (AFWA) JETRAX Contrail Forecast Algorithm. MSc Thesis. Ohio, USA: Air Force Institute of Technology; 1998.

140. Schrader ML. Calculations of Aircraft Contrail Formation Critical Temperatures. Journal of Applied Meteorology. 1997 December; 36(12): p. 1725-1729.

141. Gierens K, Kaarcher B, Mannstein H, Mayer B. Aerodynamic Contrails: Phenomenology and Flow Physics. Journal of the Atmospheric Sciences. 2009 February; 66: p. 217-226.

142. The Commision of the European Communities. Commision Regulation (EC) No 8/2008. Official Journal of the European Union. 2007 December.

143. Chandrasekaran N, Guha A. Study of Prediction Methods for NOx Emission from Turbofan Engines. Journal of Propulsion and Power. 2012 January-February; 28(1): p. 170-180.

144. Baughcum SL, Tritz TG, Henderson SC, Pickett DC. Scheduled civil aircraft emission inventories for 1992: Database development and analysis. Hampton, Virginia, USA: NASA; 1996. Report No.: CR-4700.

145. Dopelheuer A, Lecht a. Influence of Engine Performance on Emission Characteristics. In Proceedings of the Symposium on Gas Turbine Engine Combustion, Emissions and Alternative Fuels; 1998; Lisbon, Portugal.

146. Norman PD, Lister DH, Lecht M, Madden P, Park K, Penanhoat O, et al. Development of the technical basis for a New Emissions Parameter covering the whole AIRcraft operation: NEPAIR. Technical Report. European Community; 2003. Report No.: NEPAIR/WP4/WPR/01.

147. Tsalavoutas A, Kelaidis M, Thoma N, Mathioudakis K. Correlation Adapation for Optimal Emissions Prediction. In Proceedings of ASME Turbo Expo 2007: Power for Land, Sea and Air; 2007; Montreal, Canada.

148. Colantuoni S, S.Bake , J.P.Badet. Low Emissions Combustors Development for New Aero-Engines Core Applications. In Proceedings of the 5th European Congress on Computational Methods in Applied Sciences and Engineering; 2008; Venice, Italy.

149. Ashcraft SW, Padron AS, Pascioni KA, Stout GW, Huff DL. Review of Propulsion Technologies for N+3 Subsonic Vehicle Concepts. Cleveland, Ohio, USA: NASA; 2011. Report No.: TM-2011-217239.

150. Tacina RR, Wey C, Choi KJ. Flame Tube NOx Emissions Using a Lean-Direct-Wall-Injection Combustor Concept. Cleveland, Ohio, USA: NASA; 2001. Report No.: TM-2001-211105.

151. Tacina R, Wey C, Laing P, Mansour A. A Low NOx Lean-Direct Injection, Multipoint Integrated Module Combustor Concept for Advanced Aircraft Gas Turbines. Cleveland, Ohio, USA: NASA; 2002. Report No.: TM—2002-211347.

152. Tacina KM, Lee CM, Wey C. NASA Glenn High Pressure Low NOx Emissions Research. Cleveland, Ohio, USA: NASA; 2008. Report No.: TM-2008-214974.

153. Imperial College of London. Dynamic Cost Indexing. Technical Discussion Document 4.2. London: Eurocontrol; 2008. Report No.: C06/12400BE.

154. Köhler MO, Radel G, Dessens O, Shine KP, Rogers HL, Wild O, et al. Impact of Perturbations to Nitrogen Oxide Emissions from Global Aviation. Journal of Geophysical Research. 2008 June; 113(D11): p. D11305 1-15.

155. Kalnay E, Kanamitsu M, Kistler R, Collins W, Deaven D, Gandin L, et al. The NCEP/NCAR 40 Year Reanalysis Project. Bulletin of the American Meteorological Society. 1996 March; 77(3): p. 437-471.

156. Viklund A. Free Map Tools. [Online]. [cited 2013 December 1. Available from: http://www.freemaptools.com/.

157. Noppel F, Singh R, Taylor M. Contrail and Cirrus Cloud Avoidance. In Proceedings of 25th International Congress of the Aeronautical Sciences; 2006; Hamburg, Germany.

158. Lolis P, Balasubramaniam AS, Sethi V, Pilidis P. A New Empirical Aero Gas Turbine Preliminary Weight Estimation Method Based on Artificial Neural Networks (3579). In Proceedings of Society of Allied Weight Engineers 71st Annual Conference; 2012; Bad Gögging, Germany.

159. Federal Aviation Administration. Data Sheet E7WE. Type Certificate. FAA, Department of Transport; 2000.

160. Laskaridis P. Performance Investigations and Systems Architectures for the More Electric Aircraft. PhD Thesis. Cranfield, UK: Cranfield University, Department of Power and Propulsion; 2004.

161. Anderson JD. Aircraft Performance & Design. 1st ed. Kane KT, editor.: McGraw-Hill Higher Education; 1998.

162. Jenkinson L, Simpkin P, Rhodes D. Civil Jet Aircraft Design: Butterworth-Heinemann Ltd ; 1999.

163. Roskam J. Airplane Design Ottawa, Kansas, USA: Roskam Aviation and Engineering Corporation; 1985.

164. Torenbeek E. Synthesis of Subsonic Airplane Design Rotterdam, Netherlands: Delft University Press; 1976.

165. Williams JE, Vukelich SR. The USAF Stability and Control Digital DATCOM. User Manual. St. Louis, Missouri, USA: McDonnell Douglas Astronautics Company; 1979. Report No.: AFFDL-TR-79-3032.

166. Becker R, Schaefer M, Reitenbach S. Assessment of the Efficiency Gains Introduced by Novel Aero Engine Concepts (ISABE-2013-1720). In Proceedings of the 21st International Symposium on Airbreathing Engines; 2013; Busan, South Korea.

167. Gur O, Mason WH, Schetz JA. Full-Configuration Drag Estimation. Journal of Aircraft. 2010 July-August; 47(4): p. 1356-1367.

168. Hoerner SF. Fluid Dynamic Drag. 2nd ed. Bakersfield, California, USA; 1965.

169. Ojha SK. Flight Performance of Aircraft Washington D.C., USA: American Institute of Aeronautics and Astronautics; 1995.

170. Asselin M. An Introduction to Aircraft Performance. 1st ed. Washington D.C., USA: American Institute of Aeronautics and Astronautics; 1997.

171. Aircraft Commerce. A330-200 & -300 Fuel Burn Performance. Aircraft Commerce. 2008 April/May: p. 16-19.

172. Tong MT, Naylor BA. An Object Oriented Computer Code for Aircraft Engine Weight Estimation. Cleveland, Ohio, USA: NASA; 2009. Report No.: TM 2009-215656.

173. Jackson AJB. Optimisation of Aero and Industrial Gas Turbine Design for the Environment. PhD Thesis. Cranfield, UK: Cranfield University, Department of Power and Propulsion; 2009.

174. Sagerser DA, Krebs RP, Lieblein S. Empirical Expressions for Estimating Length and Weight of Axial-Flow Components of VTOL Powerplants. Cleveland, Ohio, USA: NASA; 1971. Report No.: TM X-2406.

175. Onat E, Klees GW. A Method to Estimate Weight and Dimensions of Large and Small Gas Turbine Engines. Cleveland, Ohio, USA: NASA; 1979. Report No.: CR199481.

176. Beltramo MN, Trapp DN, Kimoto BW, Marsh DP. Parametric Study of Transport Systems Cost and Weight. Moffett Field, California, USA: NASA; 1977. Report No.: CR151970.

177. Appleman H. The Formation of Exhaust Contrails by Jet Aircraft. Bulletin of American Meteorological Society. 1953; 34: p. 14–20.

178. Schumann U. Influence of Propulsion Efficiency on Contrail Formation. Journal of Aerospace Science and Technology. 2000 September; 4(6): p. 391-401.

179. Schumann U, Busen R. Experimental Test of the Influence of Propulsion Efficiency on Contrail Formation. Journal of Aircraft. 2000 November-December; 37(6): p. 1083-1087.

180. Curry JA, Webste PJ. Thermodynamics of Atmospheres and Oceans London: Academic Press Inc; 1999.

181. Vomel H. Saturation Vapor Pressure Formulations. [Online]. [cited 2011 November 15. Available from: http://128.138.136.5/~voemel/vp.html.

182. Korolev A. Limitations of the Wegener–Bergeron–Findeisen Mechanism in the Evolution of Mixed-Pahse Clouds. Journal of the Atmospheric Sciences. 2007 September; 64: p. 3372-3375.

183. Peters JL. New Techniques for Contrail Forecasting. Illinois, USA: Air Weather Service; 1993. Report No.: TR--93/001.

184. Lefebrve AH, Ballal DR. Gas Turbine Combustion. 3rd ed. Boca Raton, Florida: CRC Press; 2010.